

4. SITE 1149¹

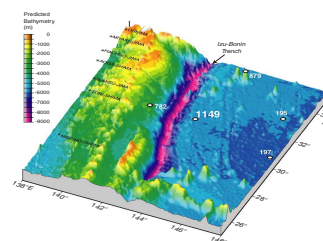
Shipboard Scientific Party²

BACKGROUND AND OBJECTIVES

In the same way as Site 801 is a reference site for Jurassic oceanic crust and overlying sediments being subducted into the Mariana Trench, Site 1149 is a reference site for Cretaceous oceanic crust and sediments being transported into the Izu-Bonin subduction zone. As discussed in the “Leg 185 Summary” chapter, the geochemical compositions of volcanic rocks erupted in the two arc systems show significant differences in key elements and, in particular, in Pb isotope compositions and Ba abundance. To understand the geochemical budgets in these arc systems, it is essential to characterize the input into the system via the subducting plate. This requires quantifying the geochemical composition of the sediments and the upper oceanic crust from which the bulk of the elements contributed from the subducting plate to the arc are derived. There is no continuously sampled section of the sediment in the Nadezhda Basin of the west Pacific Ocean that feeds the Izu-Bonin arc. In contrast sediment input to the Mariana arc has been relatively well sampled at Ocean Drilling Program (ODP) Sites 800, 801, and 802 (see Fig. F1, p. 65, in the “Site 801” chapter and Fig. F2, p. 36, in the “Leg 185 Summary” chapter). The volcanic basement in the Nadezhda Basin has been reached only once, at Deep Sea Drilling Project (DSDP) Site 197 (Fig. F1) where only 1 m of basalt was recovered. Site 1149 was thus selected from available seismic data at a position as close as possible to the Izu-Bonin Trench (see “**Tectonic Setting and Magnetic Anomalies,**” p. 2). The site was chosen based on the roughness of the basement, which indicated an absence of younger igneous intrusions in the lowermost sediments. In addition, the site chosen has a well-defined sedimentary sequence undisturbed by faulting or other structural complexities in the seismic stratigraphy.

Sampling and geochemical analysis of the recovered sediments and basement altered at low temperatures will be coupled with reconstruc-

F1. Bathymetry in area of Site 1149, p. 53.



¹Examples of how to reference the whole or part of this volume.
²Shipboard Scientific Party addresses.

tion of the cored (recovered and not recovered) lithologies by use of cored samples and logging. This will permit the calculation of a bulk geochemical composition for Cretaceous Pacific crust and its sediment cover being subducted beneath the Izu-Bonin arc. These results will be compared with those for the crustal and sedimentary sections being subducted in the Mariana arc.

Stratigraphic columns for DSDP sites in this region of the western Pacific are given in Figure F2. These are compared with a highly simplified section of the actual sequence drilled at Site 1149. The total sediment recovered in these four DSDP drill holes in Mesozoic Pacific crust is <40 m; none recovered more than 15 m. Drilling in all of the holes ran into difficulties penetrating the Mesozoic chert, chalk, and clay horizons that are found below ~200 m of pelagic sediment. These horizons are evident as strong reflectors beginning at 150–180 mbsf on seismic profiles in the Site 1149 area (see Fig. F3). The top of basement was interpreted to be located at ~400–420 mbsf. The well-defined sediment stratigraphy at Site 1149, in particular the Mesozoic section, permits

1. Testing of the Early Cretaceous paleomagnetic time scale. The site is on the older half of magnetic Anomaly M11 (Nakanishi et al., 1992) (see **“Tectonic Setting and Magnetic Anomalies,”** p. 2), which should correlate to a basement age of ~132 Ma, corresponding to the late Valanginian stage of the Early Cretaceous on the Channell et al. (1995) time scale. Coring the basement and sediment would test the proposed new time scale of Channell et al. (1995).
2. Determining Cretaceous paleolatitude history. As indicated in Figure F7, p. 41, in the “Leg 185 Summary” chapter, Site 1149 may have formed at ~5°S, drifted south to 10°S in its early history, and then gradually drifted north, crossing the paleoequator as the Pacific plate accelerated its northward motion at ~85–90 Ma. The site may thus provide constraints on the mid-Cretaceous carbonate compensation depth (CCD) and equatorial productivity zones.
3. Characterizing the pelagic sedimentation history and expected volcanic ashes in the upper 200-m section at Site 1149, which provide a complementary record to that recovered during Leg 124.

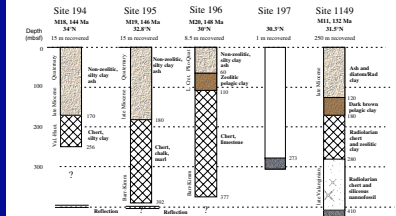
The location of Site 1149 is ~100 km east of the Izu-Bonin Trench (Fig. F1) where the westernmost extremity of the Pacific plate bends into the subduction zone and the plate surface is broken by normal faults (Fig. F4). The detailed geology and geophysics of the site are given in **“Seismic Stratigraphy,”** p. 4.

SITE GEOPHYSICS

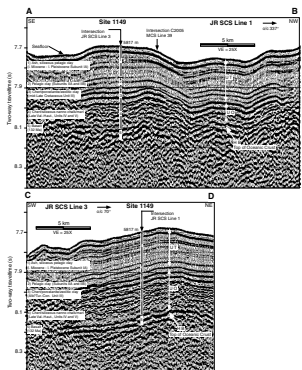
Tectonic Setting and Magnetic Anomalies

Site 1149 is located on the Pacific plate in the Nadezhda Basin south-east of Japan. It resides on a slight bathymetric high ~100 km east of the Izu-Bonin Trench where the Pacific plate is flexed upward before it enters the subduction zone (see **“Background and Objectives,”** p. 1, and Fig. F4). Nakanishi et al. (1992) charted magnetic lineations in the Site 1149 area that are part of a long, continuous reversal sequence

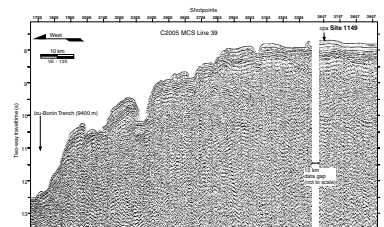
F2. Comparison of sedimentary sections, p. 54.



F3. Seismic stratigraphy at Site 1149, p. 55.



F4. MCS Line 39, p. 56.



within the Kashima fracture zone compartment, which includes Site 801 ~2200 km to the southeast (Fig. F5). This sequence ranges in age from ~125 to 180 Ma and becomes monotonically older from Early Cretaceous magnetic lineation M5 in the Nadezhda Basin near the Japan Trench, southeast through the Jurassic magnetic quiet zone in the Pigafetta Basin. This lineation pattern is part of a larger set of magnetic lineations east of Japan and north of Shatsky Rise called the Japanese magnetic lineations. These lineations were accreted to the northern boundary of the Pacific plate at a location near the paleoequator (Larson and Chase, 1972).

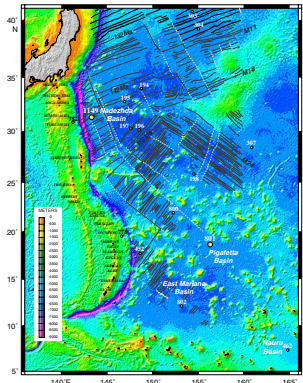
Magnetic anomalies are strongly linedated in a northeast-southwest direction (050°) in the vicinity of Site 1149. Figure F6 shows the majority of magnetic anomaly data collected by ships in the area superimposed on the predicted bathymetry. A fracture zone with a 5–10 km, right-lateral offset transects the area from north-northwest to south-southeast. This may not be an original feature of the seafloor spreading fabric as it is markedly nonorthogonal to the magnetic lineations, although it is much more orthogonal to the magnetic lineations farther south (Nakanishi et al., 1992). Thus, in the Site 1149 area the fracture zone may result from recent, northward propagation of an original transform fault because of bending stresses at the outer bulge of the subduction zone.

It appears that Nakanishi et al. (1992) identified magnetic Anomaly M12 in the vicinity of Site 1149 on their magnetic lineation chart, although that specific correlation is not described. Close inspection of the magnetic lineation pattern within the vicinity of Site 1149 suggests instead that Site 1149 lies on the older portion of magnetic Lineation M11 (Fig. F6). Using the magnetic reversal model of Channell et al. (1995), we generated the magnetic anomaly model profile with a constant half-spreading rate shown in Figure F6. The skewness (cross-sectional shape) of the profile is in accord with the original calculations of Larson and Chase (1972) and subsequent ones by Larson and Sager (1992).

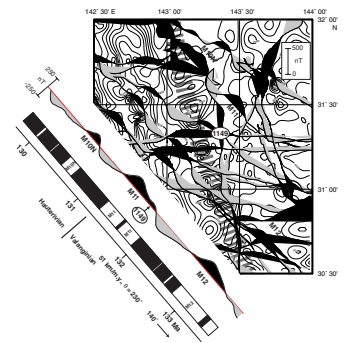
We consider this model to be a good fit to the charted magnetic anomalies, although the width of M11 on the chart is slightly less than in the constant spreading-rate model. The constant spreading rate of 51 km/m.y. is consistent with other portions of the Japanese lineation pattern of this age. The shapes of the magnetic anomalies are also in reasonable agreement with the model. In contrast, if we assume that the positive magnetic anomaly over Site 1149 is M12, such a model would require a much slower spreading rate between Site 1149 and an assumed M11 to the north and, conversely, a much faster spreading rate between Site 1149 and an assumed M13 to the south. The required spreading-rate change would be more than a factor of 2. Also, the short polarity intervals within such a model would bias the shapes of the model anomalies in ways that would be poorer matches to the charted data. Thus, we prefer the model solution shown in Figure F6; however, we cannot completely exclude the other solution where Site 1149 and magnetic Anomaly M12 are coincident.

Inspection of the location of Site 1149 relative to the magnetic reversal model suggests that Site 1149 lies on the older half of the reversed polarity interval M11. This stratigraphic position has a late Valanginian biostratigraphic age and a radiometric age of ~132 Ma on the Channell et al. (1995) time scale.

F5. Topography of study area showing magnetic lineations, p. 57.



F6. Magnetic anomalies and predicted bathymetry, p. 58.



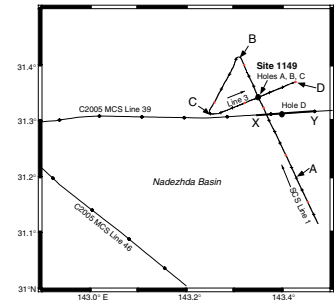
Seismic Stratigraphy

Selection for Site 1149 was initially based on two multichannel seismic (MCS) lines and sonobuoy data obtained during Cruise C2005 of the *Robert D. Conrad* in 1976. A short, single-channel seismic (SCS) and 3.5-kHz survey was conducted on approach to Site 1149 that confirmed the general seismic character and unit thicknesses observed in the MCS records. Holes 1149A, 1149B, and 1149C (near proposed site BON-10) are located at the intersection of *JOIDES Resolution* (JR) SCS Lines 1 and 3 just 3.5 km northwest of the proposed site location (Figs. F3, F7). Hole collapse in the sedimentary section and drill-string sticking problems were jeopardizing our objectives of further basement penetration and prompted us to place Hole 1149D at a location where the sediment section is significantly thinned. Following a short 3.5-kHz survey, Hole 1149D was placed at a promising location on C2005 MCS Line 39, ~5 km southeast of Holes 1149A, 1149B, and 1149C (see “Seismic Reflection Profiling,” p. 8, in the “Explanatory Notes” chapter).

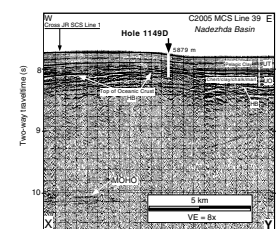
Ewing et al. (1968) originally defined the acoustic stratigraphy of large portions of the western Pacific as consisting of two or more of the following four seismic units: (1) an upper transparent layer (weakly reflective), (2) an upper opaque layer (highly reflective or well stratified), (3) a lower transparent layer, and (4) acoustic basement. Acoustic basement has been referred to as “Horizon B,” the “deep opaque layer,” and the “reverberant layer” and is characterized by an interval of flat-lying, smooth, high-amplitude, closely spaced reflections (Ewing et al., 1968; Houtz et al., 1970; Heezen, MacGregor, et al., 1973; Houtz and Ludwig, 1979). The reverberant nature of Horizon B is the result of a trailing bubble-pulse oscillation creating multiple reflections from each large impedance contrast and making it difficult to distinguish a relatively simple single interface (crust/sediment) from a sequence of stratified material. Reprocessing of the 1976-vintage MCS data included prestack predictive deconvolution, which significantly reduced the bubble-pulse amplitude but did not completely remove this often misleading artifact (Fig. F8). The use of water guns during the JR-185 SCS survey provided an implosive, bubble pulse-free source that produced a much higher resolution record of the sedimentary sequence and a clear image of the top of oceanic crust.

Early DSDP investigations (e.g., Legs 6, 7, 17, and 20) revealed the lithostratigraphic significance of the upper transparent and opaque layers in the western Pacific. The upper transparent layer corresponds to a variety of lithofacies: pelagic clay with ash in the west Pacific, pelagic clay in the central Pacific, turbidite sequences in the north and east, and biogenic oozes along the equator. The upper opaque layer has been correlated to the uppermost abundant chert in much of the north Pacific; however, DSDP Leg 32 Sites 303 and 304 (Fig. F5) on crust of Hauterivian age recovered chalk/limestone and chert within the upper opaque layer that lies directly on top of oceanic crust at these locations. Before Leg 32 in 1973 there was little direct knowledge of the lower transparent seismic unit and Horizon B in the oldest portions of the Pacific, and it was not until Legs 129 and 185 that these two deepest seismic facies were sampled in the East Mariana, Pigafetta, and Nadezhda Basins (Fig. F5). Results from DSDP Legs 6, 17, 61, 89, and 129 indicate that Horizon B in large areas of the Nauru, Pigafetta, and East Mariana Basins correlates to mid-Cretaceous volcanic material (sills, flows, and volcanogenic turbidites), which, according to magnetic anomaly identifications, significantly postdate the formation of oce-

F7. Track chart of Leg 185 SCS survey, p. 59.



F8. Seismic stratigraphy near Hole 1149D, p. 60.



anic crust (Winterer, 1976; Abrams et al., 1993; Shipley et al., 1993). DSDP Sites 303 and 304, 1600 km to the northeast, and ODP Site 801, 2200 km to the southeast, are the most proximal locations where Horizon B has proved to correlate to the top of oceanic crust of the Pacific plate (Larson, Moberly, et al., 1975; Lancelot, Larson, et al., 1992).

Reflections are most often interference patterns caused by the combined impedance effects of many thin beds, but exceptions include the sediment/oceanic crust interface or, in some cases, thick chert layers within a relatively uniform matrix. The correlations between lithologic units and the reflection image presented in Figures F3 and F8 were assigned without the guidance and constraints provided by a log-generated synthetic seismogram and should be considered a best estimate until an adequate synthetic seismogram can be generated postcruise.

The lowermost sequence, Horizon B, is characterized by a single or two to three closely spaced, high-amplitude, continuous reflector(s) when imaged with either air guns (C2005 MCS) (Fig. F8) or SCS water guns (Fig. F3). These continuous reflections range in appearance from relatively smooth and flat lying to diffractive and undulating, depending on seismic source and azimuth of profile direction. In Hole 1149B, Horizon B begins at 8.111 s two-way traveltime (s twt) or 0.42 s below seafloor (sbsf) (0.28 sbsf at the closest point of approach to Hole 1149D) and is interpreted to result from the impedance contrast between nanofossil chalk/marl and fractured basalt at 410 mbsf (307 mbsf at Hole 1149D). The velocity structure of this area is constrained by a single sonobuoy shot on the outer wall of the Izu-Bonin Trench ~50 km from Site 1149 (see Fig. F2, p. 57, in the “Explanatory Notes” chapter). This sonobuoy records refracted arrivals with velocities of 4.1 km/s increasing to 6.1 km/s beginning at ~528 mbsf, which was interpreted as a normal upper crustal section below 528 m of sediment (assuming a velocity of 2 km/s for the sediment section).

The lower transparent layer, which corresponds to Jurassic to lowest Cretaceous radiolarite and claystone at Site 801, is absent at Site 1149 where the upper opaque layer directly overlies oceanic crust (Horizon B). The single upper opaque layer as originally defined by analog air-gun records appears as two distinct seismic facies in SCS water-gun data. The upper portion of the upper opaque layer in Holes 1149A, 1149B, and 1149C extends from 0.20 to 0.28 sbsf (7.891–7.971 s twt) and consists of high-amplitude, semicontinuous reflections that mimic the underlying basement relief and appear as a stratified pelagic drape deposit of generally uniform thickness. The lower portion of the upper opaque zone appears as discontinuous, chaotic to hummocky reflections extending down to Horizon B and also exhibits pelagic sheet drape character because it is generally of uniform thickness and concordant with the underlying basement topography. The MCS air-gun record (Fig. F8) only shows a single, continuous, high-amplitude reflection ~0.167 sbsf in Hole 1149D that marks the top of the upper opaque zone. We interpret the reflection that appears regionally at ~0.16–0.2 sbsf as the shallowest abundant chert/porcelanite interbedded with clay at ~180 mbsf (Holes 1149A, 1149B, and 1149C) and 155 mbsf (Hole 1149D). This reflection is most likely the consequence of the abrupt contrasts in density and velocity that mark the boundary between Subunit IIB and Unit III (see “Density,” p. 45; “Compressional Wave Velocity Measurements,” p. 40; and “Subunit IIB,” p. 13). The change in seismic facies at ~0.28 sbsf (7.971 s twt) (Holes 1149A, 1149B, and 1149C) is interpreted as marking the increase in lithification and carbonate content (chalk/marl) of the matrix material interbedded with

chert corresponding to lithologic Unit IV (see “Unit IV,” p. 15). This boundary is marked by an abrupt increase in velocity at ~270 mbsf (see “Seismic Velocity,” p. 45). The disrupted, hummocky character of this unit may be a consequence of postdepositional deformation related to undercompaction of the open, mechanically interlocked, siliceous/carbonate-microfossil framework of the primary pelagic sediment.

The upper transparent layer is relatively thick and extends from the seafloor to ~0.16–0.2 sbsf (7.891 s twt) (Holes 1149A, 1149B, and 1149C). This unit has a pelagic sheet drape form and a relatively reflection-free seismic character in the upper portion with semicontinuous reflections of variable, but generally low, amplitude apparent in the lower portion of this interval. The “transparent” character is indicative of a relatively homogenous interval containing no significant impedance contrasts and is correlated to the unlithified siliceous ash-bearing clay of lithologic Unit IA. The weak, discontinuous reflections beginning at ~0.15 sbsf (Hole 1149A) may correlate to the Subunit IA/IIA boundary at ~118 mbsf, which is marked by abrupt changes in porosity, water content, and velocity (see “Compressional Wave Velocity Measurements,” p. 40). The relative thickness of this uppermost seismic unit is due to the significant input of volcanic ash, as well as biogenic silica, to an otherwise thin section produced from slow accumulation of pelagic clay.

OPERATIONS

Site 1149 (see Fig. F1), the second drill site of Leg 185, was located east of the Bonin Trench, ~1040 nmi northwest of Site 801 and 300 nmi south-southeast of Japan’s Boso Peninsula. Site 1149 was tentatively located on an east-west reference profile (Conrad 2005, Line 39) but a site survey was required to determine the best location for the site. The *JOIDES Resolution* approached the *Conrad* reference seismic line from the southeast, slowed to 6 kt, and streamed seismic gear ~12 nmi before crossing the reference line (see “Seismic Stratigraphy,” p. 4). The survey continued until a location with favorable basement characteristics was found (see “Seismic Stratigraphy,” p. 4). After a triangular seismic survey pattern was completed, the profiling gear was recovered and the ship returned to the Global Positioning System coordinates of the site. A positioning beacon was launched at 1500 hr on 23 May. The transit from Site 801 to Site 1149, including the 7-hr seismic survey was accomplished in 4.05 days, at an average speed of 11.4 kt.

Hole 1149A

Hole 1149A was spudded with a “mudline” core at 0200 hr on 24 May. The core barrel contained 4.2 m of core, which was interpreted as the sediment/water interface, fixing the seafloor depth at 5829.3 m from driller’s datum. Continuous advanced piston cores (APC) cores were taken with >100% recovery to 164 mbsf, when an abrupt increase in the stiffness of the sediment resulted in an incomplete APC stroke on Core 18H (Tables T1, T2).

APC cores were oriented in azimuth beginning with Core 4H. Temperature recording shoes were also run on Cores 4H, 6H, and 8H, and the Lamont-Doherty Earth Observatory (LDEO) drill string acceleration tool (DSA) was run on Cores 2H and 10H. Tracer experiments, to determine potential core contamination for microbiology studies, were car-

T1. Coring summary, p. 146.

T2. Expanded coring summary, p. 148.

ried out by fixing a bag of fluorescent microbeads into the core catchers of Cores 3H, 6H, 9H, and 12H and by pumping perfluorocarbon tracer into the drilling fluid on Cores 6H, 9H, and 11H (see [“Methods for Quantifying Potential Microbial Contamination during Deep Ocean Coring,”](#) Smith et al., 2000).

The APC system was replaced by the extended core barrel (XCB), which cored 24.3 m (i.e., Cores 19X–21X) with an average recovery of 21% in stiff clay with interbedded porcelanite (Tables [T1](#), [T2](#)). After 2.2 m penetration when cutting Core 22X, the XCB encountered a hard streak that halted penetration.

Further progress with the XCB system was highly unlikely because of the inability to penetrate the chert or porcelanite horizon. The situation had been anticipated, and the plan called for using the motor-driven core barrel (MDCB) system to attempt to core the chert layers. Although conditions were not favorable for the MDCB because of the presence of steel and tungsten carbide junk in the hole from the XCB shoe, it was nevertheless decided to attempt a MDCB core as a “last chance” to core the chert with an alternative system before tripping for the rotary core barrel (RCB) system. When the MDCB was recovered, the corehead was noted to have all the diamonds worn off the crown and to show signs of junk damage. The core barrel also showed grooving from junk. When the core catcher was removed, only 30 cm of chert and clay debris from the hole was found in the split and collapsed plastic liner. There was no indication that any core had been cut or that any new hole had been made by the corer.

Coring attempts in Hole 1149A were abandoned at that point, because there appeared to be no remaining alternatives to tripping for an RCB coring assembly. The MDCB system was rigged down, the top drive was racked, and the pipe trip began. Hole 1149A ended at 0725 hr on 26 May, when the bit arrived on deck.

Hole 1149B

Hole 1149B was 30 m northwest of Hole 1149A. No mudline core was planned, so the water depth was assumed to be the same as at Hole 1149A. The new hole was spudded at 2000 hr on 26 May and drilled ahead to core point at 161 mbsf in 3.5 hr. The “wash barrel,” which contained ~3.5 m of cored material and drilling rubble, was retrieved.

Continuous RCB coring then commenced (Tables [T1](#), [T2](#)). At ~190 mbsf, interbedded chert caused core recovery to drop sharply, and drilling conditions deteriorated. As much as 4 m of fill accumulated between cores, causing high torque, and the bit hammered on the chert ledges when the motion compensator was locked out. Only chert “rollers” were recovered in the core barrels, with traces of soft brown clay (probably representing unrecovered material). At ~261 mbsf, the ROP slowed considerably, and hole conditions improved markedly with depth. Recovered cores contained calcareous interbedded material with interbedded chert. Only a small amount of fill was present by the time basaltic basement was encountered at 410 mbsf while drilling Core 29R. Average core recovery in the cherty interval from 190 to 410 mbsf was only ~6%. Although it had penetrated >200 m of cherty sediments, the core bit had accrued only 21 rotating hr when it reached basement. The condition of the cutting structure was unknown, but the plan for the hole called for running the bit to destruction. Penetration of the highly altered basalt continued at >2 m/hr through Core 32R with a recovery rate of ~20%. At the time the core barrel for Core 33R had been

dropped, however, without warning the drill string became partially stuck. Indications were that chert or basalt fragments were wedging the bottom-hole assembly (BHA), either at the top or at the bit. The string could be moved up or down in irregular intervals before it would torque up and bind vertically. A mud pill was circulated while the string was worked free, and the inner core barrel landed during the process. Eventually three “knobby” joints were removed from the string as the bit was pulled upward. When the bit passed the approximate depth of the sediment/basalt contact, the resistance ceased. A joint of drill pipe then was added to the drill string, but circulation was nearly plugged off when the pump was restarted. Because the inner barrel had held the float valve open while the pipe was being freed, cuttings had been able to flow back into the jets of the bit. It was then necessary to make a wireline trip to retrieve the inner barrel and regain normal circulation. A total of 4½ hr was spent on the consecutive hole problems.

Although additional basement penetration was planned, the highest remaining scientific priority of Leg 185 was a good set of logs of the sediment section at Site 1149. The onset of difficulties with the hole was a reminder that coring to bit destruction could result in loss of the hole and preclude the opportunity for downhole logging. Because there was ~35 m of “rathole” for the logs to record the base of the sediment section, plans were changed to terminate coring in Hole 1149B and proceed with logging operations. When logging operations were completed at 0900 hr on 2 June, the drill string was tripped, and Hole 1149B was completed when the mechanical bit release top connector arrived on deck at 2000 hr on 2 June.

Hole 1149C

Hole 1149C was spudded at 0820 hr on 3 June and was drilled without coring to 283.6 mbsf. Two “wash” core barrels were pulled at 237 and 283.6 mbsf as a precaution because of the accumulation of loose chert fragments in Hole 1149B. After the wash core barrel at 283.6 mbsf was retrieved, preparations began for retrieving four spot cores requested by the science party. A short trip back to 188 mbsf to replace the “knobby” drilling joints was slowed by the torquing and sticking of the drill string. Although a considerable amount of soft fill was found in the hole, the string was free as it returned to total depth, and coring began.

Mud was circulated while the first core (3R) was being cut (Tables T1, T2), but torquing and sticking tendencies returned during the wireline trip to retrieve it. It was necessary to “work” the pipe for 3½ hr and to pull back to 245 mbsf before Core 4R could be cut to 303 mbsf and retrieved. Almost immediately after the barrel for Core 5R was dropped, the drill string began to torque and stick again. While the string was being worked up the hole with restricted circulation, the inner barrel landed, opening the float valve. When the next joint of pipe was removed from the string, backflow plugged the pipe. Rotation and vertical movement were possible, so the bit was pulled to 235 mbsf before a wireline trip was made to retrieve the inner barrel and re-establish normal circulation.

The cause of the hole cleaning problems was believed to be the interval of dark brown clay with lower porosity and shear strength between 150 and 180 mbsf that had stopped logging tools in Hole 1149B (see “Shear Strength,” p. 41, and “Abstract,” p. 41). Therefore, a “wiper trip” was made to 130 mbsf to ream out any clay restriction. No resis-

tance was noted in either direction until the bit returned to ~235 mbsf, where a solid ledge was encountered. Several other ledges were noted as the top drive was used to clean the hole back to total depth, and ~4 m of fill was found on bottom. After the inner barrel was pumped into place, Cores 5R and 6R were cut and retrieved without incident, but the combined recovery was only 78 cm of chert and chalk core pieces.

With a wash barrel in place, the hole was drilled ahead to 388 mbsf, the next requested core point to sample the sediment/basement interface. Because of the history of hole problems, the knobby joints were laid out and a precautionary short trip was made back up to 130 mbsf, above the unstable clay zone. No resistance registered on the weight indicator, but the top drive was picked up to ream through the clay zone and to clean the hole back to total depth with circulation and rotation. The hole was clean, with only 3 m of soft fill, but an additional 50 bbl of mud was pumped to sweep out any debris. Core 8R then was cut with all parameters normal, and 1 m of chert/chalk core was recovered.

Before the inner barrel was dropped to cut Core 9R, the pipe began to torque and stick. Additional working of the pipe resulted in more sticking. For 4 hr, various circulation rates, amounts of overpull, and stuck-pipe techniques were tried. Success was slowly achieved by “drilling up” or backreaming with tension just short of the amount that would produce stalling of the top drive. Progress up the hole of ~1 m/hr was achieved with that technique. Circulation had been held to moderate rates to avoid excessive hole erosion, but a desperation move involving use of both mud pumps at 90 strokes per minute (spm) produced enough improvement in the backreaming progress that a joint of pipe could be removed. The pipe was set on the elevators with 80 kips overpull to break out the joint. When it was reconnected to the top drive and lifted off the elevators, it was free. The string then was pulled to ~60 m of total depth with no resistance and run back to bottom, where ~4 m of fill was found. The cause of the sticking was believed to be gravel-sized chert fragments that had settled around the BHA.

Hard basement drilling was encountered 2 m into drilling Core 9R (at 401 mbsf), allowing a higher coring circulation rate to be used for the remainder of the core. The pattern of stuck pipe following core retrieval continued after both Cores 9R and 10R, with average core recovery of only ~15% (Tables T1, T2). It became apparent that chronic sticking problems were leading to excessively slow recovery of material and that continuing to operate in Hole 1149C eventually would result in loss of the hole and the BHA. While Core 11R was being cut, a decision to relocate had been made, and the trip out of the hole began as soon as the core had been recovered. The bit arrived on deck at 0215 hr on 7 June. The vessel got under way at 0300 hr, ending Hole 1149C.

Hole 1149D

The 3.5-kHz echosounder was used to refine the desired offset position on a nearby basement high. A new beacon was dropped at 0515 hr on 7 June ~3.1 nmi east-southeast of Hole 1149A, and Hole 1149D was spudded at 1530 the same day. Hole 1149D was drilled to basement without coring and without pulling the wash barrel.

Drilling parameters indicated chert stringers beginning at ~155 mbsf. No hole problems were encountered except for an incident of sticking during the rereaming of the interval to 263 mbsf. At 272 mbsf, a wash core barrel was pulled to initiate continuous coring in anticipation of

encountering basement (Tables T1, T2). Three consecutive cores then produced a combined total of 1.2 m of chert fragments. Basement was encountered at 307 mbsf while coring Core 5R. During coring of Hole 1149D, some problems were encountered with sticking and torquing of the pipe, which caused some delays. However, coring continued until through Core 19R, when the time allotted for coring had expired. Hole 1149D was deepened to a total depth of 6319.4 m (440.4 mbsf). Departure from Site 1149 was at 1615 hr on 13 June.

SEDIMENTOLOGY

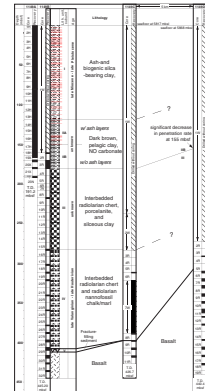
Abstract

A sedimentary section of 408 m total thickness was recovered in the four holes that were drilled at Site 1149. The sediments predominantly consist of carbonate-free clays with variable admixtures of volcanic ash and siliceous microfossils, cherts, porcelanites, and calcareous nannofossil cherts or marls. On the basis of the distribution of these lithologies, the sedimentary column between 0 and 408.2 mbsf has been divided from top to bottom into five lithologic units (Fig. F9).

Unit I, of late Miocene to late Pleistocene age, reaches 118 m thickness and consists of carbonate-free clay with common ash particles and siliceous microfossils. Unit II consists of 62 m of undated dark brown pelagic clays with several discrete ash layers in the upper 30 m (Subunit IIA). Unit II clays are barren of any siliceous or calcareous microfossils but contain ichthyoliths. At this time, however, their age is undetermined. Unit III is a 104-m-thick alternation of radiolarian chert with porcelanite and siliceous clay, the age of which is again to be determined by shore-based research. Unit IV comprises 125 m of upper Valanginian to upper Hauterivian intercalated radiolarian chert, porcelanite, and siliceous cherts or marls. Unit V, which is upper Valanginian recrystallized calcareous marlstone, was found only in fractures in the upper 2 m of basement in Hole 1149B.

The evolution of the depositional environments at Site 1149 can be divided into four broad episodes, starting in the late Valanginian (~133 Ma) with the onset of calcareous pelagic sedimentation on oceanic crust, and subsidence to below the CCD after 7 m.y.; thereafter, 100 m of radiolarian cherts, porcelanites, and clays without detectable carbonate accumulated, probably still in the Early Cretaceous. The change from siliceous deposition to the very slowly accumulated brown pelagic clays of Unit II presumably occurred during the Late Cretaceous to Paleogene. This abrupt decrease in siliceous deposition may correlate with the changing direction and the more rapid northward movement of the Pacific plate, which probably brought the site to below the oligotrophic waters of the large gyre that covered much of the mid-latitude Pacific during the Cenozoic. At some unknown point in time, but before the late Miocene, Site 1149 approached the Izu-Bonin and Japan volcanic arcs as documented by numerous discrete ash layers and significant amounts of dispersed ash in the sediments of Unit I. Subsequent to the onset of volcanic input, biosiliceous deposition resumed with the accumulation of both planktonic and benthic siliceous microfossils. Very high sediment accumulation rates and the mineral composition of the youngest sediments suggest that Site 1149 was in the reach of the Asian dust plumes after the early Pleistocene.

F9. Synthetic stratigraphic section, p. 61.



Lithostratigraphy

Site 1149 is located ~100 km east of the Bonin Trench axis in a zone of relatively thick and undeformed sediments, as discussed in “[Tectonic Setting and Magnetic Anomalies](#),” p. 2. Sediments were cored in all four holes drilled at Site 1149 with a maximum total thickness of 408.2 m in Holes 1149A and 1149B, below which volcanic basement was encountered. The basement was found to be 7 m shallower in Hole 1149C and 107 m shallower in Hole 1149D, the latter being located only 5 km to the southeast (see Fig. F5). On the basis of the distribution of the major lithologies recovered at Site 1149, as defined on the basis of shipboard smear-slide analyses (see “[Site 1149 Smear Slides](#),” p. 105), the sedimentary column between the seafloor and basement has been divided from top to bottom into five lithologic units (Table T3).

Unit I

Description: Ash- and biogenic silica-bearing clay, ash-bearing siliceous clay, radiolarian-bearing clayey ash, clay- and ash-bearing siliceous ooze, diatomaceous clay, ashy clay, and silt-bearing clay

Interval: Section 185-1149A-1H, 0 cm, through 13H-CC, 19 cm

Depth: 0.0–118.2 mbsf

Thickness: 118.2 m

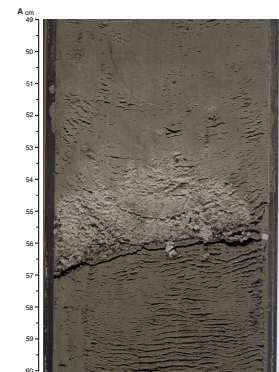
Age: late Pleistocene to late Miocene

Lithologic Unit I consists primarily of clayey lithologies with varying amounts of siliceous microfossils and volcanic grains. Colors are dominantly dark greenish gray, dark gray, or dark brown. There is a downward trend toward slightly lighter and more saturated colors (higher chroma values). Siliceous microfossils are common to abundant throughout Unit I and consist mostly of diatoms and radiolarians with minor siliceous sponge spicules and rare silicoflagellates. In the upper part of the unit there are occasional thin beds (typically 3 cm thick) that are slightly darker than the surrounding sediments that contain abundant diatom frustules. Below Core 185-1149A-11H, the abundance of siliceous microfossils decreases rapidly from common (10%–30%) to traces at the top of Core 185-1149A-13H over an interval of <15 m. Calcareous microfossils, as well as any other carbonate components, are generally absent throughout Unit I, except for trace amounts of redeposited calcareous nannofossils in Sample 185-1149A-3H-1, 83 cm (see “[Calcareous Nannofossils](#),” p. 20).

The volcanic component includes glass, centimeter-sized pumice and smaller rock fragments, and mineral grains. Apart from the volcanic particles in the background sediment, there are at least 100 discrete ash layers in Unit I. The color of the ash varies between dark gray (10Y 3/1) and light gray (10YR 6/1). Thicknesses of the discrete ash layers typically vary from a few millimeters to 5 cm. Thicker layers, however, are not uncommon. For example, ash layers in Sections 185-1149A-8H-2 and 8H-3, 10H-5, 16H-2, and 16H-3 are 20, 45, 30, and 25 cm thick, respectively. Core 185-1149A-16H not only contains two of the thicker ash layers of 30 and 25 cm, but it is also the core with maximum frequency of ash layers. Ash layers typically have sharp basal contacts and diffuse tops and are normally graded (Fig. F10). The bases of the ash layers, although sharp, are not erosional. Grain size at the base, as deter-

T3. Lithologic units, p. 158.

F10. Ash layers, Hole 1149A, p. 62.



mined visually and by examination of shipboard smear slides, is medium or fine sand to silt and grades toward the top to clay-size particles (Fig. F10A). The diffuse tops of the ash layers are in some cases clearly the result of bioturbation (Fig. F10B). In other cases, however, the diffuse tops may be the result of slower deposition and mixing of the ashes with the clays because of winnowing of the main ash fallout (Fig. F10A). Nonquantitative analysis of the sand and silt components of the ash layers in the shipboard smear slides shows that ash layers consist of 60%–98% glass shards and volcaniclastic particles. Smear-slide estimates of ash content in the background clay lithology of Unit I range from 10% to 30%.

Pumice fragments, up to 3 cm across (Fig. F11), are scattered throughout the unit. One larger piece of pumice from Sample 185-1149A-11H-6, 72–74 cm, contains planktonic foraminifers with preserved calcareous tests in a matrix of dark clay that fills fractures and vugs in the pumice (Fig. F12).

X-ray diffraction (XRD) analysis of the background sediment of Unit I has revealed reflections characteristic of quartz, feldspar, and clay minerals, including a 14 Å mineral (probably chlorite), mixed-layer minerals in the 10–15 Å range, and discrete illite (Fig. F13). Judging from the intensities of the XRD peaks of quartz and feldspar, these minerals are probably more abundant than suggested by the smear-slide data, where both minerals together usually accounted for no more than ~5%–10% of sediment. This discrepancy may be because some of these minerals probably occur in the clay and very fine silt size fraction and are difficult to identify in smear slides. High intensities around 3.19 Å and relatively low intensities at ~3.25 Å suggest that most feldspar is plagioclase. The diffractogram from the uppermost core, Core 185-1149A-1H, shows peaks at 14.3, 7.05, and 4.71 Å that are attributed to a chloritic mineral, which is subdued or nonexistent in the underlying sediment (Fig. F13).

Sedimentary structures and bioturbation are rarely discernible other than near ash layers and rare bedding planes, where sediment composition or texture change (Fig. F14). However, there are common green clay lamina, singly or in bundles, which are often associated with slightly more indurated intervals (Fig. F15). XRD of such a clayey layer in Sample 185-1149A-2H-1, 22–23 cm, revealed a composition similar to the background sediment (Fig. F13) except for the presence of a well-defined peak at 3.18 Å, that is related to plagioclase.

Unit II

Description: Ash-bearing clay and pelagic clay, ash- and biogenic silica-bearing clay, ash-bearing siliceous clay, radiolarian-bearing clayey ash, clay- and ash-bearing siliceous ooze, diatomaceous clay, ashy clay, and silt-bearing clay

Interval: Section 185-1149A-14H-1, 0 cm, through 20X-CC, 55 cm, and Section 185-1149B-2R-1, 0 cm, through 3R-CC, 10 cm

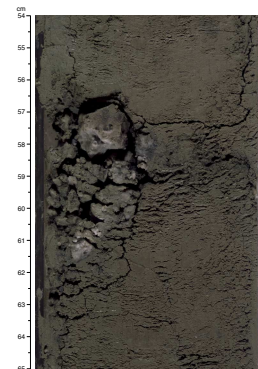
Depth: 118.2–179.1 mbsf (Hole 1149A) and 160.6–180.0 mbsf (Hole 1149B)

Thickness: 61.8 m

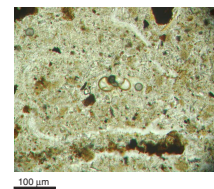
Age: Unknown

Lithologic Unit II dominantly consists of dark brown pelagic clay with rare silt- and sand-sized components. Siliceous microfossils are absent or are present in trace amounts in the upper part of the unit. The upper

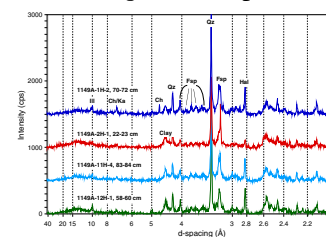
F11. Pumice in background sediment, p. 64.



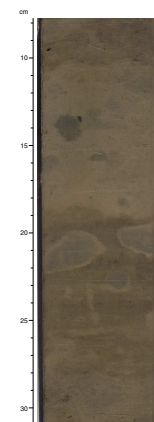
F12. Planktonic foraminifer test in vug, p. 65.



F13. X-ray diffractogram traces from lithologic Unit I, p. 66.



F14. Bioturbation of Unit I, p. 67.



boundary of Unit II was placed at the top of Core 185-1149A-14H, where siliceous microfossils disappear downhole except for occasional occurrences of dissolution-resistant siliceous sponge spicules in trace amounts. The lower boundary of Unit II corresponds to the reappearance downhole of siliceous facies, including indurated lithologies such as porcelanite and chert. Unit II is divided into two subunits.

Subunit IIA

Description: Ash- and biogenic silica-bearing clay, ash-bearing siliceous clay, radiolarian-bearing clayey ash, clay- and ash-bearing siliceous ooze, diatomaceous clay, and ashy clay, and silt-bearing clay

Interval: Section 185-1149A-14H-1, 0 cm, through 17H-2, 132 cm

Depth: 118.2–149.5 mbsf

Thickness: 31.3 m

Age: Unknown

Subunit IIA is characterized by dark brown pelagic clay with rare volcanic glass grains as a background sediment and intercalated ash layers. The upper 7 m of Subunit IIA displays a wide variety of colors, ranging from olive gray (5Y 4/2) and light reddish brown (5YR 6/4) to dark reddish gray (5YR 4/2). As in Unit I, visible bioturbation is usually restricted to interfaces of differently colored sediments (Fig. F16A, F16B, F16C, F16D).

As mentioned above, the upper boundary of Subunit IIA was placed below the last downhole occurrence of dissolution-susceptible radiolarian and diatom tests. This upper boundary of Subunit IIA corresponds to a sharp decrease in porosity from close to 80% to values generally below 70% (see “Index Properties,” p. 38). The transition to Subunit IIB was placed below the last downhole occurrence of a discrete layer with rare volcanic fragments in Sample 185-1149A-17H-2, 132 cm.

Apart from the disappearance of silica, the mineralogical composition of Subunit IIA sediments is remarkably similar to that of Unit I, especially in the upper part (Fig. F17). XRD shows that the dark brown clays have somewhat lower relative intensities of the 3.2-Å feldspar peak and a higher intensity of the nonbasal reflection of the clay minerals around 4.5 Å (Fig. F17).

Subunit IIB

Description: Ash- and biogenic silica-bearing clay, ash-bearing siliceous clay, radiolarian-bearing clayey ash, clay- and ash-bearing siliceous ooze, diatomaceous clay, and ashy clay, and silt-bearing clay

Interval: Section 185-1149A-17H-2, 132 cm, through 20X-CC, 55 cm, and Section 185-1149B-2R-1, 0 cm, through 3R-CC, 10 cm

Depth: 149.5–179.1 mbsf (Hole 1149A) and 160.6–180.0 mbsf (Hole 1149B)

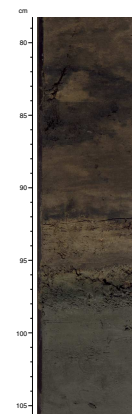
Cumulative thickness: 30.5 m

Age: Unknown

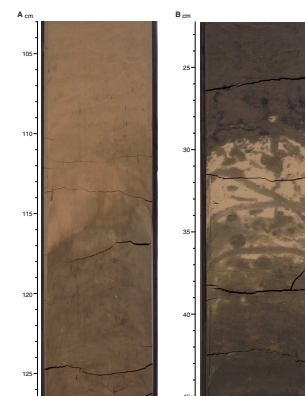
The dominant lithology of Subunit IIB is the same dark brown pelagic clay recovered in Subunit IIA, but it contains no discrete ash layers and <5% or trace amounts of volcanic particles.

The clay from the top of the subunit is mineralogically similar to the background sediment from the overlying subunit, but there is a decrease in relative quartz abundance downhole (Fig. F17). Subunit IIB

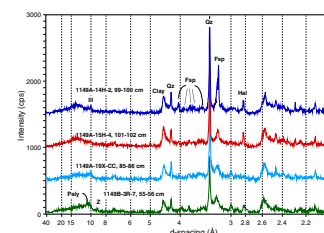
F15. Dark green indurated layer and color change of background sediment, p. 68.



F16. Bioturbation at transition in lithologic Subunit IIA, p. 69.



F17. X-ray diffractogram traces from lithologic Unit II, p. 71.



corresponds to an interval of downhole increasing gamma-ray intensity and X-ray fluorescence (XRF) K_2O/Al_2O_3 that was recorded in the cores (see “[Natural Gamma Radiation](#),” p. 39, and “[Authigenic Clay Formation: Unit II](#),” p. 32) and in the potassium spectral band of the logging data (see “[Natural Radioactivity](#),” p. 44). The potassium maximum correlates with the appearance of zeolites of the heulandite-clinoptilolite group at the bottom of the subunit (Fig. F17). Although shore-based analyses are required to determine the exact mineral species, both heulandite and clinoptilolite are known to be potassium rich (Kastner, 1979; 1981). Besides the zeolites, X-ray diffractograms from the base of the subunit show weak, but significant peaks at 10.5 and 6.4 Å that are interpreted to correspond to palygorskite. Palygorskite, a magnesium-rich fibrous clay mineral is thought to form authigenically within marine sediments, most probably from a smectitic precursor (Couture, 1977; Pletsch, 1998). Additional evidence for authigenesis comes from the anomalous chemical composition of the sediments and interstitial waters (see “[Authigenic Clay Formation: Unit II](#),” p. 32, and “[Ash Alteration and Formation of Authigenic Clays](#),” p. 28). Notably, a slight decrease in dissolved Cl^- is reported that may be related to the transformation of smectite to palygorskite, which is accompanied by the release of interlayer water. Again, shore-based analyses are required to validate the amount and the authigenic formation of palygorskite.

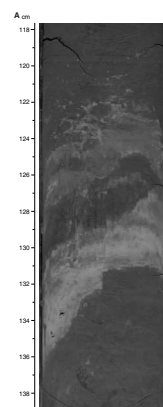
The otherwise very monotonous clays are cut by at least two steep faults, one of which shows a normal sense of displacement (Fig. F18A, F18B). Although it is unknown to which degree the core-cutting process is responsible for these faults, it seems clear that the rheological character of Subunit IIB is remarkably different from the other lithologic units because deformational features with notable displacement were not recorded in either the overlying clays or in the underlying indurated sediments. The susceptibility of Subunit IIB sediment to deformation is supported by the marked decrease in shear strength (see “[Shear Strength](#),” p. 41), a phenomenon that might be responsible for the logging and operational difficulties encountered in Holes 1149B and 1149C (see “[Hole 1149B](#),” p. 7, and “[Hole 1149C](#),” p. 8).

Unit III

Description: Radiolarian chert, radiolarian porcelanite, clayey zeolite silt, and zeolitic clay
Interval: Section 185-1149A-21X-1, 0 cm, through 23X-CC, 6 cm, and Section 185-1149B-4R-1, 0 cm, through 16R-1, 63 cm
Depth: 179.1–191.2 mbsf (Hole 1149A) and 180.0.6–282.9 mbsf (Hole 1149B)
Cumulative thickness: 103.8 m
Age: Unknown

Lithologic Unit III is characterized by the presence of alternating siliceous lithologies ranging from soft, opal-CT-rich, and zeolitic clay to hard but porous radiolarian porcelanite to vitreous and dense radiolarian chert. As with the many previous DSDP and ODP efforts to core intervals with chert layers, recovery dropped dramatically in this unit, typically to values below 5%. Given this low recovery and the tendency for softer lithologies to be washed away as an effect of the higher pumping rates (see “[Hole 1149A](#),” p. 6), even the very small amounts of soft ma-

F18. Deformational features in Unit II, p. 72.



terial recovered in the core material must be considered a major lithology of Unit III.

The top of Unit III is defined by the first occurrence of indurated siliceous lithologies such as chert and porcelanite at ~180 mbsf. Laminated zeolitic clays and radiolarian porcelanites with more massive, irregular intercalations of radiolarian chert were recovered both in the uppermost and the lowermost part of the unit (Figs. F19A, F19B, F20A, F20B, F21). These sediments often have a peculiar mineralogy that is typical for siliceous diagenetic environments (Fig. F22). Thus, opal-CT appears at the top of the unit and persists into the upper 20 m of the underlying Unit IV. Palygorskite, detected at the bottom of Unit II, is also found in Unit III (Fig. F22), and zeolite, common throughout the unit, locally forms zeolite silts. The first downhole occurrence of opal-CT is in Core 185-1149A-21X at ~180 mbsf. This level corresponds to a significant decrease in dissolved silica in the interstitial waters, which is likely related to the crystallization of opal-CT (see “Biogenic Sedimentation,” p. 31, and “Diagenesis of Biogenic Silica and Carbonate,” p. 27).

A *P*-wave velocity increase was noted in the lower part of Unit III (see “Seismic Velocity,” p. 45) that persists downsection in the more uniformly indurated lithology of Unit IV, but no concomitant lithologic change was observed in the core.

Unit IV

Description: Radiolarian chert, radiolarian porcelanite, radiolarian marlstone, and radiolarian chalk

Interval: Section 185-1149B-16R-1, 63 cm, through 29R-1, 93 cm; Section 185-1149C-3R-1, 0 cm, through 9R-1, 51 cm; and Section 185-1149D-2R-1, 0 cm, through 5R-1, 16 cm

Depth: 282.3–407.75 mbsf (Hole 1149B); 283.6–400.7 mbsf (Hole 1149C); and 272.2–300.5 mbsf (Hole 1149D)

Cumulative thickness: 125.5 m

Age: late Hauterivian to late Valanginian

Unit IV is characterized by the presence of calcareous lithologies that are either interbedded with radiolarian cherts and porcelanites similar to those of Unit III or present in vugs within, and halos around, the siliceous sediments (Fig. F23). There is a downward increase in carbonate content of the recovered calcareous lithologies (Table T4), which is supported by the logging data (see “Geochemical Log,” p. 46). The marly and chalky lithologies often show wavy, discontinuous laminations, part of which may be a result of the flattening of burrows. A significant amount of flattening is indicated where there is differential compaction around rapidly indurated parts of the sediment, such as large, sediment-filled burrows (Fig. F24A). High initial water contents are also indicated by a water escape structure that was observed in about the same interval (Fig. F24B).

One major mineralogic characteristic of Unit IV is the downhole disappearance of opal-CT below the top 20 m of the unit (Sample 185-1149-18R-1, 9–11 cm; 301.7 mbsf). Thin sections from this core show that radiolarians and diatoms make up a considerable amount of the calcareous lithologies at the top of Unit IV (Fig. F25A, F25C, F25D). The opaline skeletons are largely preserved, though probably with secondary opal-CT, as indicated by XRD data (Fig. F26), whereas the lumens are filled with chalcedony (Fig. F25B, F25C). The calcareous

F19. Lamination in lithologic Unit III, p. 74.



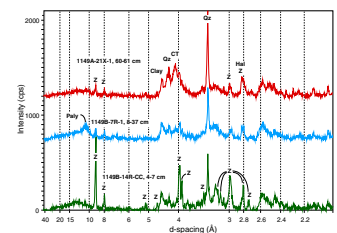
F20. Radiolarian porcelanite, p. 76.



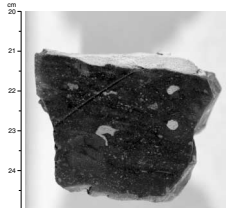
F21. Chert with vein, p. 78.



F22. X-ray diffractogram traces from lithologic Unit III, p. 79.



F23. Sediment in burrows and on bedding planes, p. 80.



T4. Carbonate content of sediments, Hole 1149B, p. 159.

component mostly consists of calcareous nannofossils, which show a broad range of preservation from very good to strongly recrystallized or broken (Fig. F25D). Common veins filled with calcite and chalcedony testify to the downward increasing recrystallization of both calcareous and siliceous components (Fig. F25E). Below ~300 mbsf, opal-CT disappears and quartz takes its place (Fig. F26). The siliceous microfossils, however, become replaced by calcite (Fig. F25F). Much of the previously dissolved silica may thus have precipitated elsewhere.

Besides the lighter colored chalks and marls, there are rare and scattered darker layers (Fig. F27). One such layer was found to contain elevated quantities of euhedral barite, along with dolomite rhombs and phosphatic fish remains. The observed increase in barium minerals is closely matched by chemical analyses that show the highest values in this interval (see “**Biogenic Sedimentation,**” p. 31). The mineral assemblage is characteristic of deposits that are, or used to be, enriched in organic matter. Strikingly, a marked gamma-ray maximum in the logging data in the same interval (see “**Natural Radioactivity,**” p. 44). Common sedimentary components with elevated uranium content are phosphate and organic matter. The peculiar mineral assemblage and the logging data may thus indicate that there was a prolonged period of enhanced carbonaceous accumulation in the late Hauterivian. Unfortunately, no organic geochemical data are available to substantiate this interpretation. Testing this hypothesis is particularly interesting because a correlative organic-rich interval has been found in the Cretaceous western Tethys (Cecca et al., 1994; Baudin et al., 1999).

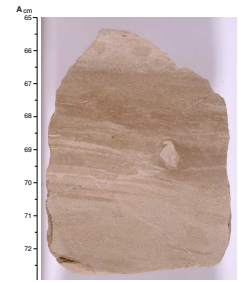
Below 300 mbsf, cherts display a wide variety of structures and colors, which include greenish and bluish tinges (Fig. F28). There are often several generations of differently colored chert in one piece, and some of these inhomogeneities resemble lamination, bedding, and bioturbation. These patterns, in particular the heavily bioturbated type (“swiss cheese chert”), were not observed in the brown cherts of Unit III. Toward the base of the unit, color changes are also observed in the calcareous lithologies (Fig. F29). The lowermost 10 m of the sedimentary section above the basalt is characterized by unusual, highly saturated colors (i.e., with high chroma values) like purplish blue and red. Most of this color change can be attributed to a visible downward increase in the proportion of manganese micronodules and iron oxides. This increase in a presumed hydrothermal component is also seen in an increase in Fe/Al in the bulk sediment geochemistry (see “**Metalliferous Sources,**” p. 31, and “**Degradation of Organic Matter and Associated Redox Environments,**” p. 27).

The more indurated calcareous lithologies of Unit IV often show subvertical and oblique dissolution seams. Although their origin is not well understood, these features seemed to have formed as a result of pervasive rupture of the semi-indurated sediment. The restriction of these deformational features to the hard limestones may provide some evidence for the relative timing of lithification in calcareous vs. siliceous lithologies (Fig. F30A, F30B, F30C).

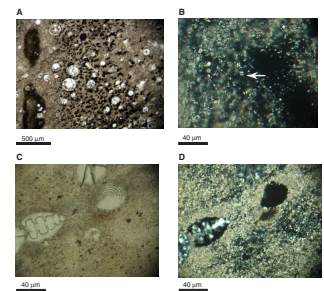
Unit V

Description: Recrystallized calcareous marlstone
Interval: Section 185-1149B-29R-1, 93 cm, through 29R-2, 139 cm
Depth: 407.7–408.2 mbsf (Hole 1149B)
Thickness: 1.96 m
Age: late Valanginian

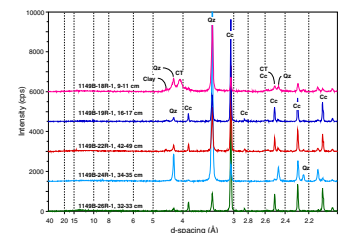
F24. An indurated burrow in radiolarian marl and a water escape structure, p. 81.



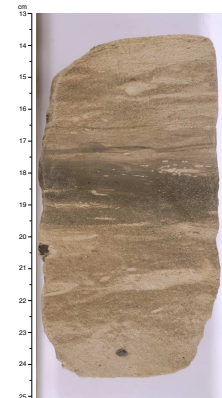
F25. Radiolarian chalk and marlstone, p. 83.



F26. X-ray diffractogram traces from lithologic Unit IV, p. 85.



F27. Discontinuous lamination in marlstone, p. 86.



Lithologic Unit V consists of calcareous marlstones that fill fractures in the brecciated basalt. The marlstones are more indurated than the sediments at the base of Unit IV. Colors are typically shades of pinkish gray. Macroscopic veins of carbonate rimmed with smectite and iron oxide are common (Fig. F11) (see “Lithologic Units,” p. 22). These altered sediments appear to be derived from a precursor that was very similar to the nanofossil marls of lithologic Unit IV, but more pervasive dissolution and overgrowth of calcareous nanofossils (see “Calcareous Nanofossils,” p. 20) has made the remnants virtually unrecognizable. In thin section, there is a noticeable increase in secondary, equant calcite crystals. Carbonate analyses (Table T4) yield ~65 wt% carbonate for the altered sediments of this interval, which is significantly lower than the average chalks of Unit IV (84–88 wt% in Samples 185-1149B-28R-2, 114–117 cm, and 29R-1, 3–4 cm) but almost exactly the same as the lowermost marls immediately overlying the basement. The lower carbonate abundance relative to the overlying lithologies is due to a downward increase in clay content.

X-ray diffractograms provide a qualitative impression of the differences between Units IV and V (Fig. F31). They show that feldspar, which is not detected in the chalks of Unit IV above the basalts, is present in Sample 185-1149B-29R-1, 134–135 cm, from the basalt fracture fill (Unit V). Smectite also shows a strong peak at 15 Å in Unit V and decreases upward. Smectite is a typical alteration product of basalt and was observed in thin section near basalt-sediment and basalt-calcite vein interfaces. Also observed in thin section were stacked aggregates of secondary clays in the sediment groundmass; these may also be smectite. The presence of feldspar may be due to thermal dehydration of primary clay minerals at the contact to the basalt. In thin section, feldspar was observed as finely disseminated, >5 µm, euhedral to subeuhedral crystals of low relief and low-order interference colors under cross-polarized light.

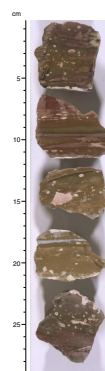
Depositional History

The overall depositional history at Site 1149 appears to be intimately related to the large-scale vertical and horizontal movements of the Pacific plate. The newly formed oceanic crust subsided to below the CCD within ~7 m.y. of its formation (see “Post-Hauterivian Carbonate-Free Siliceous Sedimentation,” p. 18, and “Sedimentation Rates,” p. 37). The plate tectonic movement of Site 1149 from low southern latitudes during the Early Cretaceous toward its current position at ~31°N resulted in crossing a number of paleoceanographic and paleoclimatic boundaries, including the high-productivity belt along the Late Cretaceous paleoequator (Lancelot and Larson, 1975; Sager and Pringle, 1988; Larson and Sager, 1992). The evolution of the depositional environments at Site 1149 is divided into four broad episodes.

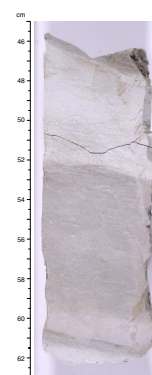
Lower Cretaceous Alternating Chert and Chalk: Onset of Pelagic Sedimentation

Upper Valanginian marls and chalks were the first sediments to be deposited in fractures within, and on top of, the freshly formed oceanic crust at Site 1149. The vivid colors and elevated iron and manganese contents in the lowermost 20 m of the sedimentary section give way to more drab colors and normal Fe/Al and Mn/Al values upsection, which probably records the increasing distance of the site from the volcanic

F28. Chert with “swiss cheese” type lenses, p. 87.



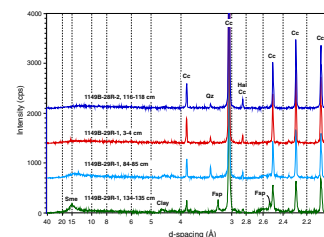
F29. Crudely laminated chalks, p. 88.



F30. Chalks and calcareous marls, p. 89.



F31. X-ray diffractogram traces from lithologic Units IV and V, p. 92.



ridge axis. Decreasing carbonate contents and increasing proportions of siliceous microfossils in the overlying calcareous lithologies probably reflect the deepening of the site in the ensuing Hauterivian.

Post-Hauterivian Carbonate-Free Siliceous Sedimentation: Subsidence below the CCD and the Equatorial Crossing

In the late Hauterivian or afterward, carbonate supply from the euphotic zone became insufficient to balance dissolution at the increasing depth of Site 1149. From this time on, sedimentation was carbonate free, except for occasional intervals where traces of calcareous material became preserved as a result of rapid sedimentation or isolation from ambient deep water. Calcareous lithologies were replaced by poorly indurated siliceous clays and radiolarian porcelanite. Most of the silica varieties, as well as several silicate minerals, probably owe their existence to the diagenesis of siliceous microfossils. The dominance of siliceous microfossils is commonly used as proxy evidence for elevated paleo-productivity at the sea surface, which in turn is usually related to upwelling of nutrient-rich waters. As such, the siliceous sediments of Unit III would indicate a period of high plankton productivity, likely related to an oceanic divergence zone. Paleomagnetic data show that Site 1149 was on or within 5° north or south of the equator during the deposition of Unit III (see "[Paleolatitude](#)," p. 36). It therefore seems likely that the high biological productivity required for the accumulation of the thick sequence of siliceous deposits was related to the position of the site below the paleoequatorial divergence.

Late Cretaceous to Paleogene? Clayey Deposition: Oceanic Events and Rapid Northward Movement

The transition from the siliceous deposits to the dark brown pelagic clays is abrupt. If the relationship between lithofacies and paleoproductivity is correct, then this dramatic change in sedimentation suggests that productivity also declined abruptly. Although the movement of the Pacific plate has changed both direction and speed in the past, this change was probably not fast enough to bring siliceous sedimentation to an abrupt end. The transition from Unit III to Unit II may be a result of a paleoceanographic crisis such as the restriction of the broad Eocene equatorial zone of biological productivity at about the Eocene/Oligocene boundary. This event was accompanied by the sharpening of latitudinal dissolution gradients in carbonates (Worsley and Davies, 1979), but the same probably applies to silica deposition. After the site moved away from the high-productivity zone, accumulation rates dropped to extremely low values, as suggested by the sizeable amounts of fish teeth and other ichthyoliths in the clays of Unit II.

Neogene Approach of the Izu-Bonin and Japan Arcs: Increasing Volcanic and Terrigenous Input

Toward the end of the pelagic sedimentation that characterizes Unit II, discrete ash layers and volcanic particles appear in the pelagic clays and become more abundant upsection in the rapidly deposited Unit I (see "[Sedimentation Rates](#)," p. 37). Since bulk sediment accumulation rates probably were more than an order of magnitude lower in Unit II, the frequency of ash layers in that interval suggests that long time intervals passed between the deposition of individual ash beds. The ash lay-

ers are interpreted to be the result of ash fallout from explosive eruptions likely west of Site 1149. An Oligocene to middle Miocene major pulse of volcanism is recorded from the Bonin-Mariana-Yap arc and from Japanese arc volcanoes (Karig, 1975) (i.e., preceding the deposition of the ash- and siliceous microfossil-bearing clays of Unit I). At this time, Site 1149 was probably relatively far away from the volcanic eruption centers, which resulted in the low accumulation rates between the volcanic events that characterize Unit II. The more frequent presence of ash layers in Unit I, of late Miocene to Pleistocene age, either points to increased subduction-related volcanic activity in the northwest or to a closer position to the volcanic centers, or both. Since paleolatitudes for Unit II were similar to present latitude (see “[Paleolatitude](#),” p. 36), the vigor and frequency of the eruptions may have played an important role, but the proximity to the Izu-Bonin arc is clearly an additional factor. Four thick layers (>20 cm) at 70.0, 86.4, 139.4, and 140.7 mbsf may result from some of the major eruptions. As the pulses of volcanism waned, volcanic ash-fall deposition greatly decreased and intervals of ash and diatom/radiolarian-bearing clay were deposited.

Although the frequency of ash layers does not significantly increase in the middle Pleistocene to Holocene part of the section and actually decreases in the uppermost core of Site 1149, the accumulation rates in this interval are on the order of 30 m/m.y. Increasing proportions of detrital quartz and terrestrial, nonvolcanogenic minerals such as chlorite provide evidence that the elevated accumulation rates in this interval may be related to an increased eolian input from mainland Asia.

BIOSTRATIGRAPHY

Abstract

Clays recovered from Unit I at Site 1149 contain an abundant assemblage of siliceous plankton—mainly diatoms, silicoflagellates, and radiolarians. The abundance of siliceous plankton decreases in Core 185-1149A-12H, and Cores 185-1149A-13H to 185-1149B-3R are completely barren. The clays from Cores 185-1149A-1H to 185-1149B-3R contain ichthyolith assemblages, which increase in abundance downhole, probably as a response to downward decreasing sedimentation rates (see “[Sedimentation Rates](#),” p. 37).

Carbonates recovered in Cores 185-1149B-16R to 29R yielded well to poorly preserved calcareous nannofossil assemblages. The assemblages have a high average diversity, which points to a fairly good preservation. Preliminary age assignments based on the study of core-catcher samples and additional paleontology analysis log (PAL) samples permit identification of the Hauterivian *Lithraphidites bollii* Zone from Core 185-1149B-16R down to 21R. Downhole assemblages are dominated by *Watznaueria barnesae*, *Cruciellipsis cuvillieri*, and *Tubodiscus* sp.; the first downhole occurrence of *Tubodiscus verenae* is in Core 185-1149B-24R and indicates the uppermost Valanginian–lowermost Hauterivian. *Rucinolithus wisei*, a species restricted to the Berriasian–Valanginian according to Thierstein (1971), occurs from Core 185-1149B-25R downhole. The persistence of *T. verenae* downhole to Core 185-1149B-29R confirms a late Valanginian age for the contact of sediment/basement consistent with magnetic Anomaly M11. This age assignment will be refined

onshore, radiolarian assemblages will be studied, and an integrated biostratigraphy will be established.

Introduction

Numerous microfossil groups are present in the cored interval. The clays and ashes in lithologic Unit I (Cores 185-1149A-1H to 11H) contain abundant assemblages of siliceous plankton, in particular, diatoms, silicoflagellates, and radiolarians. The preliminary study of silicoflagellate and diatom assemblages points to a Pliocene age for Sample 185-1149A-9H-CC, whereas 12H-CC is assigned a late Miocene age, according to Barron (1985). These age assignments are in agreement with paleomagnetic shipboard stratigraphic data (see "[Magnetostratigraphy](#)," p. 35). The abundance of the siliceous fossil groups decreases dramatically in Core 185-1149A-12H, as does the frequency of ash layers (see "[Unit I](#)," p. 11). Clays in Cores 185-1149A-13H to 185-1149B-3R are barren of siliceous plankton. Ichthyoliths are present in lithologic Units I and II, and their abundance increases downhole from Cores 185-1149A-13H to 185-1149B-3R. Cores 185-1149B-2R to 15R contain mainly porcelanite and chert pebbles, with a very low average recovery. Nevertheless, radiolarian assemblages were observed on cut surfaces of the cores under the microscope. Their relative abundance, in contrast to other fossil groups, will allow a shore-based biostratigraphic study for the otherwise unfossiliferous Unit III. The interval comprising lithologic Units I, II, and III, from Cores 185-1149A-1H to 185-1149B-15R, is barren with respect to calcareous microfossils. Unit IV, from Cores 185-1149B-16R to 29R, consists of radiolarian cherts and interbedded radiolarian nannofossil cherts/marls that contain fairly to well-preserved calcareous nannofossils, benthic foraminifers, and radiolarians.

Calcareous Nannofossils

The upper part of the stratigraphic section (lithologic Units I through III) is barren of calcareous nannofossils, with the exception of a thin, reworked layer in Core 185-1149A-3H (Sample 185-1149A-3H-1, 83 cm), that contains *Sphenolithus moriformis*, *Sphenolithus dissimilis*, *Reticulofenestra* sp., *Cyclicargolithus floridanus*, and *Reticulofenestra daviesii*; this assemblage suggests an Oligocene to early Miocene age for the reworked sediment. Scattered occurrences of calcareous nannofossils of Cenozoic age (*Cy. floridanus*, *Discoaster* sp., *Tribrachiatus orthostylus*, and *Reticulofenestra* sp.) are recorded in several samples obtained from the porcelanite recovered in Unit III; however, it is not yet understood if this represents a downhole contamination or the very poorly preserved original assemblage. Shore-based preparation of these samples, performed with maximum care to avoid contamination, will help clarify this problem.

Carbonates recovered in Cores 185-1149B-16R to 29R yielded well to poorly preserved calcareous nannofossil assemblages. The best preserved assemblages are in the least lithified lithologies, such as the nannofossil ooze recovered in small pockets in irregularly bedded cherts or in soft cherts. Low average breakage of delicate structures, such as spines and cross bars, points to a moderate compaction rate. High porosity of the sediment is responsible for relatively high dissolution that in some cases has completely obliterated the delicate central-area structures of some taxa (e.g., *Cretarhabdus* and *Crucellipsis*), hindering the determination to the species level. Occasional recrystallization pro-

cesses occur, causing overgrowth of central area structures. Assemblages from soft lithologies have a high average diversity, which confirms the fairly good preservation of calcareous nannofossils in these sediments. Preliminary data are based on the study of some 30 samples, including the core-catcher samples and several additional samples from the softer lithologies. Assemblages are dominated by the continuous and abundant occurrence of *Watznaueria barnesae*; other fairly common and long-ranging species are *Watznaueria britannica*, *Cyclagelosphaera margerelii*, *Diazomatolithus lehmanii*, *Assipetra infracretacea*, *Zeugrhabdotus embergeri*, *Helenea chiastia*, *Manivitella pemmatoidea*, *Lithraphidites carniolensis*, *Crucellipsis cuvillieri*, and *Tubodiscus jurapelagicus*. The marker species *Lithraphidites bollii* occurs from Core 185-1149B-16R to 21R, thus allowing a preliminary age assignment to the Hauterivian *L. bollii* Zone of Thierstein (1971, 1973) and corresponding to magnetic Anomalies M4 to M9/10 (Bralower, 1987; Channell et al., 1995) for the upper part of lithologic Unit IV. Downhole assemblages are dominated by *W. barnesae*, *W. britannica*, *C. cuvillieri*, *Assipetra terebrodentarius*, and *Tubodiscus* ssp. The last downhole occurrence of *A. terebrodentarius* is recorded in Core 185-1149B-20R. The first downhole occurrence of *Tubodiscus verenae* in Core 185-1149B-24R indicates the top of the magnetic Anomaly M11 (Bralower, 1987) and the uppermost Valanginian–lowermost Hauterivian (Channell et al., 1995) (see also Fig. F5, p. 60, in the “Explanatory Notes” chapter). *Rucinolithus wisei*, a species whose known range is Berriasian to upper Valanginian according to Thierstein (1971), is present from Core 185-1149B-25R downhole. The continuous occurrence of *T. verenae* downhole to Core 185-1149B-29R suggests a late Valanginian age for the sediment/basement contact. This age assignment will be refined onshore, and radiolarian assemblages will be studied and integrated with the nannofossil biostratigraphy.

A spot-cored interval in Hole 1149C (Cores 185-1149C-3R to 6R) contains assemblages that are assigned to the *L. bollii* Zone of Thierstein (1971, 1973). The sediment/basement contact, recovered in Core 185-1149C-9R in this hole, is preliminarily assigned to the late Valanginian according to the presence of *R. wisei* and *T. verenae* in the calcareous nannofossil assemblage recorded in Sample 185-1149C-8R-1, 76–77 cm. The same assemblage characterizes the carbonate sediment above the sediment/basalt contact in Hole 1149D, where this surface is much shallower (307 mbsf).

We noticed that several typical Tethyan species (*Nannoconus* spp.) were not found in this material, although they were recovered in the western Pacific in slightly younger stratigraphic intervals (Aptian–Albian at Site 878; Erba et al., 1995). Some biostratigraphic markers commonly used in this stratigraphic interval have a scattered occurrence at this site (e.g., *Calccalathina oblongata*) and cannot therefore be used for biostratigraphic purposes.

BASEMENT STRATIGRAPHY

Abstract

Basement was encountered in Hole 1149B at a depth of 407.77 mbsf, in Hole 1149C at 398.41 mbsf, and in Hole 1149D at 300.46 mbsf. A total of 195.96 m of basement was cored during Leg 185 at Site 1149. In Hole 1149B, 37.43 m was cored (Cores 185-1149B-29R through 32R) with an average recovery of 22.71%; in Hole 1149C, 28.29 m was cored

(Cores 185-1149C-9R through 11R) with an average recovery of 13.68%; and in Hole 1149D, 130.24 m was cored (Cores 185-1149D-5R through 19R) with an average recovery of 19.64% (Fig. F32A, F32B, F32C; Table T5; also see “Site 1149 Vein Log,” p. 123; also in ASCII format). Recovery was lower at this site than at Site 801, perhaps because the cored interval consisted dominantly of thin, fractured flows, pillow basalts, and breccia.

The basement rocks recovered from Holes 1149B and 1149C are all aphyric basalts. Minor amounts of plagioclase and olivine (<1%) were observed as phenocryst phases, but they were not abundant enough to permit the addition of a mineral modifier to the rock name. The aphyric basalts include a mixture of thin (<50 cm) pillows and some intermediate thickness (50 cm to 1 m) cooling units that could represent either pillows or flows. There were a few thicker cooling units (up to 2.88 m) in Hole 1149D, described as flows in Figure F32C and Table T5. However, the pieces recovered were highly fractured, and the flows could not be described as massive. In addition, several intervals of breccia and a few of interpillow sediment were recovered.

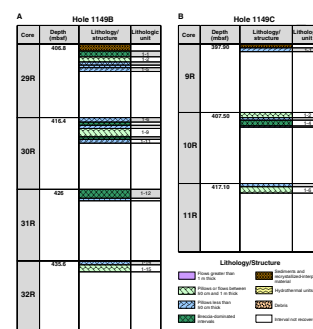
Lithologic Units

Basement lithologic units are numbered beginning with Unit 1. Holes 1149B and 1149C contain a single lithologic unit, Unit 1, that contains several subunits of breccias and individual cooling units. Unit 1 has 15 subunits in Hole 1149B and six subunits in Hole 1149C. In Hole 1149D, six lithologic units were identified. In Hole 1149D, Unit 1 consists of a single piece with a significantly higher olivine content, which was not observed in Holes 1149B or 1149C. Units 2–6 in Hole 1149D all contain subunits or cooling units. The subunits are identified on the basis of chilled or glassy contacts, fining of grain size toward the margins of pillows or flows and presence of breccia or hyaloclastite. Thin intervals of sediment or interpillow material and breccia are noted as boundaries between subunits, whereas thicker intervals (>5–10 cm) are distinguished as individual subunits.

The basement stratigraphic logs (Table T5; also see “Site 1149 Vein Log,” p. 123; also in ASCII format) include all the igneous core description data for Leg 185 Holes 1149B, 1149C, and 1149D: unit or subunit number, depth, interval thickness, lithology, texture, structure, color, presence or absence of chilled margins, comments, and the location of shipboard samples. The basement stratigraphy for Holes 1149B, 1149C, and 1149D is plotted in Figure F32A, F32B, and F32C. The following section summarizes the most important characteristics of lithologic subunits from Holes 1149B, 1149C, and 1149D.

Unit 1, in Holes 1149B and 1149C, consists of aphyric basalt pillows or thin flows. The contact between the overlying sediments and basement consists of a 0.78-m brecciated zone in Hole 1149B. There appears to have been some reaction between pink carbonate-bearing sediments and the basalt in this interval. The contacts between individual basalt pieces and the sediment are wavy and irregular with pronounced red iron staining. The sediment also appears to have been baked. The contact between the sediment and basement was not recovered in Holes 1149C or 1149D. The last few pieces of sedimentary material recovered in Sample 185-1149C-9R-1, 0–51 cm, and Sample 185-1149D-5R-1, 0–16 cm, are mainly chert (see “Unit IV,” p. 15); the remaining pieces recovered in both holes are basalts.

F32. Basement stratigraphy and unit boundaries, p. 93.



T5. Igneous core descriptions, p. 160.

The basalt in Unit 1 from both Holes 1149B and 1149C is highly altered and reddish gray in color with pronounced dark bluish gray alteration halos. Minor amounts of vesicles are present throughout Unit 1, their abundance varying between <1% and 3%. Several chilled pillow rims occur within Unit 1 (see Figs. F33, F34), and these define the individual pillows or cooling units, as noted in Table T5. In Hole 1149D, the units were assigned on the basis of mineralogical observations (see “Petrology,” p. 23). Units 2, 3, and 6 contain larger phenocrysts; Unit 2 also contains crystal clusters or microphenocrysts that were no longer observed in Unit 3. Unit 4 contains more altered and finer grained basalts with the lowest abundance of phenocrysts, and Unit 6 contains the highest abundance of olivine phenocrysts.

In Hole 1149B four subunits contain breccias (Fig. F35); in Hole 1149C one breccia subunit is present (Fig. F36). Breccias in all three holes have a carbonate or greenish clay cement, with the exception of the first breccia in Hole 1149B, where sediment is also present in the cement. For the most part, the basalt clasts are subangular to angular and vary in size from 5 to 20 cm. Some microbreccia is present in Hole 1149D (e.g., interval 185-1149D-11R-2, 104–120 cm) (Fig. F37). Thin intervals of hyaloclastite with altered glassy shards occur along pillow rims. A spectacular example of the hyaloclastite is present in Sample 185-1149D-7R-1, 29–42 cm (see Fig. F38). Some of the hyaloclastite intervals (e.g., Hole 1149B, Subunits 1–12, and Hole 1149D, Subunits 4–5), however, contain highly altered, rounded glassy clasts (see Figs. F34, F39). Interpillow material is rare at Site 1149 but not absent, (e.g., see interval 185-1149D-11R-2, 104–120 cm (Fig. F40). Fresh glass is present but not particularly common at Site 1149 (see Table T6).

Summary

Basement was penetrated in Core 185-1149B-29R, at a depth of 407.77 mbsf, in Core 185-1149C-9R, at 398.41 mbsf, and in Core 185-1149D-5R, at 300.46 mbsf. All basement rocks recovered in Holes 1149B and 1149C are assigned to the same basement lithologic unit, Unit 1. In Hole 1149D six lithologic units are identified. All three holes consist of aphyric basalt pillows or thin flows similar to those encountered in Hole 801C. Several interpillow breccia intervals are also present. The basalt is highly altered, reddish gray in color, and has pronounced dark blue-gray alteration halos. Minor amounts of plagioclase and olivine phenocrysts and small vesicles are present throughout.

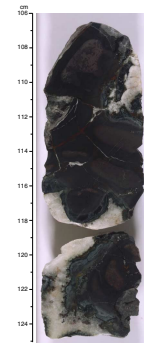
IGNEOUS PETROLOGY AND GEOCHEMISTRY

Petrology

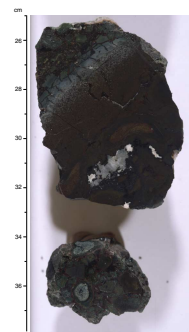
The igneous rocks from Holes 1149B, 1149C, and 1149D are described together in this chapter. Descriptions are based on hand specimen examination of all cores, and on four thin sections from Holes 1149B and 1149C (Table T7). Most basement rocks are aphyric pillow basalts containing <1% phenocrysts. Pillow rims are glassy to hypocrystalline, whereas pillow interiors are microcrystalline (Fig. F41).

The first piece from Hole 1149D (Piece 13 from Section 185-1149D-5R-1) differs in primary mineralogy and alteration from the other rocks and is given a separate unit designation (Unit 1, see “Lithologic Units,” p. 22). This piece contains ~2% olivine glomerocrysts and lacks

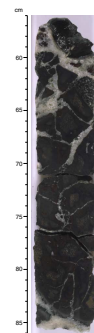
F33. Chilled pillow rims with crystalline interpillow material, p. 96.



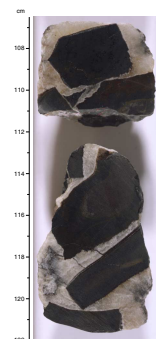
F34. Altered chilled pillow rim, p. 97.



F35. Brecciated basalt from Hole 1149B, p. 98.



F36. Brecciated basalt from Hole 1149C, p. 99.



alteration halos. The matrix and abundance of plagioclase phenocrysts are otherwise similar to the other rocks. Olivine phenocryst abundance increases at the bottom of Hole 1149D, exceeding 1% in the last 30 m of the hole (below 417 mbsf) in Unit 6 (see the Igneous Mineralogy Description Logs in the “[Supplementary Materials](#)” contents list). The maximum phenocryst sizes are observed toward the bottom of the hole (Fig. [F42](#)).

Throughout the basement sections phenocrysts are generally rare (<1%), but euhedral plagioclase is the most common and ranges in size from 0.1 to 1.2 mm. Olivine, the second most common phenocryst (always much less than 1%), is euhedral to subhedral in shape and 0.1–1 mm in size. Pyroxene phenocrysts were observed only in Section 185-1149B-29R-2 (Piece 13). These occur as glomerocrysts with plagioclase and olivine, have euhedral crystal shapes, and range in size from 0.2 to 0.4 mm. One thin section of a pillow rim was investigated. It consists of 94% altered glass and includes 2% plagioclase phenocrysts and 1% olivine phenocrysts (Fig. [F43](#)).

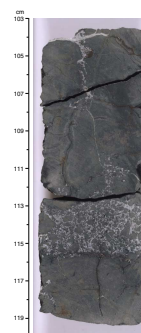
Plagioclase and olivine phenocrysts are altered to smectite and Fe oxide (Figs. [F44A](#), [F44B](#), [F45](#)). The cores of plagioclase are altered but the rims are unaltered, whereas olivine is completely altered. Interstitial material in the groundmass is intensely altered (see “[Basement Alteration](#),” p. 29). Vesicles are filled with saponite, Fe oxides, celadonite, and calcite.

Geochemistry

Two samples of basalt from Hole 1149B were analyzed with shipboard XRF. These samples and a further 15 samples (four from Hole 1149B, four from Hole 1149C, and seven from Hole 1149D) were analyzed in a shore-based laboratory by inductively coupled plasma-atomic emission spectroscopy (ICP-AES) and ICP-mass spectrometry (ICP-MS) for major elements and trace elements (Table [T8](#)). The samples analyzed represent the least-altered basalts recovered from the three drill holes, although alteration in this uppermost sequence is intense and pervasive (see “[Basement Alteration](#),” p. 29).

The Site 1149 basalts are distinctly lower in Fe_2O_3 and higher in MgO than tholeiites recovered from Hole 801C (Fig. [F46](#)). If these values are primary, they would indicate that Site 1149 lavas are more primitive than those from Hole 801C. Although MgO for Site 1149 basalts is within the range of the modern East Pacific Rise (EPR) (Langmuir et al., 1986), Fe_2O_3 is anomalously low, and alteration may have affected the Fe and/or the Mg contents of these basalts. Sample 185-1149B-30R-1, 91–94 cm, with the lowest Fe_2O_3 and highest MgO, contains ~100 ppm Ba, which is surprisingly high for a mid-ocean-ridge basalt (MORB), and may be the result of alteration. With the exception of the basalts from the base of Hole 1149D (Unit 6), the immobile trace elements in basalts from Site 1149 are comparable to those in normal MORBs from both Site 801 and the modern EPR but displaced to lower trace element abundances, consistent with their higher MgO contents (Fig. [F46](#)). The basalts encountered at the base of Hole 1149D (Unit 6) are enriched MORBs (E-MORBs) with higher Zr/Y and Nb abundances. These are nonetheless comparable to E-MORBs from the EPR. Thus, Unit 6, which lies below a major breccia unit, is notable because of a major change in both its chemical composition and phenocryst content.

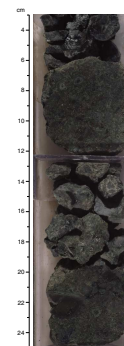
F37. Brecciated basalt from Hole 1149D, p. 100.



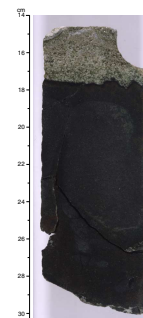
F38. Hyaloclastite from Hole 1149D, p. 101.



F39. Hyaloclastite/brecciated glassy basalt fragments from Hole 1149D, p. 102.



F40. Pillow rim and interpillow material from Hole 1149D, p. 103.



BASEMENT ALTERATION

Basement was cored in Holes 1149B, 1149C, and 1149D, with basement penetrations of 38.4, 28.8, and 135.1 m, respectively. At all sites the basement is made up of pillow lavas, pillow breccias, hyaloclastites, and thin flows. Alteration of basement from the three holes is generally similar, with Hole 1149D providing some documentation of variations with depth.

All basalt types are pervasively and strongly altered by oxidizing water/rock interactions. Complex multicolored alteration halos occur along fractures and other surfaces that were exposed to circulating fluids. These halos concentrically encircle kernels of host rock bounded by fractures (Fig. F47A). The halos are as wide as 2 cm and range in color from brown at the exposed surfaces to dark green for the main portion of the halos to a narrow (1–2 mm) brown band at the boundary with the host rock. The contact between the outer brown zone and the dark green halo is gradational, but that between the dark green and inner brown band is sharp, as is the contact with the host rock. Halos comprise ~34 vol% of the recovered basalt, and dark green and brown halos comprise 14 and 20 vol%, respectively. Unaltered glass is exceptional and is found only in small amounts in a few pieces (Table T6).

The host rock surrounded by fractures and halos generally exhibits dusky red to dark red colors and displays a light gray to brown mottling. The mottling is variable in intensity, ranging from complete to slight patchy replacement. In the cases of slight replacement the patches form a subdendritic pattern. In the single available thin section of this material, the mottles correspond to zones lacking primary Ti magnetite and may have formed by leaching of Fe oxide. These mottled regions appear to be present only where outer brown halos are associated with the bounding vein.

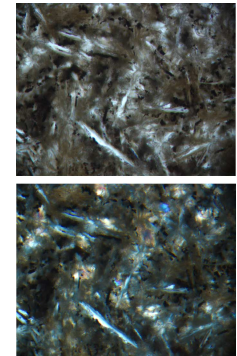
Some significant variations occur with depth in Hole 1149D. In three intervals (Sections 185-1149D-11R-1 through 11R-2, 13R-1, and 16R-1 through 16R-2), the basalt is pervasively altered and displays a cloudy, dark brown to orange-tan color (Fig. F47B). Because of the fine-grained texture and fracturing of these rocks, alteration is pervasive and no distinct halos are visible. These same cores contain hyaloclastite and pillow-rim breccias in which the basaltic glass has been totally replaced and cemented by dark saponite, green phyllosilicates (celadonic?), and minor calcite. Section 185-1149D-11R-3 is completely made up of basaltic breccia with calcite cement. The basalt clasts exhibit the same cloudy alteration as the basalt pieces in surrounding cores. This interval in Hole 1149D likely had a high permeability that facilitated more intensive alteration at high water-rock ratios.

The distribution and abundance of veins, halos, and breccias logged in Holes 1149B, 1149C, and 1149D are shown in Figure F48 (data in Table T9; also see “Site 1149 Vein Log,” p. 123; also in ASCII format). All basement cores are cut by veins in varying proportions (1.5–7 vol%). The three holes exhibit the same features and are characterized by a relatively high density of veins with an average of 35 veins/m. An extreme value of 50 veins/m is recorded in Core 185-1149C-7R. Calcite and clay minerals (saponite and/or celadonite) are the dominant vein and hyaloclastite components, with lesser Fe oxyhydroxides (Fig. F49). Veins can be filled by a single phase but are most commonly filled by several different phases (Tables T9, T10). Where clay minerals and calcite are present in the same vein, calcite is generally the last phase to precipi-

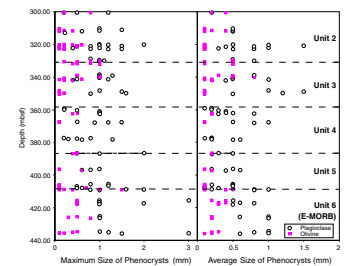
T6. Location of volcanic glass, p. 167.

T7. Primary mineralogy of thin sections, p. 168.

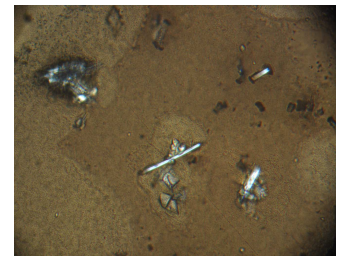
F41. Typical groundmass of the basalts, p. 104.



F42. Maximum and average phenocryst size vs. depth, p. 105.



F43. Euhedral plagioclase and olivine phenocrysts in a glassy pillow rim, p. 106.



tate. Carbonate-rich veins are thicker (1.5 mm) and have wide associated alteration halos (~5.6–6.3 mm wide), whereas saponite-rich veins are thinner (0.2–0.4 mm) and are associated with narrower halos (~3.7–4.6 mm wide). The brown, orange, and reddish veins are composed of Fe oxides and hydroxides mixed with clays. Pure Fe oxyhydroxide veins are very scarce, but ~40% of the veins logged are estimated to contain between 10% and 20% of Fe oxyhydroxides, associated mostly with saponite.

Only one thin section of an alteration halo was made on ship; hence, such observations are very preliminary in character. We suggest that the alteration in cores from Site 1149 results from a succession of at least three low-temperature alteration stages that all proceed from open fissures and exposed surfaces:

1. Formation of centimeter-thick dark halos as a result of precipitation of celadonitic phyllosilicates (probably celadonite-smectite mixtures) in cracks, vesicles, miarolitic voids, and replacing the olivine and mesostasis.
2. Oxidation of the above phyllosilicates or addition of Fe oxide to these zones to produce goethite and/or mixtures of clay minerals + goethite (i.e., “iddingsite”). The fluids responsible for this stage followed the same pathways as those of the first stage, as well as new hairline cracks. This second stage resulted in the formation of orange-brown halos, generally <1 cm in thickness, observed between the fracture and the dark halos, as well as the brown band at the boundary between the halo and host rock.
3. Final precipitation of calcium carbonates in the same cracks as those responsible for Stages 1 and 2, and along newly formed fissures.

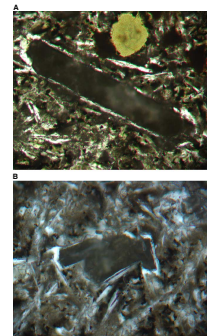
Besides the abundant alteration halos, the abundance of red Fe oxyhydroxide in veins and fractures is one of the more striking features of cores recovered in Holes 1149B and 1149C (as much as 3.9 vol% of Fe oxyhydroxides). Oxidation of early secondary Fe sulfides in veins or alteration of igneous Fe oxides could contribute to this enrichment. The late calcite in saponite veins suggests that many veins were reopened after circulating fluid had changed composition. Different generations of halos are also delineated by their different colors, though a gradation of color may be present within a single alteration halo. A common chronology of veins and halos includes (1) early fracturing of basalt with filling of veins by clay minerals (mostly saponite, as well as celadonite?) and development of celadonite-bearing dark halos; (2) progressive alteration and oxidation of host basalt with the progression of a brown oxidation halo away from the fracture and into the rock; and (3) reopening of veins allowing the circulation of fluids and precipitation of carbonate and reworking of previous halos.

INTERSTITIAL WATER CHEMISTRY AND HEADSPACE GAS

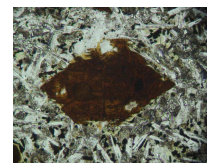
Abstract

The interstitial water program at Site 1149 consisted of the extrusion and analysis of 46 samples from Hole 1149A as well as 6 samples from Hole 1149B. Despite poor core recovery through the porcelanites and

F44. Altered plagioclase phenocrysts, p. 107.

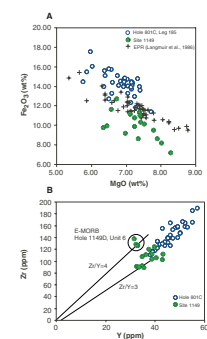


F45. Altered olivine phenocryst, p. 108.

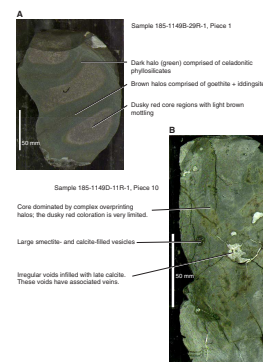


T8. XRF and ICP-AES and -MS analyses, p. 169.

F46. MgO vs. Fe₂O₃ and Zr vs. Y for basalts, Sites 1149 and 801, p. 109.



F47. Variation in intensity alteration, p. 110.



cherts of lithologic Unit III (see “Unit III,” p. 14), enough samples were gathered to provide adequate coverage of the entire sedimentary sequence, with the shallowest sample acquired at 1.4 mbsf and the deepest 0.60 m above the sediment/basement contact in Section 185-1149B-29R-1. Interstitial water data are given in Table T11.

The chemical composition of the interstitial waters at this site reflect several processes, including organic matter degradation, diagenetic formation of chert and porcelanite, carbonate diagenesis, ash alteration, authigenic clay formation, and basement alteration. In the following sections we show how the interstitial water chemistry at this site illustrates each of these various processes. The cherts and porcelanites of Unit III inhibit but do not totally restrict diffusive communication between the upper and lower portions of the sediment section. The low average sedimentation rate at Site 1149 (see “Sedimentation Rates,” p. 37) results in the recording of long-term diagenetic reactions in a relatively thin sedimentary sequence.

Degradation of Organic Matter and Associated Redox Environments

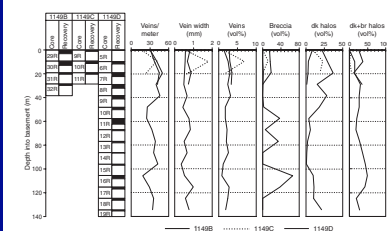
The organic loading at this site is minimal, as reflected by the low alkalinity and the slight enrichments in dissolved NH_4^+ to $\sim 200 \mu\text{M}$ and PO_4^{3-} to $\sim 35 \mu\text{M}$ (Fig. F50). Dissolved SO_4^{2-} decreases only slightly downhole, and Fe is below the analytical detection limit throughout the entire sequence (Fig. F51). Dissolved Mn is present only in the upper 150 mbsf. These distributions are consistent with the very low concentrations of CH_4 in the headspace gases (Table T12) and collectively indicate only a slightly suboxic diagenetic environment at Site 1149.

Dissolved PO_4^{3-} reaches a maximum within the upper 10 mbsf, whereas dissolved NH_4^+ reaches a maximum through the upper 50 mbsf, reflecting the sequential release of these species during organic matter degradation. The decrease in dissolved NH_4^+ below this interval reflects uptake during clay diagenesis. Concentrations of dissolved PO_4^{3-} decrease sharply below this shallow maximum and reach a strong local minimum at ~ 20 mbsf, indicating a local sink of dissolved PO_4^{3-} at this depth. Dissolved Mn (Fig. F51) also records a minimum at this horizon, suggesting that the precipitation of diagenetic Mn oxides also removes PO_4^{3-} from the interstitial waters. The increases in dissolved Mn from 20 to 100 mbsf suggests a redox change through this depth interval, which will be addressed in greater detail in postcruise studies. Further downhole, from 100 to 150 mbsf, the rapid decrease in dissolved Mn suggests the precipitation of Mn oxides through lithologic Unit II. This decrease is broadly coincident with the decrease in dissolved PO_4^{3-} to essentially zero, suggesting that these Mn oxides also scavenge dissolved PO_4^{3-} from the interstitial waters. Considering the varying redox behavior in this portion of the sedimentary section, some of the sedimentary features identified as “ash layers” may in fact be relict Mn oxide precipitation horizons.

Diagenesis of Biogenic Silica and Carbonate

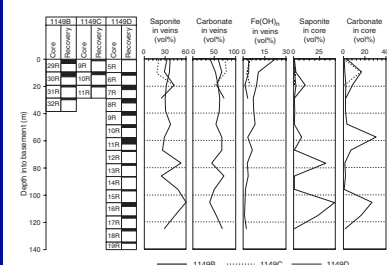
Dissolved silica is well above the representative concentration in seawater in even the shallowest sample recovered at Site 1149 (Fig. F52).

F48. Data on veins, breccia, and alteration halos, p. 111.



T9. Vein types, Holes 1149B and 1149C, p. 170.

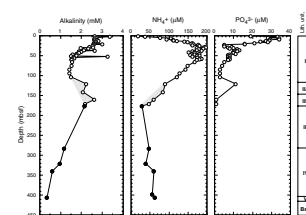
F49. Compositions of veins and proportions of saponite and carbonate, p. 112.



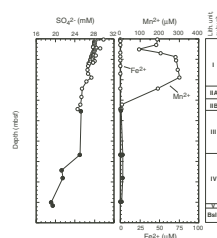
T10. Vein types, Hole 1149D, p. 171.

T11. Interstitial water data, p. 172.

F50. Concentration profiles of alkalinity, dissolved NH_4^+ , and PO_4^{3-} , p. 113.



F51. Concentration profiles of dissolved SO_4^{2-} , Mn^{2+} , and Fe^{2+} , p. 114.



Concentrations increase to maximum values at 100 mbsf, before decreasing precipitously to low values of ~230 μM through lithologic Unit II. Concentrations increase at the bottom of Hole 1149A and into Hole 1149B. Below Unit III, concentrations decrease with increasing depth to low values of ~230 μM again, with a local maximum in Unit V.

This dissolved silica profile is influenced by the diagenesis of biogenic silica as well as by the formation of authigenic clay minerals (the latter will be discussed more fully below). The steady increase through Unit I reflects the continual dissolution of biogenic opal from the diatoms contained in this lithologic unit. Were it not for the strong sink of dissolved silica caused by the ash and clay alteration occurring in Unit II, we predict the concentration of dissolved silica would have continued to increase to the opal-A–opal-CT transition found at ~170 mbsf. The first occurrence of opal-CT, however, is observed in Core 185-1149A-21X (~179.7 mbsf) (see “Unit III,” p. 14), and this diagenetic transformation is the likely cause of the somewhat lower concentrations of dissolved silica at the top of Hole 1149B. The last occurrence of opal-CT is found in Core 185-1149B-18R (~301.7 mbsf) (see “Unit IV,” p. 15), and the transition to diagenetic quartz draws down dissolved silica concentrations in Unit IV.

Considering the Adara temperature measurements made in Cores 185-1149A-6H and 8H, which indicate temperatures of 5.687° and 6.390°C, respectively (see “Run 1,” p. 42), we estimate that the opal-A–opal-CT transition occurs at 6°–7°C, and the opal-CT–quartz transition occurs at 11°–12°C. These values are consistent with previous results from open-ocean depositional regimes (e.g., Hein et al., 1978).

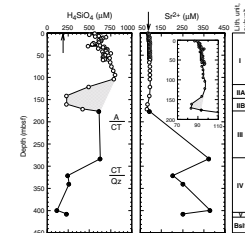
Because there is little sedimentary carbonate in Units I, II, or III (see “Abstract,” p. 10), increases in dissolved Sr^{2+} are minimal throughout this portion of the sedimentary section (Fig. F52). Through the uppermost 50 mbsf there is an increase in dissolved Sr^{2+} to values slightly above that of average seawater (see inset in Fig. F52). Below the sharp decrease in Unit II (see inset of Fig. F52), concentrations in dissolved Sr^{2+} increase at least in part as a result of the recrystallization of sedimentary carbonate in Unit IV. This is not the sole mechanism influencing the distribution of dissolved Sr^{2+} , however, as shown by the widely varying concentrations at the depth where the effect of local sources and sinks may be important.

Ash Alteration and Formation of Authigenic Clays

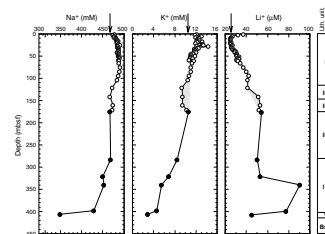
Diagenetic processes acting within the ash- and clay-rich sediments of Units I and II (see “Unit I,” p. 11, and “Unit II,” p. 12) dramatically affect several constituents of the interstitial waters. The concentration of dissolved silica exhibits a pronounced minimum in Unit II (see shaded area in Fig. F52), reaching values as low as those found in the diagenetic quartz portion of Unit IV much deeper in Hole 1149B. The dark brown pelagic clays of Unit II clearly define a unique diagenetic environment compared to the other units at this site. Concomitant depletions are observed in dissolved Sr^{2+} (see inset in Fig. F52) and dissolved K^+ (Fig. F53), whereas enrichments are present in alkalinity and dissolved NH_4^+ (Fig. F50) and dissolved Li^+ (Fig. F53), reflecting the effects of cation exchange and authigenic clay formation. Additionally, there is a slight decrease in dissolved Cl^- as well, which may reflect dehydration during authigenesis.

F12. Concentrations of CH_4 , p. 174.

F52. Concentration profiles of dissolved silica and Sr^{2+} , p. 115.



F53. Concentration profiles of dissolved Na^+ , K^+ , and Li^+ , p. 116.



The uppermost several tens of meters of the sedimentary section are also active in terms of clay-mineral diagenesis. Through the upper 10–20 mbsf, dissolved Na^+ increases, whereas dissolved Li^+ shows a pronounced depletion (Fig. F53). These changes may in part reflect ion exchange between the microbially produced NH_4^+ (Fig. F50) and Li^+ . General changes with depth of these and other cations also most likely reflect a contribution by clay alteration.

Basement Alteration

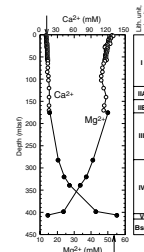
Drilling at Site 1149 recovered the sediment/basement contact in Core 185-1149B-29R. Sediments in the overlying Units IV and V were un lithified enough to yield several interstitial water samples, allowing a terrific chance to document diffusional signals responding to basement alteration.

The distributions of dissolved Ca^{2+} and Mg^{2+} record the release of Ca^{2+} and uptake of Mg^{2+} during basalt alteration (Fig. F54). The interstitial water samples record an extreme enrichment in dissolved Ca^{2+} , reaching 135 mM at 407 mbsf, along with a depletion of dissolved Mg^{2+} to a low value of 15 mM at the same depth. The greatest change in both concentration profiles occurs through Units IV and V, indicating that the decreased permeability of the cherts and porcelanites effectively inhibits diffusion through this portion of the sedimentary section.

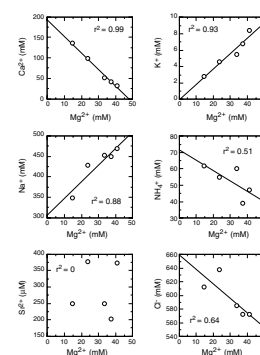
The strongly linear relationship between dissolved Ca^{2+} and Mg^{2+} in the lower reaches of the sedimentary section ($r^2 = -0.99$; see upper left panel in Fig. F55), along with the shape of the paired concentration-depth profiles, argues persuasively for a dominantly diffusive control on the concentration of these species in Units IV and V. This is consistent with many previous observations of dissolved Ca^{2+} and Mg^{2+} in other sedimentary sequences (e.g., Gieskes, 1983). We can use the well-documented relationship between dissolved Ca^{2+} and Mg^{2+} to assess the effect of basement alteration on other dissolved species at Site 1149 (Fig. F55). Considering the five interstitial water samples recovered from Units IV and V, and assuming Mg^{2+} is quantitatively removed by basement alteration (and thus an end-member concentration of 0 mM), we can assess the effect of basement alteration on other dissolved constituents by comparing the linearity of their relationship to Mg^{2+} . This indicates that the distributions of dissolved K^+ and Na^+ appear to be dominated by diffusion into basement alteration products, that the distribution of dissolved NH_4^+ appears to be moderately affected, and that the distribution of dissolved Sr^{2+} appears to be unaffected by basement alteration (Fig. F55). Thus, basement alteration is sequestering Mg^{2+} , K^{2+} , and Na^{2+} . The inverse relationship with dissolved NH_4^+ may reflect cation exchange in the sediments involving other species. Finally, the slight net increase in dissolved silica in the deepest sample (Fig. F52) suggests the release of silica during basement weathering.

In Units III and IV, with the exception of the deepest sample, concentrations of dissolved Cl^- increase toward the basement (Fig. F56). These concentrations are moderately correlative to those of dissolved Mg^{2+} ($r^2 = -0.64$). Whereas the increase in dissolved Cl^- with depth over the uppermost 20 mbsf most likely reflects the freshening (with time) of ocean water since the last glaciation, the sharp increase in dissolved Cl^- with depth toward the bottom of the hole indicates hydration of the basaltic crust.

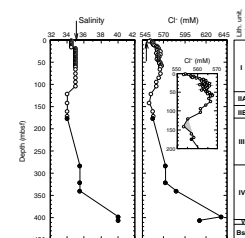
F54. Concentration profiles of dissolved Ca^{2+} and Mg^{2+} , p. 117.



F55. Relationships between dissolved constituents, p. 118.



F56. Concentration profiles of salinity and dissolved Cl^- , p. 119.



Summary

The relatively simple sedimentary sequence at Site 1149 provides an exceptional natural laboratory to examine diagenetic processes operating over a long time scale (~135 m.y.) in a sequence bounded by basaltic crust and the oceanic reservoir. At this site, the distribution of dissolved constituents in the interstitial waters is affected, in a broad burial sequence, by degradation of organic matter and associated changes in the redox environment, authigenic clay formation, diagenetic recrystallization of biogenic silica and carbonate, and basement alteration.

These processes cannot be considered in isolation from one another. For example, release of dissolved PO_4^{3-} is followed by sequestering in Mn oxides, whereas the release of dissolved silica by the dissolution of diatoms is followed by sequestering in the authigenic clays of Unit II, and cation exchange of species influenced by basaltic alteration (e.g., Na^{2+} and K^+) affects other constituents (e.g., NH_4^+) in the deepest recovered interstitial waters. Although further shore-based research will refine the preliminary observations discussed here and identify further problems to study, it is clear that the chemical environment at Site 1149 is responding to the combined effects of a variety of sources and sinks throughout the sedimentary and basaltic sequence.

SEDIMENTARY GEOCHEMISTRY

Abstract

The sedimentary geochemistry analytical program for Site 1149 consisted of XRF analyses to determine the bulk major- and trace-element composition of 19 samples distributed throughout the entire sequence. We provide in Table T13 a brief description of the lithologies from which the analyzed samples were taken. The shallowest sample was collected at 2.18 mbsf, whereas the deepest was taken at 397.97 mbsf, <10 m from the sediment/basalt interface (Table T14). The downhole coverage provided by these samples allows for a preliminary assessment of the chemical composition of the complete sequence, with the exception of the fracture-filling calcareous marlstones of Unit V.

Chemical data are given in Table T14 (carbonate-poor samples) and Table T15 (carbonate-rich samples). For the carbonate-rich sediments, only the major elemental ratios discussed below are reported because calibration difficulties for the high-carbonate matrix preclude determination of the absolute concentrations. In most cases, data are normalized to Al (or Al_2O_3) concentration in order to remove the effects of compositional dilution by carbonate (in the limestones) or silica (in the cherts and porcelanites).

Four signals dominate the record of the bulk chemistry of the sediment. In stratigraphic order, these are: (1) metalliferous sedimentation through Unit IV, (2) the enrichment in biogenically associated elements such as Ba and Sr through Units IV and III, (3) the authigenic clays of Unit II, and, finally, (4) the influence of volcanic ash in Unit I. Each of these geochemical signatures is discussed below.

T13. XRF sample lithologies, p. 175.

T14. Geochemical data for carbonate-poor sediments, p. 176.

T15. Geochemical data for carbonate-rich sediments, p. 177.

Metalliferous Sources

The distribution of Fe/Al shows a very well defined decrease upsection away from the basement, which we interpret as recording the waning influence of hydrothermal metalliferous sources as Site 1149 traveled away from the ridge crest (Fig. F57). Although most of this decrease occurs through Unit IV, it appears that Fe/Al values in excess of those in average shale are maintained through Unit III as well. Based on the few shipboard analyses through this particular interval, however, it is difficult to determine where the Fe/Al ratios reach values near that of average shale. Higher frequency postcruise study should resolve this issue.

The distribution of MnO/Al₂O₃ also records maximum values nearest the basement (Fig. F57), although the continual decrease upsection is not as smooth as the Fe/Al trend. Nonetheless, the very high values in the lowermost section are consistent with a metalliferous (ridge) source of the Mn in Unit IV.

Through Unit IV, P₂O₅/Al₂O₃ values also record a sharp decrease with increasing distance above the basement (Fig. F57) and maintain relatively high values through Unit III (the latter is discussed in “Biogenic Sedimentation,” p. 31). We interpret the decrease in P₂O₅/Al₂O₃ to reflect the scavenging of dissolved PO₄³⁻ from seawater by metalliferous plume particles, a process that becomes less significant with distance from the ridge. This scavenging is observed in modern ridge systems as well as in other sedimentary sequences, and is an important sink in terms of global budgets of PO₄³⁻ (e.g., Feely et al., 1996).

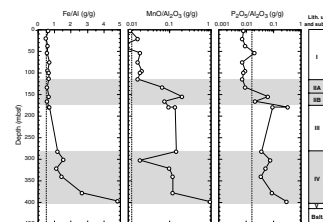
This data set indicates that there is a substantial hydrothermal metalliferous contribution to the sediments below 350 mbsf. A measurable, yet less important, component appears to be present from at least 350 to 280 mbsf, whereas the influence through deposition of Unit III requires further study.

Biogenic Sedimentation

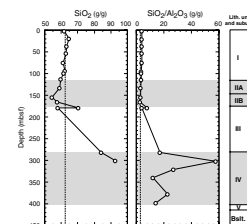
The depositional process that resulted in the cherts and porcelanites of Unit III, as well as the carbonates of Unit IV, supplied SiO₂, Ba, Sr, and P to the seafloor to a greater extent than if sedimentation had occurred only by terrigenous or metalliferous inputs. The cherts and porcelanites of Unit III are identified by the high SiO₂, with respect to average shale (Fig. F58). Normalizing SiO₂ to Al₂O₃ indicates that even though carbonate is the dominant lithology through Unit IV, there is still enough biogenic silica in these sediments to elevate the SiO₂/Al₂O₃ ratio significantly above that of average shale. The high variability of SiO₂/Al₂O₃ within Unit IV indicates local variations in silica diagenesis, the degree of which will be better determined with higher frequency sampling during postcruise studies.

Barium and strontium are also supplied to the seafloor by biogenic sedimentation. Barium is relatively refractory compared to SiO₂; at this site, where dissolved SO₄²⁻ is not significantly depleted from the interstitial waters (see “Diagenesis of Biogenic Silica and Carbonate,” p. 27), barium may be a general indicator of biogenic input. Indeed, Ba (Table T14) and Ba/Al (Fig. F59) are significantly elevated through Units III and IV and increase steadily toward basement. Strontium (Table T14) and Sr/Al (Fig. F59) also record this deep increase, reflecting an increase in carbonate with depth in the sediment column. There are several pro-

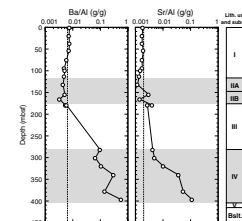
F57. Profiles of Fe/Al, MnO/Al₂O₃, and P₂O₅/Al₂O₃, p. 120.



F58. Profiles of SiO₂ and SiO₂/Al₂O₃, p. 121.



F59. Profiles of Ba/Al and Sr/Al, p. 122.



cesses that affect the sediment composition through Unit IV. With respect to Ba, the deepest samples probably also record a hydrothermal source, and postcruise statistical analyses will target resolving these different sources of Ba. With respect to Sr, the decrease of Sr/Al with distance above the basalt is consistent with thermal subsidence of the oceanic crust away from the ridge and below the CCD. Thus, the sediments at Site 1149 provide an excellent chemical record from which we hope to resolve metalliferous and biogenic sedimentation, as well as the depth of the CCD during the time period within which Unit IV was deposited.

Authigenic Clay Formation: Unit II

As described in “Unit II,” p. 12, and “Ash Alteration and Formation of Authigenic Clays,” p. 28, the authigenic clays of Unit II are a unique sedimentary unit at Site 1149. Solid-phase chemical changes are generally much less sensitive to diagenetic change than the interstitial waters because of the high distribution coefficients between the solid and aqueous phases. Nonetheless, the preliminary bulk XRF data record authigenic clay formation. Because clay mineral authigenesis often involves cation exchange (see “Ash Alteration and Formation of Authigenic Clays,” p. 28), tracking variations in sedimentary K, Na, and Mg (Fig. F60) provide an important data set complementary to the interstitial water chemistry.

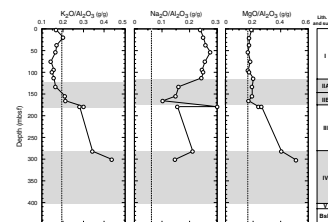
The authigenic clays of Subunit IIB are enriched in K relative to the clays of Unit I, but, they appear depleted in Na with respect to Unit I, which may include a contribution from sea salt. The clearest signal is seen in the MgO/Al₂O₃ ratio (Fig. F60), which shows an increase completely bounded by Unit II. These changes in the alkalis and Mg are also apparent in the interstitial water profiles (see “Ash Alteration and Formation of Authigenic Clays,” p. 28). Finally, it appears these clays are depleted in SiO₂ (Fig. F58).

Dispersed Ash in Unit I

The pelagic clays of Unit I include many discrete ash layers (see “Unit I,” p. 11). Whereas many elements and elemental ratios record values near that of average shale through Unit I (Figs. F57, F58, F59, F60), the inclusion of ash in the sediment affects its bulk chemical composition for other elements. We exploit this effect by using the chemical deviations from average shale to infer the degree to which dispersed ash is included in the sediment. In this context, we refer to “dispersed” ash as the ash that is not contained in visually obvious discrete layers (which are commonly up to several centimeters thick). This dispersed-ash component includes discrete layers that have been pervasively bioturbated as well as ash that has been deposited directly to the seafloor as part of the pelagic rain. In either case, this dispersed component is quantitatively significant; smear-slide studies (see “Abstract,” p. 10) estimate that 25%–35% of the sediment may consist of ash particles.

We provide a first-order estimate of the amount of discrete ash in Unit I through a normative approach. Whereas postcruise study of other elements, along with statistical analyses, will yield a more robust result than that described below, these preliminary results yield reasonable estimates that are consistent with the smear-slide studies. We first estimate the amount of “terrigenous clay and ash” by normalizing the

F60. profiles of K₂O/Al₂O₃, Na₂O/Al₂O₃, and MgO/Al₂O₃, p. 123.



concentration of Al in each sample with that in average shale, according to

$$\text{Terrigenous clay and ash (wt\%)} = (\text{Al}_{\text{sample}}/\text{Al}_{\text{shale}}) \times 100. \quad (1)$$

Although it may seem inappropriate to use the Al concentration in an average shale for a sediment that is known to include both terrigenous clay and ash, in practice, the influence of the ash on the bulk content of Al is minimal because Al in ash is relatively near to that in average terrigenous materials. Through Unit I, this calculation yields values of ~85–90 wt% for the terrigenous + ash fraction, indicating that diatomaceous material, oxides, structurally bound water, and perhaps other non-Al-bearing phases are present to ~10–15 wt%. Because the SiO₂/Al₂O₃ ratio in Unit I is very similar to that of average shale (Fig. F58), the contribution of diatoms to the sediment is relatively small. The calculation yields unrealistically large (i.e., >100%) values of terrigenous material through Unit II, confirming that these pelagic clays (which have been significantly diagenetically altered) are not composed of average shale type material. Because of this, we are unable at this point to quantify the abundance of dispersed ash in Subunit IIA. The concentration of terrigenous material decreases through the cherts, porcelanites, limestones, and metalliferous sediments of Units III and IV, recording compositional dilution.

How quantitatively significant is the dispersed ash in Unit I? The Al/Ti and Nb/Al ratios in Unit I are significantly different from those in average shale, both suggesting the presence of dispersed ash (Fig. F61). Al/Ti values are higher than average shale, whereas Nb/Al values are lower. In consideration of the near constancy in Al concentrations between terrigenous matter and ash, these contrasts reflect a depletion in both Ti and Nb, which in turn result from the presence of both basaltic and rhyolitic compositions of the dispersed ash.

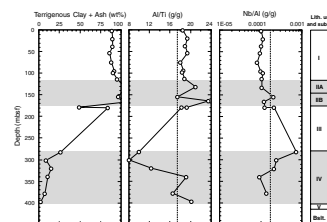
Because Nb is depleted in arc ashes and enriched in average shale (19 ppm; Taylor and McLennan, 1985) (0.5–6 ppm; Taylor and Nesbit, 1998), we use the Nb concentrations of the bulk sediment along with the results of Equation 1 to calculate the amount of dispersed ash in a given sample according to

$$\begin{aligned} \text{Dispersed ash (\%)} = & \text{Terrigenous clay and ash (wt\%)} \\ & - [(\text{Nb}_{\text{sample}}/19) \times 100], \end{aligned} \quad (2)$$

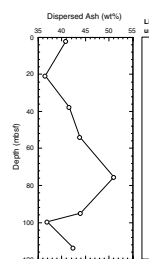
which assumes a constant value of 19 ppm Nb in average shale and zero in ash. Equation 2, therefore, subtracts the terrigenous component from the mixed “clay and ash” result of Equation 1. Ideally, we would like to be able to use in Equation 2 a chemical element that had zero concentration in the ash, but our limited data set at this point precludes doing so. Because actual Nb concentration in the ashes may be as much as 4–6 ppm, the third term in Equation 2 overestimates the amount of terrigenous clay; thus, the final calculation yields a minimum estimate of dispersed ash.

The results of this calculation for the samples in Unit I indicate that these sediments contain 35–50 wt% dispersed ash (Fig. F62). These values are somewhat higher than the smear-slide estimates of 25%–35%, which tend to underestimate ash, not only because fine-grained particles are underestimated but also because some of the originally ashy material may be altered to clay and thus be difficult to distinguish from

F61. Profiles of “terrigenous clay and ash,” Al/Ti, and Nb/Al, p. 124.



F62. Profile of dispersed ash, p. 125.



terrigenous material. Thus, given the uncertainties in our calculations, we believe these results are likely to be accurate to within 5–10 wt%.

Summary

Overall, the preliminary sedimentary chemistry reveals several critical intervals that should be targeted during postcruise studies. In stratigraphic order, Site 1149 records a well-developed hydrothermal metalliferous sedimentary profile that documents the decreasing influence of plume precipitation with lateral distance from the ridge. Diagenetic enrichments of silica, and perhaps other elements through the cherts and porcelanites of Unit III, modify to a certain degree the primary depositional signal beneath the elevated high productivity of equatorial deposition, although some paleoproductivity indicators (e.g., Ba/Al) may prove useful. Authigenic clay formation in Unit II is identified in both the solid and aqueous phases. Lastly, the high proportion of dispersed ash in Unit I, which is both visually identified in smear slides and chemically quantifiable on the basis of bulk chemical analyses, can perhaps be more accurately partitioned into basaltic and rhyolitic contributions by expanding the chemical data set with further shore-based analyses.

PALEOMAGNETISM

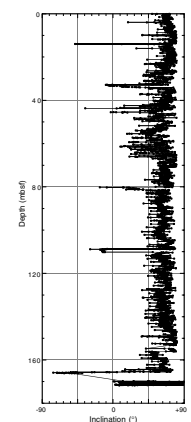
Introduction

All of the archive halves of the soft sedimentary sequence, lithologic Units I and II (see “Unit I,” p. 11, and “Unit II,” p. 12), were measured and demagnetized with the shipboard-automated long-core cryogenic magnetometer. Recovery in lithologic Units III and IV was quite discontinuous; therefore, each chert, porcelanite, marl, or chalk piece was placed separately in the magnetometer with the bedding planes carefully oriented to geographic vertical (depositional orientation). In this manner, inclination was obtained, although the polarity of inclination was not known. These data allow paleolatitude to be obtained. Site 1149 is located on the same tectonic plate as the sites of Leg 129 (Sites 800, 801, and 802) for which paleolatitudes had been determined in detail (Steiner and Wallick, 1992). Projection of the paleolatitude records of Sites 800 and 801 to Site 1149 indicates that Site 1149 was located in southern latitudes during the deposition of lithologic Unit IV and most likely in low southerly paleolatitudes during deposition of Unit III. Measurement and demagnetization of bedding-plane oriented fragments of siliceous and carbonate sedimentary rocks allow a record of paleolatitude to be constructed. Finally, vertically oriented pieces of the basaltic basement also were measured and demagnetized with the shipboard magnetometer.

Remanent Magnetization

The natural remanent magnetization (NRM) inclinations of the archive halves of all cores obtained from Holes 1149A and 1149B are shown in Figure F63. Nearly all inclinations have values between +60° and +80°, whereas the present geomagnetic field inclination at this site is only 51°. This result was surprising because it indicates nearly com-

F63. Inclinations of natural remanent magnetization, p. 126.



plete overprinting of the original remanent magnetization by a drilling remanence.

Magnetostratigraphy

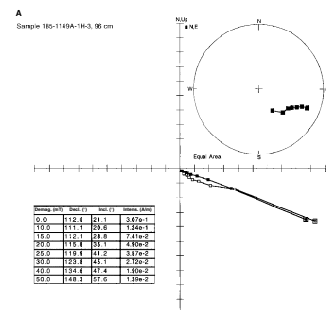
The main objective in measuring the archive halves of the cores recovered at Site 1149 was to obtain a magnetostratigraphy for dating and correlation purposes in sedimentological and paleontological shipboard studies. Because of the volume of core obtained and the rate at which cores were recovered, a brief blanket demagnetization procedure was undertaken to apply to all cores of similar lithology. Detailed alternating-field (AF) demagnetization was performed on one section of the first core recovered. That section was demagnetized at field strengths of 10, 15, 20, 25, 30, 40, and 50 mT. A large part of the drilling remanence overprint was removed by 10 mT (Fig. F64); complete removal required at least 25 mT, and even 35 mT was insufficient in some strata to completely remove the secondary magnetization. Because of the anhysteretic remanence (see “Paleomagnetism,” p. 27, in the “Explanatory Notes” chapter) imposed by the AF demagnetization apparatus, the cores were not treated higher than 25–35 mT. The 25-mT step generally is a good representation of the true remanence, as it displays in detail the magnetic polarity reversal pattern. For the sake of speed in a high core volume setting, all cores were demagnetized at 25 mT; some also were demagnetized at 15 and 35 mT. Toward the bottom of the unlithified sedimentary section in Hole 1149B (lithologic Unit II, see “Unit II,” p. 12), even 35 mT was unable to adequately remove the coring overprint.

The results from the upper 110 m of the sedimentary sequence (lithologic Unit I) (see “Unit I,” p. 11) were remarkable. A complete replica of the magnetic polarity time scale for 0–6.3 Ma was obtained after demagnetization to 25 mT. Cores 185-1149A-4H through 19H were oriented with the tensor tool; therefore, absolute declination as well as inclination was obtained in the paleomagnetic data. Figure F65 displays the declination (left) and inclination (right) for this sedimentary interval. Figure F60, p. 131, in the “Site 801” chapter compares those data to the most recent Cenozoic magnetic polarity time scale (Berggren et al., 1995); a remarkable one-to-one match with the known behavior of the geomagnetic field is exhibited.

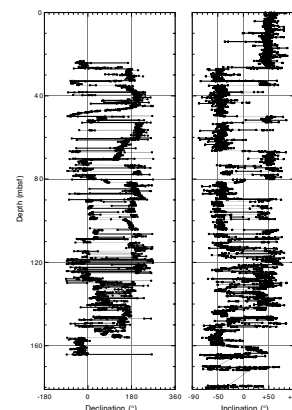
Through this magnetostratigraphic record, the upper 110 m of the sedimentary section (Cores 185-1149A-1H through 13H) can be very accurately dated (Fig. F66). Paleomagnetic and $^{40}\text{Ar}/^{39}\text{Ar}$ studies of volcanic rocks from the last 7 m.y. have determined the ages of the geomagnetic field reversal record to an accuracy of two decimal places (see time scale of Berggren et al., 1995). The well-known ages of these reversals allows sedimentation rates to be calculated. The magnetostratigraphy shows that sedimentation rates during the current Brunhes normal geomagnetic polarity interval were a remarkable 34 cm/k.y. A number of rate changes are obvious between late Miocene and the present (see “Sedimentation Rates,” p. 37).

An abrupt change in remanence is present between Sections 185-1149A-13H-1 and 13H-2. The change is obvious both in NRM and the demagnetized data. Beginning at Section 185-1149A-13H-2, the consistency of magnetic directions from centimeter to centimeter within the core decreases, resulting in a degraded magnetic polarity signature. However, some indications of polarity structure remain evident down through Core 185-1149A-20X (Fig. F65). Although not well defined,

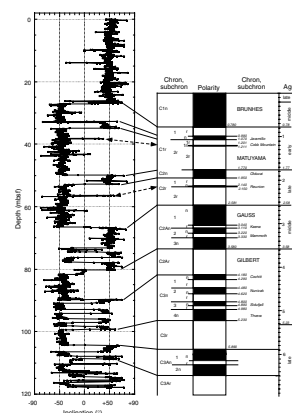
F64. Alternating field demagnetization, p. 127.



F65. Magnetostratigraphy after demagnetization at 25 mT, p. 129.



F66. Inclinations of Unit I compared to the late Cenozoic magnetic polarity time scale, p. 130.



therefore not identifiable to the chron and subchron level, an overall pattern still is obvious. A large proportion of the strata between ~114 and 134 mbsf exhibits a dominance of normal polarity with a suggestion of frequent, poorly defined polarity changes. No information is available regarding hiatuses in this part of the section; therefore, the validity of matching lithologic Unit II to the polarity time scale immediately preceding the last identified chron in lithologic Unit I (late Miocene Chron C3Ar) may not be supportable. Nevertheless, the dominance of normal polarity and suggested abundant polarity changes in the data of lithologic Unit II bears a resemblance to a compressed version of some part of perhaps the late Oligocene through the early late Miocene geomagnetic polarity time scale. Considering the sedimentation rates, it is possible that the large amount of reversed polarity exhibited between ~150 and 166 mbsf represents the reversed polarity of latest Eocene–early Oligocene time; at present, however, these are merely speculations based on available data.

Paleolatitude

A major objective of the study of the paleomagnetism of Site 1149 was to obtain a paleolatitude tract for this more northern Pacific plate site to compare it to those produced at Sites 800, 801, and 802, 10°–15° to the south. Numerous paleolatitude data were accumulated. These data will be fully analyzed and reported in a later publication. At present, a few generalizations can be made. The site appears to have achieved approximately its present latitude by the Miocene or earlier. The inclination from the upper Miocene to the Pleistocene in lithologic Unit I appears to be constant and similar to the present inclination (50.6°) at this 31.3°N latitude site. The approximate mean inclination for Unit I is 47°–48°, corresponding to a paleolatitude of 28°–29°N. Lithologic Unit II, when magnetically well defined, has inclinations that are the same or slightly shallower (35°–50°) than at present. These inclinations suggest paleolatitudes of 20°–30°N and may correspond to Eocene–Miocene time. The top of Unit III (Cores 185-1149B-4R through 13R) has approximately zero inclinations, within ±5°–10°, suggesting that the site was on or near the equator. Because these core pieces are predominantly unoriented, and as yet undated, paleomagnetic results cannot define whether the site was north or south of the equator at the time of deposition of lithologic Unit III. The distribution of inclinations suggests that the site was located on the equator and that it remained on the equator for the entire time of deposition of this lithologic unit. Lithologic Units IV and V (within the basement) have shallow, but non-equatorial inclinations.

The basaltic basement displays a large amount of alteration and, perhaps consequently, displays a complicated magnetization. Oriented basaltic basement pieces were measured in all three holes that penetrated basement (Holes 1149B, 1149C, and 1149D). Normally, a multi-component magnetization is observed, and the components are not adequately separated by the AF demagnetization performed shipboard. Some samples in all of the basement holes (Holes 1149B, 1149C, and 1149D) display a seemingly single-component magnetization, as judged by linear behavior during increasing AF treatment. Samples with this behavior become more abundant deeper in the basement (Hole 1149D). These samples all have positive inclination magnetizations, indicative of reversed polarity in the Southern Hemisphere, consistent

with the predicted M11 age. A very preliminary estimate of the inclination value is $+20^{\circ}$ – 30° , corresponding to a paleolatitude of 10° – 16° S.

Summary

Three major results came from paleomagnetic measurement of samples from Site 1149. The magnetostratigraphic record contained in the upper strata (lithologic Unit I) replicates, in great detail, the magnetic polarity time scale between 0 and 6.3 Ma. The detail obtained places tight age constraints on the upper 110 m of the sedimentary record and demonstrates very high sedimentation rates (~ 30 m/m.y.) for the upper Neogene. A paleolatitude record for the site was obtained from Units I, III, IV, and the basement, which shows that plate motion was nonuniform as the site moved from $\sim 10^{\circ}$ – 15° S in Early Cretaceous time to its present location of 31° N. The magnetization of the basaltic basement has reversed polarity, consistent with the location of Site 1149 on the reversed polarity magnetic Anomaly M11A.

SEDIMENTATION RATES

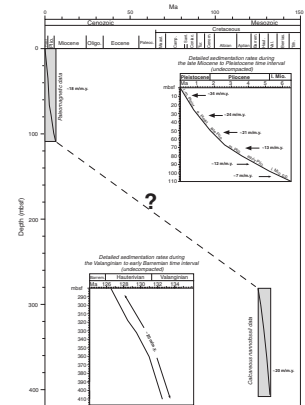
The distribution of ages and sediment thicknesses allows the calculation of sedimentation rates for lithologic Units I and IV (see “Unit I,” p. 11, and “Unit IV,” p. 15). Although the sedimentary section has not been decompacted, some patterns have been observed (Fig. F67). Sedimentation rate reconstruction in the upper 108.7 mbsf is based on paleomagnetic age constraints (see “Magnetostratigraphy,” p. 35) and on the preliminary biostratigraphic age assignment of Core 185-1149A-9H to the Pliocene and of Core 12H to the late Miocene, according to their siliceous plankton assemblages. The sedimentation rate averages 18 m/m.y. but was notably higher during the late Pliocene (~ 21 m/m.y.), the early Pleistocene (~ 24 m/m.y.), and during the middle to late Pleistocene (34 m/m.y.). A slower sedimentation rate (~ 7 to ~ 13 m/m.y.) characterizes the late Miocene to the mid-Pliocene. Unit I is characterized by widespread volcanic ash layers (see “Unit I,” p. 11); therefore, these abnormally high sedimentation rates for an open-ocean sedimentary basin may be the result of the volcanic input. Figure F67 shows that the sedimentation rates were much slower during the late Miocene to mid-Pliocene; this suggests that the volcanic input was lower during these time intervals but increased rapidly after the late Pliocene. A low sedimentation rate during the Miocene is also suggested by the abundance of ichthyolith assemblages.

No biostratigraphic or well-constrained paleomagnetic data are available for Unit II; nevertheless, it is noteworthy that the abundance of ichthyolith assemblages constantly increases downhole, possibly mirroring a further decrease of the sedimentation rate in this unit (Cores 185-1149A-13H to 185-1149B-3R; 108.7–170.3 mbsf).

No biostratigraphic data or paleomagnetic constraints are available at this time for Unit III, thus hindering reconstruction of the sedimentation rates. Shore-based radiolarian biostratigraphic studies will provide age constraints for this unit and will allow sedimentation rate reconstruction.

Sedimentation rates for Unit IV are based on calcareous nannofossil biostratigraphic data and show average values close to 20 m/m.y., similar to modern equatorial oceanic carbonate sedimentation rates (Murray

F67. Sedimentation rate curve for Site 1149, p. 131.



and Leinen, 1993). The preliminary data suggest that the sedimentation rate was steady during the Valanginian and Hauterivian.

PHYSICAL PROPERTIES

Measurements Made on Site 1149 Cores

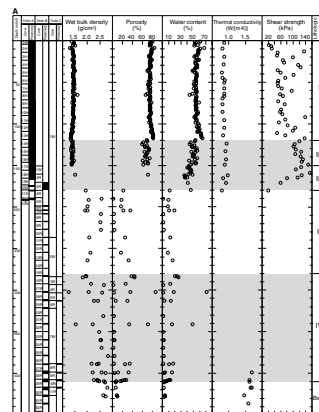
Physical properties measurements of whole-core sections from Site 1149 using the multisensor track (MST) included gamma-ray attenuation porosity evaluator (GRAPE), magnetic susceptibility meter (MSM), and natural gamma radiation (NGR). *P*-wave velocity logging (PWL) data were measured only in soft sediments in APC cores. We determined *P*-wave velocities from split cores in liners in the transverse *x* direction within both sediment and hard rock using contact probe systems PWS3, and in the transverse (*x* and *y*) and longitudinal (*z*) directions using PWS1, PWS2, and PWS3 on soft sediments. Velocity measurements were also obtained for cut cubes and minicores in the transverse (*x* and *y*) and longitudinal (*z*) directions using PWS3. Index properties on discrete samples, including wet bulk density, grain density, porosity, void ratio, and water content were calculated from measurements of wet mass, dry mass, and dry volume. We also measured thermal conductivity on whole-round or split cores and obtained shear-strength data on split cores of soft sediments.

Index Properties

We obtained index properties data using gravimetric methods on 189 samples from Site 1149. The results are presented in Table T16 and displayed in Figure F68. The average wet bulk density, porosity, and velocity of each lithologic unit and each lithology are listed in Table T17. From the seafloor to 100 mbsf in lithologic Unit I (ash- and diatom/radiolarian-bearing clay) (see “Unit I,” p. 11), the wet bulk density and grain density have almost constant values with averages of 1.42 and 2.62 g/cm³, respectively. The porosity and water content decrease slightly with depth, and the averages are 75.5% and 54.8%, respectively. The porosity and water content slightly decrease at 38, 65, and 92 mbsf without apparent lithologic changes. Between 100 and 118.2 mbsf in lithologic Unit I, the wet bulk density decreases with depth, and the porosity and water content increase. At 118.2 mbsf, there is an abrupt change in most of the index properties (Fig. F68). This boundary corresponds to the lithologic contact between ash- and diatom/radiolarian-bearing clay (Unit I) and dark brown pelagic clay (Subunit IIA) (see “Subunit IIA,” p. 13). Between 118.2 and 149.5 mbsf in Subunit IIA (dark brown pelagic clay with ash), the wet bulk density is slightly lower than that of Unit I, with an average of 1.38 g/cm³; however, the porosity and water content are significantly lower than those of Unit I, with averages of 67.1% and 49.9%, respectively. A second large contrast in index properties occurs at the lithologic Unit II/Unit III boundary where the average value of wet bulk density increases to 2.20 g/cm³ and porosity and water content decrease to 14.57% and 7.46%, respectively. Some of these large contrasts in average values are due to the preferential recovery and measurement of chert and porcelanite rather than the zeolite-bearing clay component of Unit III. The change in average index property values is much less dramatic across the Unit III/Unit IV boundary. Averages of wet bulk density and grain density increase slightly to

T16. Physical properties of discrete samples, p. 178.

F68. Index properties, thermal conductivity, and shear strength, p. 132.



T17. Average values of physical properties, p. 181.

2.28 and 2.63 g/cm³, respectively, whereas porosity and water content averages decrease to 21.7% and 11.9%, respectively.

Index properties that require volume measurements were not obtained for most samples from Subunit IIB because the pycnometer could not attain a stable helium pressure. We speculate that helium continued to be absorbed within what must be extremely small-scale porosity in the clay structure.

The relationship between the wet bulk density and porosity is displayed in Figure F69 and indicates the expected negative linear correlation. Chert and some marl samples have relatively high wet bulk density and low porosity. Intermediate values are measured for some cherts, porcelanite, marl, and chalk, whereas clay in Unit I, Subunits IIA and IIB, and nannochalk has the lowest density and highest porosity.

GRAPE Density Measurement

Wet bulk density was measured by the GRAPE every 4 cm for 4 s on unsplit sections of core from Site 1149. These data are shown in Figure F70. The continuous GRAPE density measurements can be compared to discrete samples of wet bulk density in Table T16. In Unit I, these densities show quite similar patterns and values, with an average of 1.42 g/cm³. GRAPE bulk density values are generally lower than those of gravimetric measurements in hard rock (Units III, IV, and basement) because of the effects from the discontinuous core with fractures and open space between core and liner. The GRAPE and gravimetric wet bulk density averages are 1.40 and 2.19 g/cm³ in Unit III and 1.37 and 2.28 g/cm³ in Unit IV, respectively. However, the GRAPE bulk densities are higher than the gravimetric values in Subunits IIA and IIB (pelagic clay). The GRAPE and gravimetric density averages are 1.46 and 1.38 g/cm³ in Subunit IIA and 1.56 and 1.40 g/cm³ in Subunit IIB, respectively. Shore-based investigation of microscale texture and composition within clay minerals in Unit I and Subunits IIA and IIB may reveal why GRAPE density values are higher in this unusual interval.

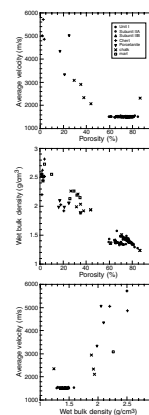
Magnetic Susceptibility

Magnetic susceptibility was measured every 4 cm for 4 s on unsplit sections of core from Site 1149. The data are shown in Figure F70. Magnetic susceptibility in Unit I and Subunits IIA and IIB displays semiperiodic variations punctuated with distinct peaks, which may correlate with discrete ash layers. Magnetic susceptibility is very low in chert/chalk/marl samples and abruptly jumps to maximum values in altered basalt encountered at ~410 mbsf.

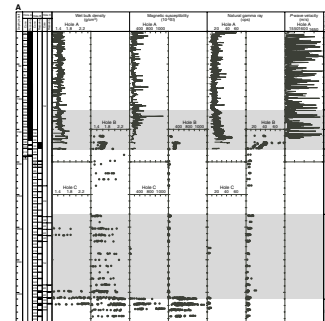
Natural Gamma Radiation

NGR was measured every 10 cm for 20 s on unsplit sections of core from Site 1149. The data are shown in Figure F70. High NGR counts occurred just below the seafloor (0–5 mbsf) in lithologic Unit I and from 160 to 180 mbsf in Subunit IIB (pelagic clay without ash). The NGR profile above 180 mbsf (above chert) exhibits fluctuations and general trends that are matched by those observed in the downhole spectral gamma-ray logging data (see “Natural Radioactivity,” p. 44). In Units III and IV the NGR counts are relatively low (<20 cps) compared to those of Unit I and Subunits IIA and IIB because of chert and carbonate dilution of clay. NGR counts appear to generally decrease

F69. Crossplots of physical properties, p. 134.



F70. MST measurement on whole cores, p. 135.



downsection in Unit IV. NGR remains below 20 cps in the igneous basement section with slightly higher values than in Unit VI.

Compressional Wave Velocity Measurements

Compressional wave velocity (*P*-wave velocity) was measured using two instruments, the *P*-wave logger (PWL) on the MST (y direction) and PWS1 (z direction), PWS2 (y direction), and the PWS3 (x direction) on split cores. The PWL was used only in soft sediments in APC cores. We also determined *P*-wave velocities from split cores in liners in the transverse x direction within both sediment and hard rock and on cube and minicore samples in x, y, and z directions of chert, chalk, and marl. The soft sediments in Hole 1149A, measured by PWS1, PWS2, and PWS3, are listed in Table T18 and displayed in Figure F71. The PWL data from Hole 1149A are compared with other MST data in Figure F70. The sediments and rocks recovered in Holes 1149B, 1149C, and 1149D were measured by PWS3 (x direction) in split core and discrete cube or minicore samples (Table T18; Fig. F71). In Unit I (0–118.2 mbsf) *P*-wave velocities range from 1480 to 1589 m/s and average 1520 m/s. In Subunits IIA and IIB (118.2–180 mbsf) usually only velocity in the x direction was measured by PWS3 because most split cores were too stiff to penetrate using the probes of PWS1 and PWS2. These values range from 1492 to 1544 m/s and the average of x-direction velocity in Subunits IIA and IIB is 1520 and 1515 m/s, respectively. These velocities are similar to those measured in situ by downhole logging tools (see “Seismic Velocity,” p. 45). In Units III and IV (180–398.4 mbsf), the velocities are much higher than those of Unit I and Subunits IIA and IIB. In Unit III (180–282.9 mbsf), insufficient quantities of the soft interbedded pelagic clay were recovered; therefore, velocities were measured only on radiolarian chert and porcelanite samples in split core liners. Velocities range from 2540 to 6382 m/s, and the average velocity of radiolarian chert is 5167 m/s; that of porcelanite is 3429 m/s. In Unit IV (282.9–398.4 mbsf) recovered lithologies are classified as chert, chalk, and marl (see “Unit IV,” p. 15). The *P*-wave velocity of radiolarian cherts ranges from 4439 to 5493 m/s, and the average is 4958 m/s. The average values of siliceous nannofossil chalk and marl are 2280 and 2676 m/s, respectively. Igneous basement samples range in velocity from 3408 m/s in a hyaloclastite sample to 5647 m/s in aphyric basalt. The average velocity from all samples (aphyric basalt, hyaloclastites, breccia) in the igneous section is 4821 m/s.

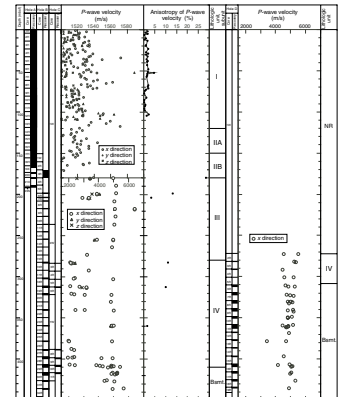
Relationships among the wet bulk density, porosity, and velocity are shown in Figure F69. The average velocity displays the expected positive linear correlation with wet bulk density and negative linear correlation with porosity. Samples of radiolarian chert have the highest velocity and density and lowest porosity. The velocities of pelagic clay from Unit I and Subunits IIA and IIB are nearly constant at ~1520 m/s, with no apparent relation to porosity and wet bulk density. The average *P*-wave velocity of each lithology calculated from x-direction data from Site 1149 is listed in Table T17.

Thermal Conductivity

Thermal conductivity measurements were taken once per core on either a whole round section or split section. The results are listed in Table T19 and plotted with depth in Figure F68. The values in Unit I and Subunits IIA and IIB are almost constant, and the average is 0.85

T18. Compressional wave velocities, p. 182.

F71. Compressional wave velocity on split cores and discrete cube samples, p. 137.



T19. Thermal conductivity values, p. 186.

W/(m·K). Measurements were not obtained in Units III and IV because of the poor recovery.

Shear Strength

Measurements of shear strength, using a mechanical vane, were made on split cores from Holes 1149A and 1149B. The results are listed in Table T20 and plotted with depth in Figure F68. Between the seafloor and 150 mbsf, the values gradually increase with increasing burial depth and range from 20.4 to 147.2 kPa. Undrained shear strength of soft sediments is generally related to their consolidation state, which is partly controlled by overburden pressure, which is in turn influenced by burial depth. It seems unusual, therefore, that shear strength values rapidly decrease between 150 and 180 mbsf in Subunit IIB. This zone corresponds to the dark brown pelagic clay of Subunit IIB, which is associated with the highest NGR counts, the presence of palygorskite clay, and a minimum in chloride concentration in interstitial waters, as well as collapsing hole conditions (see “Authigenic Clay Formation: Unit II,” p. 32, and “Subunit IIB,” p. 13).

T20. Shear strength, p. 187.

Summary

Physical properties are clearly related to changes in the primary lithologies recovered at Site 1149. There is a general gradient of increasing velocity and density and decreasing porosity in the primary lithologies from pelagic clay to chalk to marl, porcelanite, and finally to basalt and chert. Even though recovery within Units III and IV was poor, representative samples were taken that will allow a correlation between core and continuous downhole log data.

Distinct physical and chemical properties mark the brown pelagic clay of Subunit IIB, including relatively low shear strength, the highest NGR counts, anomalous behavior in the pycnometer, the occurrence of palygorskite clay, and a minimum in chloride concentration in interstitial waters, as well as collapsing hole conditions.

DOWNHOLE MEASUREMENTS

Abstract

Downhole measurements in Hole 1149B were made during Leg 185 after completion of drilling with the RCB. Five logging runs were performed, consisting of one pass with the triple combo tool string, two passes with the geochemical tool string (GLT), and two passes with the Formation MicroScanner (FMS)/sonic tool string. The triple combo tool string provided the most physically complete logging run (342 m of section) from ~10 m above the volcanic basement contact (~410 mbsf; Core 185-1149B-29R) to within the clay-volcanic ash section (~63 mbsf; Core 185-1149A-8H). The subsequent logs were limited by additional fill in the bottom of the hole and/or by a 20-m-thick section of tight hole in the pelagic clays (Cores 185-1149A-16H to 18H) just above the uppermost cherts. It is likely that this tight section of hole resulted from overburden pressure that forced the incompetent clays into the open hole rather than from “swelling clays” caused by an uptake of water within the clay matrix. A more detailed account of the five logging runs in Hole 1149B is provided below.

Run 1

The triple combo tool string was deployed first and measured porosity, density, resistivity, and natural gamma-ray emissions to within ~10 m above the volcanic basement contact and 45 m above the total hole depth. The tool string included the hostile environment natural gamma sonde (HNGS), hostile environment lithodensity sonde (HLDS), accelerator porosity sonde, phasor dual induction tool (DIT-E), and temperature acceleration pressure sensor. Tool deployment was hampered by a 20-m-thick tight spot in the dark brown clay section just above the uppermost cherts (see “Unit II,” p. 12); however, repeated working of the tool string eventually allowed penetration through this tight zone to a point 10 m above volcanic basement, where soft fill prevented further lowering of the tool string. The upward logging run through the tight spot in the clay section was uneventful.

Run 2

The GLT, deployed next, measured some of the major element constituents of the sedimentary section. The GLT included the natural-gamma spectrometry tool (NGT), the compensated neutron log, the aluminum activation clay tool (AACT) and the induced gamma-ray spectrometry tool (GST). The tool string was deployed, and we attempted to reach the same level in the hole as the triple combo; however, the lighter weight of the GST and possible additional tightening of the hole in the clay section just above the uppermost cherts did not allow it to pass below that level. Therefore, the first GLT run was conducted from the top of the constricted clay section (~145 mbsf; Core 185-1149A-16H) to the bottom of pipe within the clay-volcanic ash section (~63 mbsf; Core 185-1149A-8H). This short logging run of ~79 m was uneventful.

Run 3

Before the second GLT run, the drill string was lowered through the tight spot in the pelagic clays and positioned ~10 m below the top of the uppermost cherts with the elevator in the down position so that a full stand of pipe could be raised during the logging run. The GLT tool string was then run into the open hole and through the chert section without incident, bottoming ~25 m above the top of volcanic basement in the lithologic Unit IV (~385 mbsf; Core 185-1149B-26R). Logging proceeded without incident up ~227 m to the lowermost pelagic clays (~160 mbsf; Core 185-1149A-18H) after the drill string was raised ~30 m to accommodate the uppermost portion of the logging run. A repeat run was conducted in the lowermost 70 m of the logged interval because a few erratic spots were detected in the primary GLT logging run.

Run 4

The FMS/sonic tool string was used to measure microresistivity, seismic velocity, inclination of the hole from vertical, magnetic field intensities, and natural gamma-ray emissions. The tool string included the NGT, dipole shear sonic imager (DSI), FMS, and general purpose inclinometer tool. Problems with the DSI prevented the measurement of seismic velocities during this lowering; however, the other tools pro-

vided continuous data. The strategy for logging the FMS/sonic runs was the same as in the second geochemical logging run—namely, to position the bottom of the drill string just below the top of the uppermost cherts, send the tool string to the bottom of the hole, and log up while raising the drill string 30 m to log the contact between the uppermost cherts and overlying pelagic clays. In this first FMS/sonic run, the bottom of the hole was reached only a few meters higher than in the geochemical run, still equivalent to Core 185-1149B-26R (~385 mbsf). Logging proceeded without incident up ~223 m to the lowermost pelagic clays (~160 mbsf; Core 185-1149A-18H).

Run 5

For the second FMS/sonic run, the tool string was brought on deck and the long spacing sonic sonde (LSS) was inserted in place of the DSI tool to obtain seismic velocity measurements. The modified tool string then was lowered to the bottom of the hole. This was still within the carbonate marl section (~369 mbsf; Core 185-1149B-24R) but at a level 16 m shallower than on the previous attempt because of additional fill in the hole. Logging proceeded ~207 m without incident to the lowermost pelagic clays (~160 mbsf; Core 185-1149A-18H). Because the LSS record was very noisy in several sections within the chert interval, it was decided to make a repeat sonic run with the FMS tool arms closed on the possibility that this might eliminate some “road noise” in the sonic measurements. Thus, the tool string was again lowered to the bottom of the hole, 4 m higher than before, but still within Core 185-1149B-24R. Logging proceeded ~219 m without incident to the lowermost pelagic clays (~160 mbsf; Core 185-1149A-18H). The LSS record, however, was still quite noisy.

Preliminary Observations

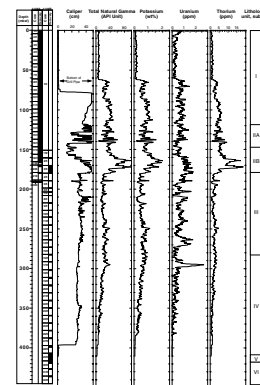
The postprocessing of the data produced nearly continuous and good-quality records of downhole logging measurements. Degraded borehole conditions, ranging from washed out to constricted, in the uppermost portion of the logged interval resulted in logs of decreased quality. Fortunately, core recovery within this region was >95%. In deeper portions of the borehole, where core recovery was poor (<10%), borehole conditions were very good and yielded very high quality logs. The data from the various measurement tools are in good agreement, and the general character of the logging data matches the observations made from the recovered cores.

Borehole Characteristics

The size, shape, and borehole deviation with respect to north can be described from data recorded by the calipers within the inclinometer section of the FMS/sonic tool string and within the slim-hole lithodensity logging tool (HLDT) section of the triple combo tool string. These data are important for the calculation of correction factors required for postprocessing of certain data types (e.g., HNGS, seismic velocity, and magnetic field data). In addition, the uniformity and smoothness of a borehole can often be an indicator of the quality of data collected as well as the integrity and rock type comprising the borehole walls.

The borehole walls generally become smoother and more uniform with depth (Fig. F72) and suggest that the quality of the logging data

F72. Radioactive element logging measurements, p. 138.



improves with depth within the interval logged. The upper portion of the borehole (80–180 mbsf) is very rugose with borehole dimensions ranging from 6 in (less than the drilled diameter) to 18 in (maximum limit of the calipers). The main source of the varied borehole character is a layer of dark brown pelagic clay and volcanic ash (lithologic Unit II) (see “Unit II,” p. 12) that appears to be “flowing” back into the borehole. The middle portion of the borehole (180–270 mbsf) is moderately rugose and is associated with the carbonate-free interbedded chert and clay layers comprising lithologic Unit III. The lowermost portion of the logged interval (270–395 mbsf) is significantly smoother and more uniform. This section of the borehole appears to be associated with the lowermost chert layer from lithologic Unit III and the chalk, chert, and marl layers in lithologic Unit IV.

Natural Radioactivity

On each logging run, natural radioactivity was measured continuously downhole with either the HNGS or NGT. Both tools utilize scintillation detectors to determine the gamma radiation emitted by the radioactive decay of materials within the formation. Spectral processing of the measured gamma radiation identifies characteristic radiation peaks that are used to determine the concentrations of potassium (in weight percent), thorium (in parts per million), and uranium (in parts per million). These values are combined to provide a measure of the total gamma-ray counts and uranium-free or computed gamma-ray counts. Shipboard corrections to the HNGS are made to account for variability in borehole size and borehole-fluid potassium concentrations.

Except for a broad peak in the central portion of the logged interval (155–170 mbsf), the overall character of the total gamma-ray record exhibits a general, but not monotonic, decrease in radioactivity with depth (Fig. F72). The interbedded clay and ash layers of lithologic Unit I and Subunit IIA in the shallow part of the hole (63–155 mbsf) exhibit intermediate, but variable, gamma-ray values. The ash-free pelagic clays in the deeper portion of lithologic Subunit IIB (160–180 mbsf) have relatively high gamma-ray values with distinctive peaks at 163 and 172 mbsf. These peaks are especially noticeable in the thorium log. The remainder of the deep portion of the borehole exhibits relatively low gamma-ray values that steadily decrease to the deepest part of the logged interval.

The potassium and thorium concentrations closely mimic the total gamma-ray pattern, but the uranium log is significantly different (Fig. F72). The uranium concentration appears to maintain intermediate concentrations from the top of the logged interval to the bottom of the carbonate-free cherts and clays of lithologic Unit III. A broad swell in uranium concentration occurs in concert with the other increases in radioactive elements in lithologic Subunit IIB; however, the elevated values appear to be maintained into the upper Si-rich portion of lithologic Unit III. A distinctive peak in uranium also is observed at the top of the carbonate-rich chert and marl layers in lithologic Unit IV (290–300 mbsf). The source of this peak is uncertain, but may be related to organic-rich sediments similar to those sampled slightly deeper in the section (Core 185-1149B-19R).

Resistivity

The downhole electrical resistivity was measured with the DIT-E tool and provides a rough, inverse estimate of the porosity of the formation. The DIT-E provides three measurements of the formation electrical resistivity, labeled “deep,” “medium,” and “shallow” on the basis of respective depth of penetration of the current into the formation. All of these values are virtually identical throughout the depth of the measured borehole except when the DIT-E entered the drill pipe (Fig. F73).

The resistivity data nicely delineate the main lithology types observed in the sediment column at Site 1149 (Fig. F73). The predominantly pelagic clay and interbedded ash layers in the upper part of the logged interval (63–180 mbsf) are characterized by very uniform resistivity values (<1 Ωm). Slightly elevated and variable resistivity values (1–10 Ωm) are observed within the carbonate-free interbedded chert and clay layers (180–300 mbsf) throughout lithologic Unit III. The largest resistivity values in this interval are observed at the top and bottom of this section and are associated with two Si-rich zones identified in the geochemical logs described below. The chalk, chert, and marl unit (300–395 mbsf) exhibits resistivity values that are relatively uniform but vary with depth over a wavelength of ~40 m.

Density

The HLDT uses the detection of scattered gamma rays from a radioactive cesium source to determine the bulk density of rock units. These measurements are very sensitive to the integrity and smoothness of the borehole walls; so the bulk density values along the more rugose sections of the borehole may be of lower quality than the data obtained along the more uniform sections.

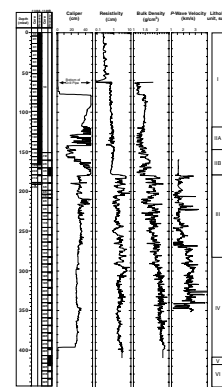
The density data also nicely delineate the main lithology types observed in the sediment column at Site 1149 (Fig. F73). Extremely low density values (~1.5 g/cm^3) characterize the predominantly pelagic clay and interbedded ash layers in the upper part of the logged interval (63–180 mbsf), suggesting a relatively high porosity for these units. A sudden increase in density occurs at the interface between lithologic Units II and III (~180 mbsf), and the density continues to increase with depth throughout the unit. The short wavelength variability of the density in this section may be indicative of interbedded chert and clay layers. It is surprising that the transition from lithologic Unit III to Unit IV is gradual in the density log, in contrast to the sonic log where a sharp increase occurs at 270 mbsf. The density continues to increase with depth within the chalk, chert, and marl unit, but the rate of increase is noticeably reduced. The amplitude of the short wavelength variability is also reduced in this section.

Seismic Velocity

The LSS uses two acoustic transmitters and two receivers to record the full waveform of sound waves that travel along the borehole wall. Compressional wave velocity (V_p) is determined through the depth-derived compensation principle where acoustic traveltimes recorded at one depth are combined with a second set of readings at another given depth.

Compressional wave velocities delineate three distinct sections within the logged interval. These sections, however, do not correspond

F73. Geophysical logging measurements, p. 139.



exactly with the identified lithologic units (Fig. F73). The shallowest interval (160–180 mbsf) is characterized by extremely uniform, low seismic velocities and corresponds to the predominantly pelagic clay unit of lithologic Subunit IIB. An increase in magnitude and variability of the compressional wave velocities is associated with the interbedded chert and clay in Unit III, although a significant increase in velocities is observed at the base of this unit (~270 mbsf). This sudden increase in velocity is associated with absolute maximum values of silicon (Fig. F74) and may be related to changes in the physical properties of the chert layers as they evolve from amorphous opal to quartz. These elevated compressional wave velocities are maintained within the chalk, chert, and marl layers of lithologic Unit IV.

Geochemical Log

Shipboard processing of the logging data obtained with the AACT and the GST provides initial measurements or yields of the relative abundances of Al, Ca, Si, Fe, Cl, H, and S within the logged formation. Postcruise processing also provides measurements of Ti, Gd, and K. Additional shore-based processing is necessary to compute the absolute dry-weight fractions of the major oxides. Although the GST can be used inside the drill pipe and the effect of the pipe can be estimated, only the data obtained outside of the drill pipe for the various logging runs are included for preliminary analysis (Fig. F74). Overall, the relative changes in the yields of the various elements correspond well with the lithologies obtained from the cored intervals.

Elevated Si yields are observed in depth intervals in which chert was recovered (>180 mbsf), and relatively low Si levels are present in the predominantly pelagic clay intervals (60–180 mbsf) (Fig. F74). It is notable that the average Si yield through the chert interval is not uniform. The highest Si yields are observed at the top (180–205 mbsf) and bottom (270–305 mbsf) of lithologic Unit III, and these depth intervals correspond to regions of high resistivity values. The lower Si-rich interval also corresponds to the region in which elevated compressional wave velocities are observed.

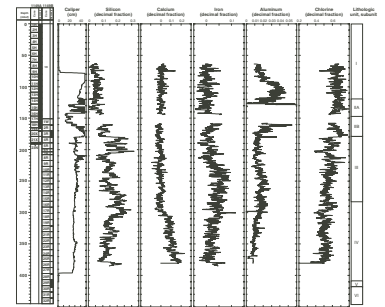
The relative yield of Ca is fairly uniform and low for the majority of the logged interval, but the relative concentration begins to increase markedly at the top of the chalk, chert, and marl interval (Fig. F74). The Ca yield increases rapidly downward at first within a transition zone (295–305 mbsf) and then continues to increase more slowly with depth for the remainder of the interval logged (305–370 mbsf).

The Fe yield is puzzling and does not appear to correlate to any of the identified lithologic boundaries. In the upper half of the logged interval (60–210 mbsf), the Fe yield is fairly featureless except for the possible increase within the dark brown pelagic clay unit (Fig. F74). In the lower half (210–370 mbsf), the Fe yield reaches a maximum at ~240 mbsf and then slowly decreases with depth.

The Al yield exhibits significantly high values within the pelagic clay intervals and slightly elevated values in the deeper portion of the borehole (230–310 mbsf) (Fig. F74). The Al yields are especially high within the lower portion of lithologic Unit I (80–120 mbsf). The broad region of elevated Al abundance appears to correspond to the lower half of lithologic Unit III and the upper portion of lithologic Unit IV.

The Cl yield is relatively high in the pelagic clay and ash layers and exhibits a general decrease with depth (Fig. F74). A noticeable increase in Cl yield is associated with the lowermost portion of the dark brown

F74. Geochemical logging measurements, p. 140.



pelagic clay unit (160–180 mbsf). Slightly lower abundances of Cl are observed at 180–210 and 290–310 mbsf and appear to exhibit an inverse relationship with the Si yields. This relationship is much more apparent for the shallower of the two intervals. Since the measured Cl is primarily associated with the formation pore waters, these changes in Cl yield may be used as proxy for the porosity of the formation.

Formation MicroScanner

The two passes of the FMS in Hole 1149B provided almost complete coverage of lithologic Units III and IV; recovery was very poor in these units dominated by interbedded pelagic clay, chert, chalk, and marl. Figure F75 shows the entire image recorded during the first pass.

The dynamic normalization performed underlines the very fine alternation of conductive (dark) and resistive (light) layers, with the more resistive features likely being chert layers. The results of the dipmeter analysis of these images is shown (Fig. F75), with “tadpoles” indicating the dip and strike of individual features and “fan plots” indicating the dip azimuth distribution averaged over 20-m intervals. Figure F76 shows smaller intervals where individual dipping features are identified by sinusoids and the associated tadpoles. The different images indicate a change in the general dipping orientation from north-northeast above ~280 mbsf (Fig. F76A, F76B) to south below this depth (Fig. F76C, F76D). The transition between the two structural regimes seems to coincide with the lithologic change between lithologic Units III and IV. The origin of this structural change is not clear, but postcruise biostratigraphic studies might provide evidence for a hiatus. The sedimentation rates calculated from paleomagnetic data in the upper section of the hole and from calcareous nannofossils in the deeper chert layers suggest that there could have been a hiatus during the Late Cretaceous and the Miocene. If such a hiatus can be tied with the base of Unit III, it could be associated with some tectonic event that might explain the change in the dipping orientations between the two units.

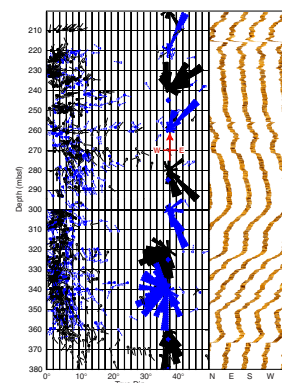
MICROBIOLOGY

Sediments

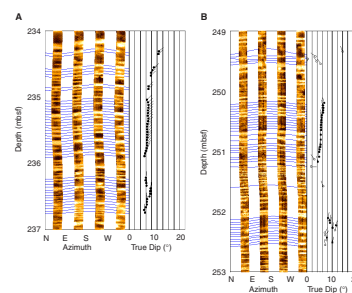
Introduction

Sediment samples from Holes 1149A, 1149B, and 1149C at Site 1149 were collected to characterize the microbial community inhabiting this environment. Whole rounds, cut on the catwalk, were used for both microbiological analyses and contamination tests. Surface seawater was collected to enumerate and characterize background levels of microbes possibly introduced during drilling. Interstitial water from the whole rounds was collected after the microbiological samples and analyzed for major elements, iron, manganese, and nutrients (see “[Interstitial Water Chemistry and Headspace Gas](#),” p. 26). These analyses will allow interpretation of the microbiological data in a geochemical context.

F75. Dipmeter analysis and FMS images, p. 142.



F76. FMS images and dip analysis, p. 143.



Microbiological Analyses

A list of samples taken at Site 1149 for microbiological analyses is shown in Table T21. The analyses include (1) adenosine triphosphate (ATP) analysis to estimate total biomass, (2) most probable number (MPN) cultivation at 1 atm, (3) enumeration of cells by epifluorescence microscopy, (4) DNA extraction and community characterization, and (5) maintenance at in situ pressure. Shipboard work included ATP analysis, initiation of MPN cultures in anaerobic media, and preservation of samples for shore-based analyses (see “Microbiology,” p. 31, in the “Explanatory Notes” chapter for procedures).

Tracer tests were carried out as a part of Leg 185 microbiology studies to investigate if the drilling and sample-handling processes contaminate cores. At Site 1149, tests were carried out using perfluorocarbon (PFT) and fluorescent microspheres in four cores (Tables T22, T23). Methods used for these tests can be found in “Methods for Quantifying Potential Microbial Contamination during Deep Ocean Coring” (Smith et al., 2000). The PFT was present on the exterior of the sediment samples in all cases. The interior of the unconsolidated sediments sampled with the APC remained uncontaminated in most cases (Table T22), whereas consolidated sediments sampled with the RCB contained traces of the PFT (Fig. F77; see also Fig. F75, p. 149, in the “Site 801” chapter). Fluorescent microspheres were not observed in the interior of any sediment sample, and they were not abundant on the outside of the cores (Table T23; see also Table T16, p. 213, in the “Site 801” chapter).

Igneous Rock

One igneous sample was collected for microbial analyses from Site 1149. The sample was a carbonate and clay vein, Sample 185-1149B-32R-1 (Piece 9, 83–86 cm). Interior parts of the vein were isolated in the anaerobic chamber with sterile techniques. The sample was used to inoculate anaerobic cultures, preserved for enumeration of total cells, for DNA extraction and community analysis, scanning electron microscopy, and in situ hybridization.

Core 185-1149B-32R was cored with microspheres added to the drilling fluid (see “Methods for Quantifying Potential Microbial Contamination during Deep Ocean Coring” [Smith et al., 2000]). Sample 185-1149B-32R-1 (Piece 2, 22–42 cm) was washed, and microspheres were observed in the wash water, indicating that spheres were delivered to the core. The crushed rock for the microbiology sample was filtered onto a polycarbonate filter and observed with epifluorescence microscopy. No microspheres were observed. This indicates that the microbiology sample was isolated without contamination from the outside of the core.

Two additional samples were maintained at in situ pressure for shore-based culturing. Sample 185-1149B-29R-1, 148–149 cm, is a mixture of basalt and chalk from the sediment/basement interface. Sample 185-1149C-10R-2, 0–4 cm, consists of a carbonate vein with alteration halos plus the host basalt.

Water Samples

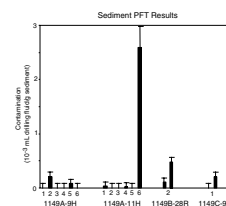
A sample of the water in the drill string was collected when the pipe was opened to retrieve Core 185-1149C-10R. This sample contained 4.4

T21. List of microbiological samples, p. 188.

T22. Results of PFT tests, p. 189.

T23. Results of fluorescent microsphere tests on sediment samples, p. 190.

F77. Sediment PFT results, p. 145.



$\times 10^5$ ($\pm 1.3 \times 10^5$) cells/mL. A surface-water sample was collected from the bow of the ship at the location of Hole 1149D. This sample contained 5.8×10^5 ($\pm 1.0 \times 10^5$) cells/mL. These numbers are typical for surface waters and not significantly different from each other.

A sample of sepiolite mud that is added to the drilling fluid to flush the borehole was also collected for microbial analyses. Total cells could not be enumerated because of the high background fluorescence of the sample. All three of the above samples were inoculated into anaerobic growth media and incubated at 25°C. Samples were filtered and/or frozen for DNA extraction and community analyses. These samples will aid in evaluation of microbes that may have been introduced as contaminants. Evaluation of cultures and DNA extraction will be shore-based analyses.

Summary

The majority of the microbiological data will not be available until after significant sample analysis has been completed at shore-based facilities. The results of the contamination experiments are very encouraging and suggest that these samples will be extremely useful in characterizing the microbial community in deep sediments. The particulate tracers were not found in the interior of any of the samples taken for microbiological analysis. The chemical tracer was either absent or at extremely low levels (nanoliters of seawater per gram of sediment) (Fig. F77; see also Fig. F75, p. 149, in the "Site 801" chapter). Coordinated effort in analyzing the microbiological data along with the chemistry data should result in a more coherent view of microbiological processes in deep Pacific sediments.

REFERENCES

- Abrams, L.J., Larson, R.L., Shipley, T.H., and Lancelot, Y., 1993. Cretaceous volcanic sequences and Jurassic oceanic crust in the East Mariana and Pigafetta basins of the Western Pacific. *In* Pringle, M.S., Sager, W.W., Sliter, W.V., and Stein, S. (Eds.), *The Mesozoic Pacific: Geology, Tectonics, and Volcanism*. Geophys. Monogr., Am. Geophys. Union, 77:77–101.
- Barron, J.A., 1985. Miocene to Holocene planktic diatoms. *In* Bolli, H.M., Saunders, J.B., and Perch-Nielsen, K. (Eds.), *Plankton Stratigraphy*: Cambridge (Cambridge Univ. Press), 763–809.
- Baudin, F., Bulot, L.G., Cecca, F., Coccioni, R., Gardin, S., and Renard, M., 1999. Un équivalent du “Niveau Faraoni” dans le bassin du sud-est de la France, indice possible d’un événement anoxique fini-hauterivien étendu à la Tethys méditerranéenne. *Bull. Soc. Geol. Fr.*, 170:487–498.
- Berggren, W.A., Kent, D.V., Swisher, C.C., III, and Aubry, M.-P., 1995. A revised Cenozoic geochronology and chronostratigraphy. *In* Berggren, W.A., Kent, D.V., Aubry, M.-P., and Hardenbol, J. (Eds.), *Geochronology, Time Scales and Global Stratigraphic Correlation*. Spec. Publ.—Soc. Econ. Paleontol. Mineral. (Soc. Sediment. Geol.), 54:129–212.
- Bralower, T.J., 1987. Valanginian to Aptian calcareous nannofossil stratigraphy and correlation with the upper M-sequence magnetic anomalies. *Mar. Micropaleontol.*, 11:293–310.
- Cecca, F., Marini, A., Pallini, G., Baudin, F., and Begouen, V., 1994. A guide-level of the uppermost Hauterivian (Lower Cretaceous) in the pelagic succession of Umbria-Marche Apennines (Central Italy): the Faraoni Level. *Riv. Ital. Paleontol. Stratigr.*, 99:551–568.
- Channell, J.E.T., Erba, E., Nakanishi, M., and Tamaki, K., 1995. Late Jurassic–Early Cretaceous time scales and oceanic magnetic anomaly block models. *In* Berggren, W.A., et al. (Eds.), *Geochronology, Time Scales and Global Stratigraphic Correlation*. Spec. Publ.—Soc. Econ. Paleontol. Mineral., 54:51–63.
- Couture, R.A., 1977. Composition and origin of palygorskite-rich and montmorillonite-rich zeolite-containing sediments from the Pacific Ocean. *Chem. Geol.*, 19:113–130.
- Erba, E., Premoli Silva, I., and Watkins, D.K., 1995. Cretaceous calcareous plankton biostratigraphy of Sites 872 through 879. *In* Haggerty, J.A., Premoli Silva, I., Rack, F., and McNutt, M.K. (Eds.), *Proc. ODP, Sci. Results*, 144: College Station, TX (Ocean Drilling Program), 157–169.
- Ewing, J., Ewing, M., Aitken, T., and Ludwig, W.J., 1968. North Pacific sediment layers measured by seismic profiling. *In* Knopoff, L., Drake, C.L., and Hart, P.J. (Eds.), *The Crust and Upper Mantle of the Pacific Area*. Geophys. Monogr., Am. Geophys. Union., 12:147–173.
- Feely, R.A., Baker, E.T., and Marumo, K., 1996. Hydrothermal plum particles and dissolved phosphate over the superfast-spreading southern East Pacific Rise. *Geochim. Cosmochim. Acta*, 60:2297–2323.
- Gieskes, J.M., 1983. The chemistry of interstitial waters of deep-sea sediments: interpretation of deep-sea drilling data. *In* Riley, J.P., and Chester, R. (Eds.), *Chemical Oceanography* (Vol. 8): London (Academic), 221–269.
- Heezen, B.C., MacGregor, I.D., et al., 1973. *Init. Repts. DSDP*, 20: Washington (U.S. Govt. Printing Office).
- Hein, J.R., Scholl, D.W., Barron, J.A., Jones, M.G., and Miller, J., 1978. Diagenesis of late Cenozoic diatomaceous deposits and formation of the bottom simulating reflector in the southern Bering Sea. *Sedimentology*, 25:155–181.
- Houtz, R.E., Ewing, J., and Buhl, P., 1970. Seismic data from sonobuoy stations in the northern and equatorial Pacific. *J. Geophys. Res.*, 75:5093–5111.

- Houtz, R.E., and Ludwig, W.J., 1979. Distribution of reverberant subbottom layers in the southwest Pacific Basin. *J. Geophys. Res.*, 84:3497–3504.
- Karig, D.E., 1975. Basin genesis in the Philippine Sea. In Karig, D.E., Ingle, J.C., Jr., et al., *Init. Repts. DSDP*, 31: Washington (U.S. Govt. Printing Office), 857–879.
- Kastner, M., 1979. Silica polymorphs. In Burns, R.G. (Ed.), *Marine Minerals*. Mineral. Soc. Am., *Rev. Mineral.*, 6:99–111.
- , 1981. Authigenic silicates in deep sea sediments: formation and diagenesis. In Emiliani, C. (Ed.), *The Sea* (Vol. 7): *The Oceanic Lithosphere*: New York (Wiley), 915–980.
- Lancelot, Y., and Larson, R.L., 1975. Sedimentary and tectonic evolution of the northwestern Pacific. In Larson, R.L., Moberly, R., et al., *Init. Repts. DSDP*, 32: Washington (U.S. Govt. Printing Office), 925–939.
- Langmuir, C.H., Bender, J.F., and Batiza, R., 1986. Petrological and tectonic segmentation of the East Pacific Rise, 5°30'N–14°30'N. *Nature*, 322:422–429.
- Larson, R.L., and Chase, C.G., 1972. Late Mesozoic evolution of the western Pacific Ocean. *Geol. Soc. Am. Bull.*, 83:3637–3644.
- Larson, R.L., Lancelot, Y., et al., 1992. *Proc. ODP, Sci. Results*, 129: College Station, TX (Ocean Drilling Program).
- Larson, R.L., Moberly, R., et al., 1975. *Init. Repts. DSDP*, 32: Washington (U.S. Govt. Printing Office).
- Larson, R.L., and Sager, W.W., 1992. Skewness of magnetic anomalies M0 to M29 in the northwestern Pacific. In Larson, R.L., Lancelot, Y., et al., *Proc. ODP, Sci. Results*, 129: College Station, TX (Ocean Drilling Program), 471–481.
- Millero, F.J., and Sohn, M.L., 1992. *Chemical Oceanography*: Boca Raton (CRC Press).
- Murray, R.W., and Leinen, M., 1993. Chemical transport to the seafloor of the equatorial Pacific Ocean across a latitudinal transect at 135°W: tracking sedimentary major, trace, and rare earth element fluxes at the Equator and the Intertropical Convergence Zone. *Geochim. Cosmochim. Acta.*, 57:4141–4163.
- Nakanishi, M., Tamaki, K., and Kobayashi, K., 1989. Mesozoic magnetic anomaly lineations and seafloor spreading history of the Northwestern Pacific. *J. Geophys. Res.*, 94:15437–15462.
- Nakanishi, M., Tamaki, K., and Kobayashi, K., 1992. Magnetic anomaly lineations from Late Jurassic to Early Cretaceous in the west-central Pacific Ocean. *Geophys. J. Int.*, 109:701–719.
- PLATES Project, 1998. Atlas of paleogeographic reconstructions (PLATES Progress Report No. 215), *Univ. Texas Inst. Geophys. Tech. Rep.*, 181.
- Pletsch, T., 1998. Origin of lower Eocene palygorskite clays in the Côte d'Ivoire-Ghana Transform Margin, eastern equatorial Atlantic. In Mascle, J., Lohmann, G.P., and Moullade, M. (Eds.), *Proc. ODP, Sci. Results*, 159: College Station, TX (Ocean Drilling Program), 141–156.
- Sager, W.W., and Pringle, M.S., 1988. Mid-Cretaceous to Early Tertiary apparent polar wander path of the Pacific Plate. *J. Geophys. Res.*, 93:11753–11771.
- Shipley, T.H., Abrams, L.J., Larson, R.L., and Lancelot, Y., 1993. Extent of Cretaceous volcanic sequences in the Jurassic Nauru Basin, western Pacific. In Pringle, M.S., Sager, W.W., Sliter, W.V. and Stein, S. (Eds.), *The Mesozoic Pacific: Geology, Tectonics and Volcanism*. Geophys. Monogr., Am. Geophys. Union, 77:77–102.
- Smith, D.C., Spivack, A.J., Fisk, M.R., Haveman, S.A., Staudigel, H., and the Leg 185 Shipboard Scientific Party, 2000. Methods for quantifying potential microbial contamination during deep ocean coring. *ODP Tech. Note*, 28 [Online]. Available from World Wide Web: <<http://www-odp.tamu.edu/publications/tnotes/tn28/INDEX.HTM>>. [Cited 2000-05-23]
- , in press. Drilling-induced microbial contamination at deep-sea crust. *Geomicrobiol. J.*
- Smith, W.H.F., and Sandwell, D.T., 1997. Global seafloor topography from satellite altimetry and ship depth soundings. *Science*, 277:1956–1962.

- Steiner, M.B., and Wallick, B.P., 1992. Jurassic to Paleocene paleolatitudes of the Pacific Plate derived from the paleomagnetism of the sedimentary sequences at Sites 800, 801, and 802. *In* Larson, R.L., Lancelot, Y., et al., *Proc. ODP, Sci. Results*, 129: College Station, TX (Ocean Drilling Program), 431–446.
- Taylor, R.N., and Nesbitt, R.W., 1998. Isotopic characteristics of subduction fluids in an intra-oceanic setting, Izu-Bonin Arc. *Earth Planet. Sci. Lett.*, 164:79–98.
- Taylor, S.R., and McLennan, S.M., 1985. *The Continental Crust: Its Composition and Evolution*: Oxford (Blackwell Scientific).
- Thierstein, H.R., 1971. Tentative Lower Cretaceous calcareous nannoplankton zonation. *Eclogae Geol. Helv.*, 64:458–488.
- , H.R., 1973. Lower Cretaceous calcareous nannoplankton biostratigraphy. *Abh. Geol. Bundesanst.*, 29:1–52.
- Wessel, P., and Smith, W.H.F., 1995. New version of the Generic Mapping Tools released. *Eos*, 76:329.
- Winterer, E.L., 1976. Anomalies in the tectonic evolution of the Pacific. *In* Sutton, G.H., Manghnani, M.H., and Moberly, R. (Eds.), *The Geophysics of the Pacific Ocean Basin and its Margin*. Geophys. Monogr., Am. Geophys. Union, 19:269–278.
- Worsley, T.R., and Davies, T.A., 1979. Cenozoic sedimentation in the Pacific Ocean: steps toward a quantitative evaluation. *J. Sediment. Petrol.*, 49:1131–1146.

Figure F1. Bathymetric map of area around Site 1149 showing the Izu-Bonin Trench and Islands. Locations of DSDP Sites 195 and 197 and ODP Sites 782 and 879 are indicated. * = Izu-Bonin volcanic arc.

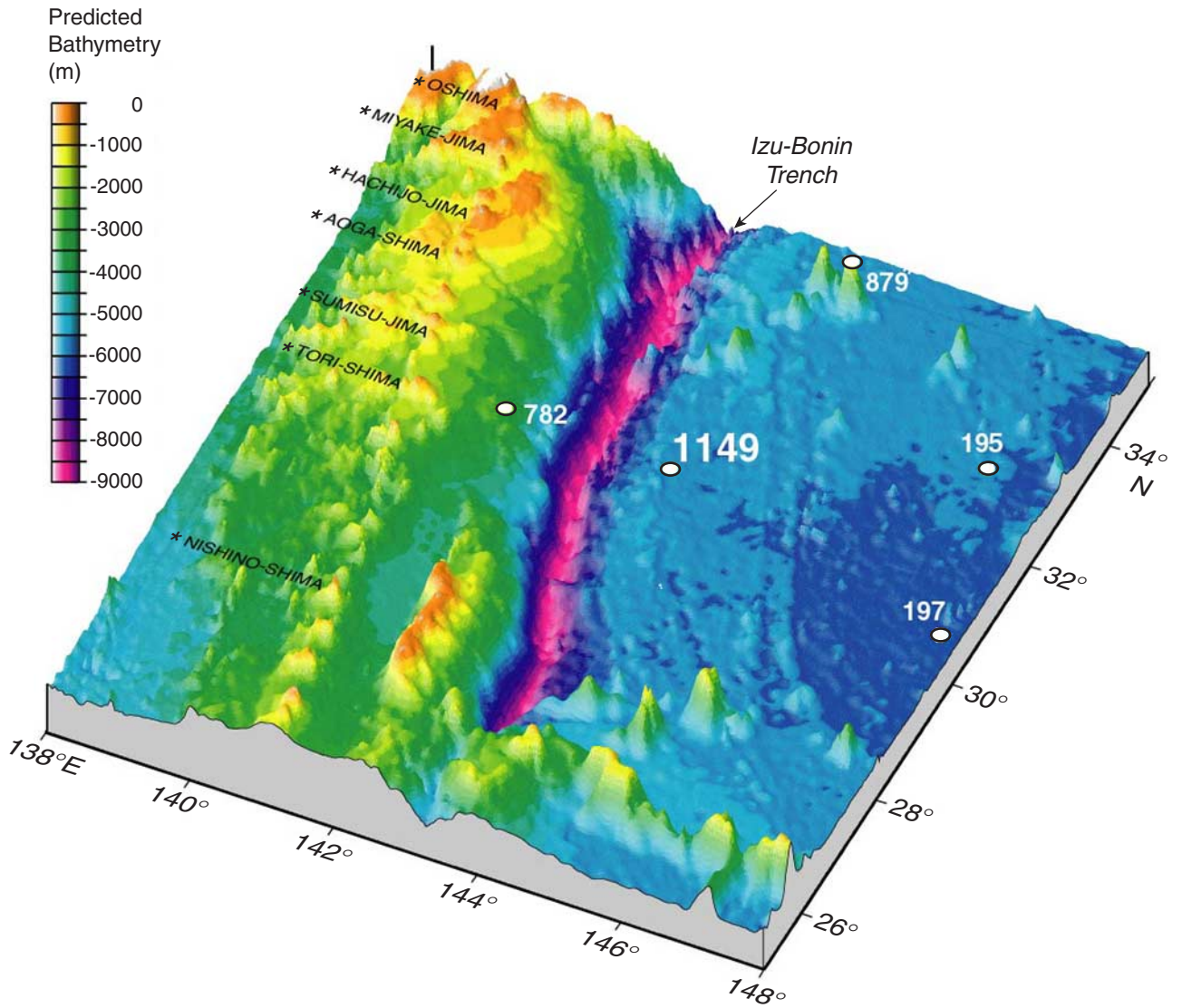


Figure F2. Sedimentary section at Site 1149 compared to DSDP Sites 194–197.

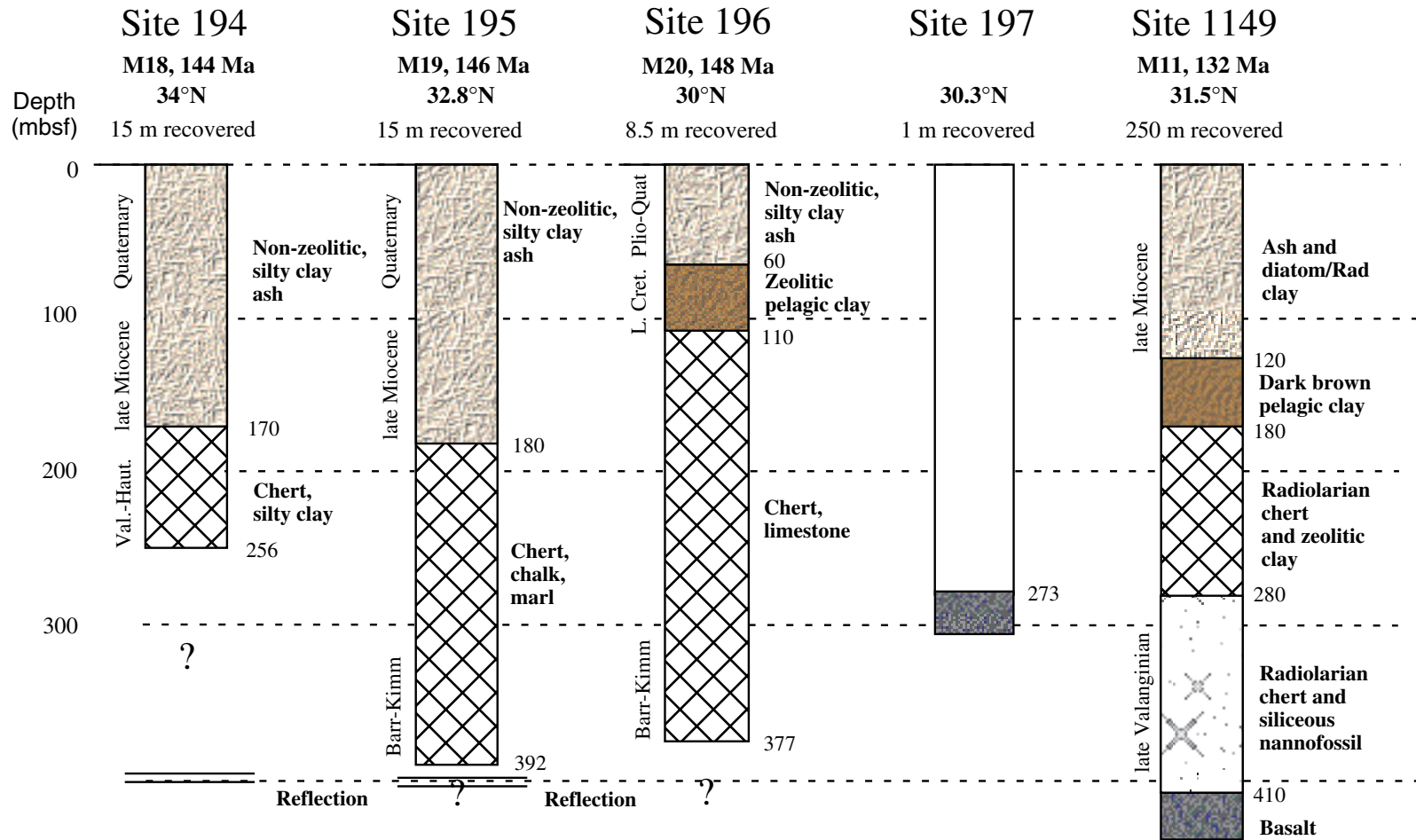


Figure F3. Summary of seismic stratigraphy in Holes 1149A, 1149B, and 1149C showing generalized correlations with lithologic units, ages, and seismic facies. UT = upper transparent; UO = upper opaque; and HB = Horizon B. The basement age of 132 Ma corresponds to Chron M11 from Channell et al., 1995. Holes 1149A, 1149B, and 1149C imaged with SCS water guns (two 80 in³) obtained on approach to Site 1149 during Leg 185. Track-line orientation and locations are shown in Figure F7, p. 59. Seismic data were processed and displayed with the following parameters: mute; band-pass filter 30–100 Hz; three-trace mix; skip every other trace; 500-ms automatic gain control; and vertical exaggeration of ~25× at the seafloor.

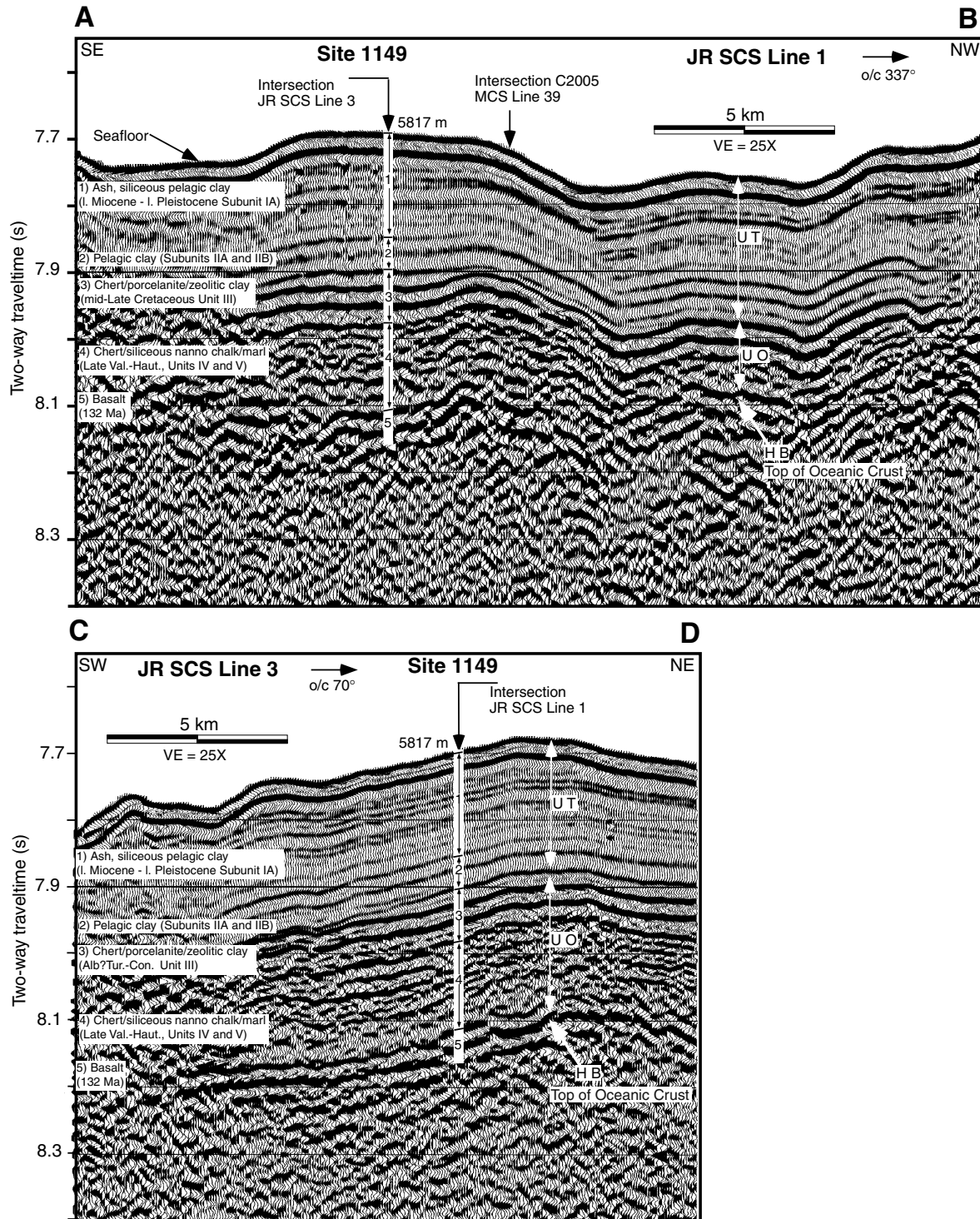


Figure F4. MCS Line 39 recorded in 1976 during *Robert D. Conrad* Cruise 2005 illustrating the proximity of Site 1149 to the Izu-Bonin Trench axis. cpa = closest point of approach.

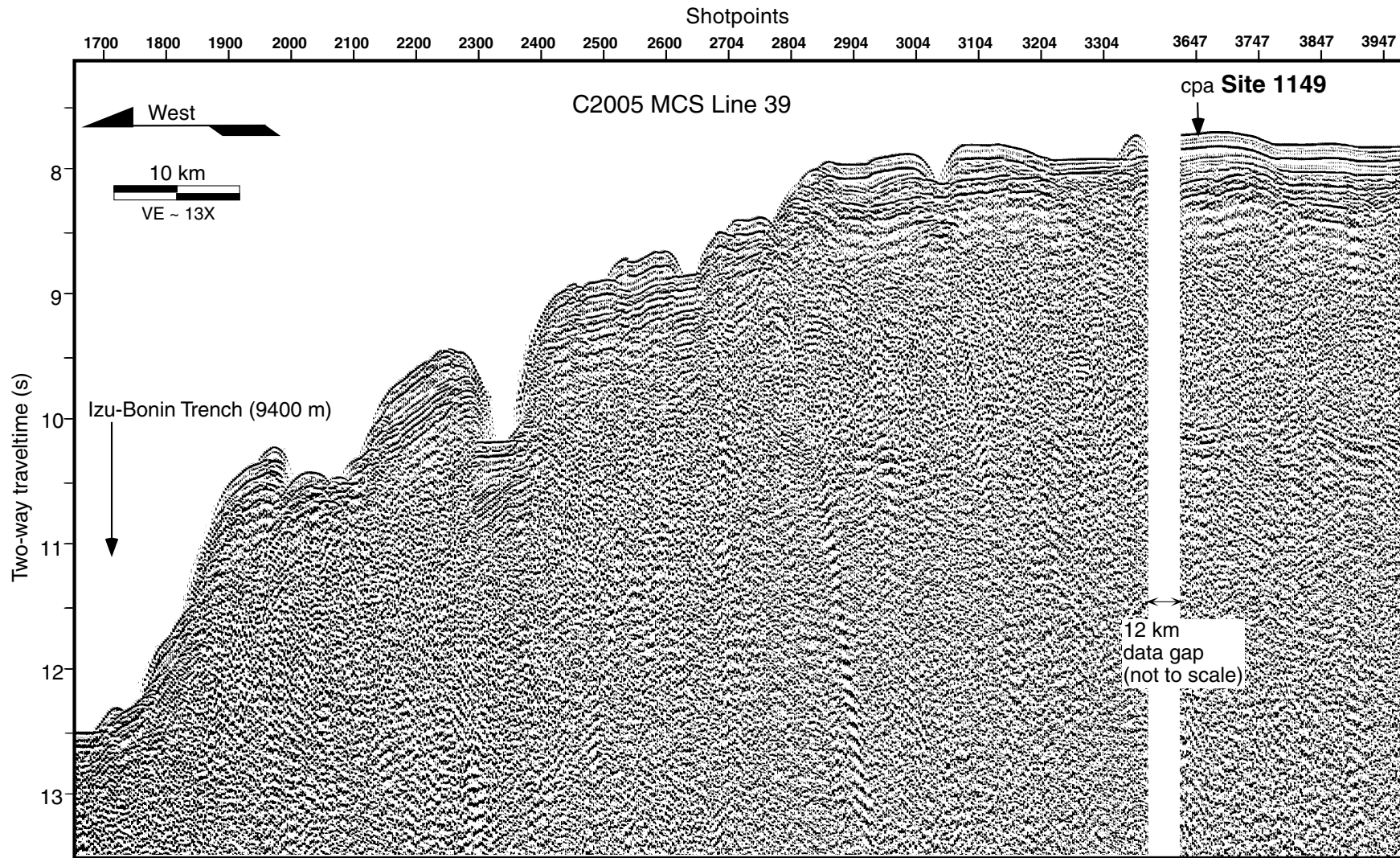


Figure F5. Predicted topography (Smith and Sandwell, 1997) and magnetic lineations (compiled from Nakanishi et al. [1989] and the PLATES Project [1998]) of the western Pacific. Ages of selected lineations (solid black lines) are given using the time scale of Channell et al. (1995). Open circles show locations of selected DSDP/ODP Sites. Site 1149 is located 2200 km northwest of Site 801 along a fracture zone bounded flow line spanning ~38 m.y. White dashed lines = locations of fracture zones. Figure was generated using the GMT software of Wessel and Smith (1995).

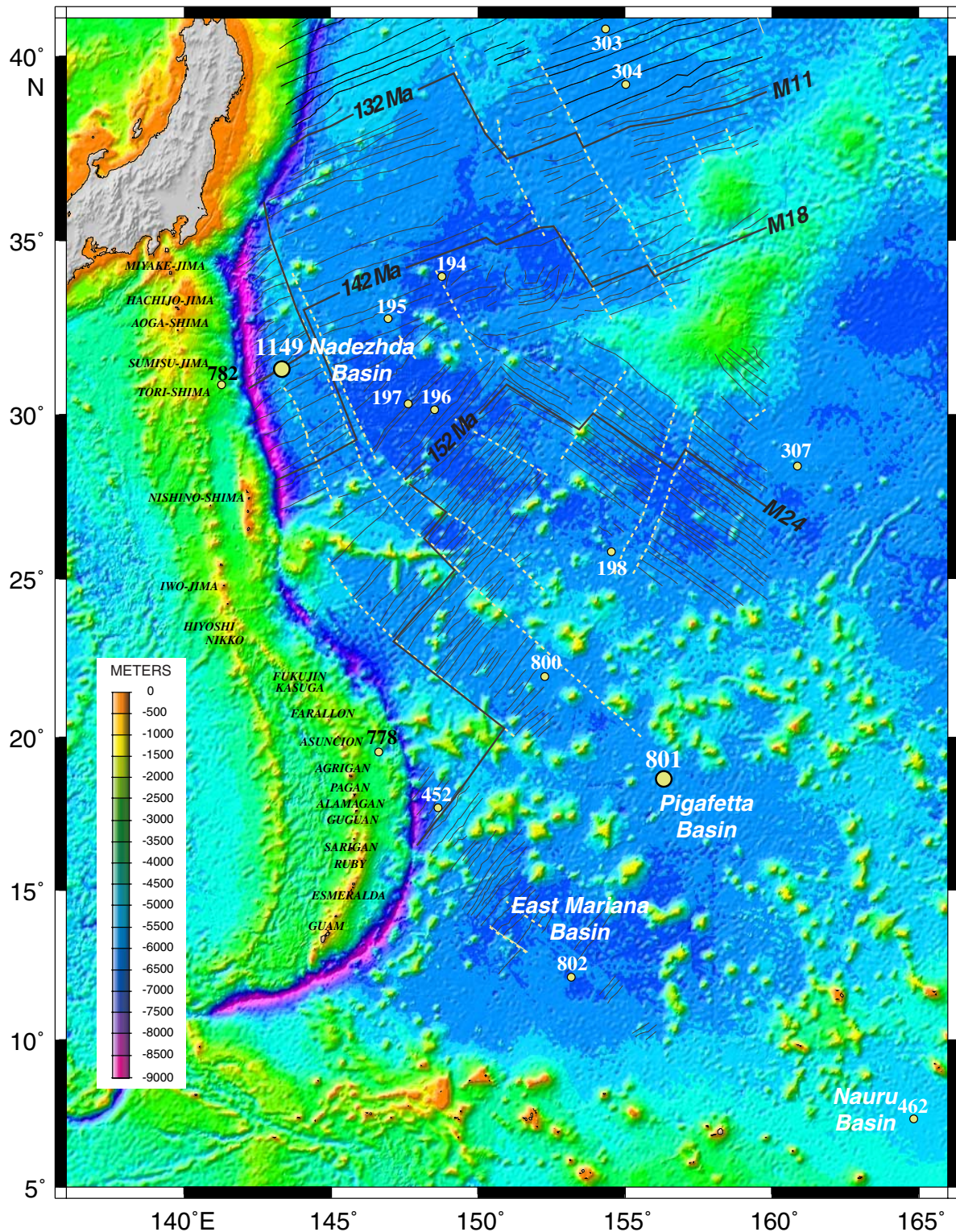


Figure F6. Magnetic anomalies and predicted bathymetry in the vicinity of Site 1149. Contour interval = 100 m. Magnetic anomalies are plotted along ship tracks with positive anomalies shown in black and negative anomalies in gray. Model magnetic anomaly profile calculated to match the lineated magnetic Anomalies M10N, M11, and M12 on the chart. Black blocks are normally magnetized, and white blocks are reversely magnetized. The magnetic reversal and biostratigraphic time scale are from Channell et al. (1995). Model parameters: spreading half rate = 51 km/m.y.; skewness = 230°; and trend of profile toward older anomalies = 140°.

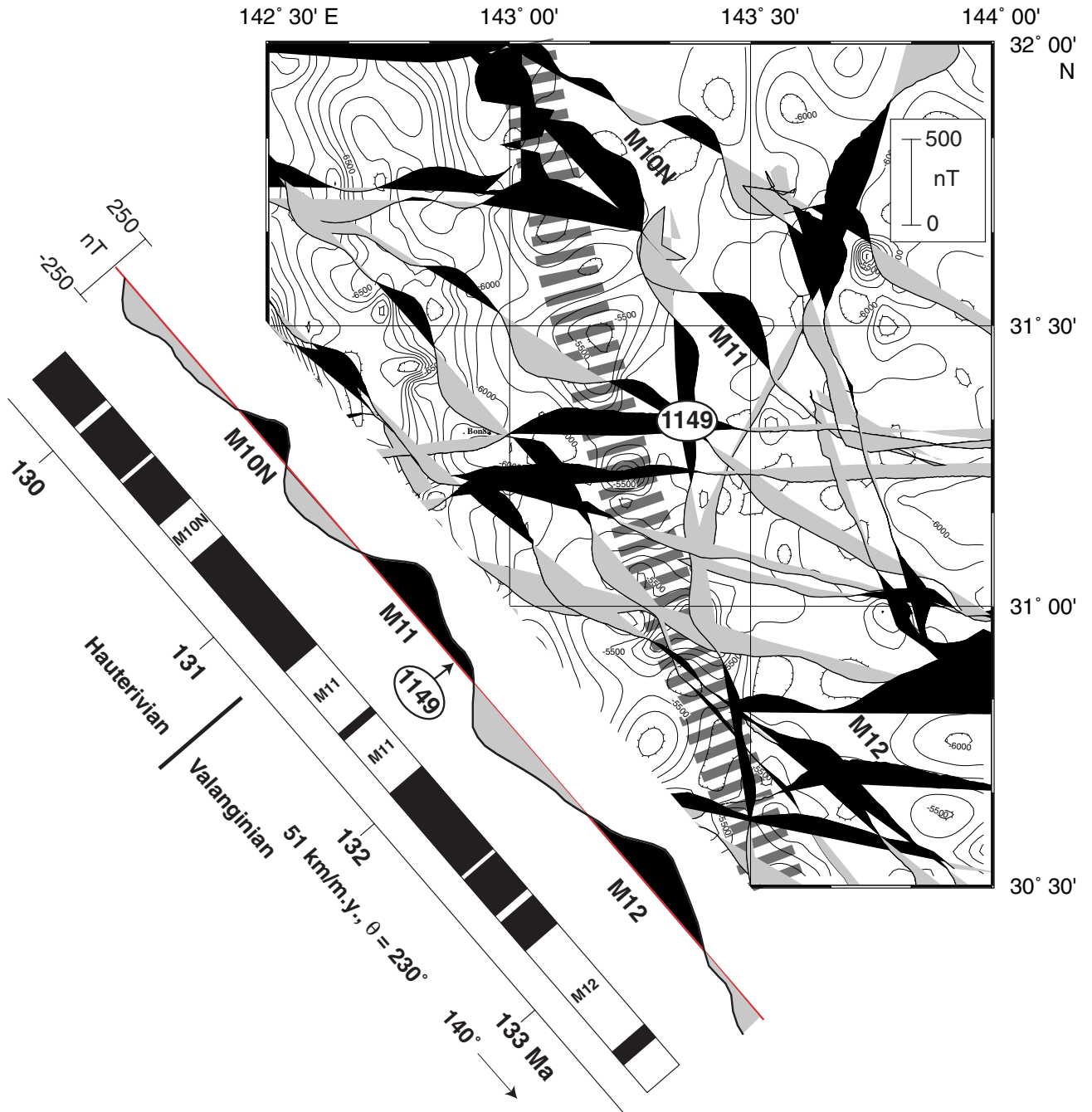


Figure F7. Track chart of the entire SCS survey conducted during Leg 185 (SCS Lines 1, 2, 3) and portions of C2005 MCS Lines 39 and 46. The end points of the seismic profiles shown in Figures F3, p. 55, and F8, p. 60, are marked in capital letters (A–B, C–D, X–Y). Solid circles locate hole positions.

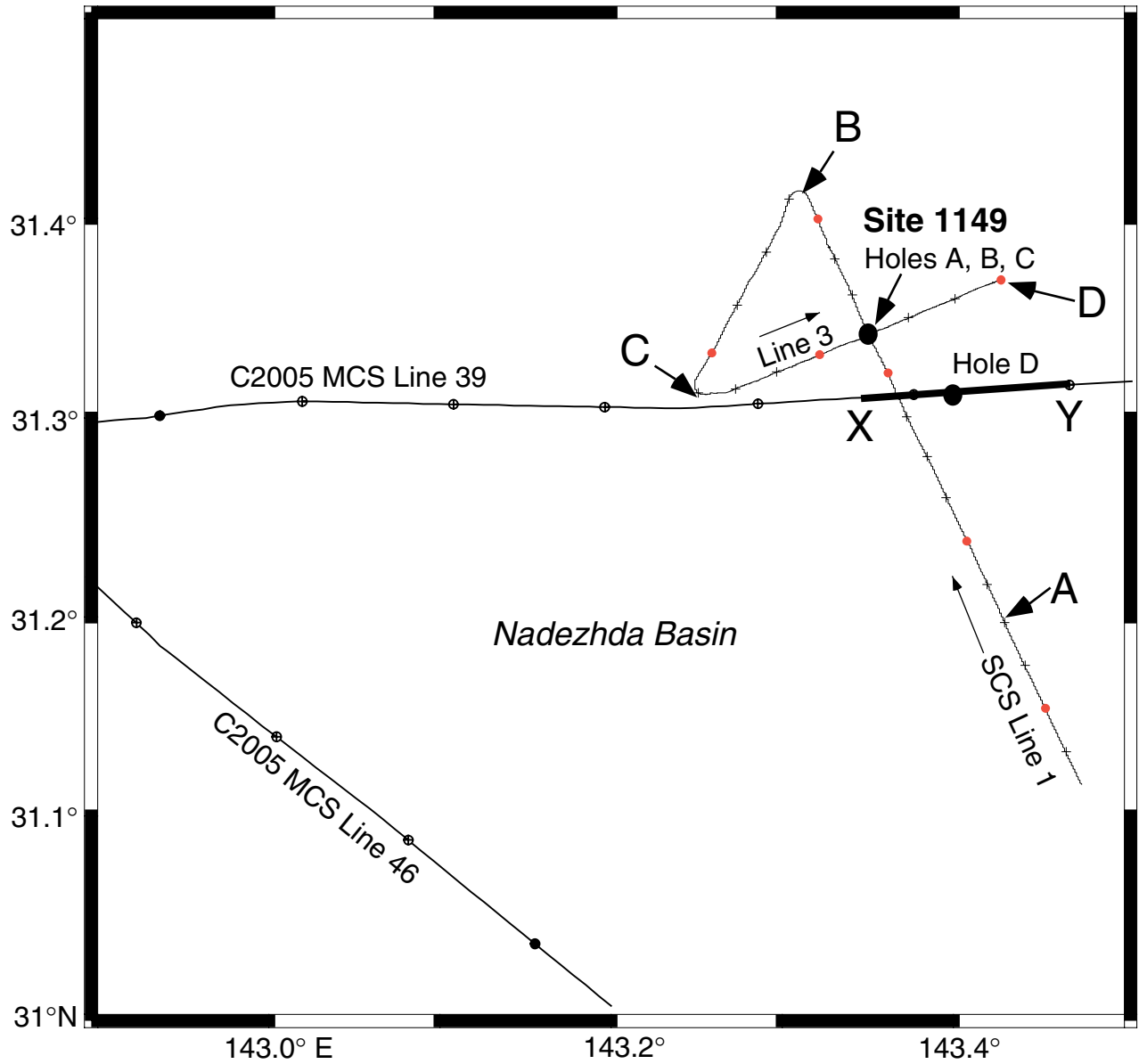


Figure F8. Summary of seismic stratigraphy near Hole 1149D showing generalized correlations with lithologic units, ages, and seismic facies. UT = upper transparent, UO = upper opaque, and HB = Horizon B. Hole 1149D imaged with MCS air guns ($4 \times 466 \text{ in}^3$) of C2005 Line 39 collected in 1976. The location was chosen where the sediment section appeared to thin onto a basement high. Track-line orientation and location are shown in Figure F7, p. 59. Seismic data were reprocessed from CDP gathers and displayed with the following parameters: prestack predictive deconvolution; 24-fold stack; noise filter; band-pass filter 5–40 Hz; spherical divergence gain; and vertical exaggeration of $\sim 8\times$ at the seafloor.

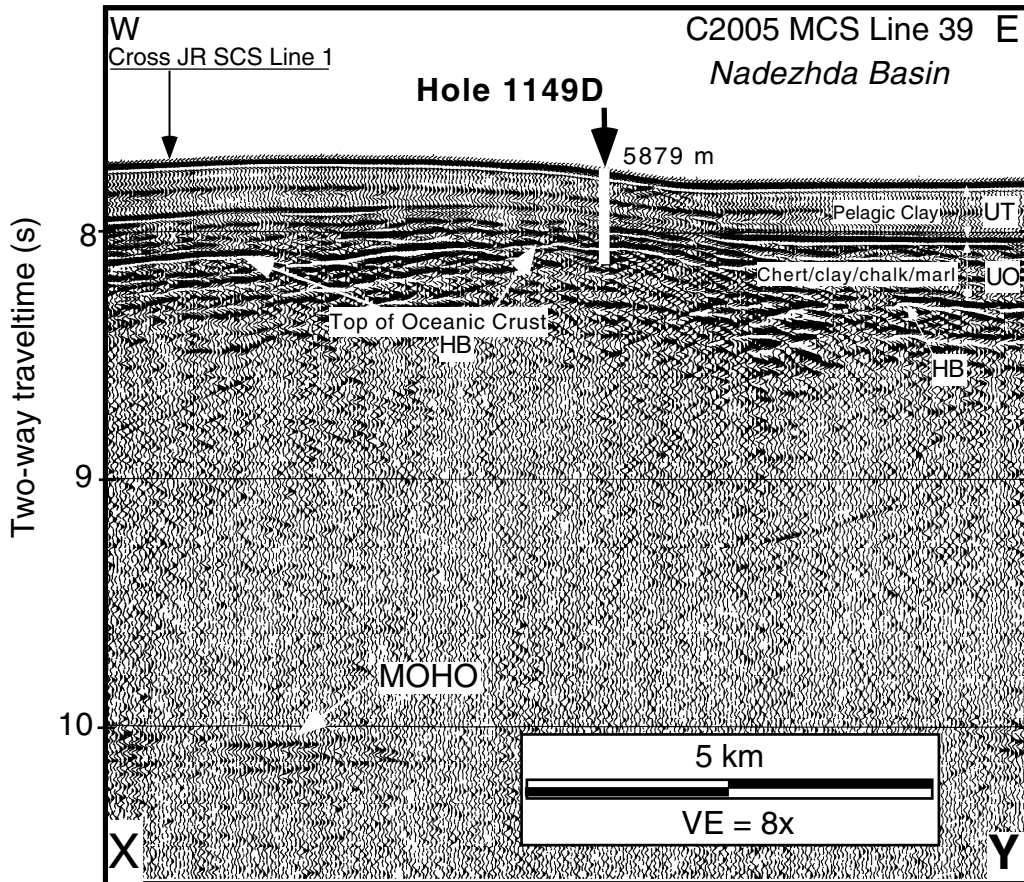


Figure F9. Synthetic stratigraphic section of Holes 1149A, 1149B, 1149C, and 1149D. Basement depth in the graphic lithology column was arbitrarily set to 407.7 mbsf, where it was observed in Hole 1149B. Note that Hole 1149D was offset ~5 km to reach volcanic basement at a shallower depth. Lines extending from the lithology to the lithologic unit and subunit column represent ash layers.

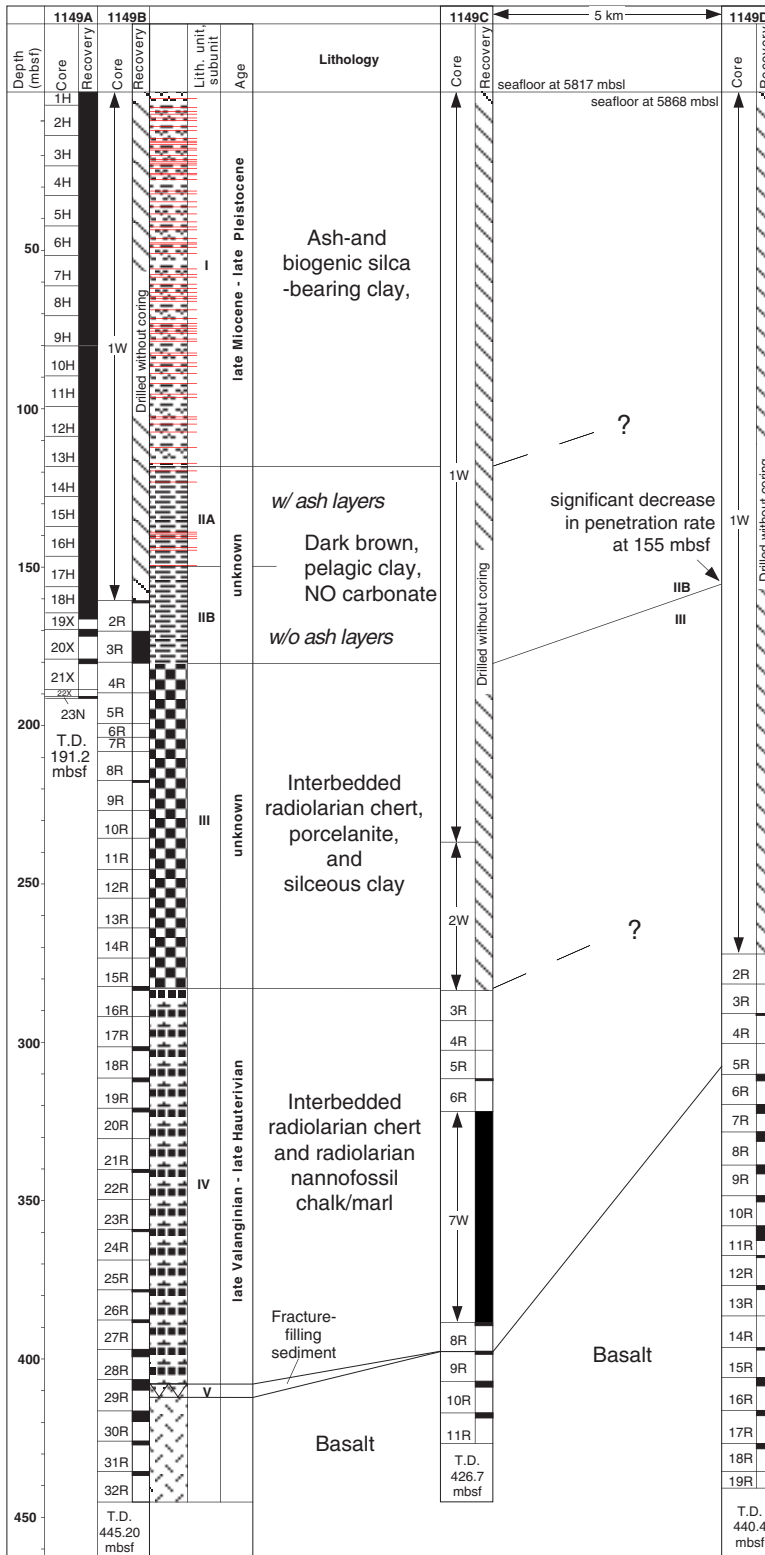


Figure F10. Ash layers in Hole 1149A. A. Interval 185-1149A-2H-3, 49–60 cm. (Continued on next page.)

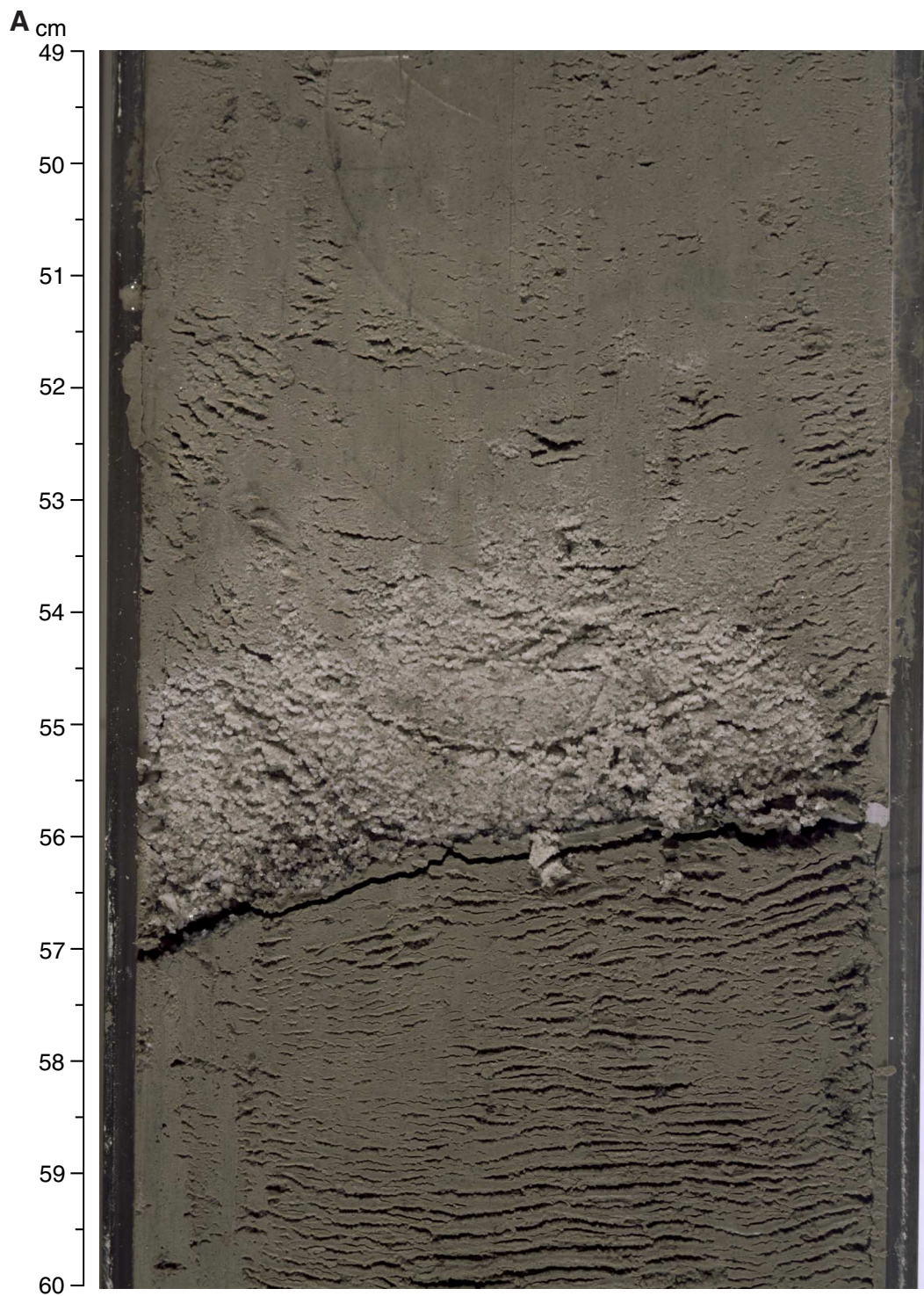


Figure F10 (continued). B. Interval 185-1149A-5H-6, 52–62 cm.

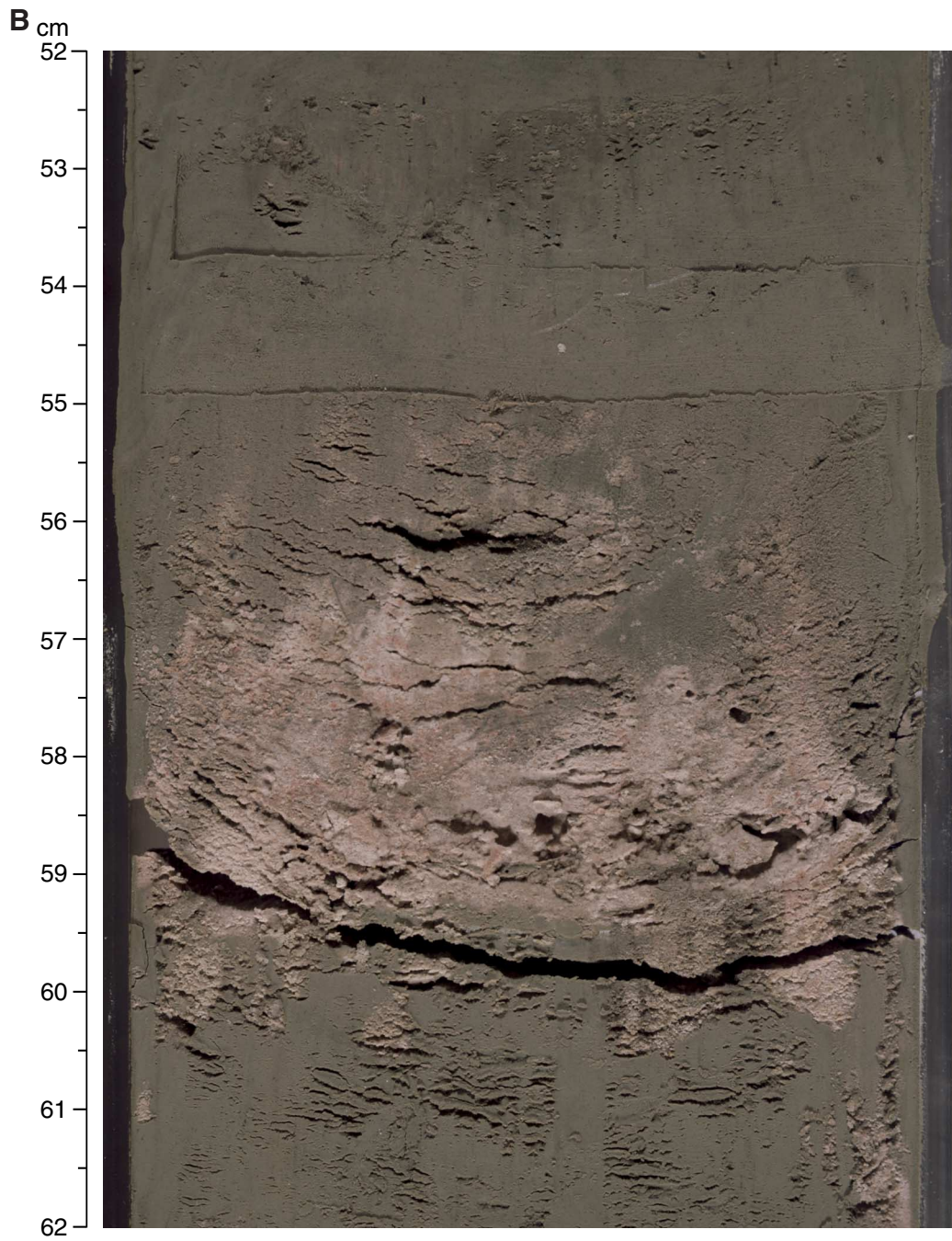


Figure F11. Pumice in clayey background sediment of lithologic Unit I (interval 185-1149A-4H-1, 54–65 cm).

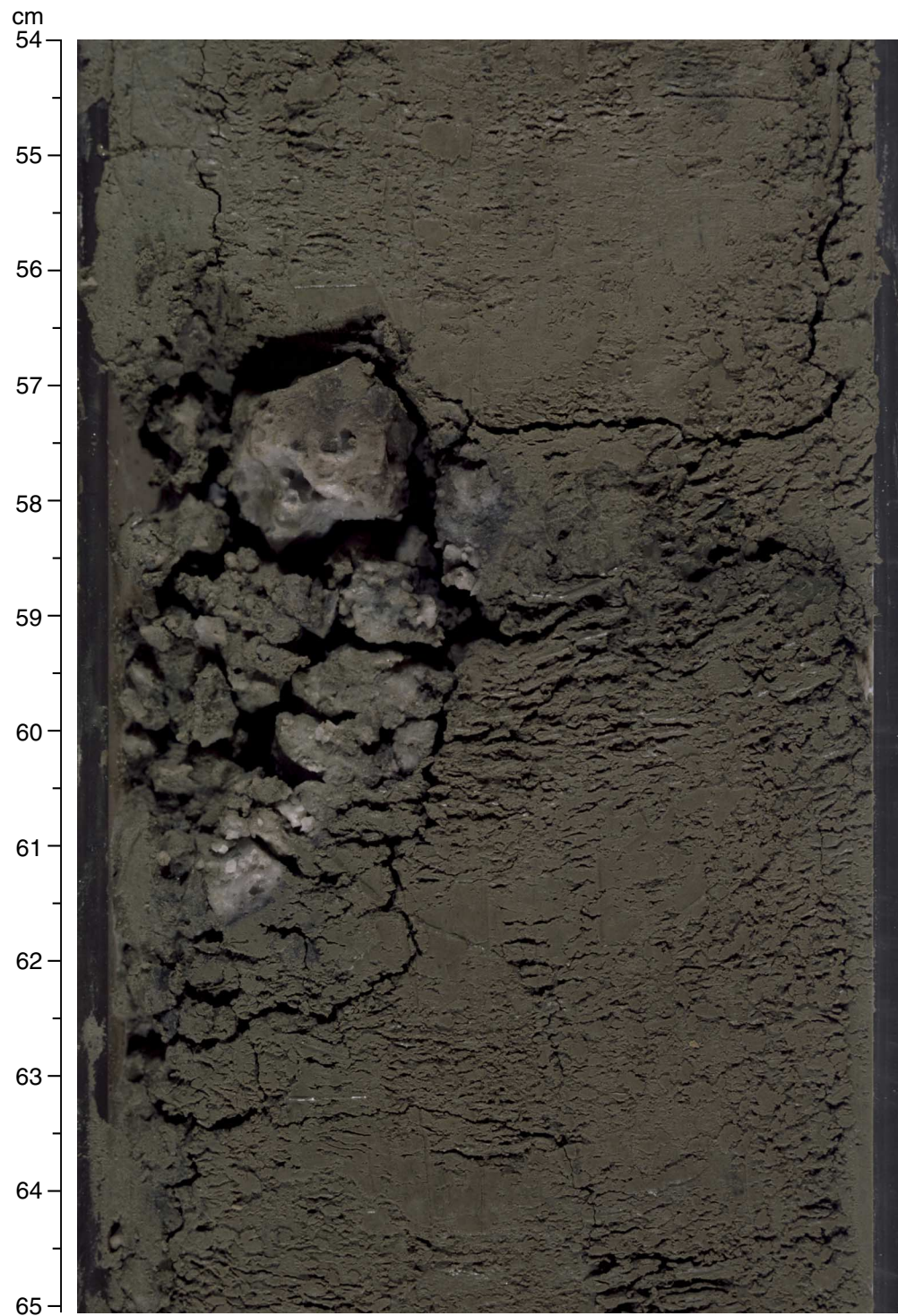
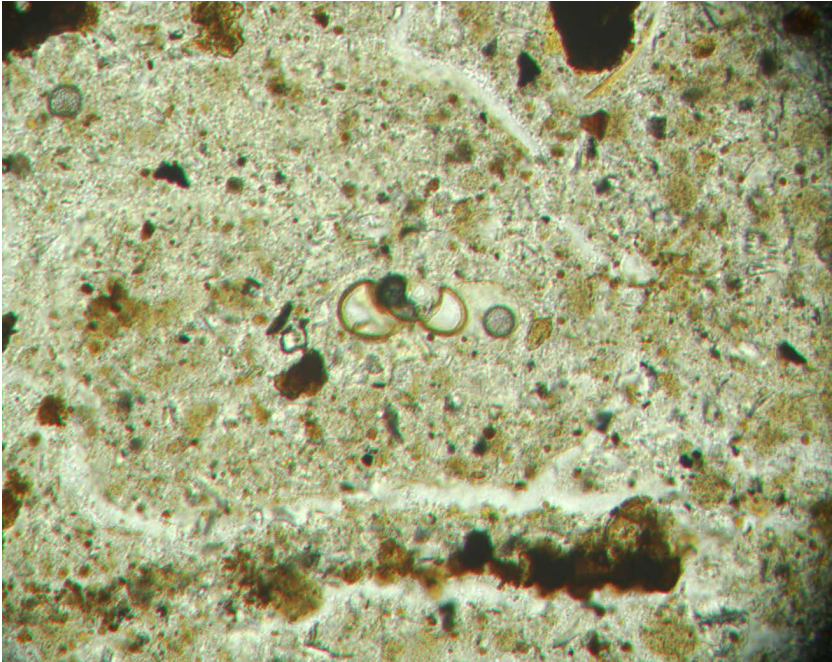


Figure F12. Planktonic foraminifer with preserved calcareous test in clay-filled vug of a pumice cobble. Thin-section micrograph taken with plane-polarized light (interval 185-1149A-11H-6, 72–74 cm).



100 μm

Figure F13. X-ray diffractogram traces of samples from lithologic Unit I. Ill = illite; Ch/Ka = chlorite and/or kaolinite; Ch = chlorite; Qz = quartz; Fsp = feldspar; Hal = halite; and Clay = nonbasal clay-mineral reflection. Halite is from seawater. Samples from Cores 185-1149A-1H, 11H, and 12H are from monotonous background sediment. Sample 185-1149A-2H-1, 22–23 cm, is from a slightly indurated green clay lamina. Note the well-defined plagioclase peak at 3.18 Å in this diffractogram and that individual diffractograms are offset by 500 cps for clarity.

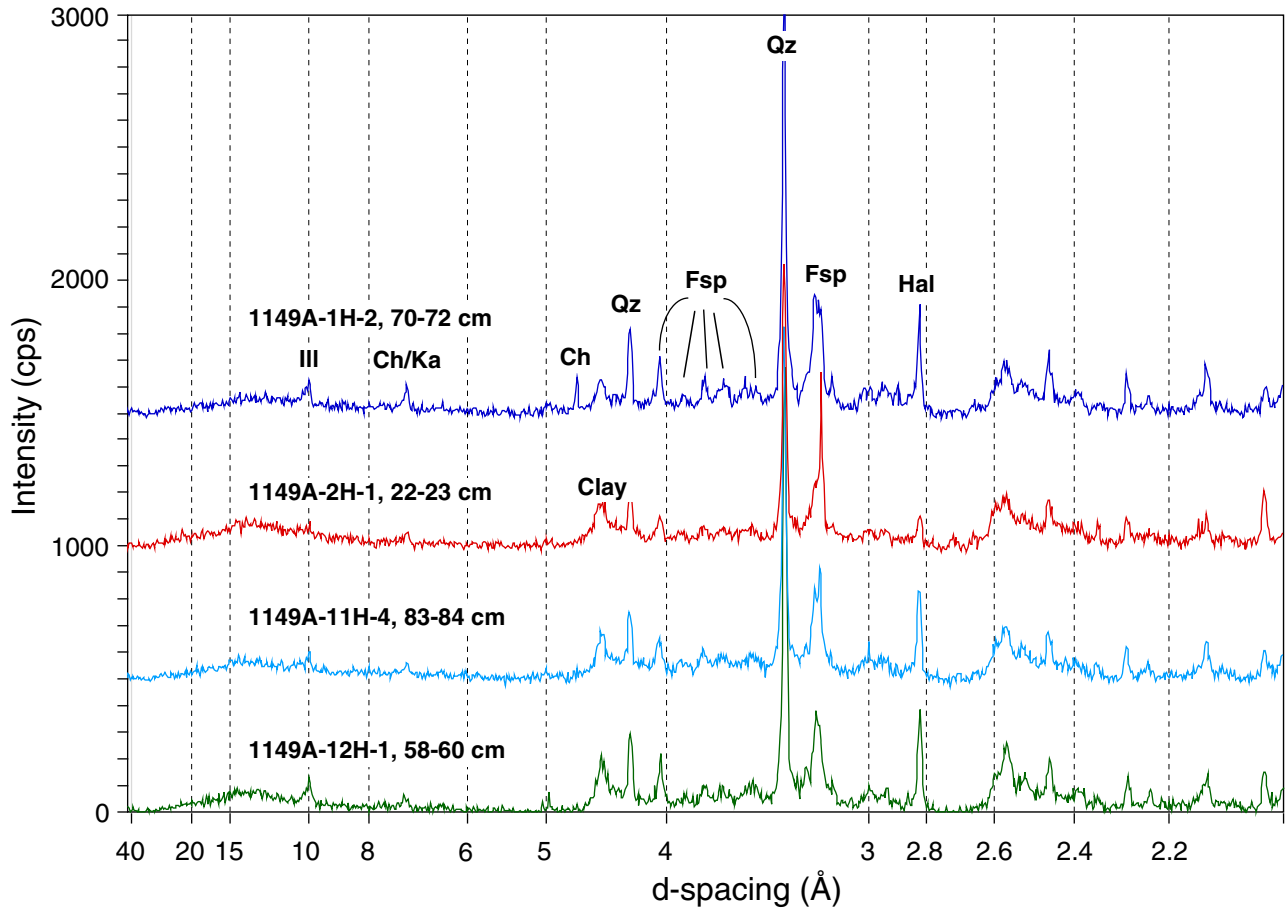


Figure F14. Bioturbation of Unit I sediment (interval 185-1149A-1H-2, 8–31 cm).

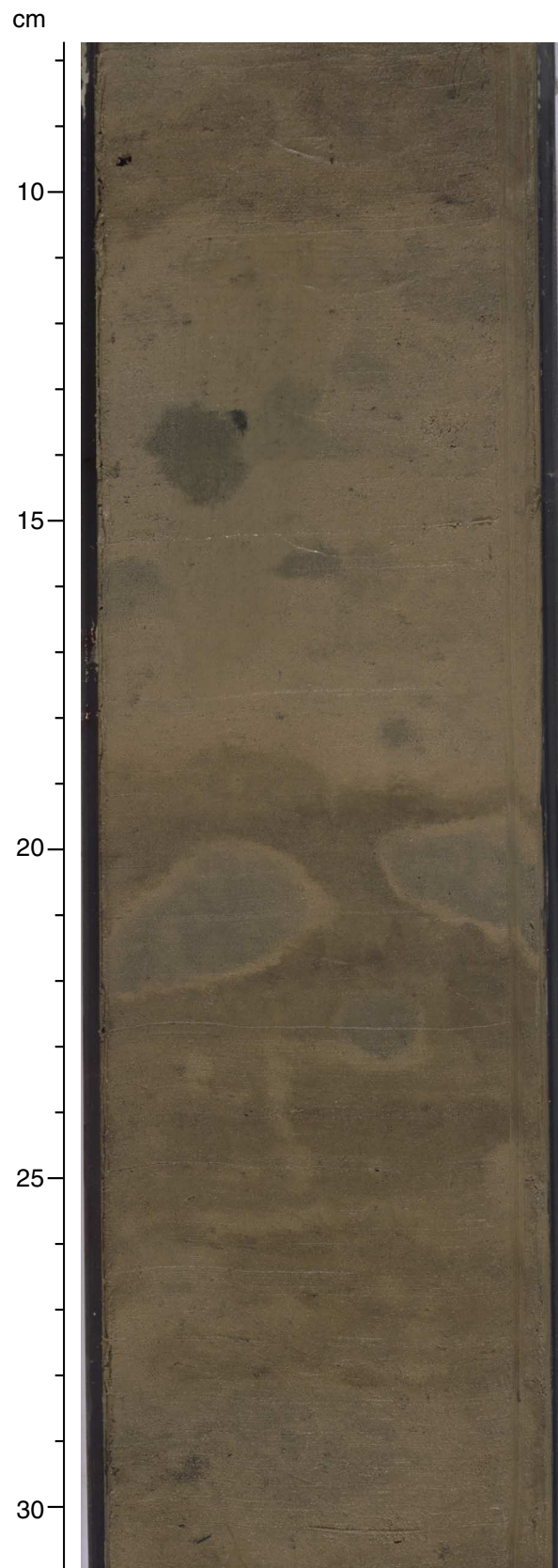


Figure F15. Dark green indurated layer and color change of background sediment at the top of lithologic Unit I (interval 185-1149A-1H-3, 79–106 cm).

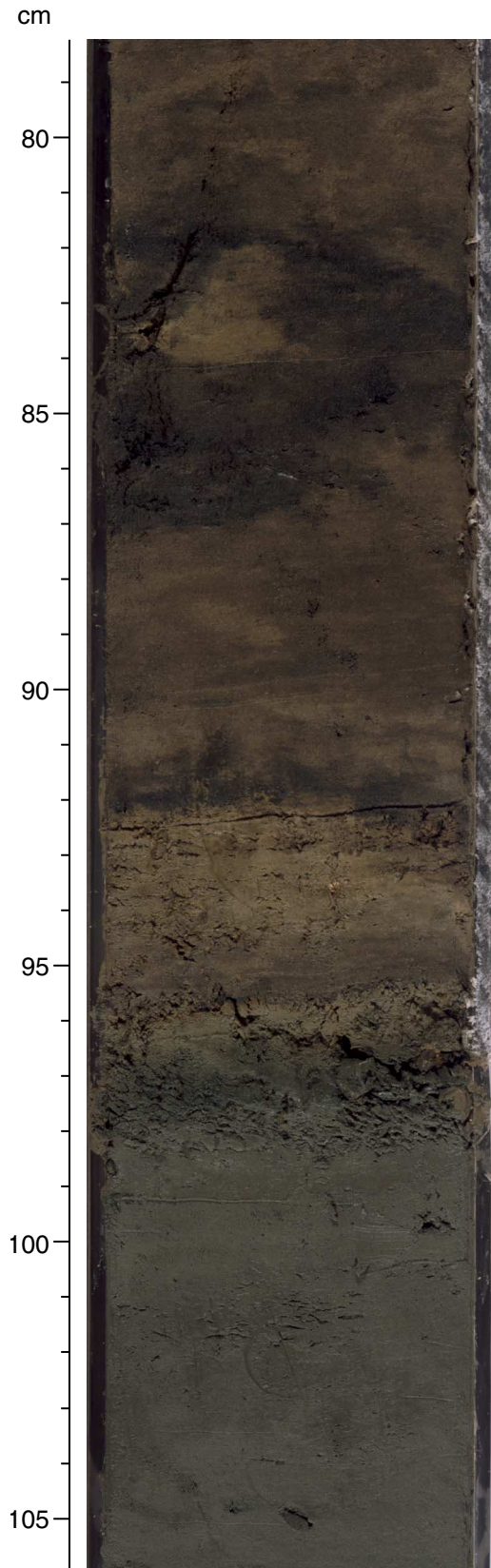


Figure F16. Bioturbation at transition between compositionally similar, but differently colored sediments in lithologic Subunit IIA. **A.** Difference in color is related to minor changes in the abundance of Mn micronodules (interval 185-1149A-14H-3, 103–126 cm). **B.** Bioturbated ash layers (interval 185-1149A-16H-6, 23–45 cm). (Continued on next page.)

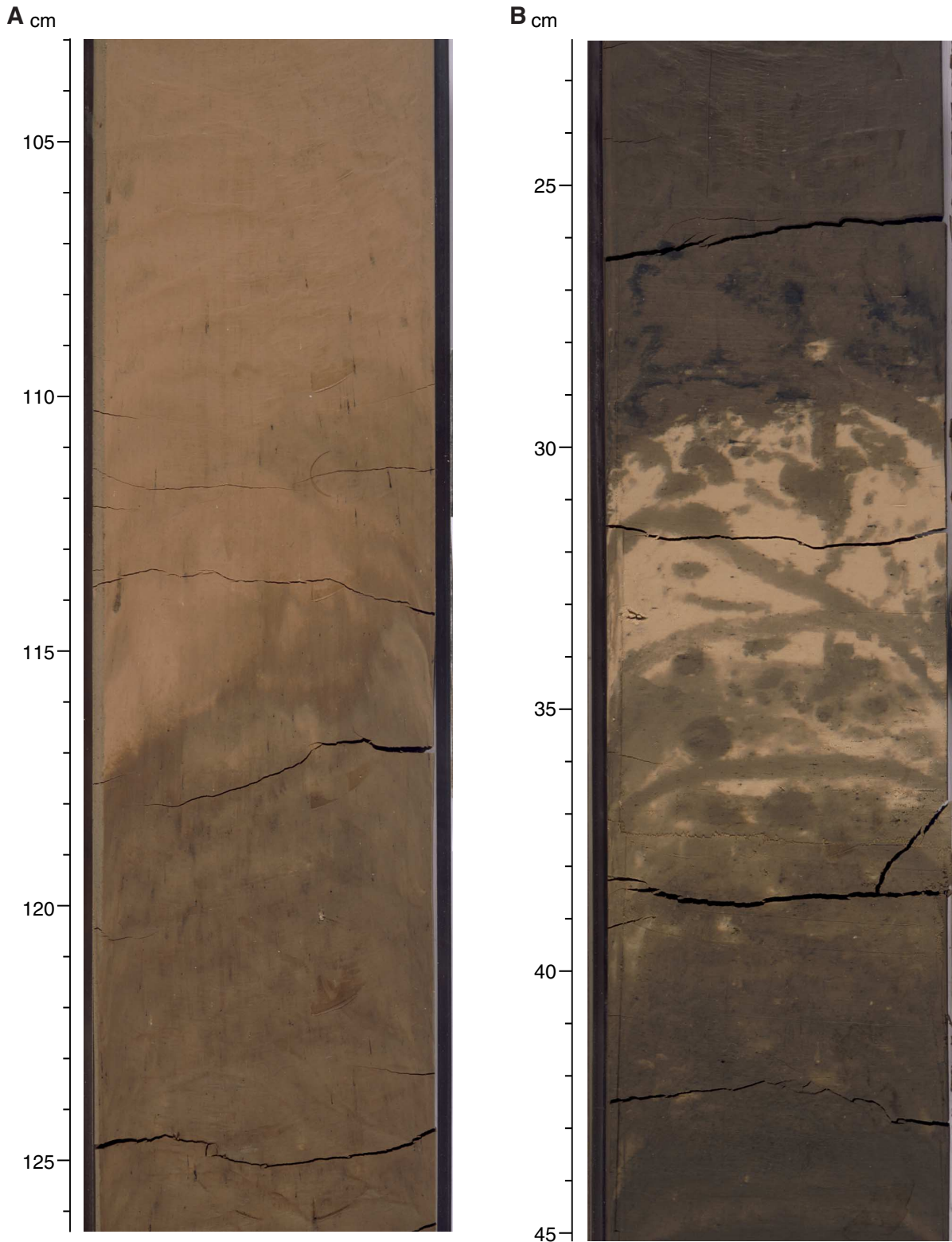


Figure F16 (continued). C. Interval 185-1149A-16H-3, 15–50 cm. D. Interval 185-1149A-16H-3, 105–130 cm.

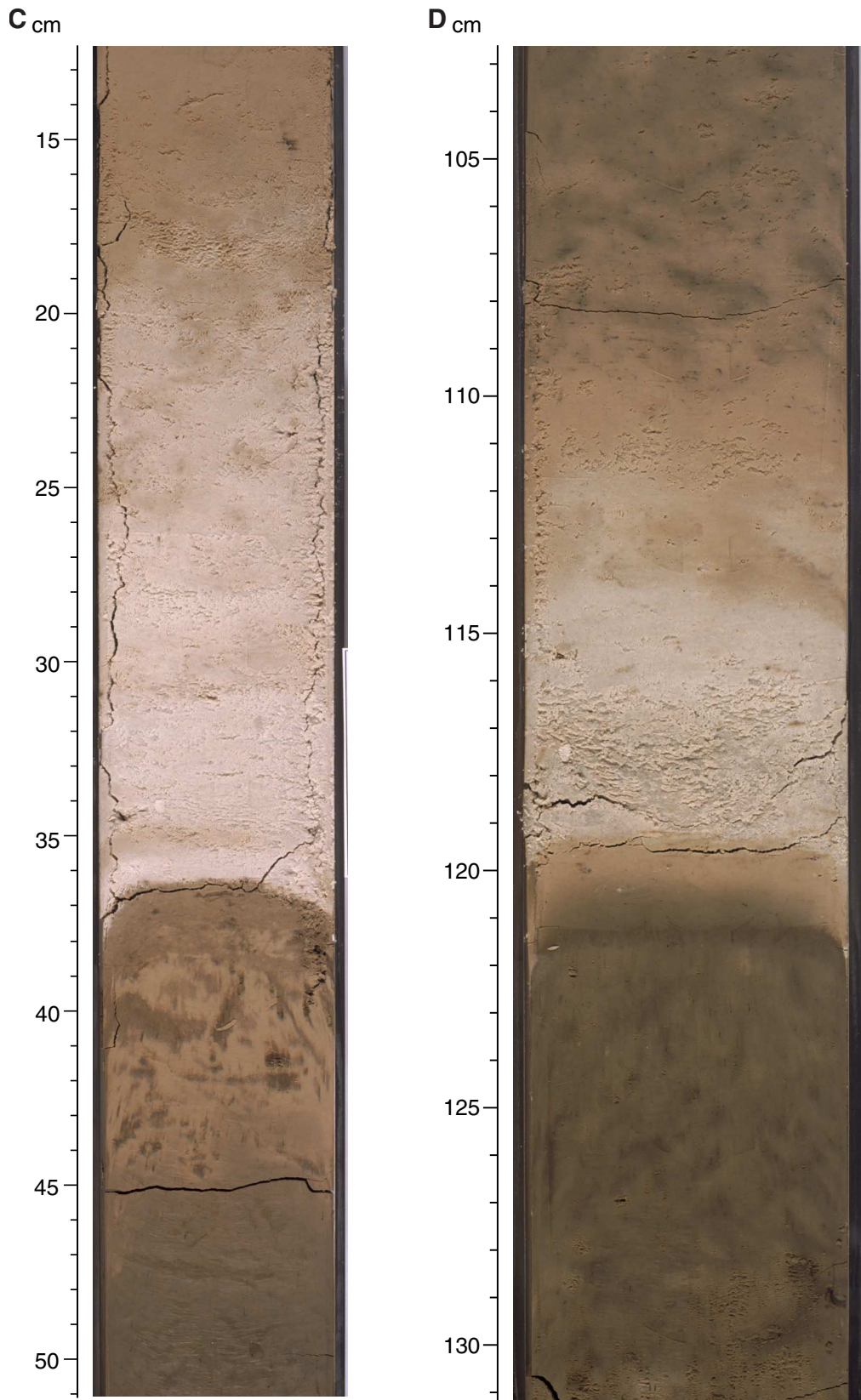


Figure F17. X-ray diffractogram traces of samples from lithologic Unit II. Ill = illite; Clay = nonbasal clay mineral reflection; Qz = quartz; Fsp = feldspar; Hal = halite; Paly = palygorskite; and Z = zeolite. Halite is from seawater. All samples are from monotonous background sediment. Note that the XRD pattern of background sediment from Core 185-1149A-14H is very similar to that of Unit I clays (Fig. F13, p. 66). Note that individual diffractograms are offset by 500 cps for clarity.

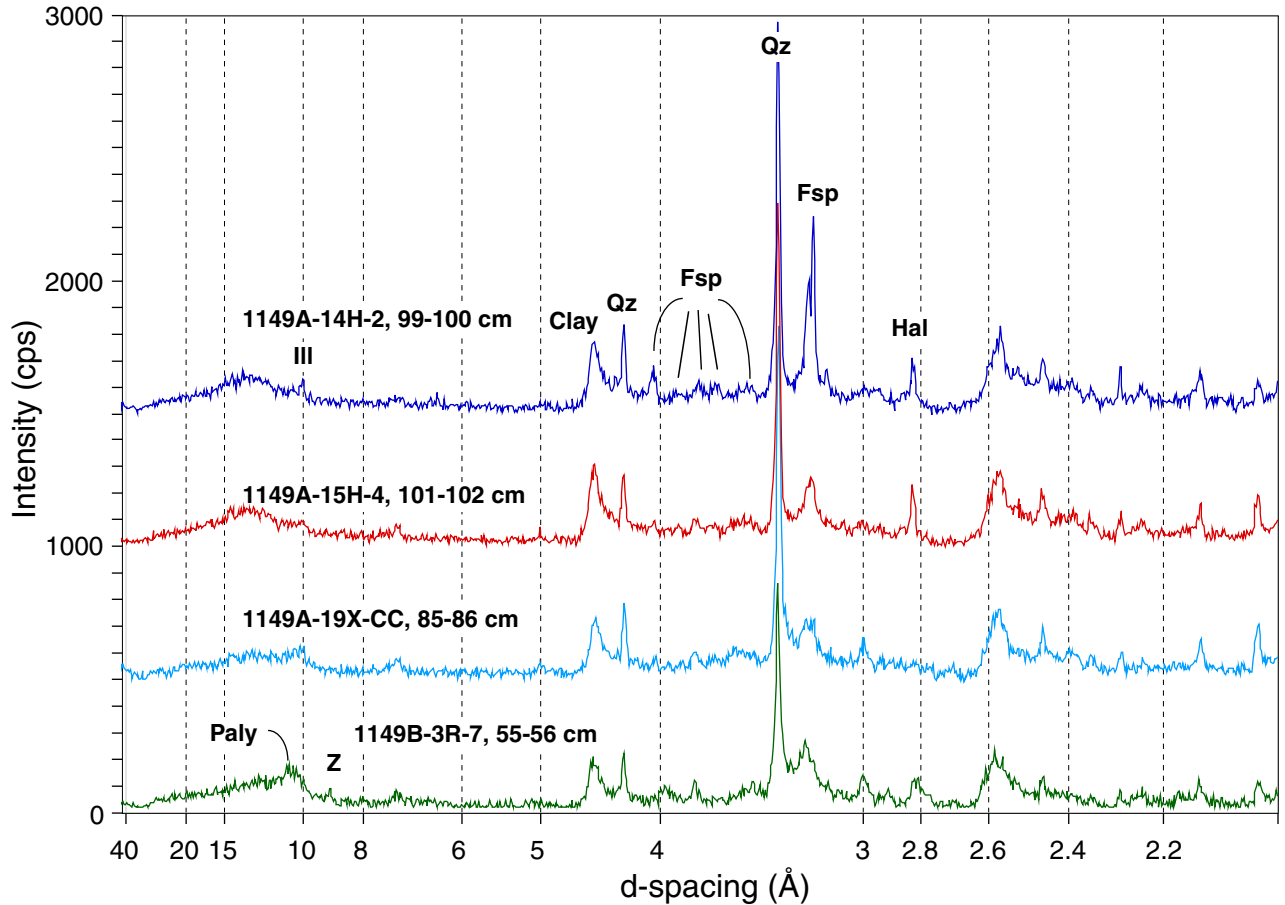


Figure F18. Deformational features in lithologic Unit II. **A.** Steep normal fault offsets lighter colored clay layers in dark brown clay matrix with downward increasing throw. Bottom of deformed light layer contains rare volcanic glass fragments and marks boundary between Subunits IIA and IIB (interval 185-1149A-17H-2, 118-138 cm). (Continued on next page.)

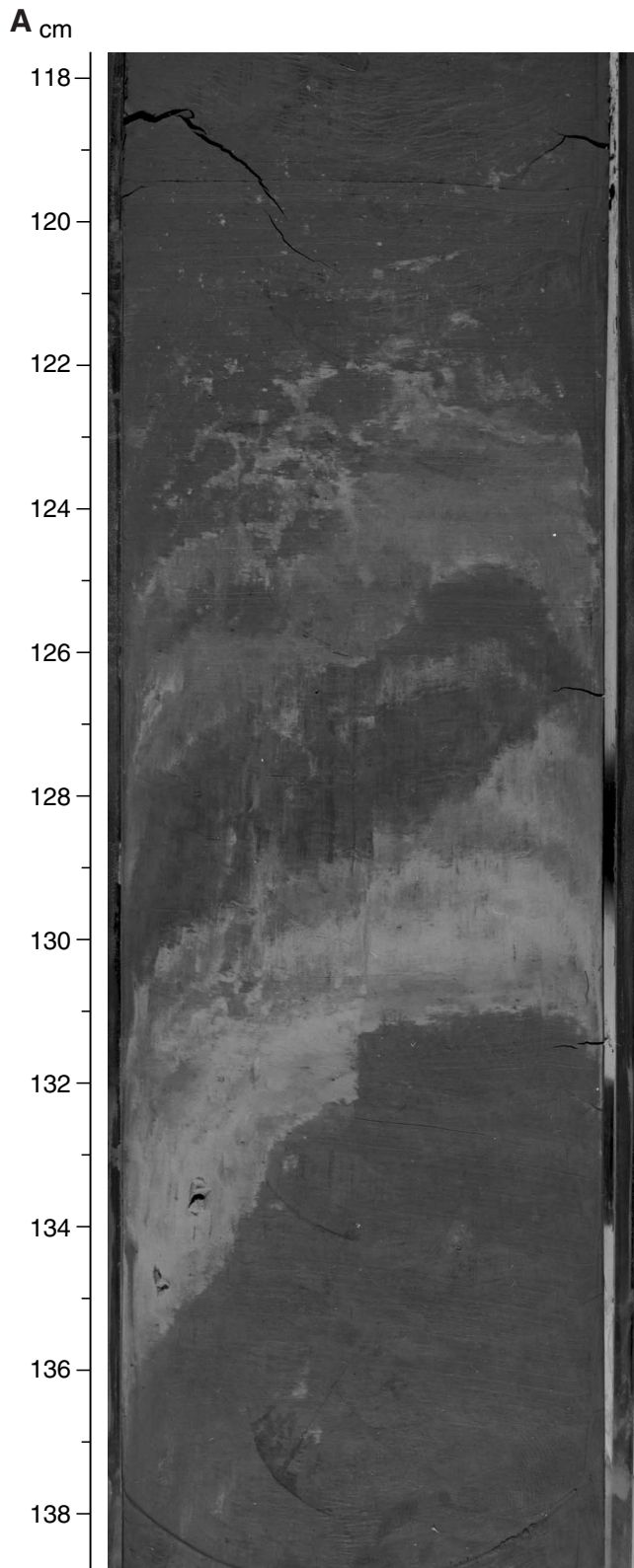


Figure F18 (continued). B. Steep, splaying fault trace without recognizable displacement (interval 185-1149A-18H-4, 6–50 cm). Note that deformation is found close to the center of the core and seems to be unrelated to coring-induced bending at core edges.

B cm

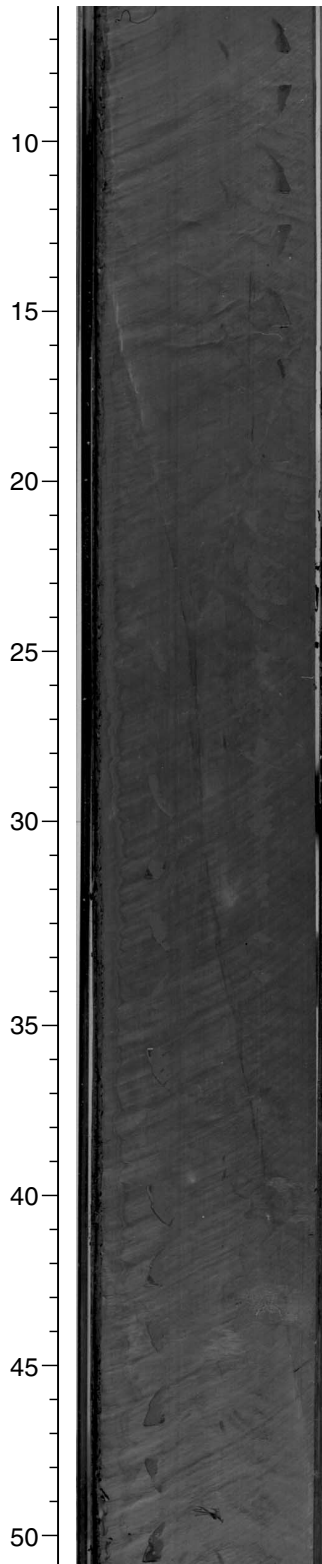


Figure F19. Lamination in zeolitic clay and radiolarian porcelanite in lithologic Unit III. A. Interval 185-1149A-21X-1, 11-32 cm. (Continued on next page.)

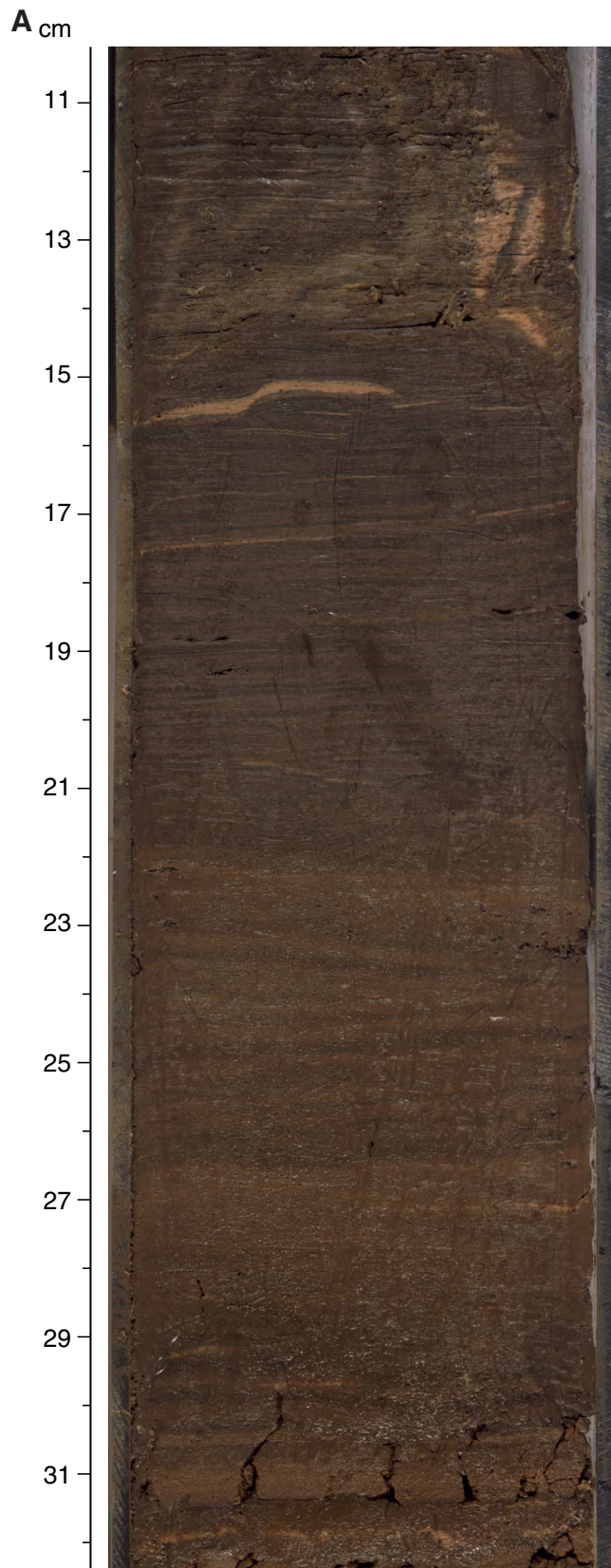


Figure F19 (continued). B. Interval 185-1149A-21X-1, 62-74 cm.

B cm

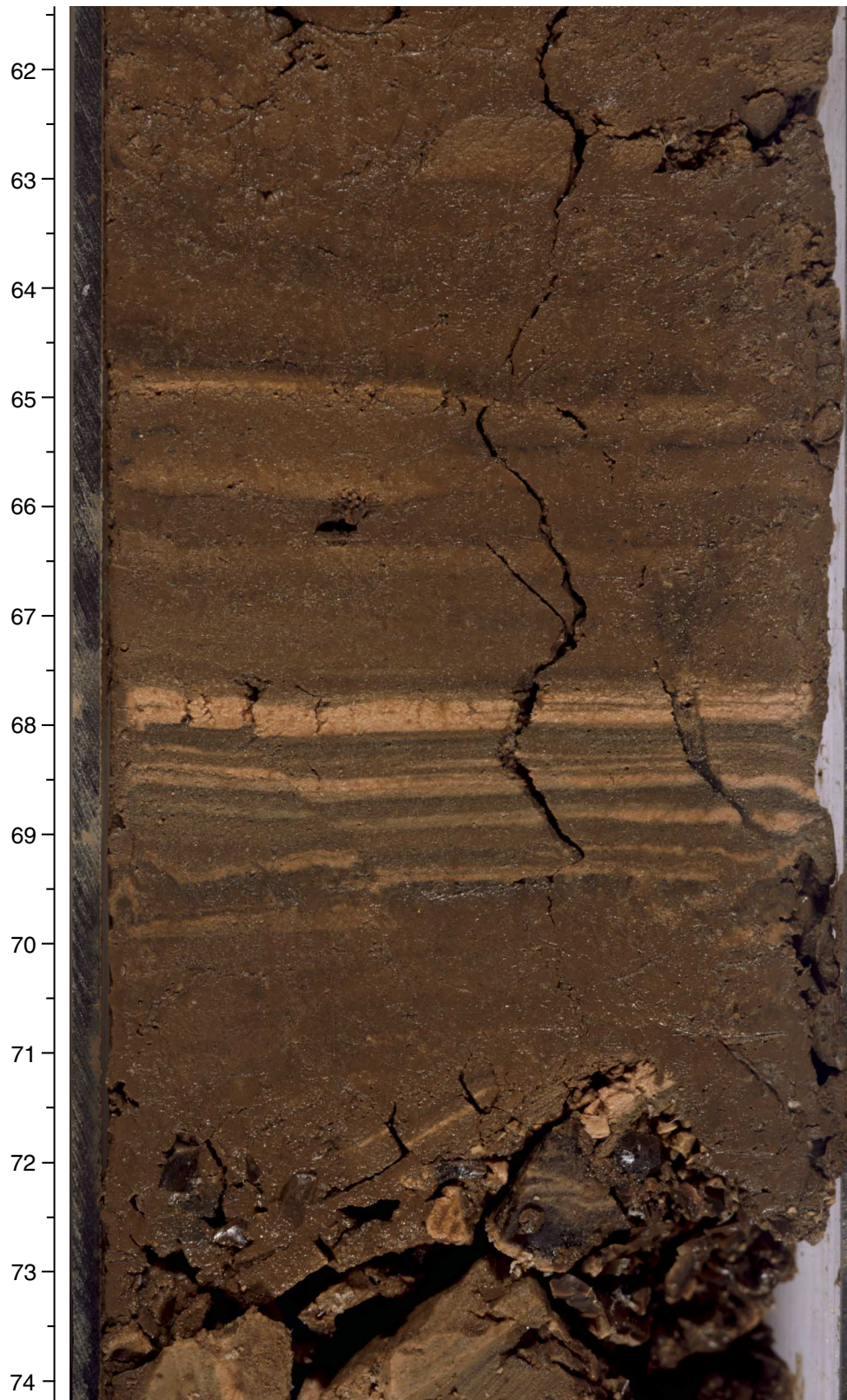


Figure F20. Radiolarian porcelanite. A. Interval 185-1149B-4R-1, 6–12 cm. (Continued on next page.)

A



Figure F20 (continued). B. Interval 185-1149B-16R-1, 7–52 cm. C. Interval 185-1149B-16R-1, 98–118 cm.

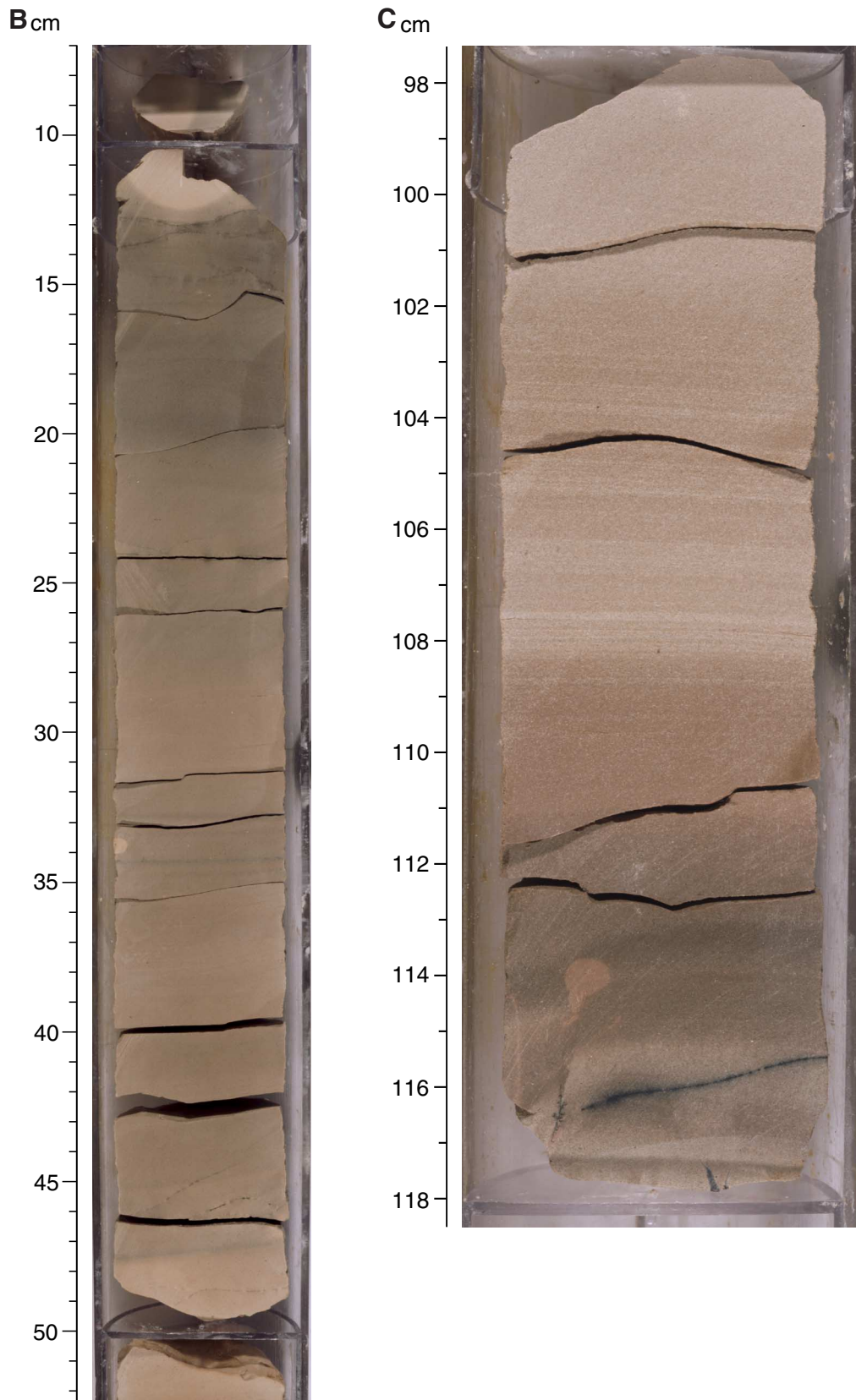


Figure F21. Pink chert with chalcedony-filled vein. Note light pink-colored lenses of porous porcelainite (interval 185-1149B-6R-1, 20–25 cm).



Figure F22. X-ray diffractogram traces of samples from lithologic Unit III. Z = zeolite; Clay = nonbasal clay mineral reflection; Qz = quartz; CT = opal-CT; Hal = halite; and Paly = palygorskite. Halite is from seawater. Sample 185-1149A-21X-1, 60–61 cm, is from the laminated zeolitic clay shown in Figure F19, p. 74. Sample 185-1149B-7R-1, 8–37 cm, is from clay layers intercalated with radiolarian chert and porcelanite. Sample 185-1149B-14R-CC, 4–7 cm, is from a clayey zeolite silt. Note the presence of palygorskite. Note that individual diffractograms are offset vertically for clarity.

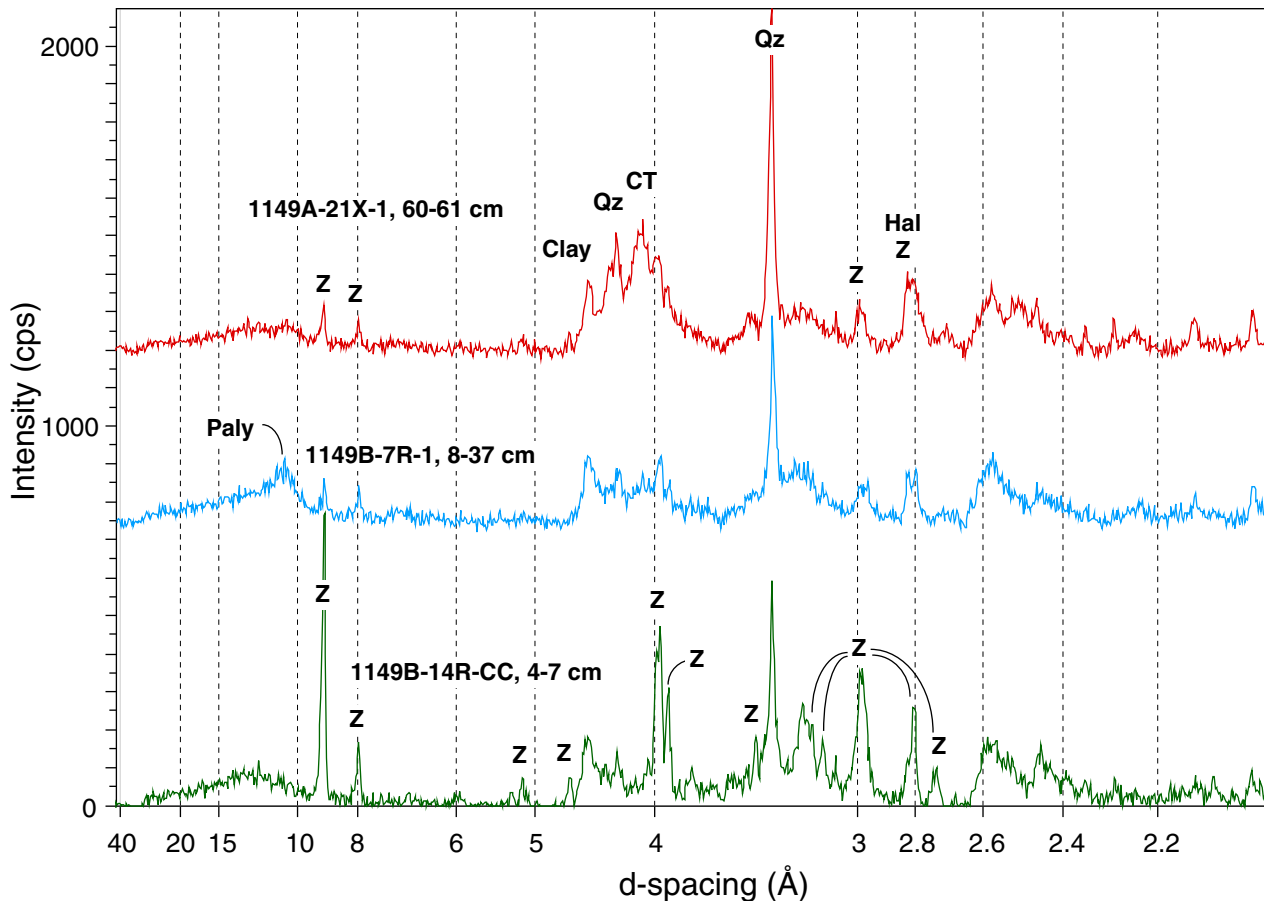


Figure F23. Soft calcareous sediment in burrows and on bedding planes of radiolarian chert (interval 185-1149B-24R-1, 21–25 cm).

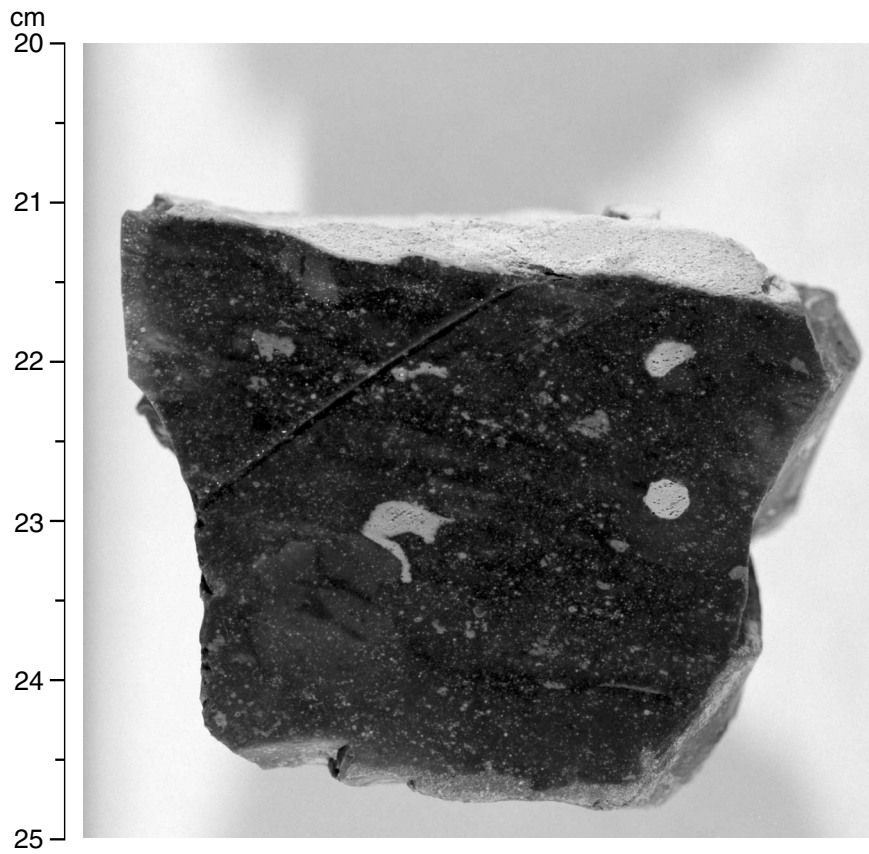


Figure F24. A. Wavy, discontinuous lamination and differential compaction around an early indurated burrow in radiolarian marl of lithologic Unit IV (interval 185-1149B-18R-1, 65–73 cm). (Continued on next page.)

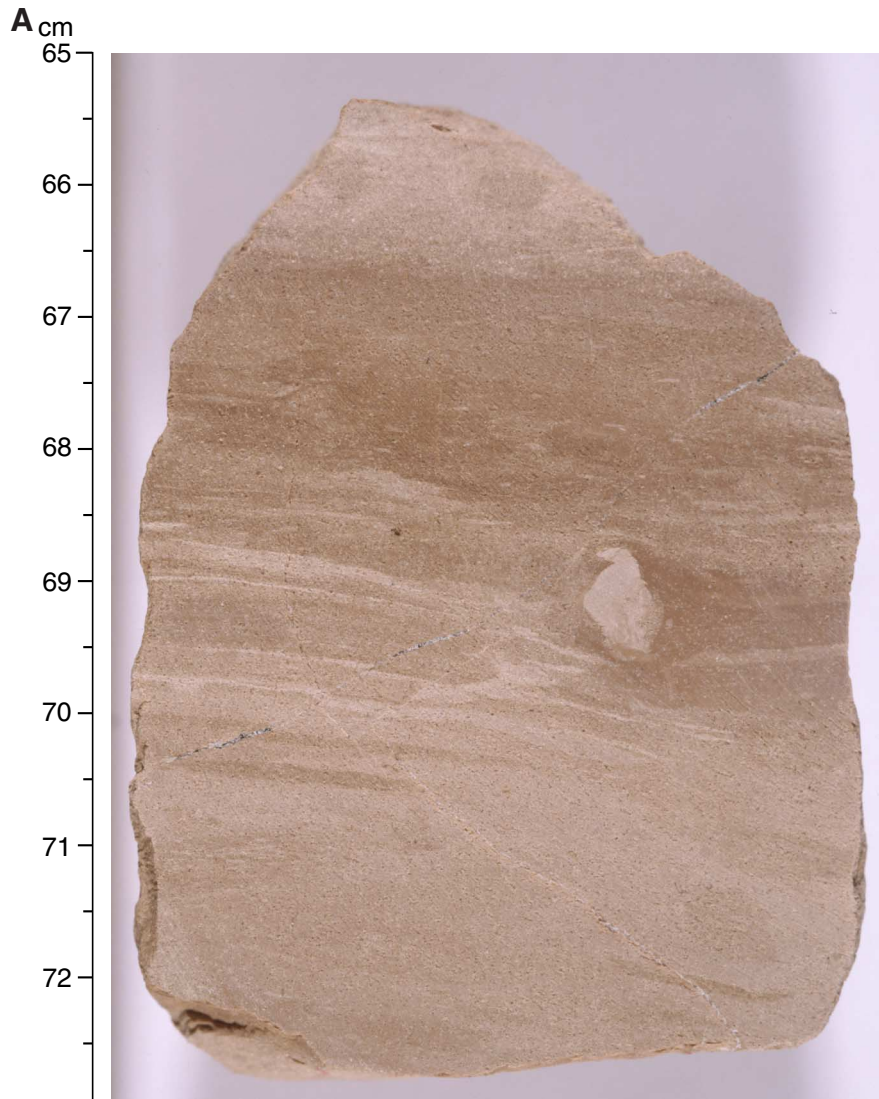


Figure F24 (continued). B. Water escape structure at 89.5 cm (indicated by arrow) (interval 185-1149B-18R-1, 83–93 cm).

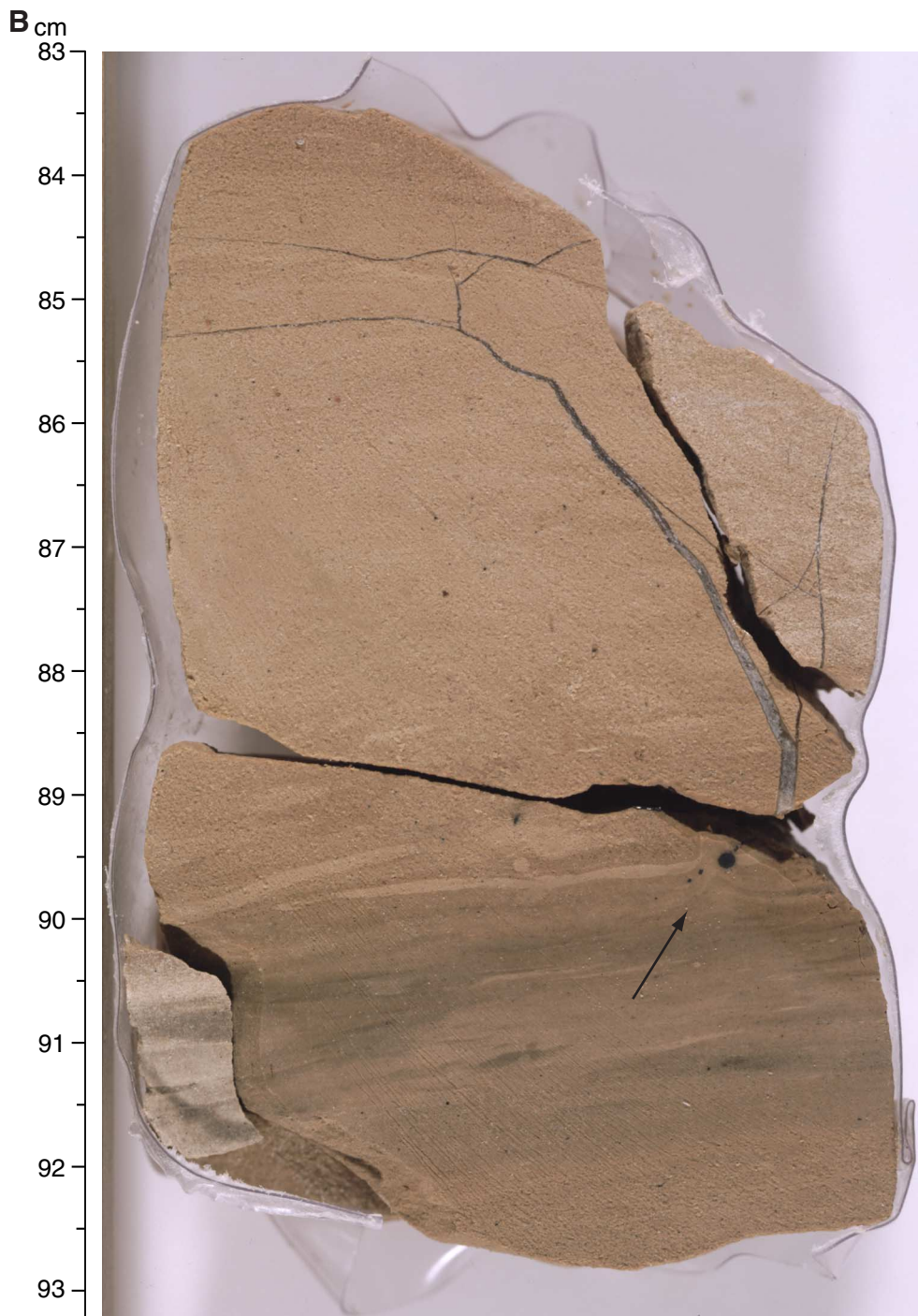
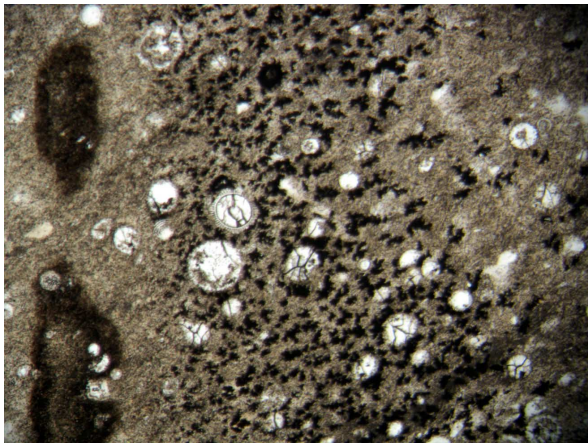


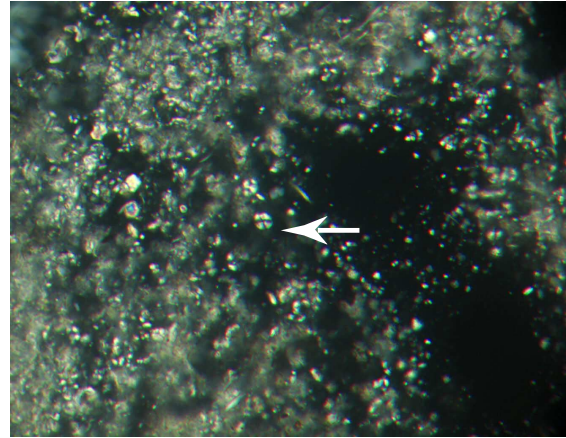
Figure F25. Photomicrographs of radiolarian chalk and radiolarian-bearing calcareous marlstone showing various stages of silica diagenesis and alteration of siliceous microfossils in radiolarian marlstones of lithologic Unit IV. **A.** Clear spheres are radiolarians at various stages of alteration from opal-CT to quartz (most are chalcedony). Dark patches are richer in clay minerals in a dominantly calcareous groundmass. Taken under plane-polarized light; Sample 185-1149B-18R-1, 69–71 cm (301.7 mbsf). **B.** Close-up view of carbonate groundmass, which largely consists of recrystallized, partially dissolved, and broken calcareous nanofossils (indicated by arrow). Taken under cross-polarized light; Sample 185-1149B-18R-1, 69–71 cm (301.7 mbsf). **C.** Diatom and radiolarians in calcareous matrix. Taken under plane-polarized light; Sample 185-1149B-18R-1, 69–71 cm (301.7 mbsf). **D.** Same field of view as in (C). Diatom to the right of the center is optically isotropic test indicating a composition of opal (opal-CT according to XRD data in Sample 185-1149B-18R-1, 9–11 cm). Taken under cross-polarized light. Radiolarian left of the center with moderately preserved morphology and optically isotropic test, whereas the infill is birefringent chalcedony. The radiolarian “ghost” partially captured at the top center of the photomicrograph shows complete conversion to chalcedony. The close juxtaposition of these different stages of diagenetic alteration suggests an overlap of the stability regimes for opal-CT and quartz. (Continued on next page.)

A



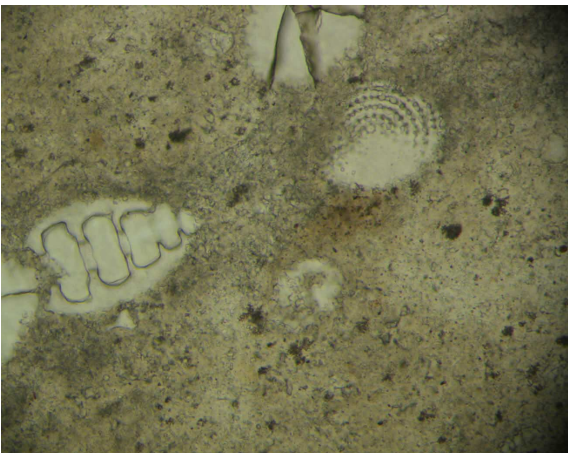
500 μm

B



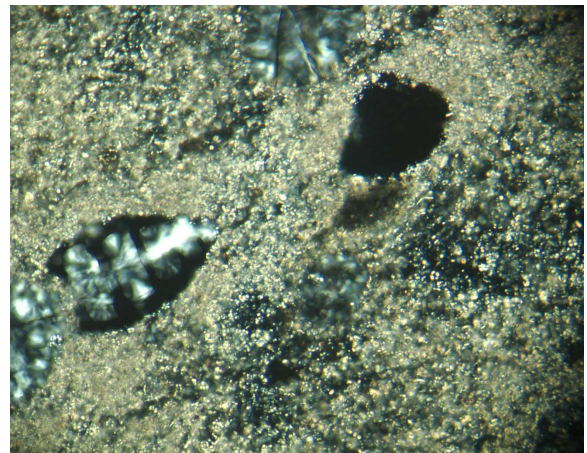
40 μm

C



40 μm

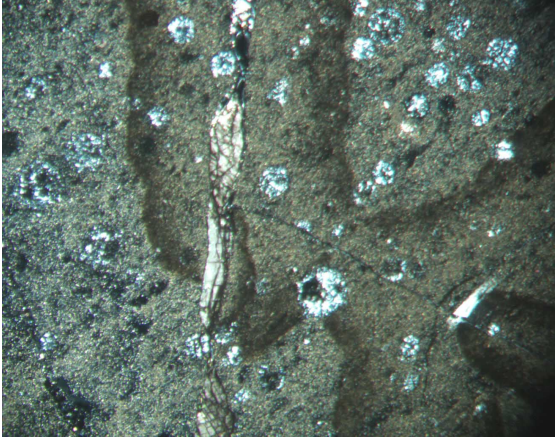
D



40 μm

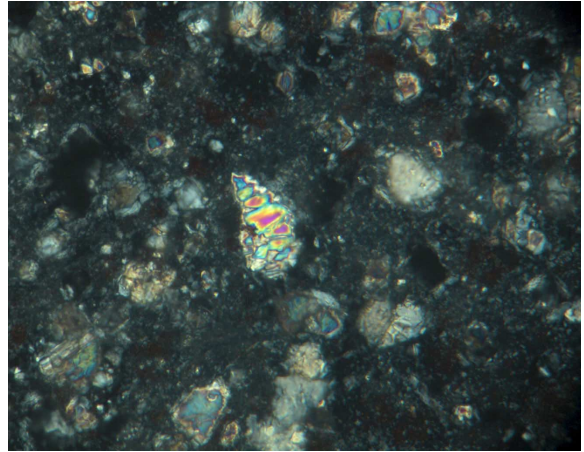
Figure F25 (continued). E. Calcite-filled vein intersecting thin, dark chalcedony vein. Note the halo associated with vein filling. Taken under cross-polarized light. F. Radiolarian from deeper in lithologic Unit IV (interval 185-1149B-20R-1, 52–55 cm; 321.5 mbsf) that has undergone complete recrystallization to calcite. Image taken under cross-polarized light.

E



500 μm

F



40 μm

Figure F26. X-ray diffractogram traces of samples from lithologic Unit IV. Clay = nonbasal clay mineral reflection; Qz = quartz; CT = opal-CT; and Cc = calcite. Samples are from background carbonate sediments. Diffractograms from the other major lithology of Unit IV, which is chert and porcelanite, are not shown here. Note presence of opal-CT along with quartz and calcite in Sample 185-1149B-18R-1, 9–11 cm. Also note that individual diffractograms are offset vertically for clarity.

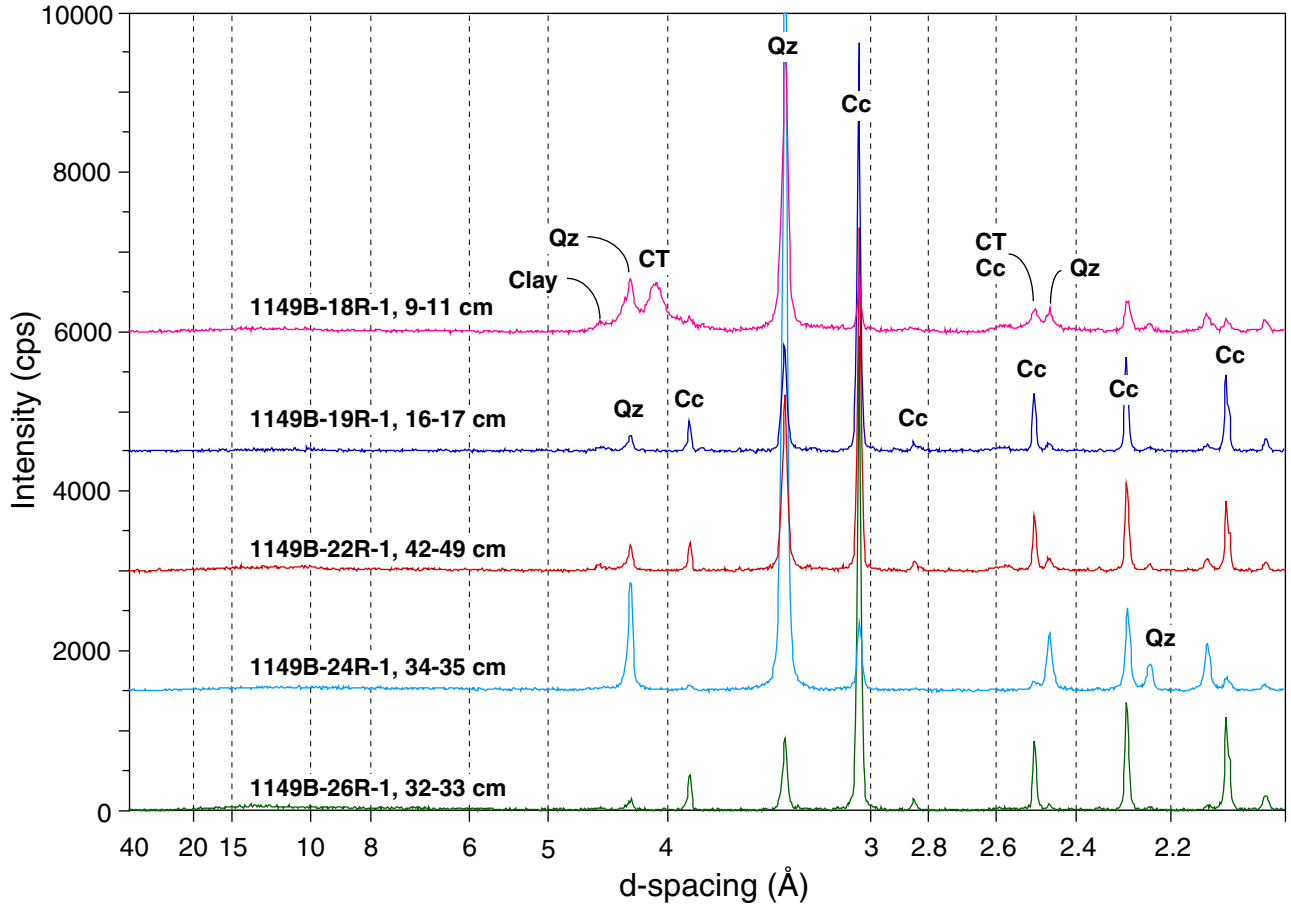


Figure F27. Wavy, discontinuous lamination in radiolarian-bearing marlstone of lithologic Unit IV. Dark interval is enriched in barite, dolomite, and phosphatic fish remains (interval 185-1149B-19R-1, 13–25 cm).

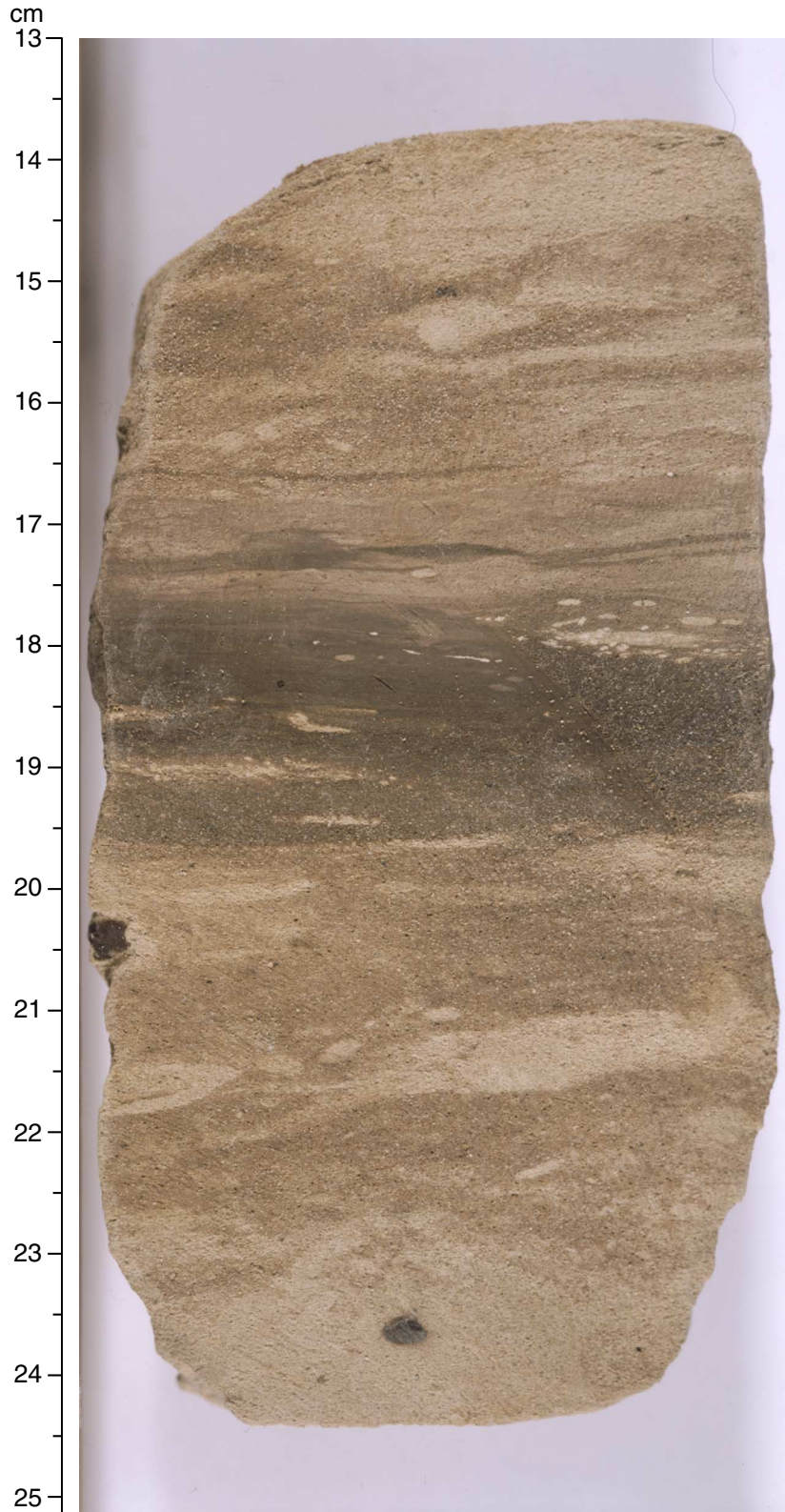


Figure F28. Chert pieces with “swiss cheese” type lenses of less indurated, partly calcareous material (interval 185-1149B-25R-1, 0–29 cm).



Figure F29. Color changes in crudely laminated radiolarian-bearing chalks from the base of lithologic Unit IV (Sample 185-1149C-8R-1, 46–62 cm).

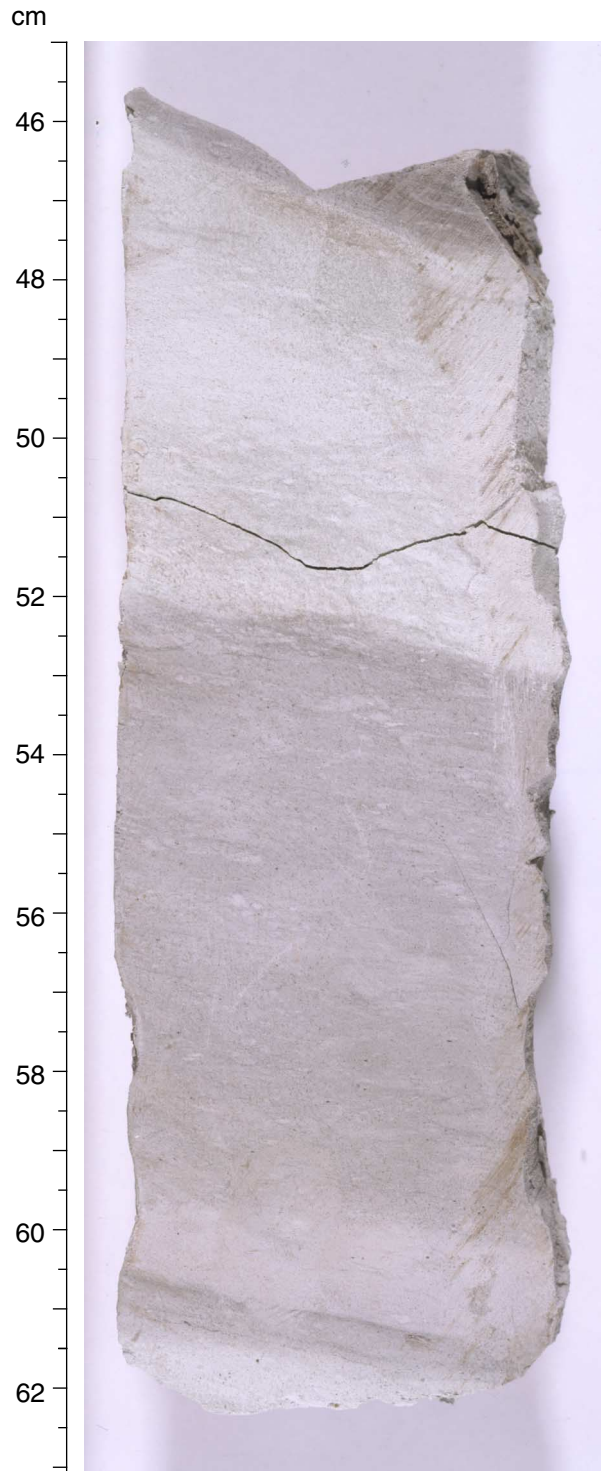


Figure F30. Crudely laminated radiolarian-bearing chalks and calcareous marls with dissolution seams in the more indurated, carbonate-rich intervals. A. Interval 185-1149B-19R-1, 28–33 cm. (Continued on next two pages.)

A



Figure F30 (continued). B. Interval 185-1149B-19R-1, 122–131 cm. Note textural artifact from drying bubbles and fingerprints.

B cm

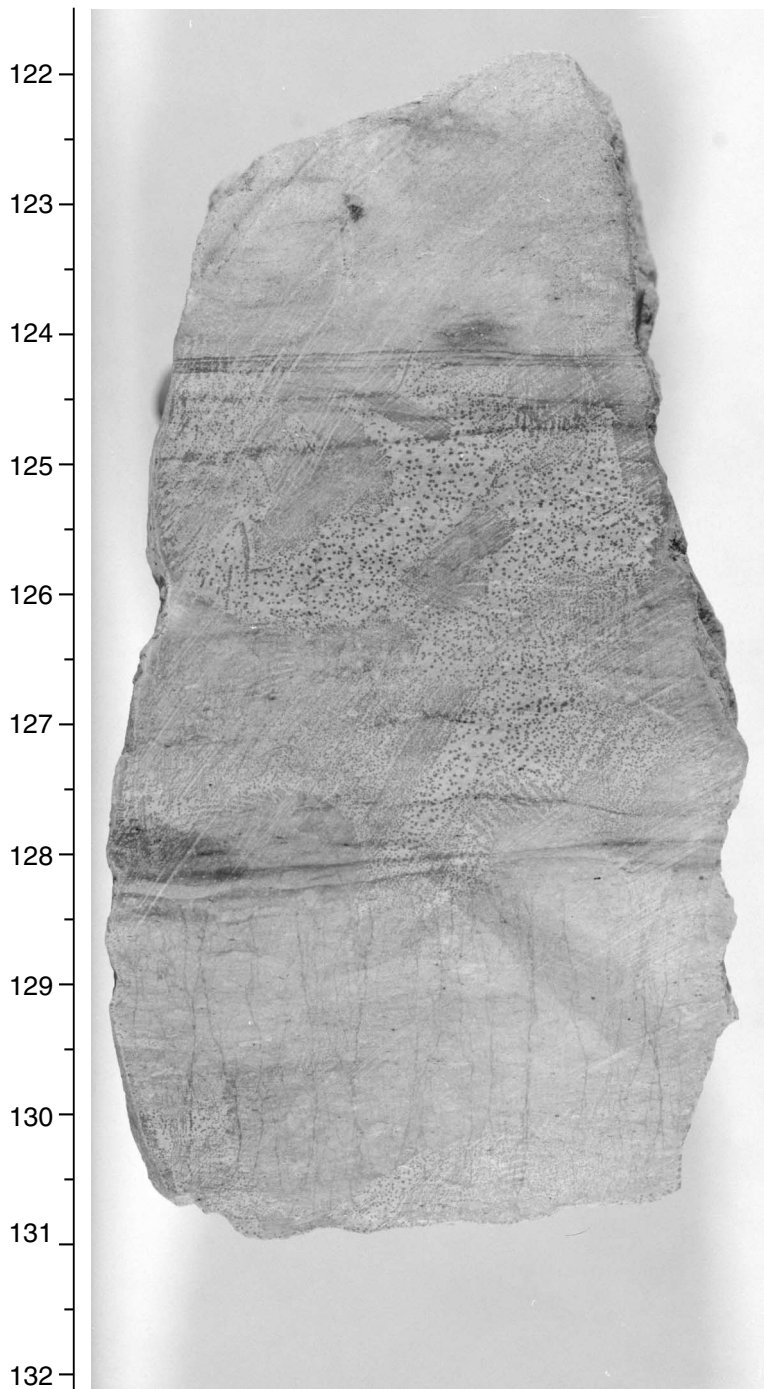


Figure F30 (continued). C. Interval 185-1149B-27R-1, 13–30 cm.

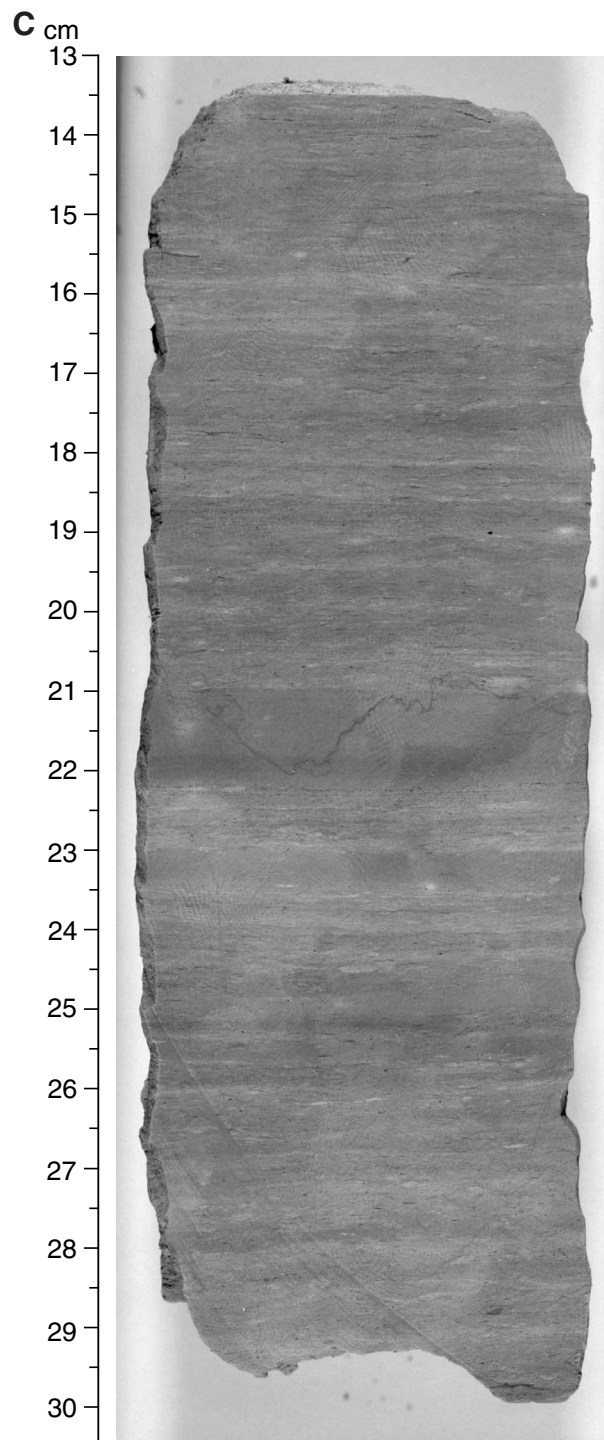


Figure F31. X-ray diffractogram traces of samples from lithologic Units IV and V. Cc = calcite; Qz = quartz; Hal = halite; Sme = smectite; Clay = nonbasal clay mineral reflection; and Fsp = feldspar. Samples are from background carbonate sediments. Diffractograms from the other major lithology of Unit IV, which is chert and porcelanite, are not shown here. Note that individual diffractograms are offset vertically for clarity.

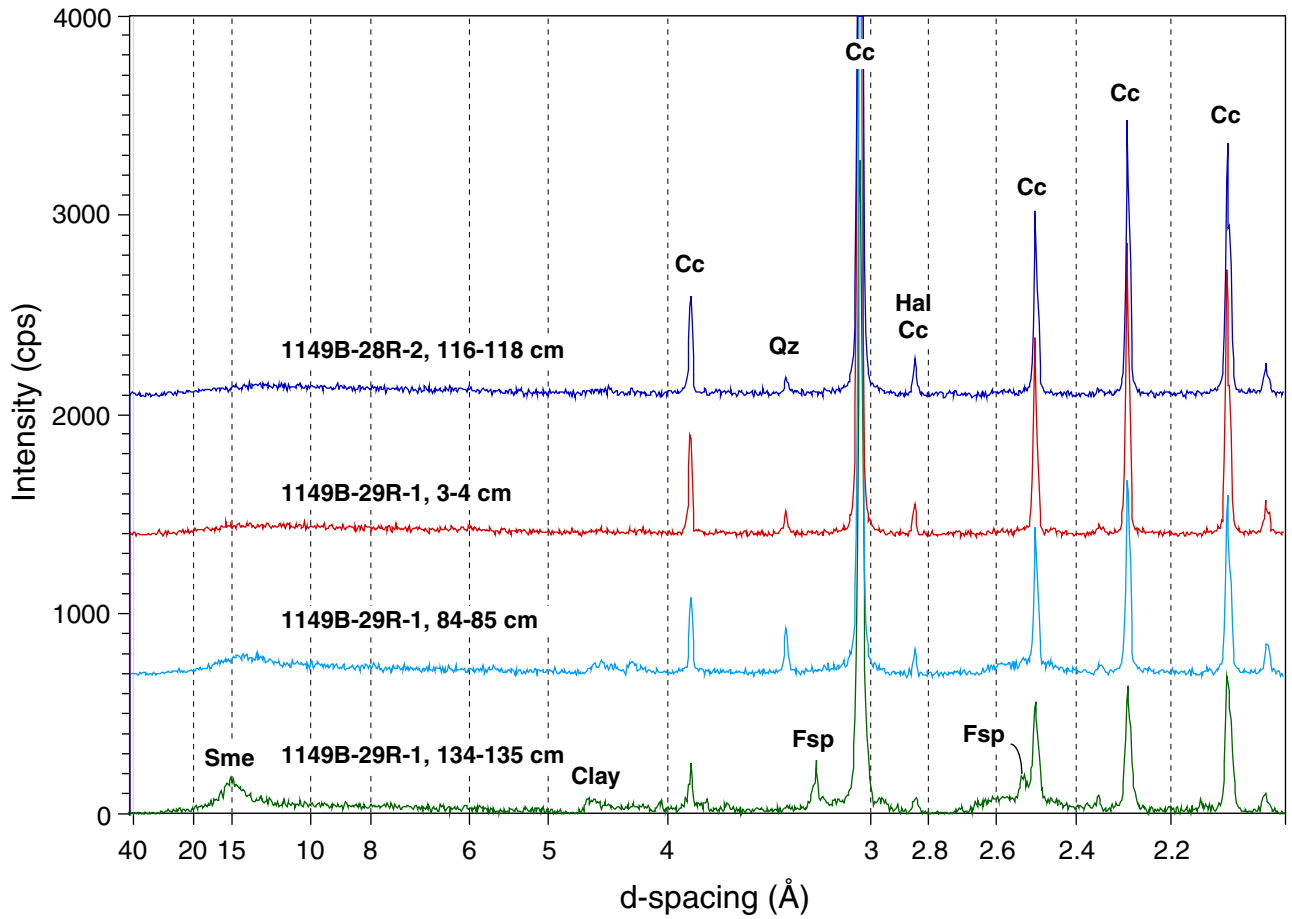


Figure F32. Basement stratigraphy and unit boundaries. Depths are in meters below seafloor to the top of each core. Where subunits or cooling units are present, they are represented by a line and/or a change in lithology in the lithology/structure column. All data used to compile this figure are included in Table T5, p. 160. A. Hole 1149B. B. Hole 1149C. (Continued on next two pages.)

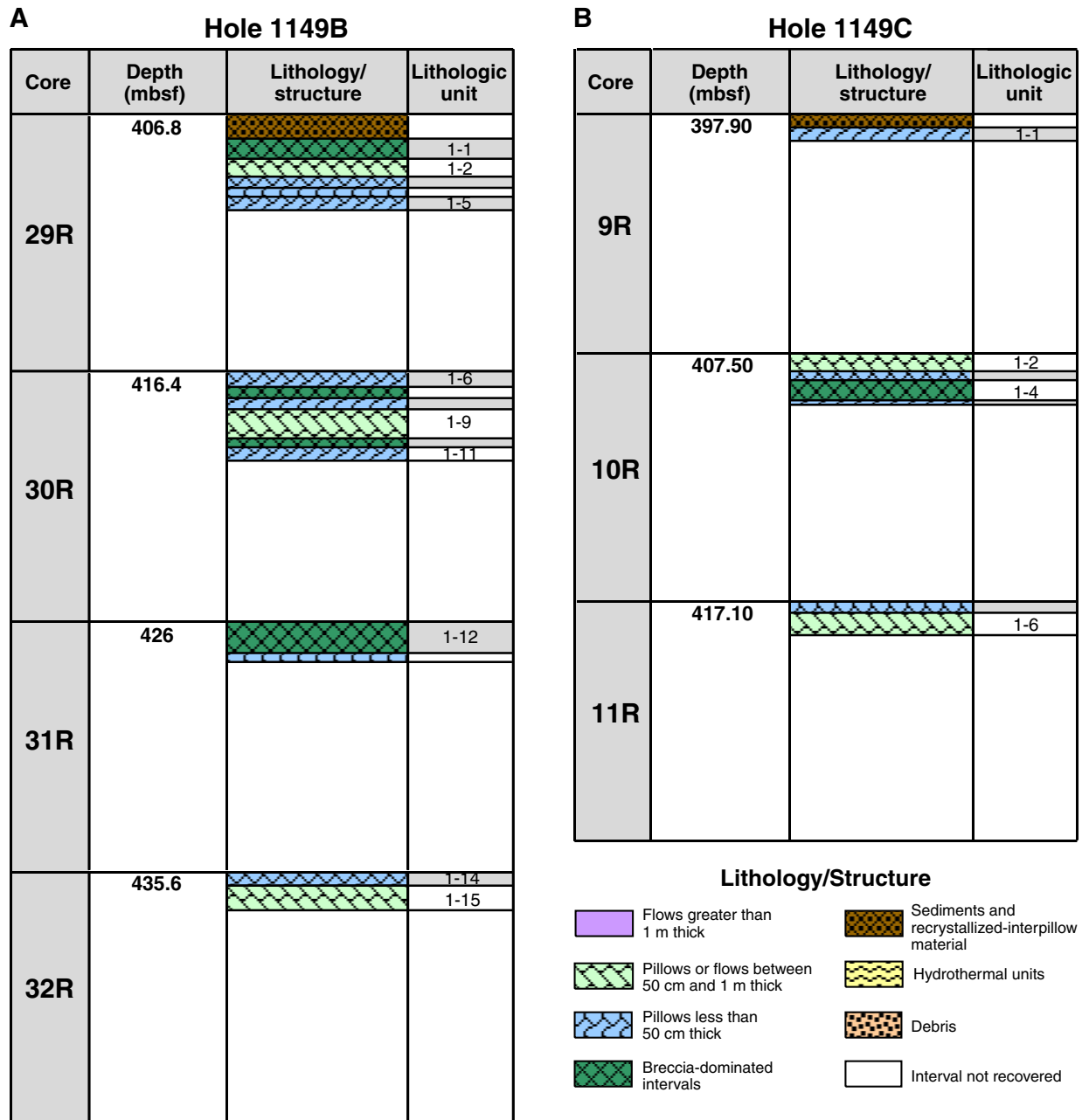


Figure F32 (continued). C. Hole 1149D.

C **Hole 1149D**







Core	Depth (mbsf)	Lithology/structure	Lithologic unit
5R	300.30		
6R	310.00		2-1
7R	319.70		2-6
			2-8
			2-9
8R	329.30		2-10
			3-2
			3-3
			3-4

Hole 1149D

Core	Depth (mbsf)	Lithology/structure	Lithologic unit
9R	338.80		3-8
			3-9
			3-10
			3-11
10R	348.40		3-13
			3-16
11R	357.90		4-1
			4-2
			4-3
12R	367.40		4-5
	377.00		4-6
			4-8

Figure F32 (continued).

Hole 1149D

Core	Depth (mbsf)	Lithology/structure	Lithologic unit
13R			
	386.60		
14R			
	396.3		5-5
15R			
	405.9	 	5-6 5-7
16R			
	415.50	 	5-8 6-1

Hole 1149D




Core	Depth (mbsf)	Lithology/structure	Lithologic unit
17R			
	425.10		6-3
18R			
	434.70	 	6-5 6-6
19R			

Figure F33. Chilled pillow rims with crystalline interpillow material (interval 185-1149B-30R-2, 106–125 cm).

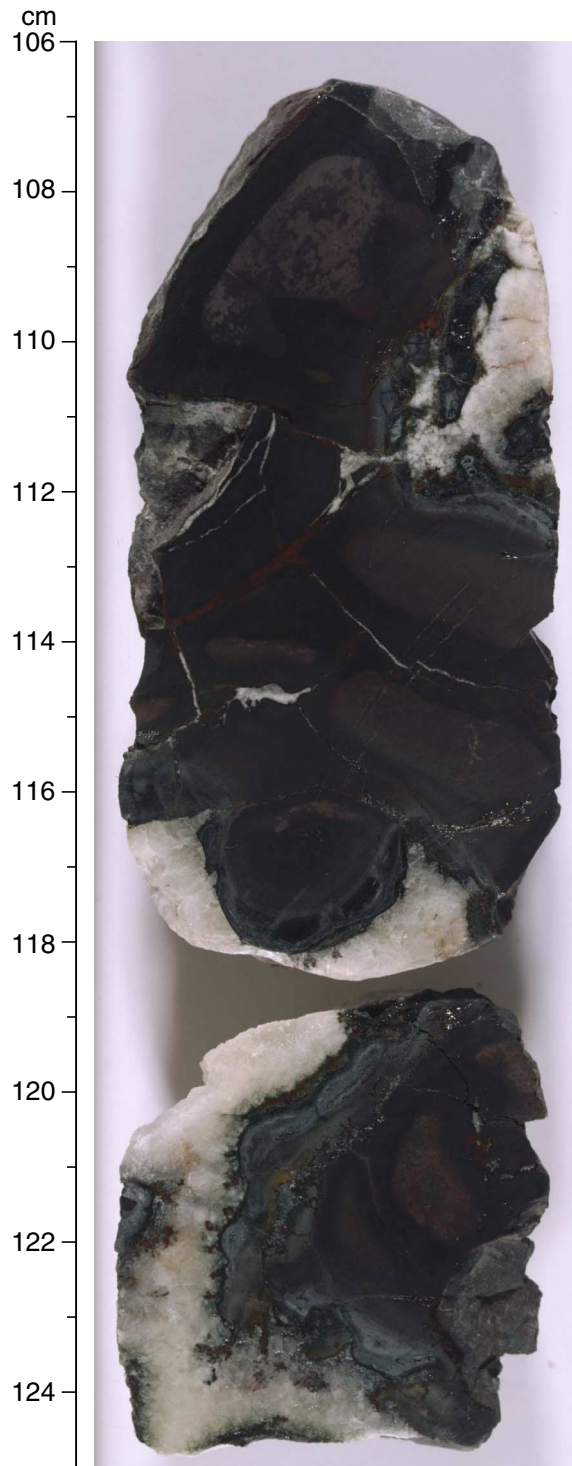


Figure F34. Altered chilled pillow rim (interval 185-1149B-31R-1, 25–38 cm).

cm

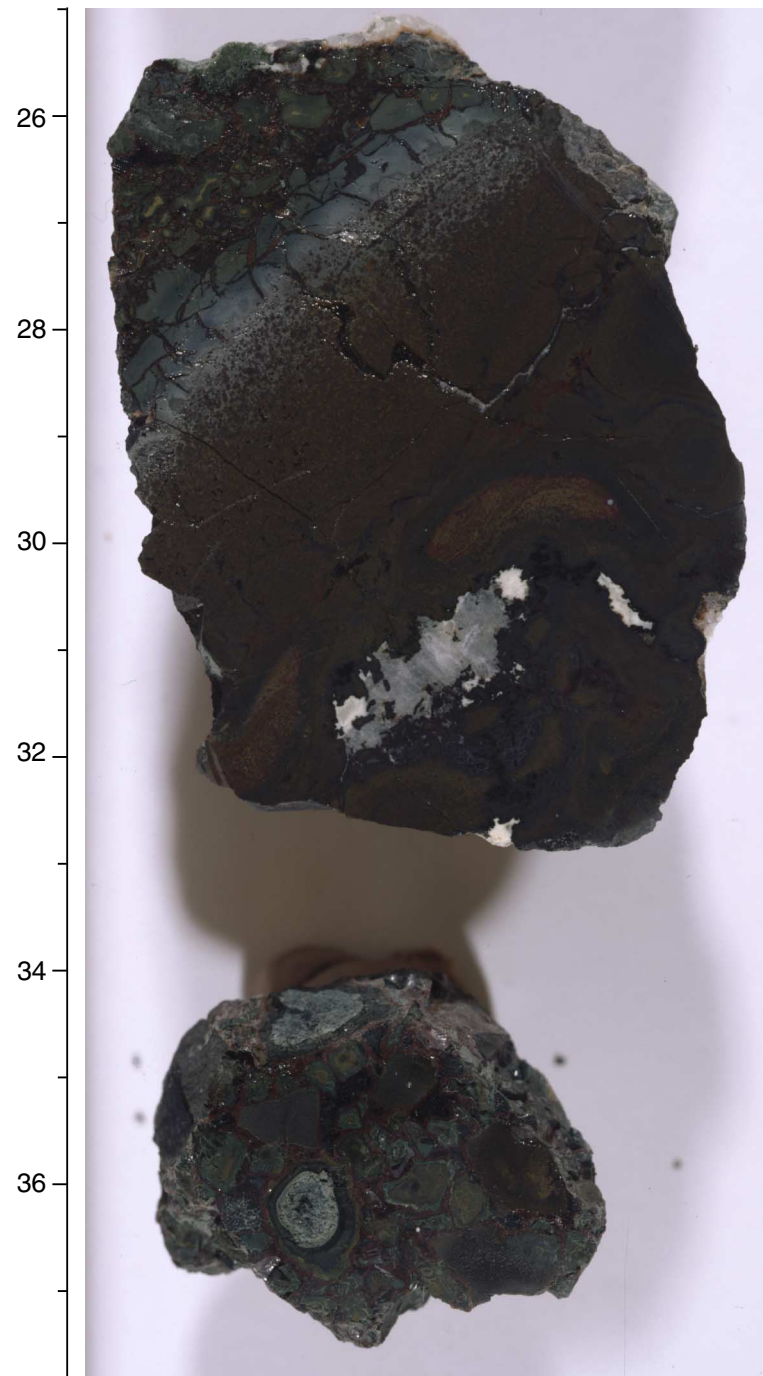


Figure F35. Brecciated basalt from Hole 1149B. Breccia consists of angular basalt pieces and medium-grained calcite cement (interval 185-1149B-30R-1, 56–86 cm).

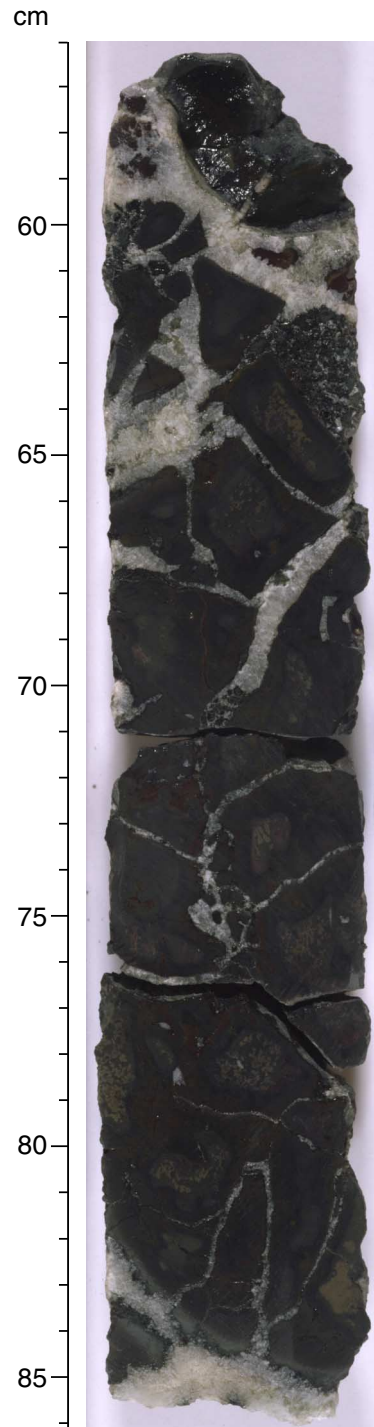


Figure F36. Brecciated basalt from Hole 1149C. The breccia consists of angular basalt pieces and medium-grained calcite cement (interval 185-1149C-10R-1, 107–121 cm).



Figure F37. Brecciated basalt from Hole 1149D. Breccia consists of angular basalt pieces and medium-grained calcite cement. However, this interval also contains a microbreccia with basalt clasts all <1 cm in diameter (interval 185-1149D-11R-2, 103–119 cm).



Figure F38. Hyaloclastite from Hole 1149D. Angular and elongate altered glassy shards in a green clay cement, with some carbonate present (interval 185-1149D-7R-1, 29–62 cm).



Figure F39. Hyaloclastite from Hole 1149D (interval 185-1149D-13R-1, 3–25 cm).

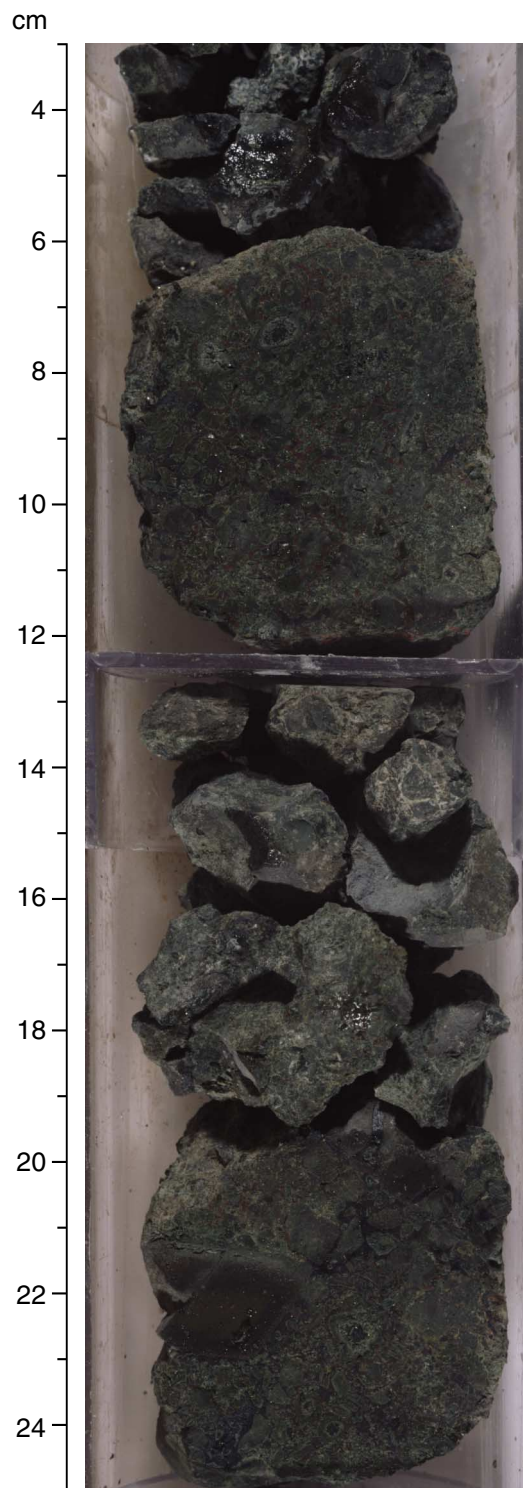


Figure F40. Pillow rim or flow margin and interpillow material from Hole 1149D (interval 185-1149D-8R-2, 14–30 cm).

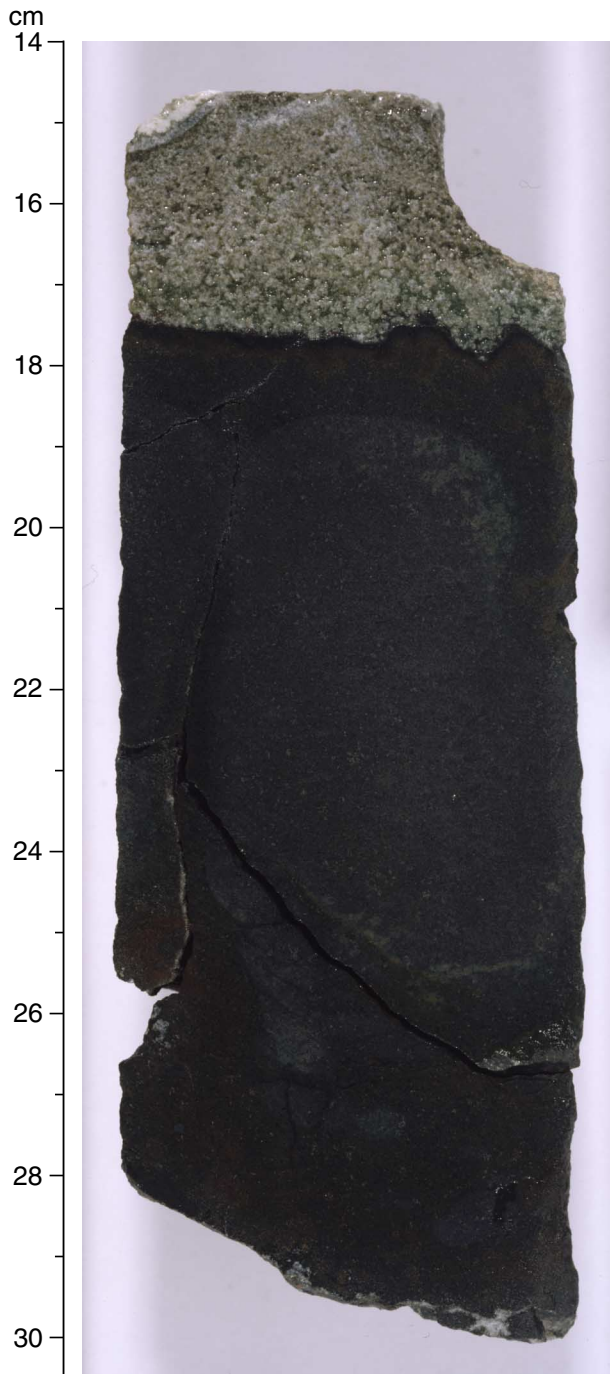


Figure F41. Typical groundmass of the basalts. Skeletal, subhedral plagioclase laths are the major component. Anhedral pyroxenes, magnetite, and interstitial materials are present in between. Thin-section number 95; plane-polarized light; magnification = 200 \times ; and field of view = 0.5 mm.

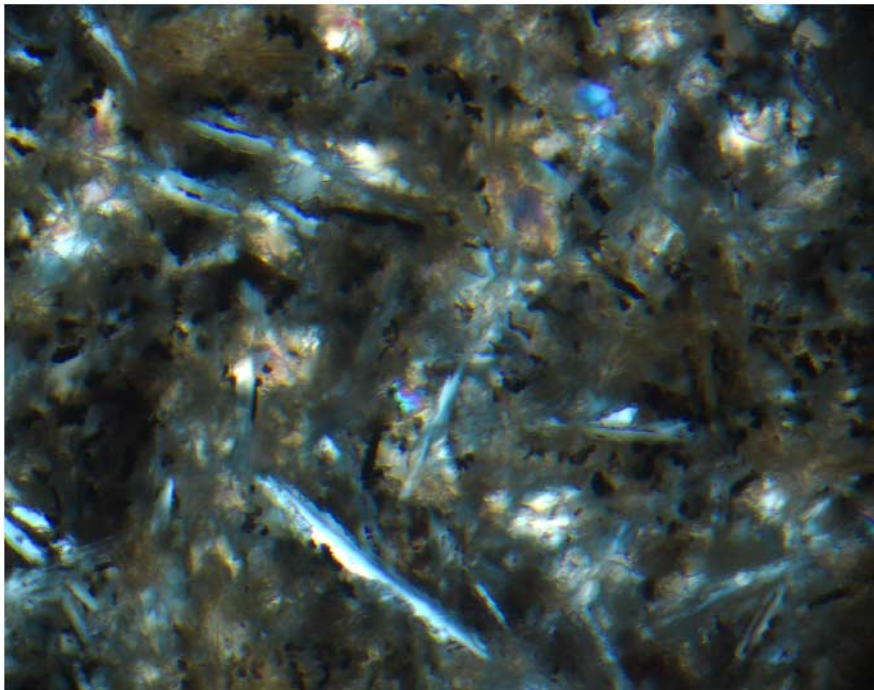
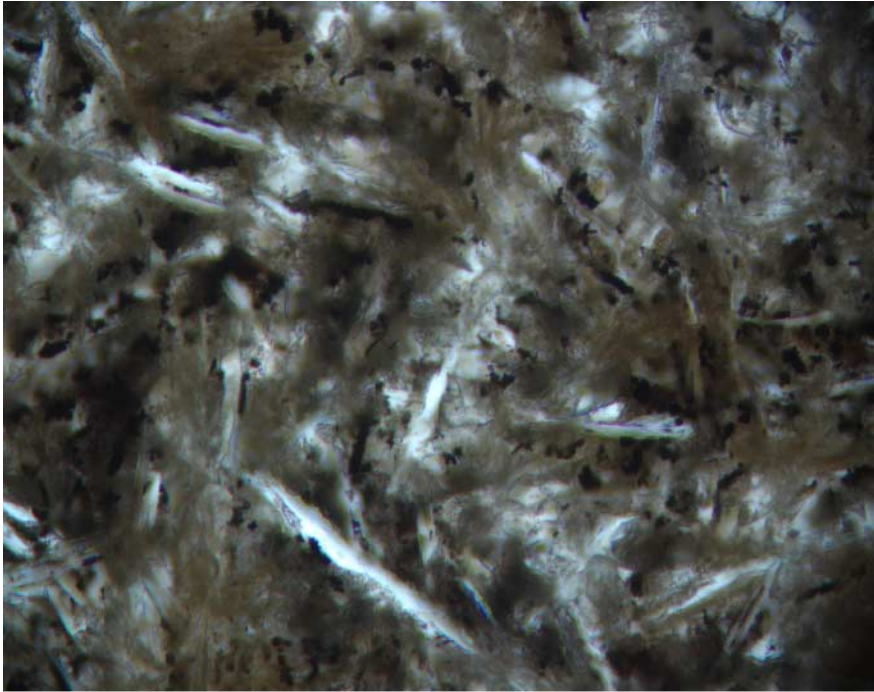


Figure F42. Maximum and average phenocryst size vs. depth. E-MORB = enriched-mid-ocean-ridge basalt.

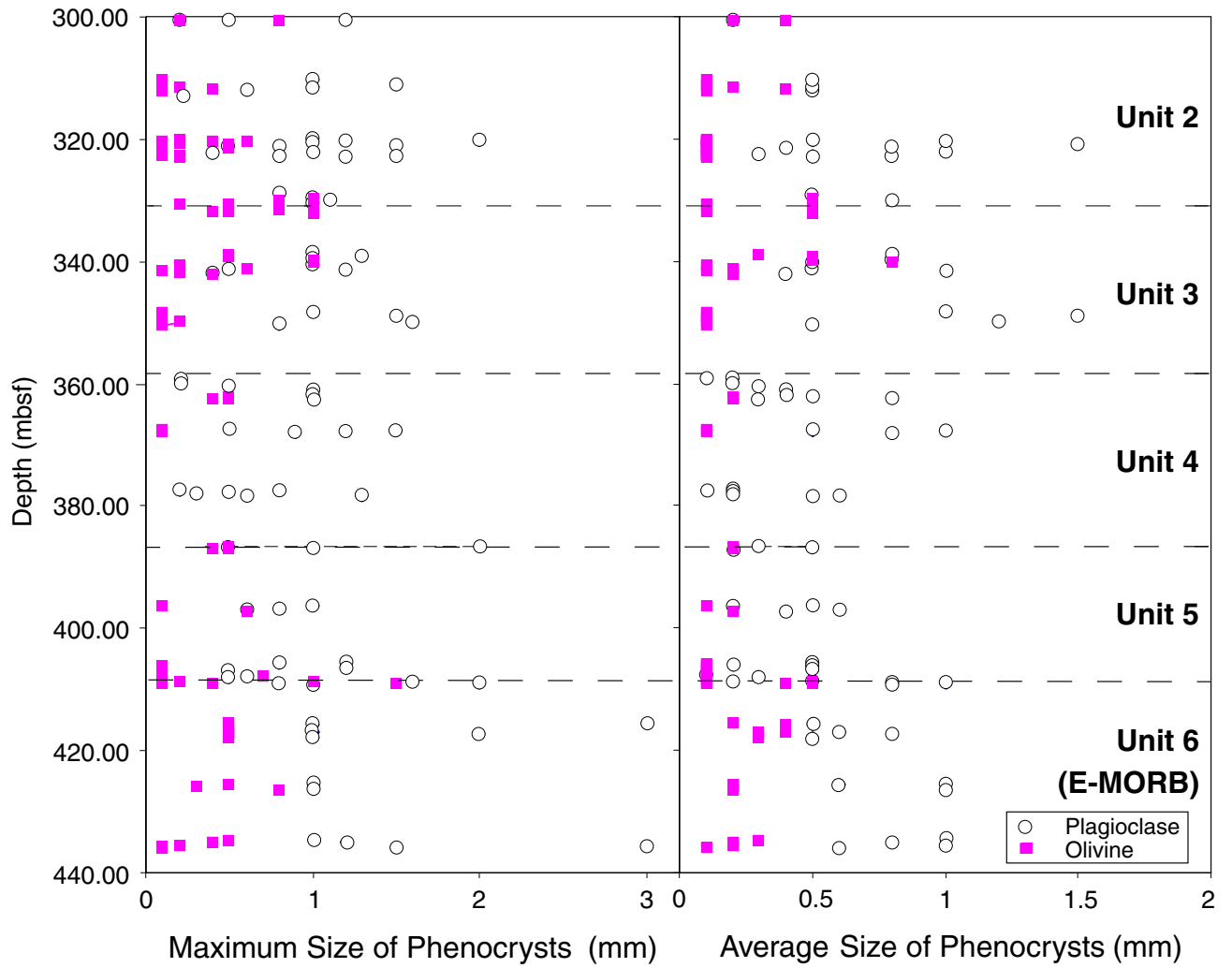


Figure F43. Euhedral plagioclase and olivine phenocrysts in a glassy pillow rim (Sample 185-1149C-11R-1 (Piece 3, 43–45 cm). Plane-polarized light; magnification = 200 \times ; and field of view = 0.5 mm.

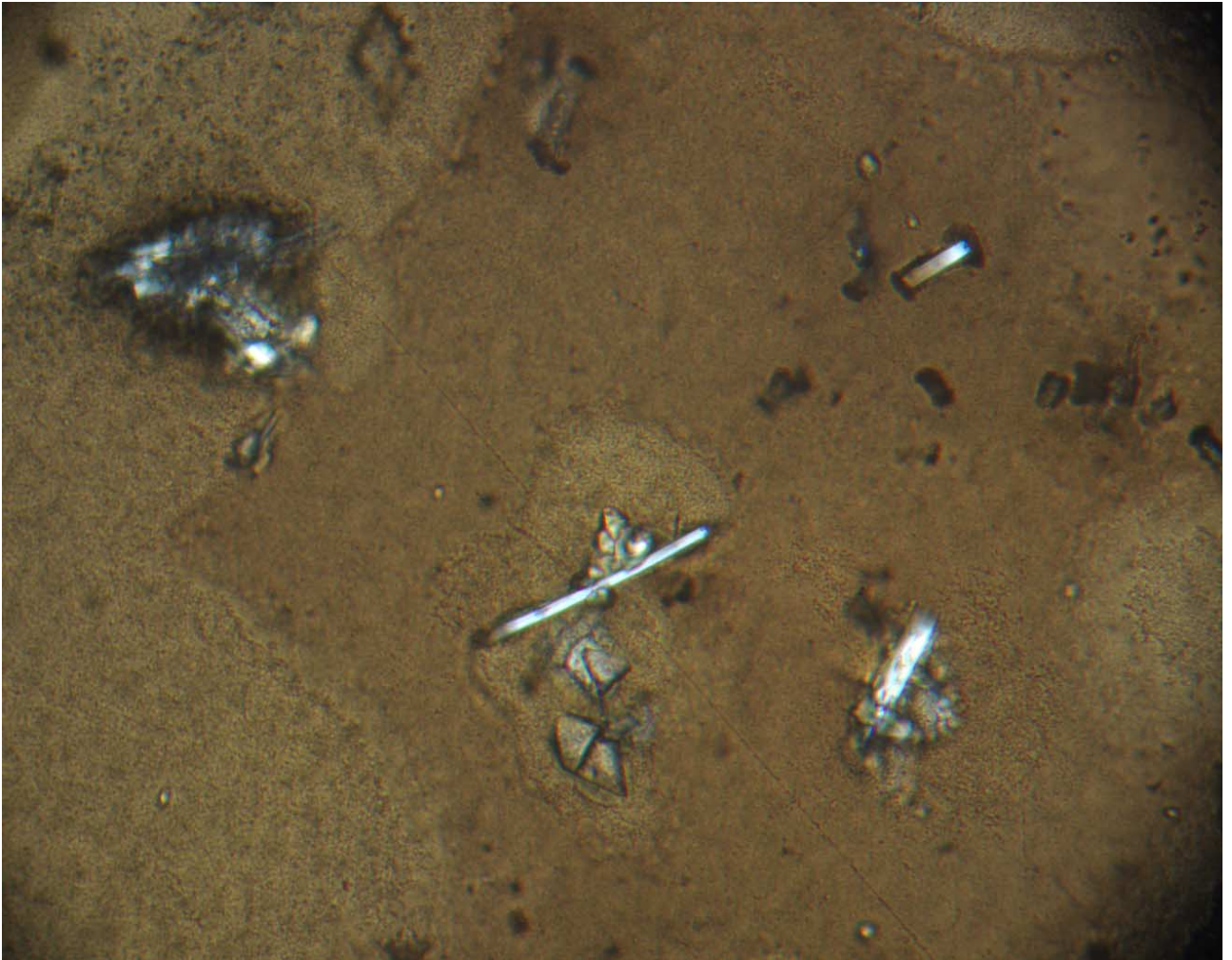
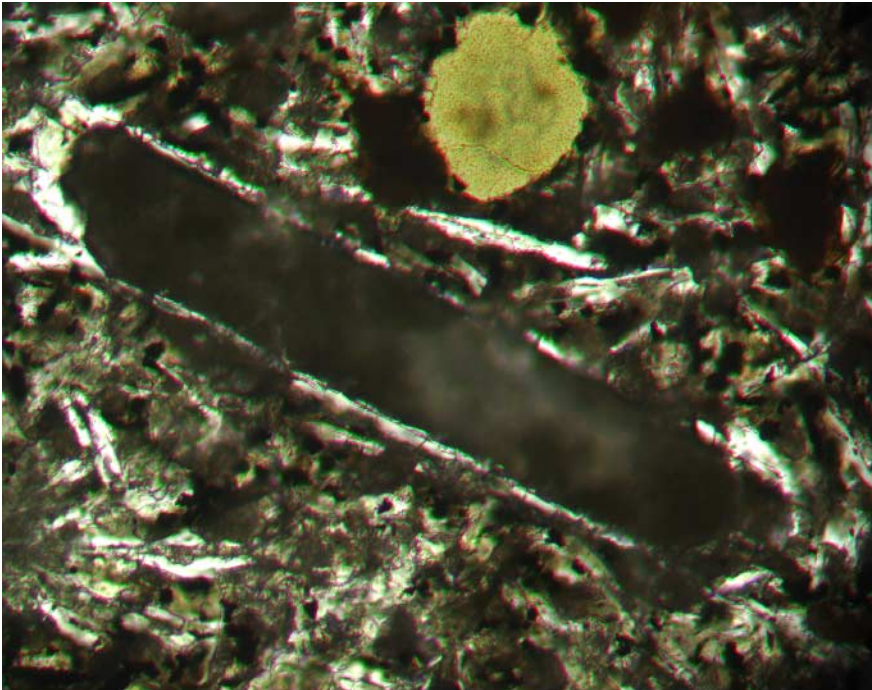


Figure F44. Altered plagioclase phenocrysts. The interior of the lath-shaped plagioclase is completely altered to smectite. Plane-polarized light; magnification = 200 \times ; and field of view = 0.5 mm. A. Thin section 92. B. Thin section 95.

A



B

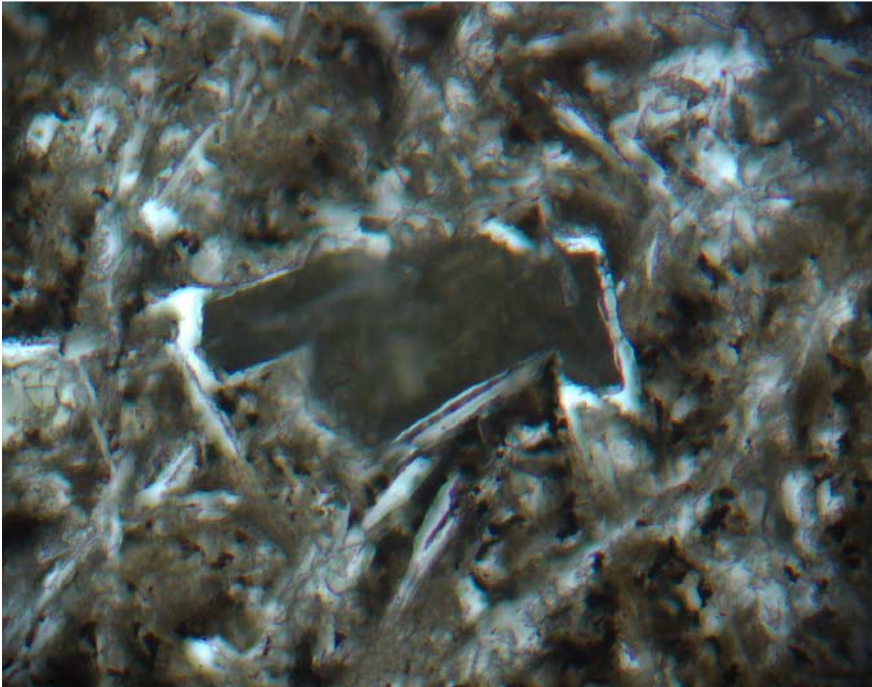


Figure F45. Altered euhedral olivine phenocryst in Sample 185-1149B-29R-2 (Piece 2, 27–32 cm). Plane-polarized light; magnification = 200×; and field of view = 0.5 mm.

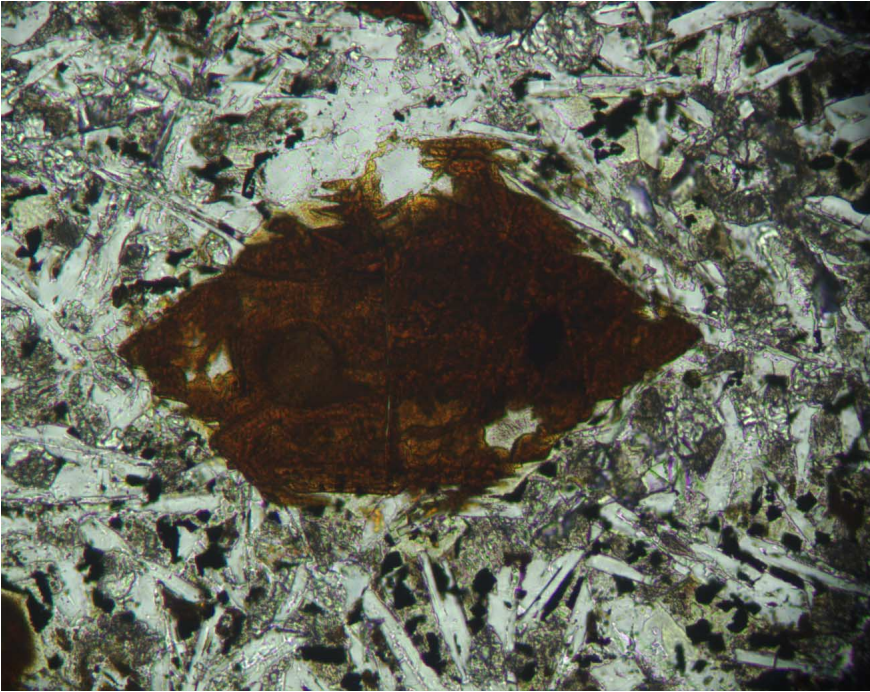


Figure F46. A. MgO vs. Fe₂O₃, and B. Zr vs. Y for Site 1149 and Site 801 tholeiitic lavas. Solid (black) circles = Site 1149 basalts; open (blue) circles = Hole 801C tholeiites; and crosses (red) = data from modern East Pacific Rise (Langmuir, et al., 1986). EPR = East Pacific Ridge.

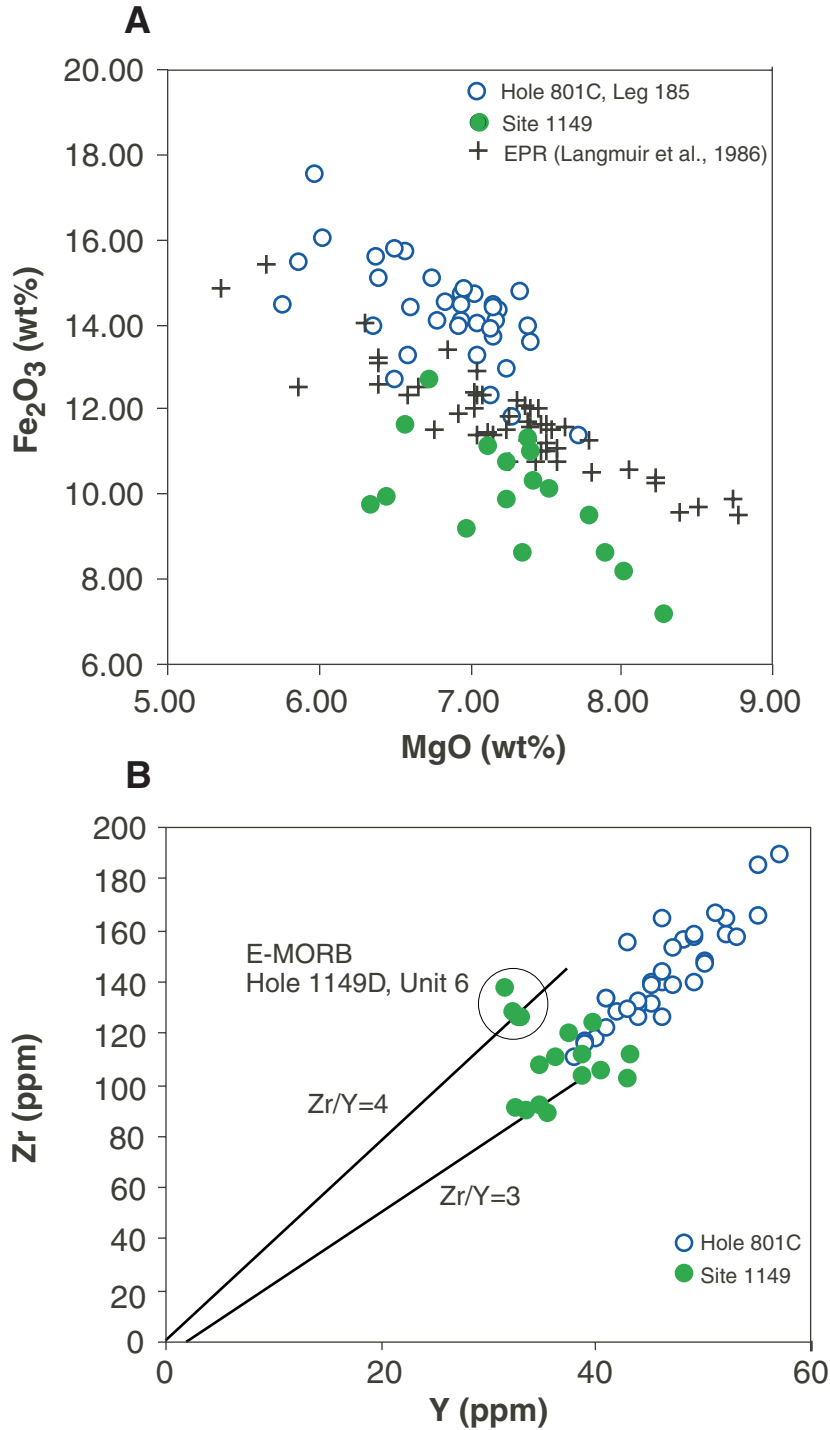
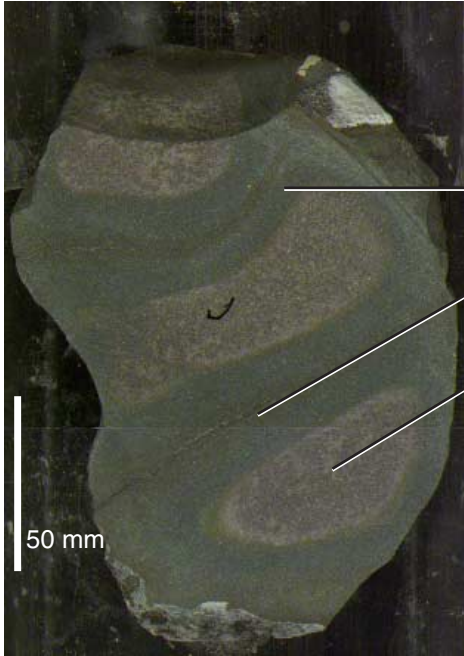


Figure F47. Variation in intensity of alteration between typical basalt and fine-grained, chilled volcanic eruption breccia. **A.** Typical basalt consists of internal kernels of dusky red with some light brown-gray mottling. These are surrounded by dark halos (green) and a brown-orange halo adjacent to the vein. **B.** In the brecciated rock the alteration is much more chaotic. The intense fracturing facilitated the more intense and pervasive development of dark alteration halos.

A



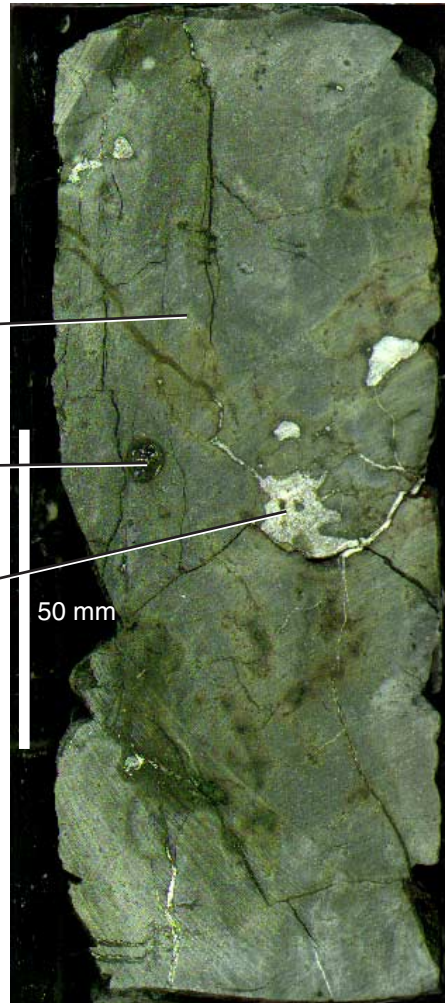
Sample 185-1149B-29R-1, Piece 1

Dark halo (green) comprised of celadonic phyllosilicates

Brown halos comprised of goethite + iddingsite

Dusky red core regions with light brown mottling

B



Sample 185-1149D-11R-1, Piece 10

Core dominated by complex overprinting halos; the dusky red coloration is very limited.

Large smectite- and calcite-filled vesicles

Irregular voids infilled with late calcite. These voids have associated veins.

Figure F48. Abundance and distribution of veins, breccia, and alteration halos. Dk halos = dark green halos; dk + br = mixed dark green and brown halos.

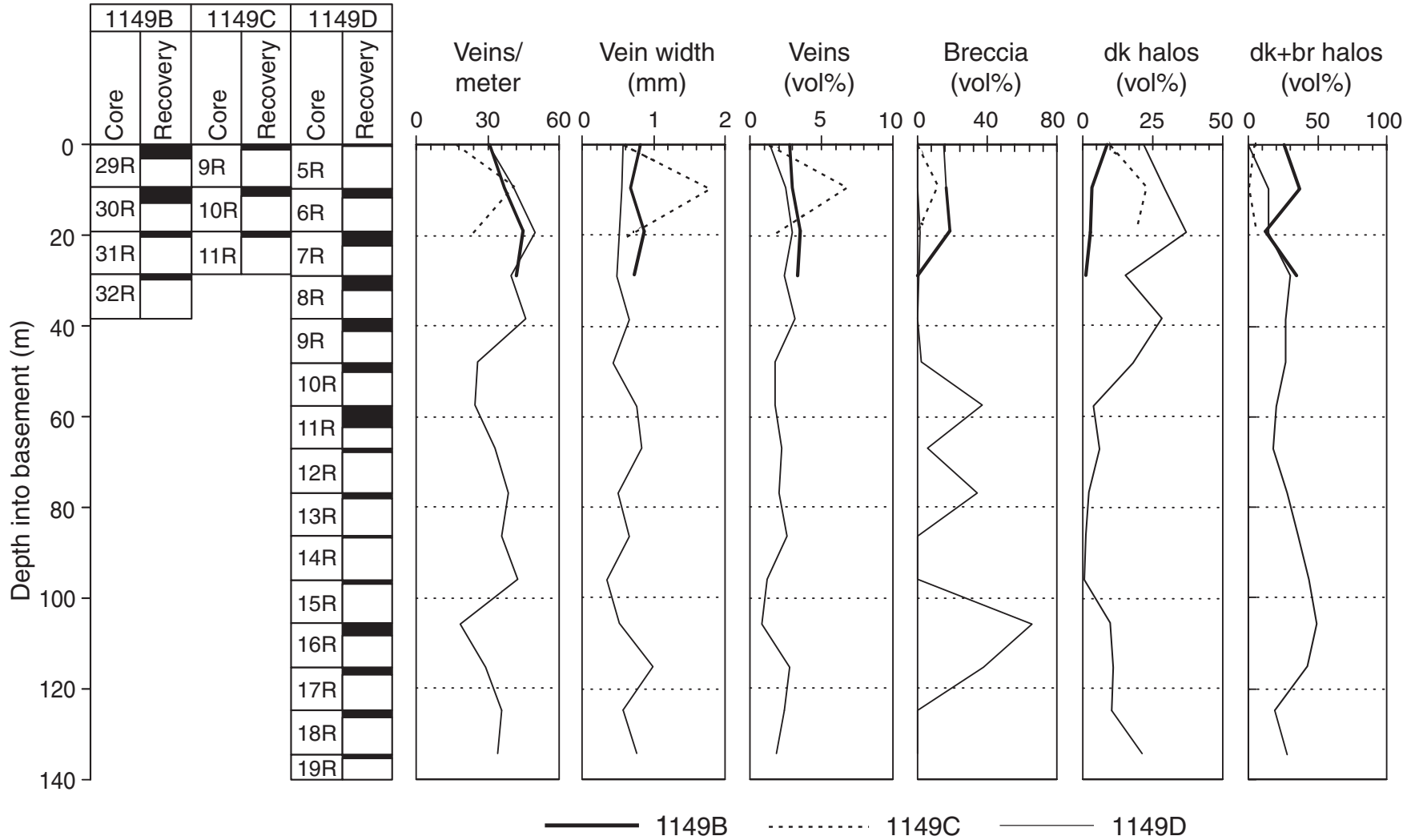


Figure F49. Compositions of veins and proportions of saponite and carbonate per core.

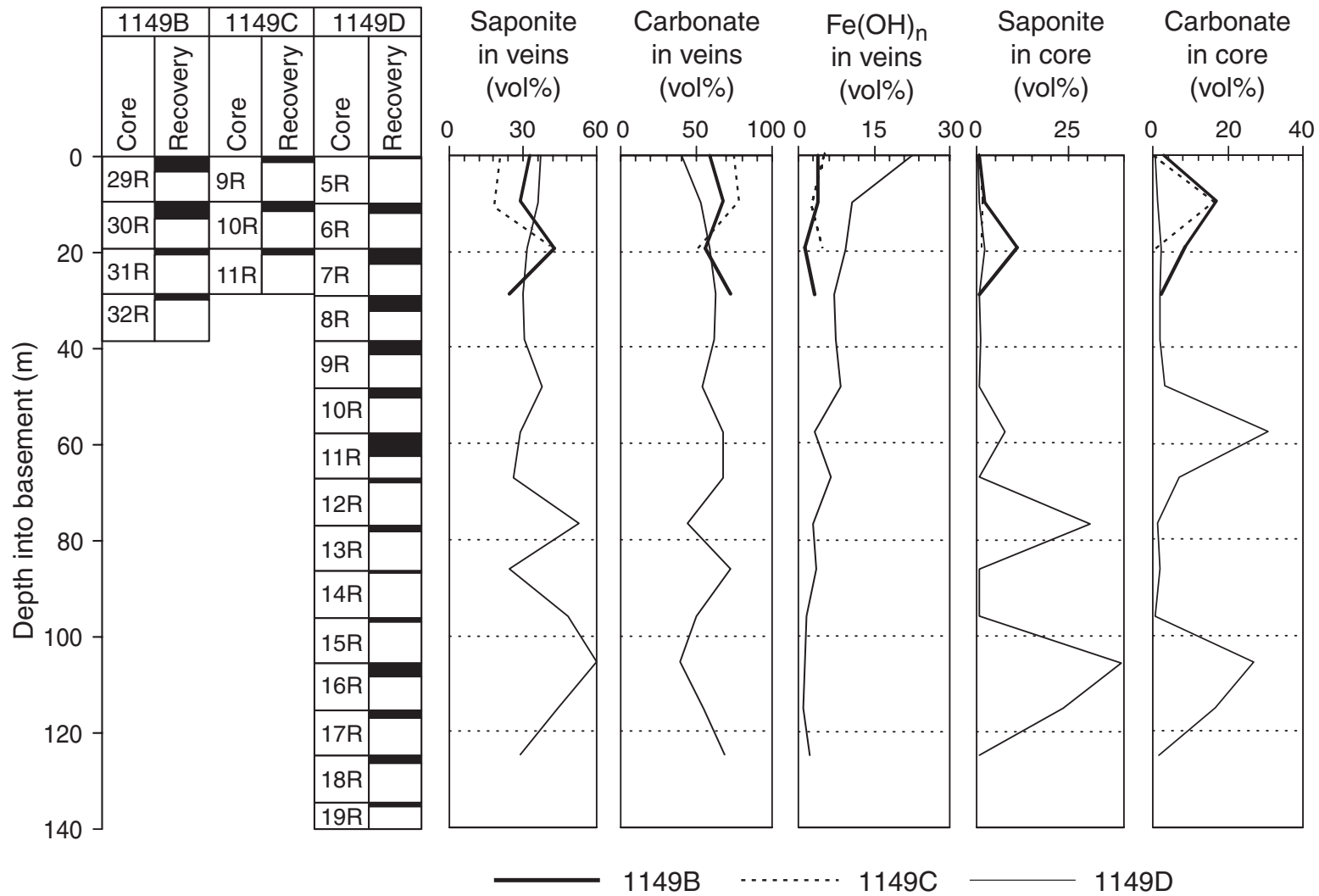


Figure F50. Concentration profiles of alkalinity, dissolved NH_4^+ , and PO_4^{3-} at Site 1149. Open circles = Hole 1149A; solid circles = Hole 1149B. Lithostratigraphic units and subunits are as defined in "Lithostratigraphy," p. 11. Shaded regions indicate the position of the suggested clay alteration zone of Subunits IIA and IIB.

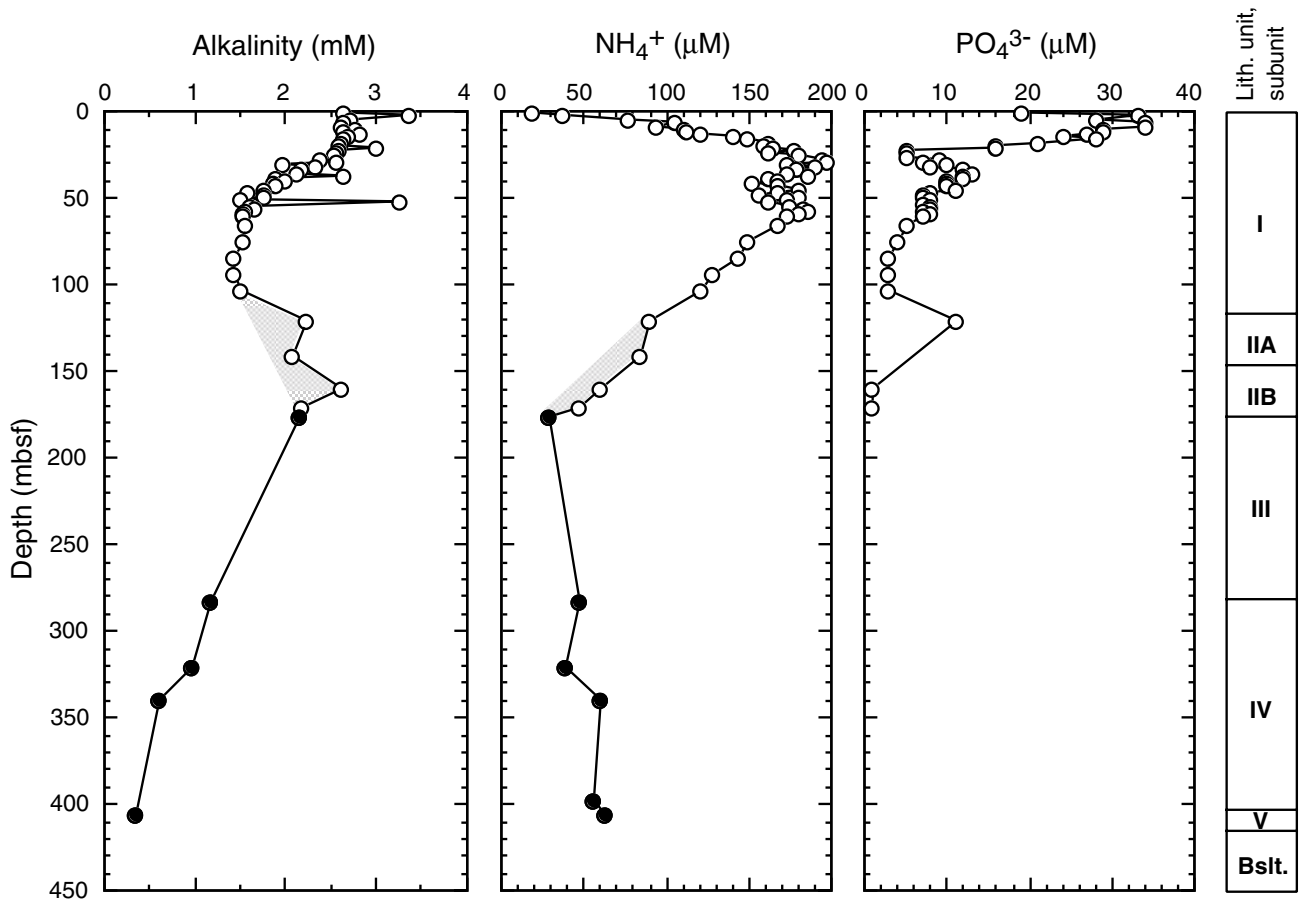


Figure F51. Concentration profiles of dissolved SO_4^{2-} , Mn^{2+} , and Fe^{2+} at Site 1149. Open circles = Hole 1149A; solid circles = Hole 1149B. Lithologic units and subunits are defined in "Lithostratigraphy," p. 11.

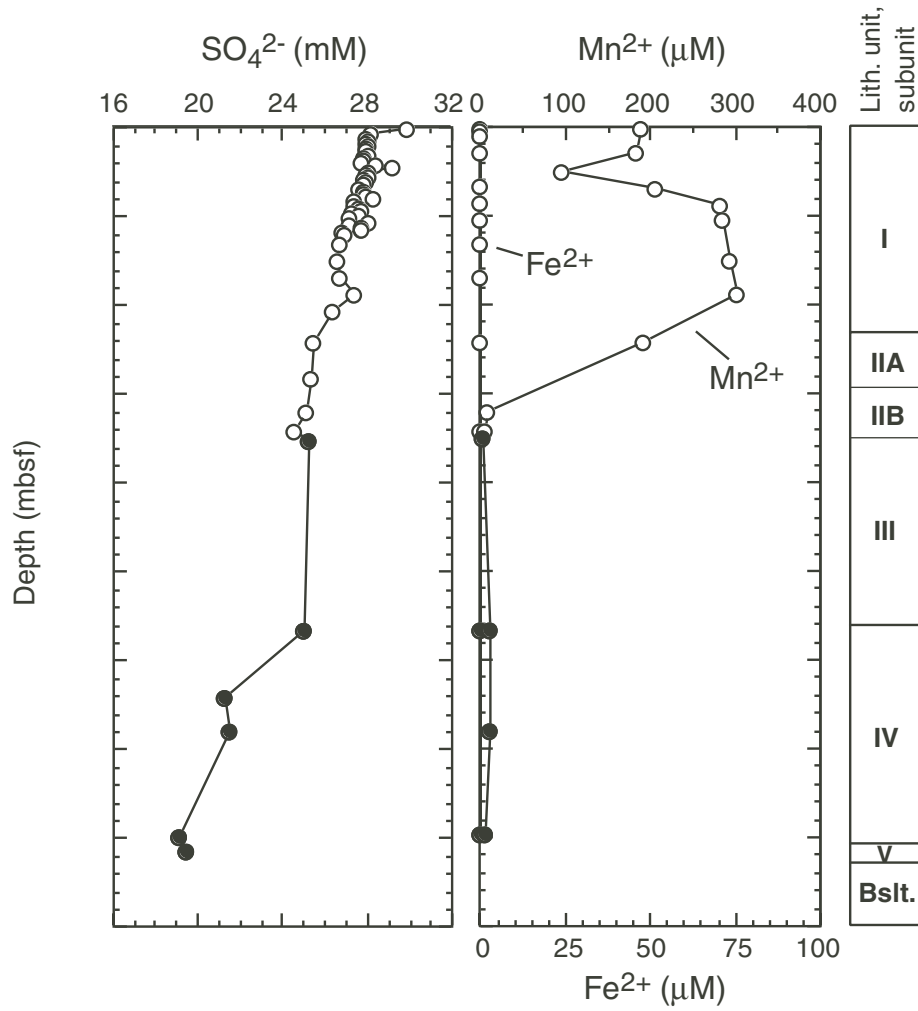


Figure F52. Concentration profiles of dissolved silica and Sr²⁺ at Site 1149. Open circles = Hole 1149A; solid circles = Hole 1149B. Lithostratigraphic units and subunits are as defined in "Lithostratigraphy," p. 11. Shaded regions indicate the position of the suggested clay alteration zone of Subunits IIA and IIB. Inset in the right-hand panel shows the 0–200 mbsf portion at an expanded concentration scale. "A/CT" and "CT/Qz" indicate positions of first and last occurrence of opal-CT (also see "Unit III," p. 14, and "Unit IV," p. 15). Arrows indicate average concentrations in seawater (Millero and Sohn, 1992) (for silica this value is the highest of a given range).

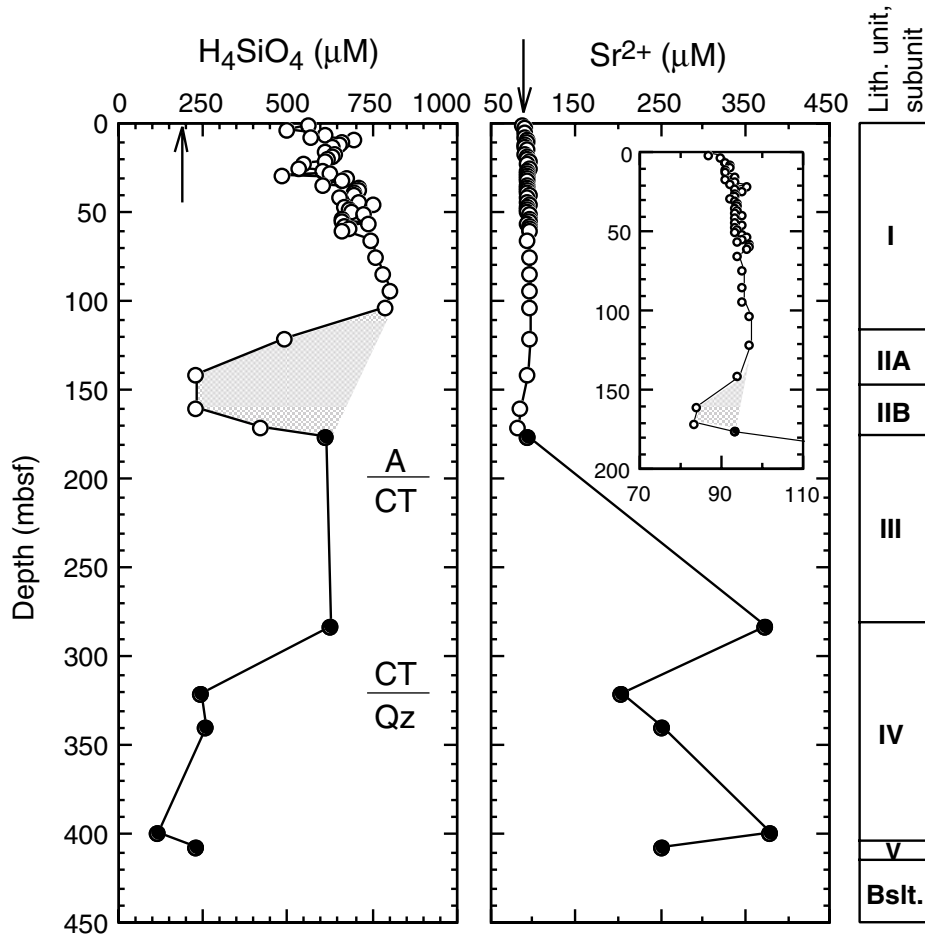


Figure F53. Concentration profiles of dissolved Na^+ , K^+ , and Li^+ at Site 1149. Open circles = Hole 1149A; solid circles = Hole 1149B. Lithostratigraphic units and subunits are as defined in "Lithostratigraphy," p. 11. Shaded regions indicate the position of the suggested clay alteration zone of Subunits IIA and IIB. Arrows indicate average concentrations in seawater (Millero and Sohn, 1992).

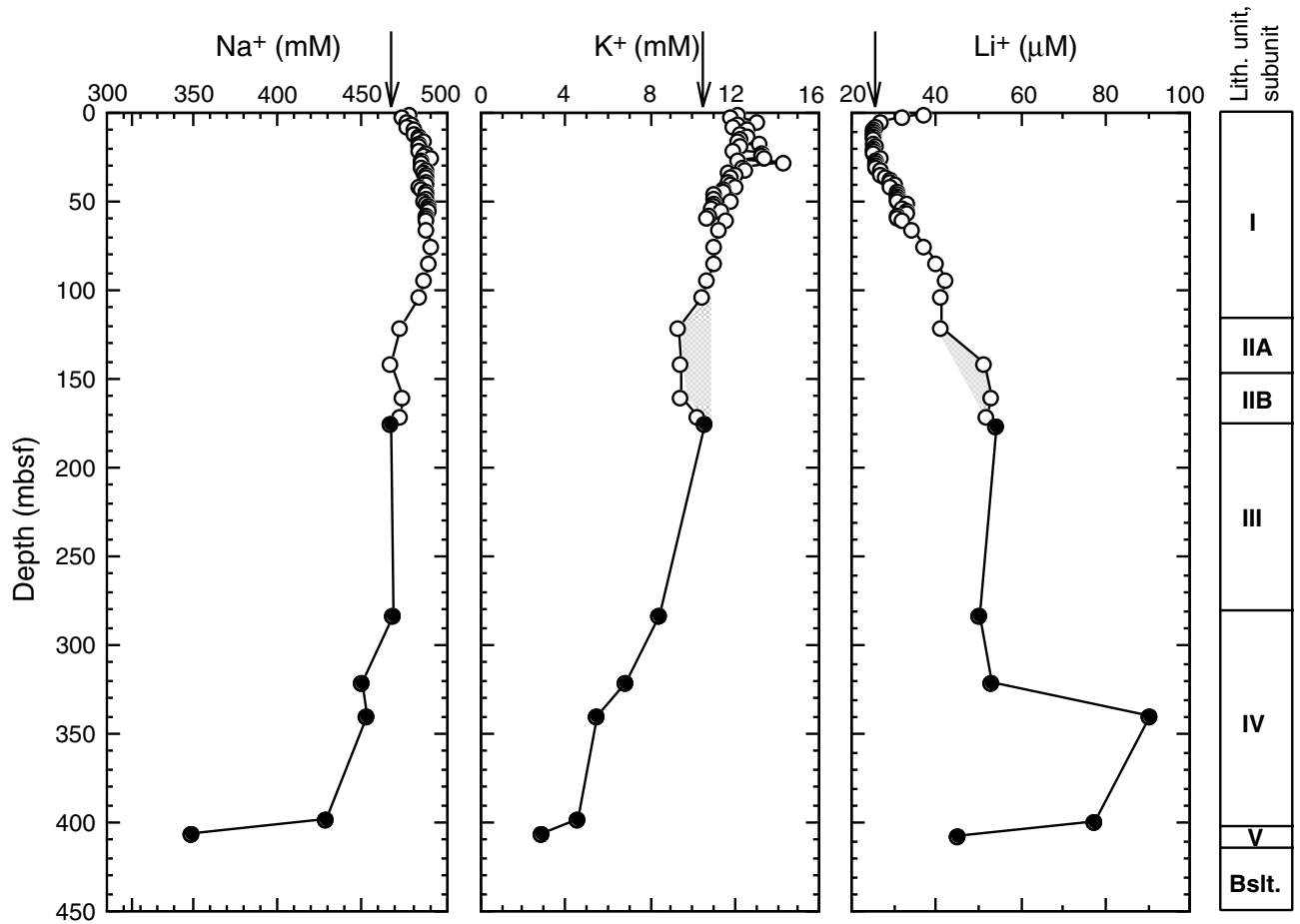


Figure F54. Concentration profiles of dissolved Ca^{2+} and Mg^{2+} at Site 1149. Open circles = Hole 1149A; solid circles = Hole 1149B. Lithostratigraphic units and subunits are as defined in "Lithostratigraphy," p. 11. Arrows indicate average concentrations in seawater (Millero and Sohn, 1992).

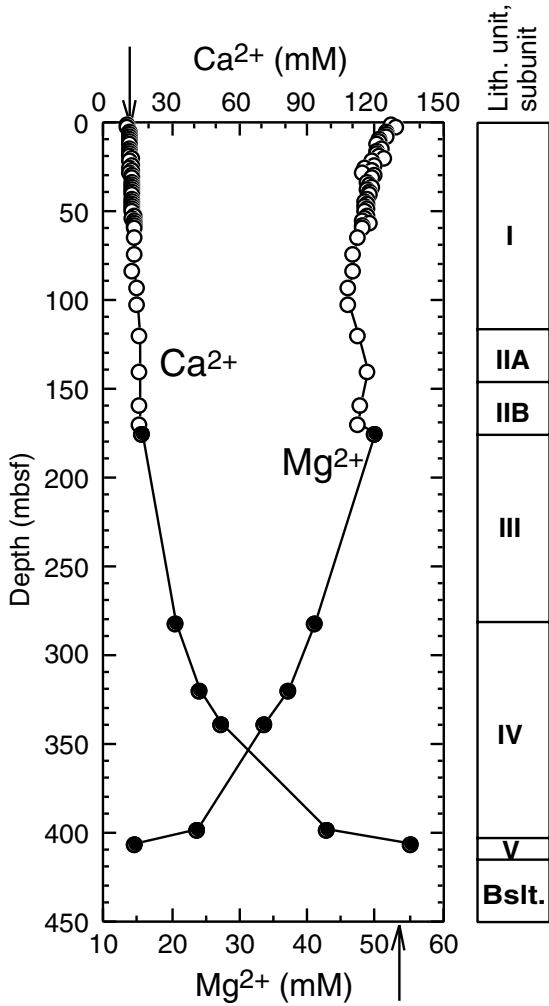


Figure F55. Assessment of the linearity of the relationships between concentrations of various dissolved constituents and that of Mg^{2+} in Unit IV interstitial waters.

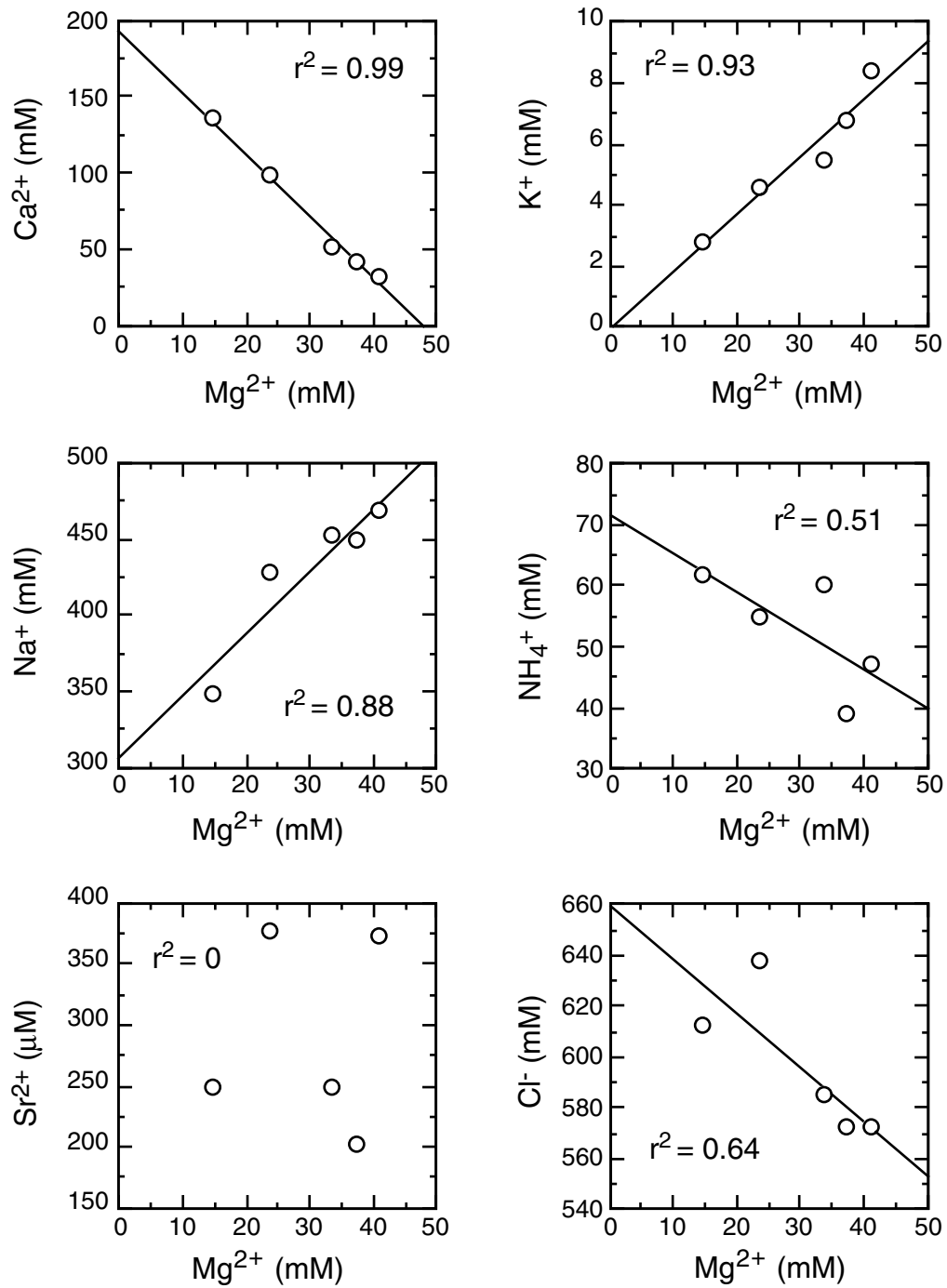


Figure F56. Concentration profiles of salinity and dissolved Cl^- at Site 1149. Open circles = Hole 1149A; solid circles = Hole 1149B. Inset in the right-hand panel shows the 0–200 mbsf portion at an expanded concentration scale. Lithologic units and subunits are as defined in “Lithostratigraphy,” p. 11. Arrows indicate average concentrations in seawater (Millero and Sohn, 1992).

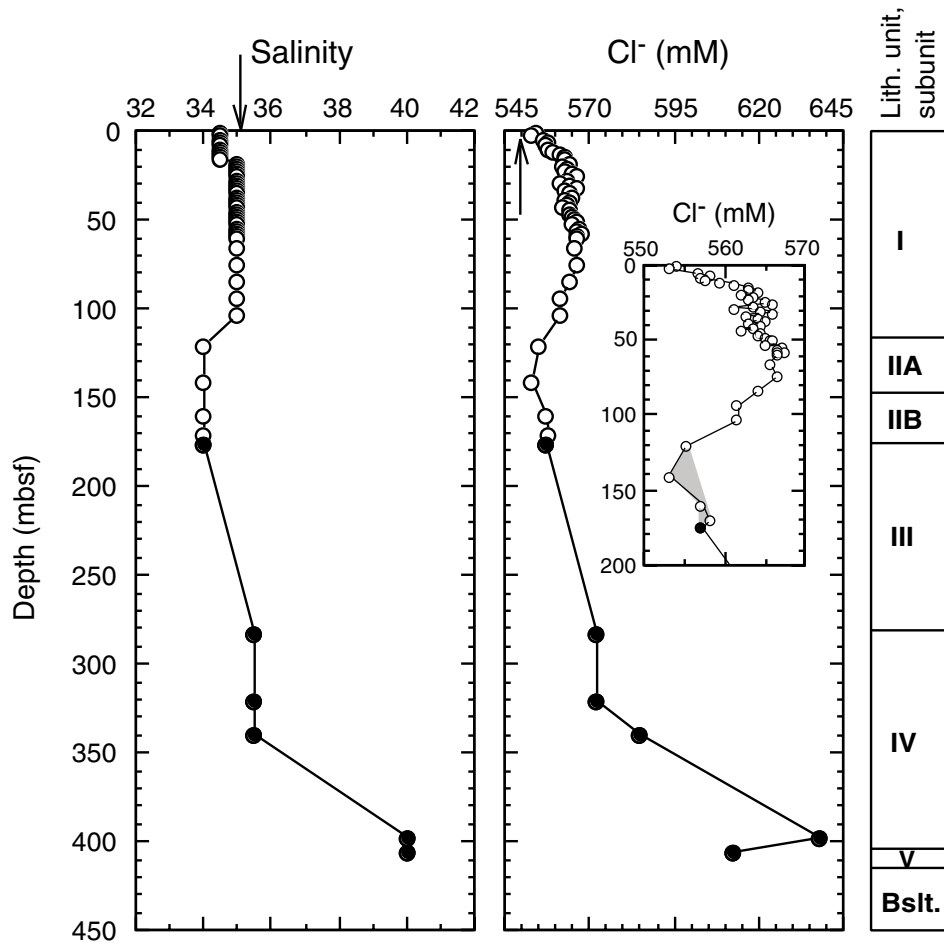


Figure F57. Downcore profiles of Fe/Al, MnO/Al₂O₃, and P₂O₅/Al₂O₃ in bulk sediment, Site 1149 (see Table T14, p. 176). Dashed line = values in average shale.

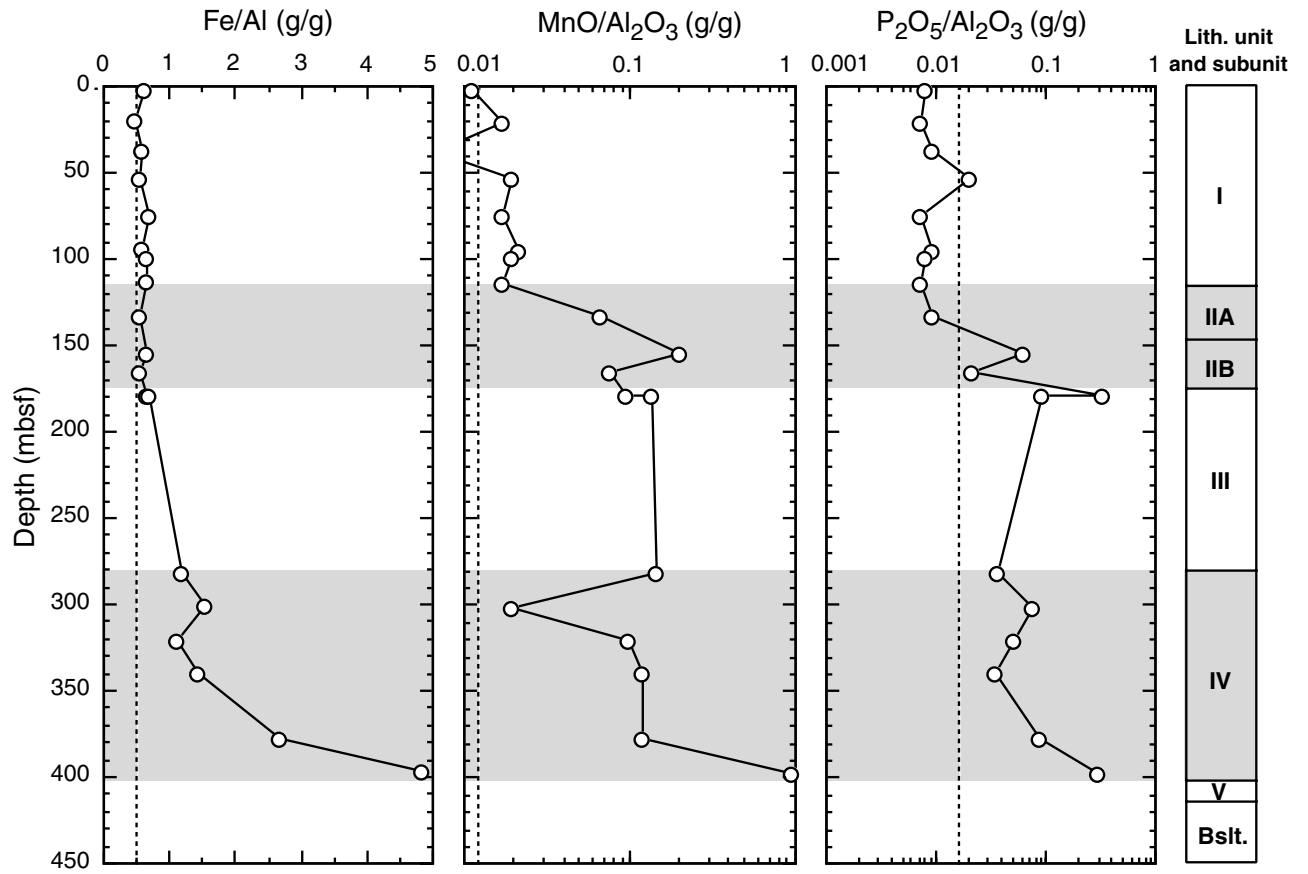


Figure F58. Downcore profiles of SiO_2 and $\text{SiO}_2/\text{Al}_2\text{O}_3$ in bulk sediment, Site 1149 (see Table T14, p. 176). Dashed line = values in average shale.

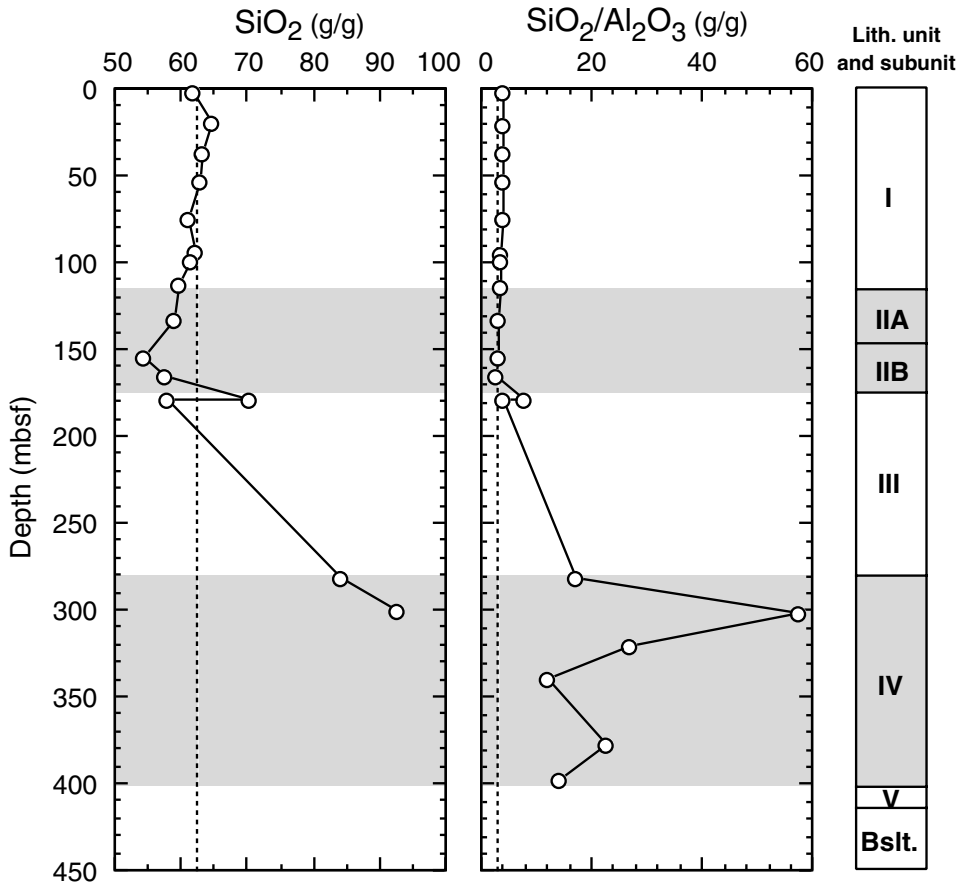


Figure F59. Downcore profiles of Ba/Al and Sr/Al in bulk sediment, Site 1149 (see Table T14, p. 176). Dashed line = values in average shale.

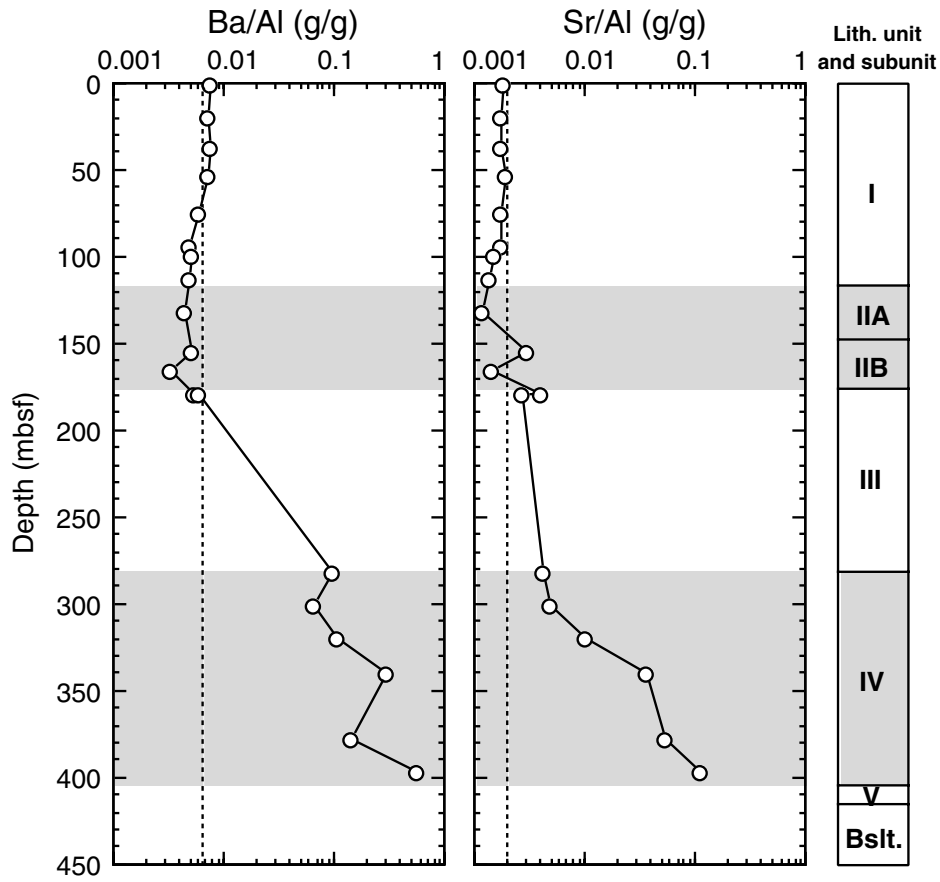


Figure F60. Downcore profiles of K_2O/Al_2O_3 , Na_2O/Al_2O_3 , and MgO/Al_2O_3 in bulk sediment, Site 1149 (see Table T14, p. 176). Dashed line = values in average shale.

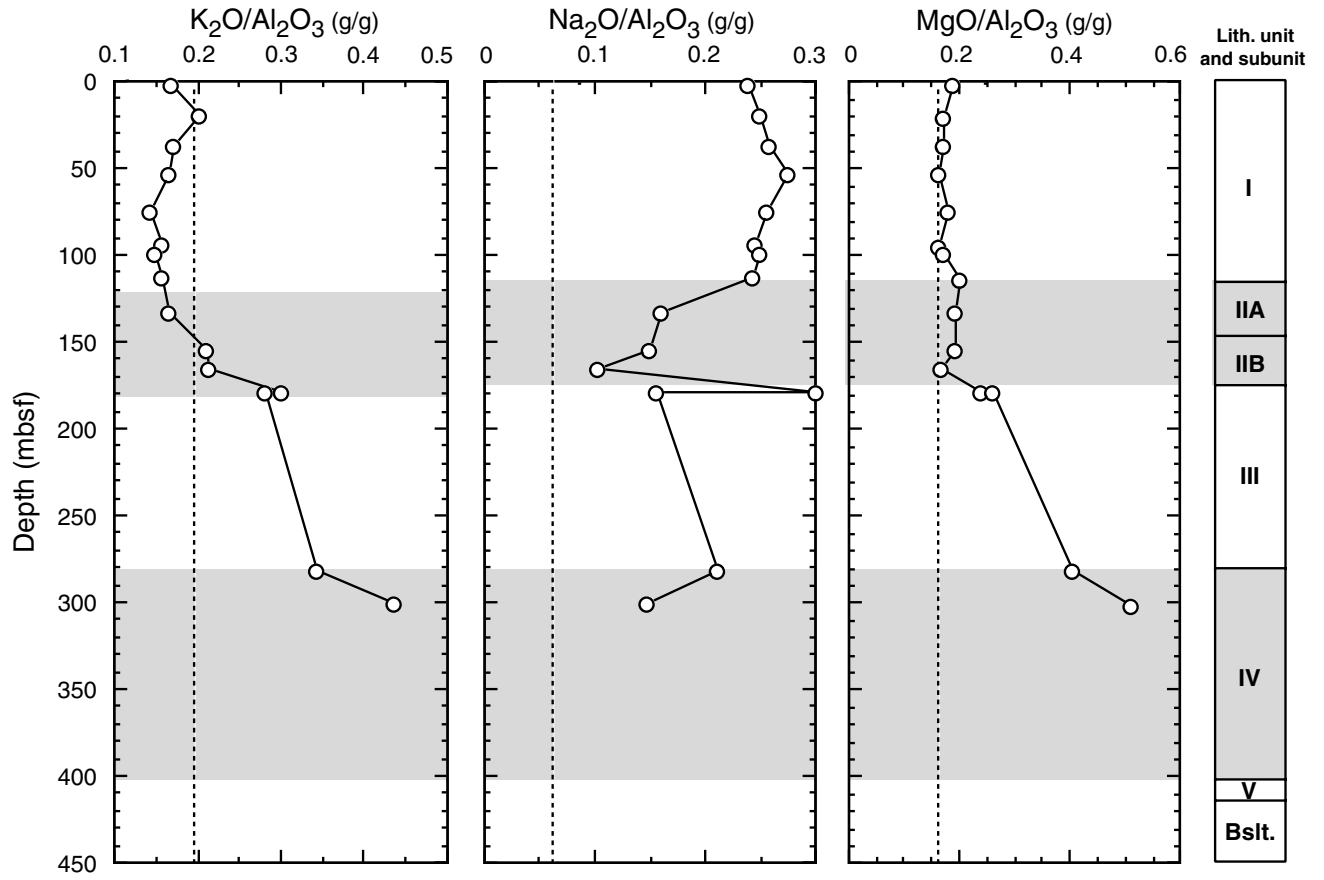


Figure F61. Downcore profiles of "terrigenous clay and ash," Al/Ti, and Nb/Al in bulk sediment, Site 1149 (see Table T14, p. 176). Dashed line = values in average shale.

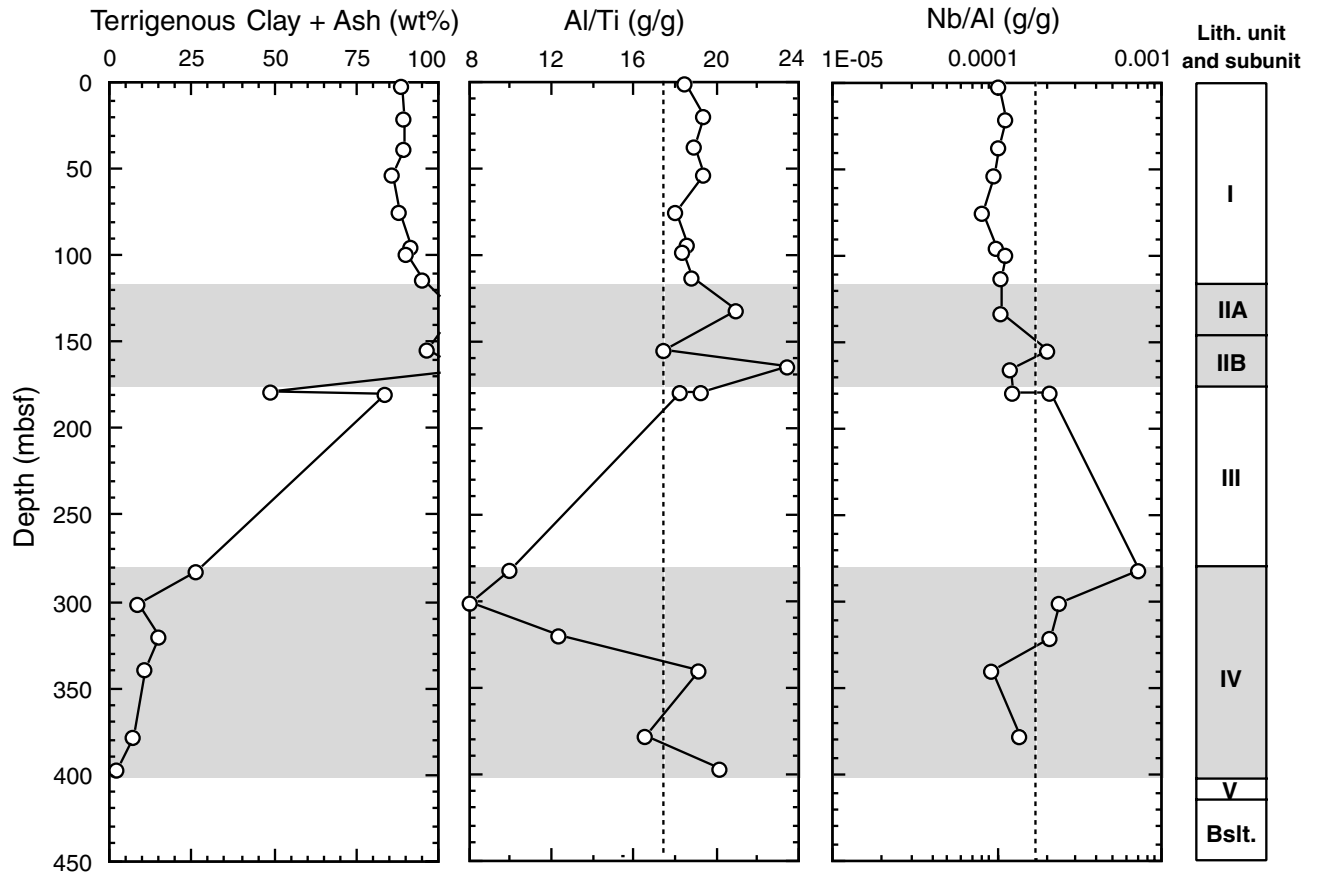


Figure F62. Downcore profile of dispersed ash in bulk sediment, Site 1149, as calculated from normative Equation 1, p. 33, and Equation 2, p. 33.

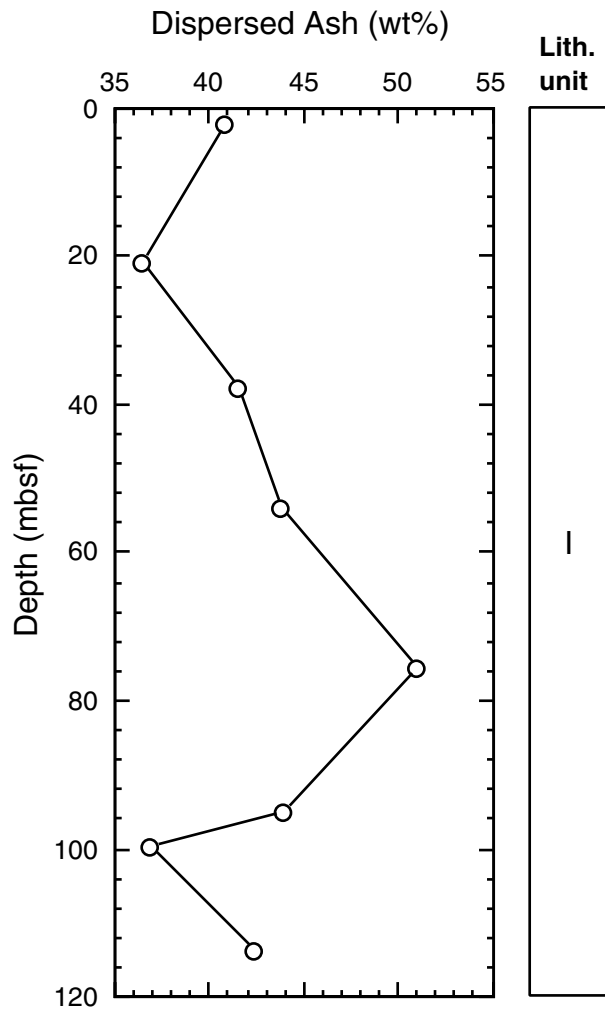


Figure F63. Inclinations of the natural remanent magnetization measured in lithologic Units I and II, Holes 1149A and 1149B.

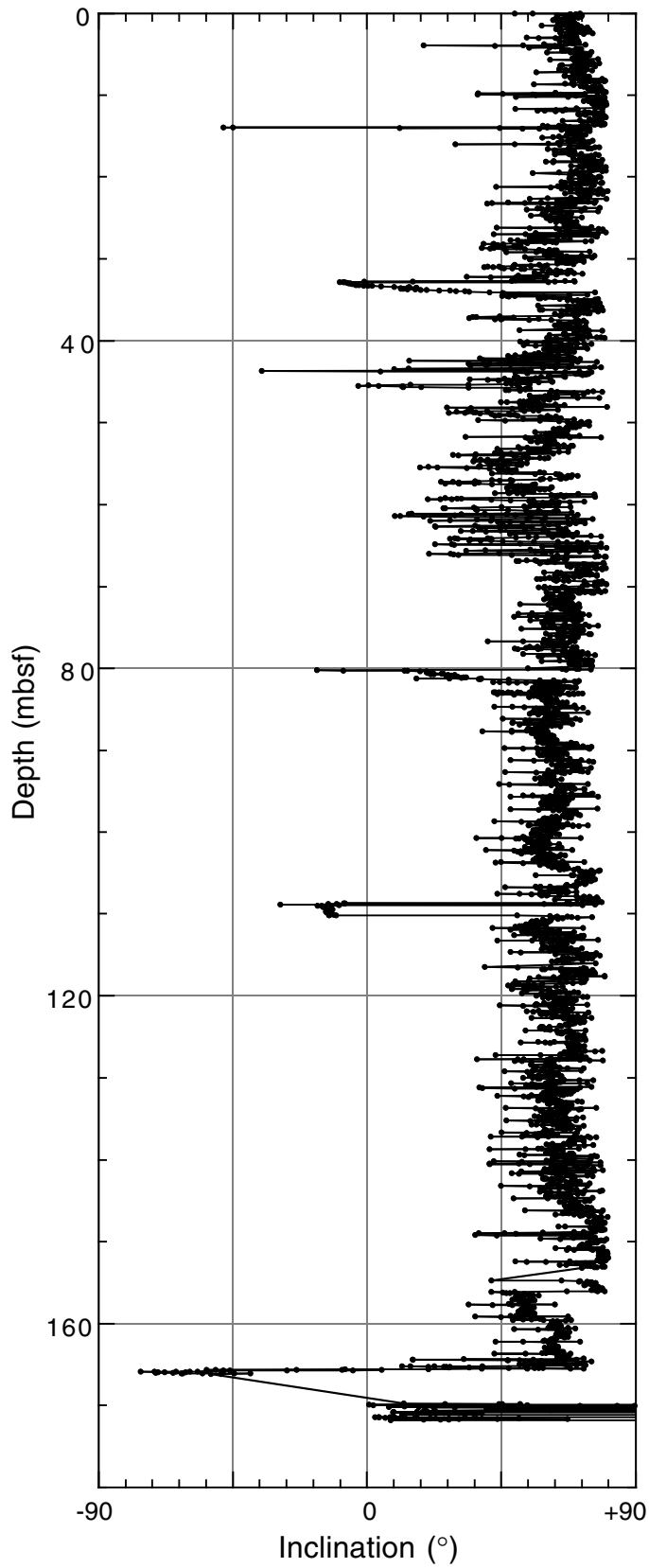


Figure F64. Alternating field demagnetization of two segments of Section 185-1149A-1H-3. A. The predominant, single-component demagnetization response. (Continued on next page.)

A

Sample 185-1149A-1H-3, 96 cm

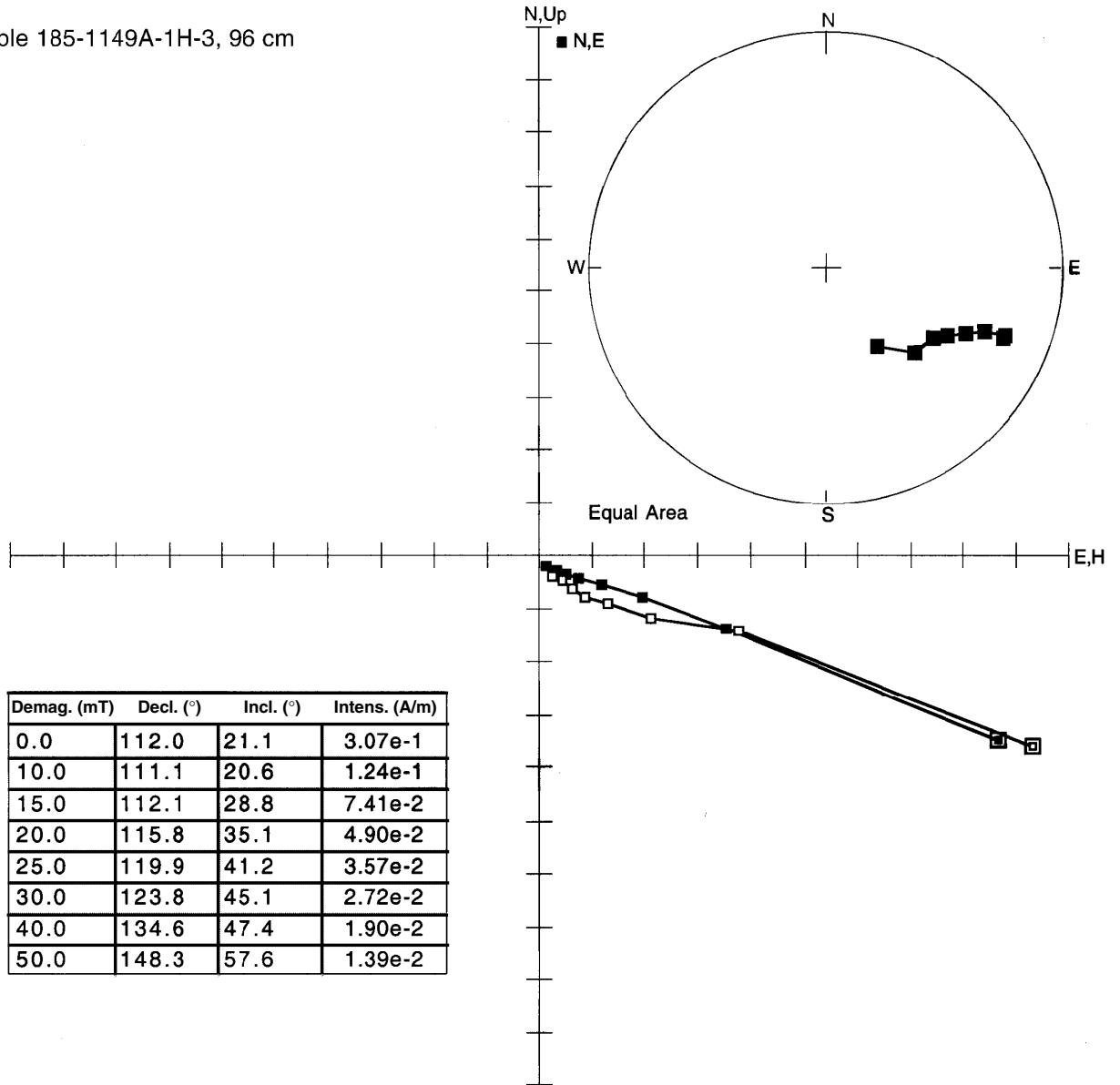


Figure F64 (continued). B. A multicomponent demagnetization response.

B

Sample 185-1149A-1H-3, 4 cm

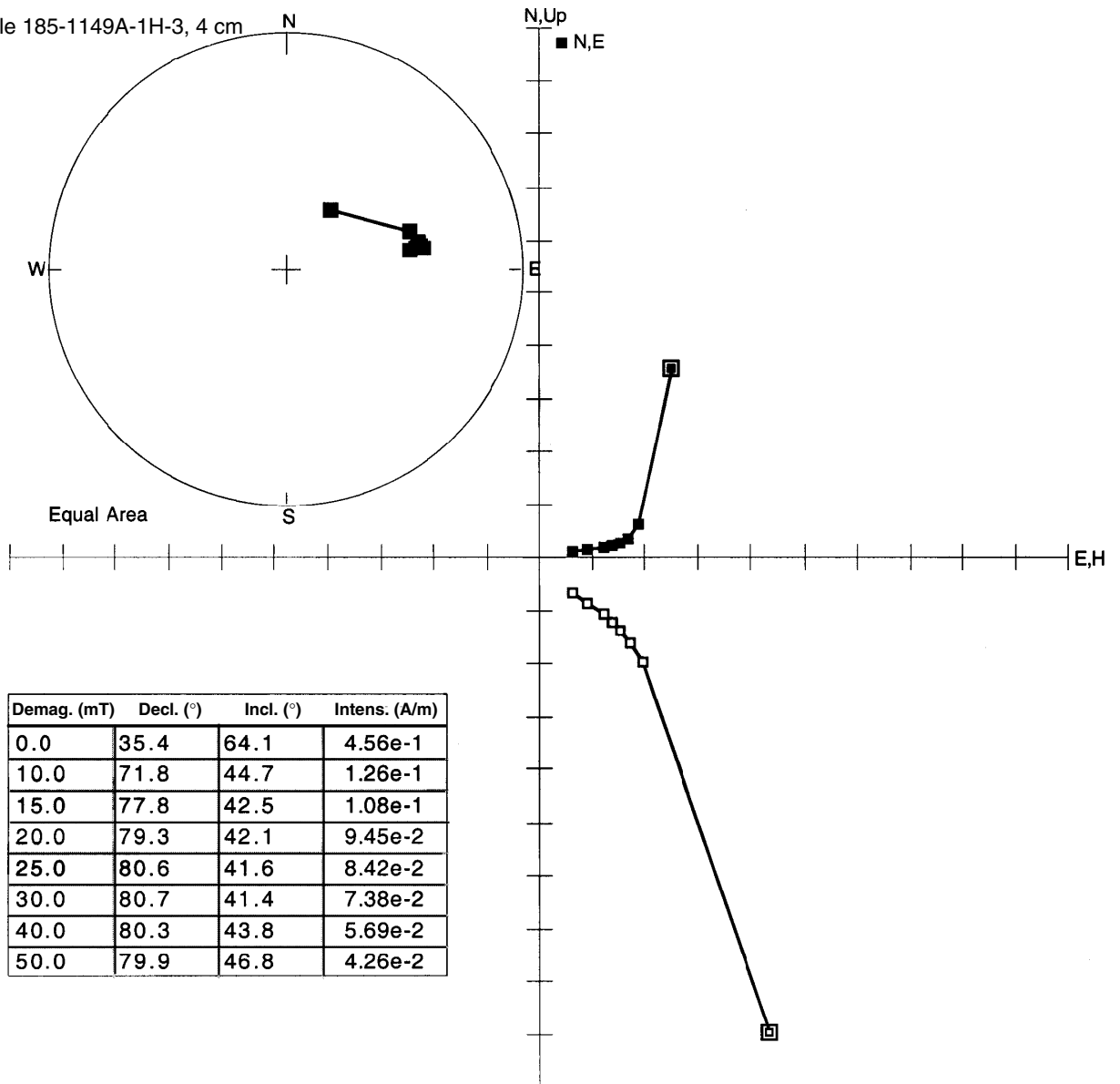


Figure F65. Magnetostratigraphy of Holes 1149A and 1149B (lithologic Units I and II) after demagnetization at 25 mT. True declination (left) was obtained by orientation with the tensor tool; inclinations are shown on the right.

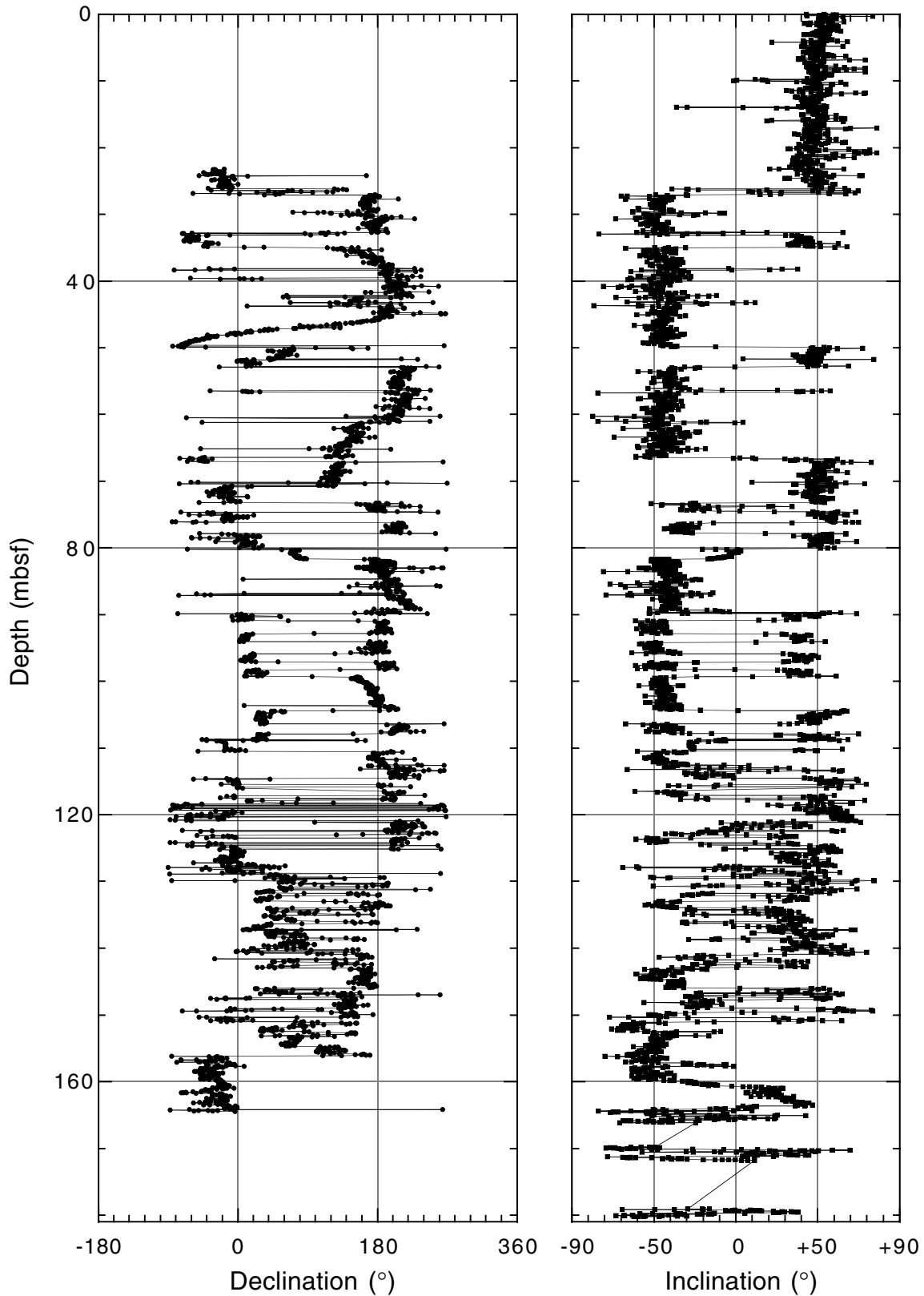


Figure F66. The inclinations of lithologic Unit I (Cores 185-1149A-1H through 13H) compared to the late Cenozoic magnetic polarity time scale (Berggren et al., 1995).

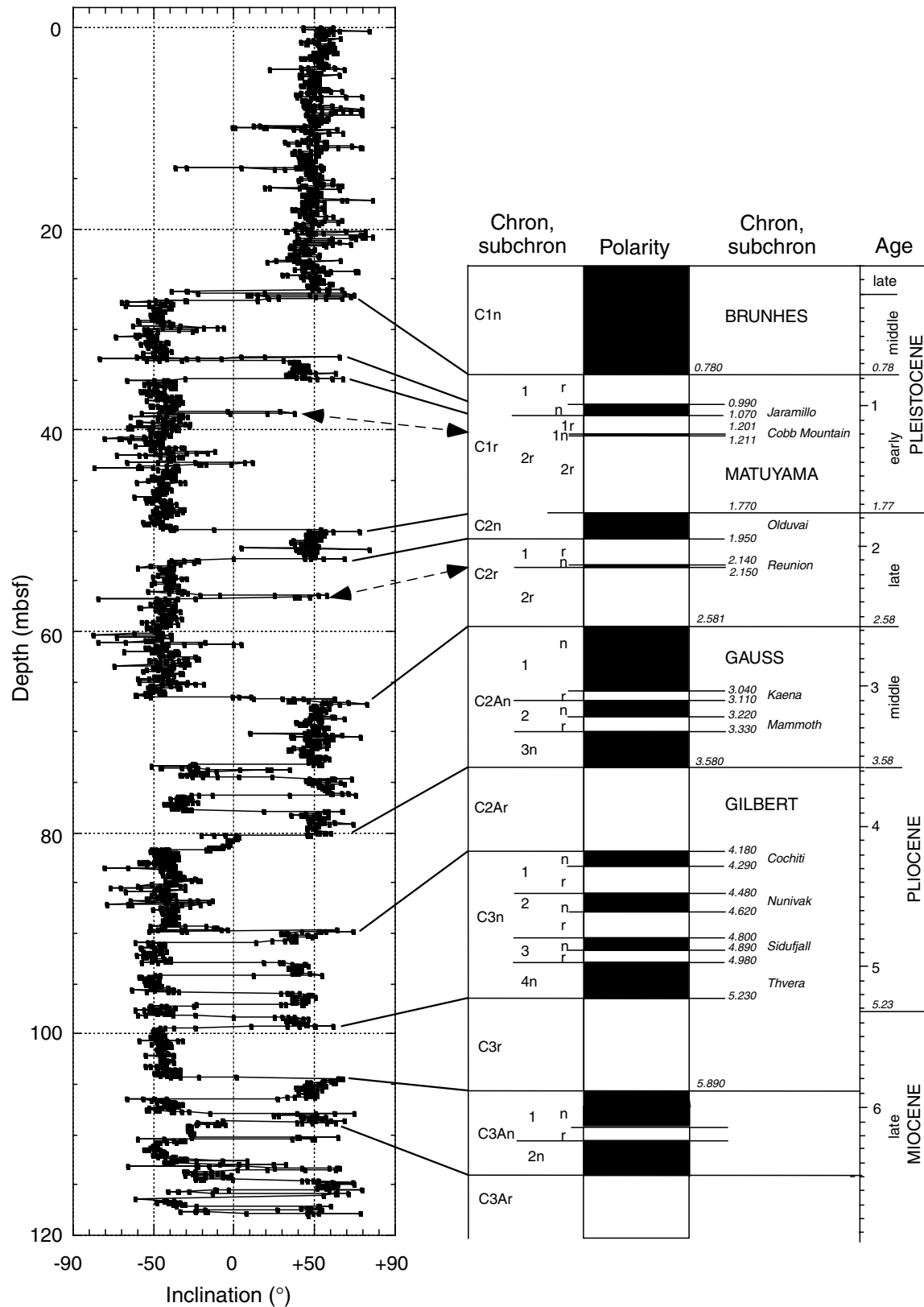


Figure F67. Cumulative sedimentation rate curve for Site 1149 based on paleomagnetic and calcareous nannofossil data. p.p. = pro parte.

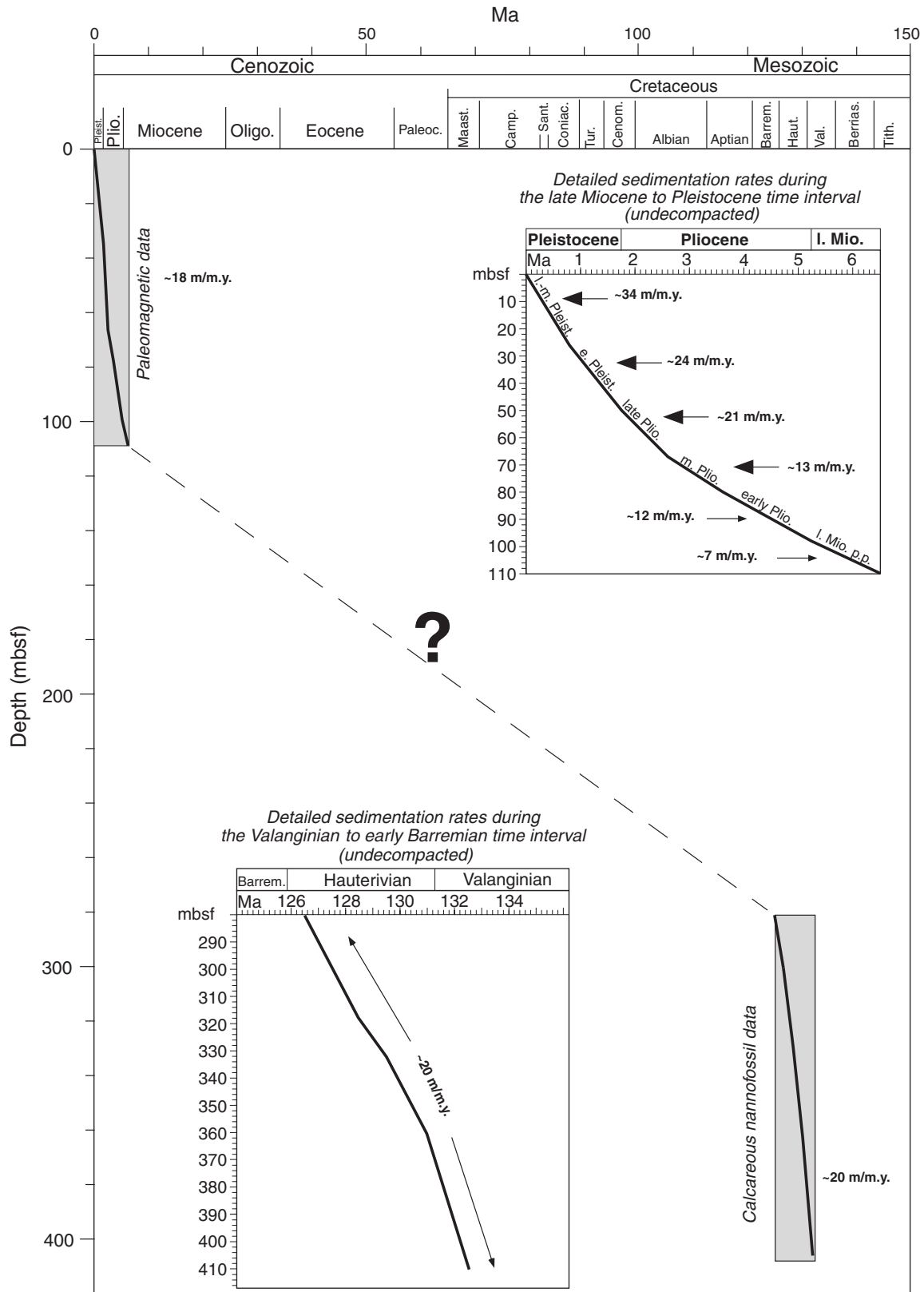


Figure F69. Crossplots of wet bulk density, porosity, and average velocity from discrete samples selected where depth of velocity measurements exactly match depth of index properties.

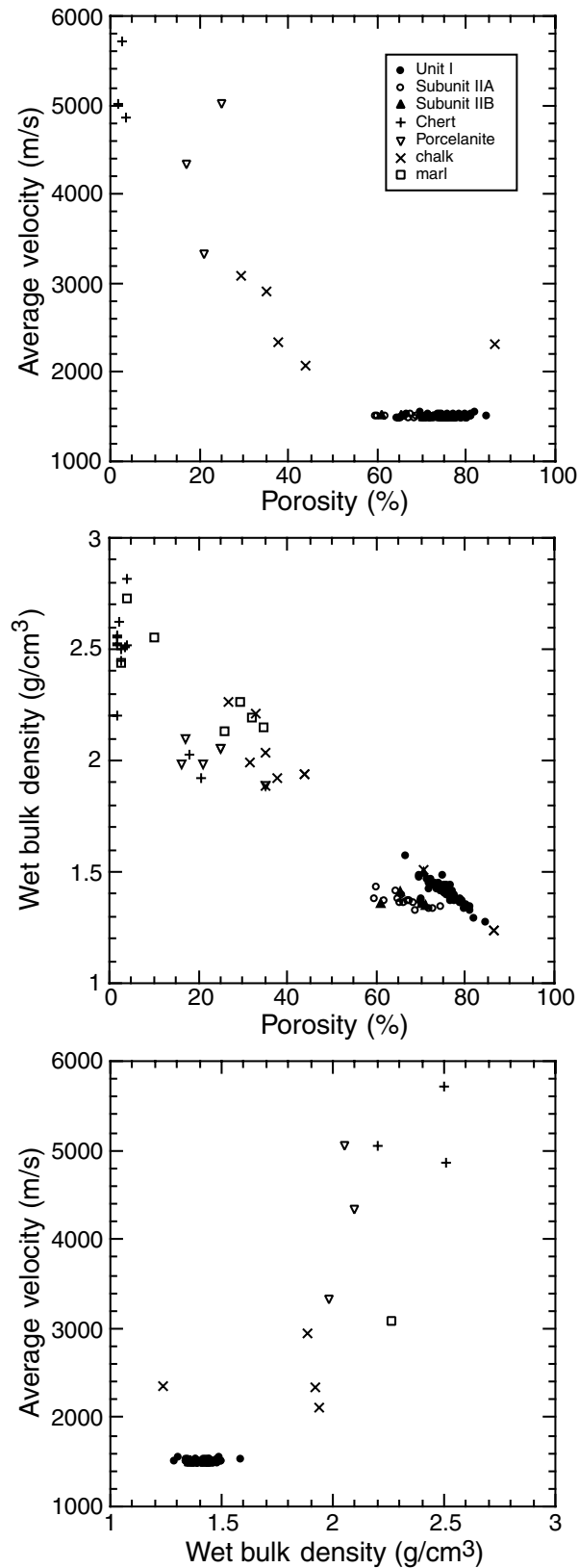


Figure F71. Compressional wave velocity on split cores and discrete samples. Note the scale change at 180 mbsf. NR = not recovered.

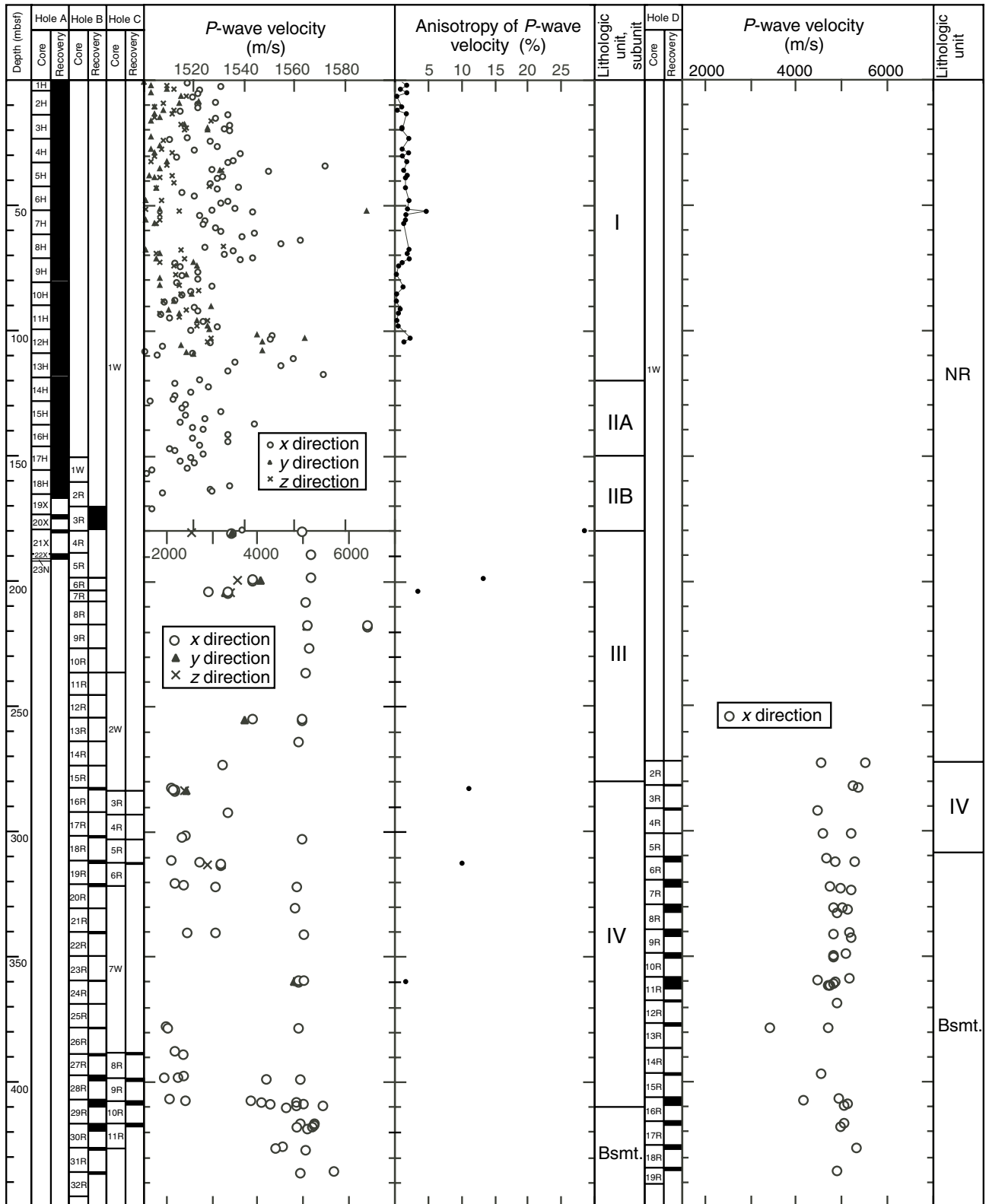


Figure F72. Radioactive element logging measurements in Hole 1149B are shown with lithologic units determined from cored intervals from Holes 1149A and 1149B. High gamma radiation values are observed between 160 and 180 mbsf and correlate to the ash-free, dark brown pelagic clay intervals of lithologic Subunit IIB. Elevated uranium concentrations are also observed throughout the majority of the logged interval, including a significant peak at 290–300 mbsf. Note the sudden change in logging parameters at the bottom of the drill pipe.

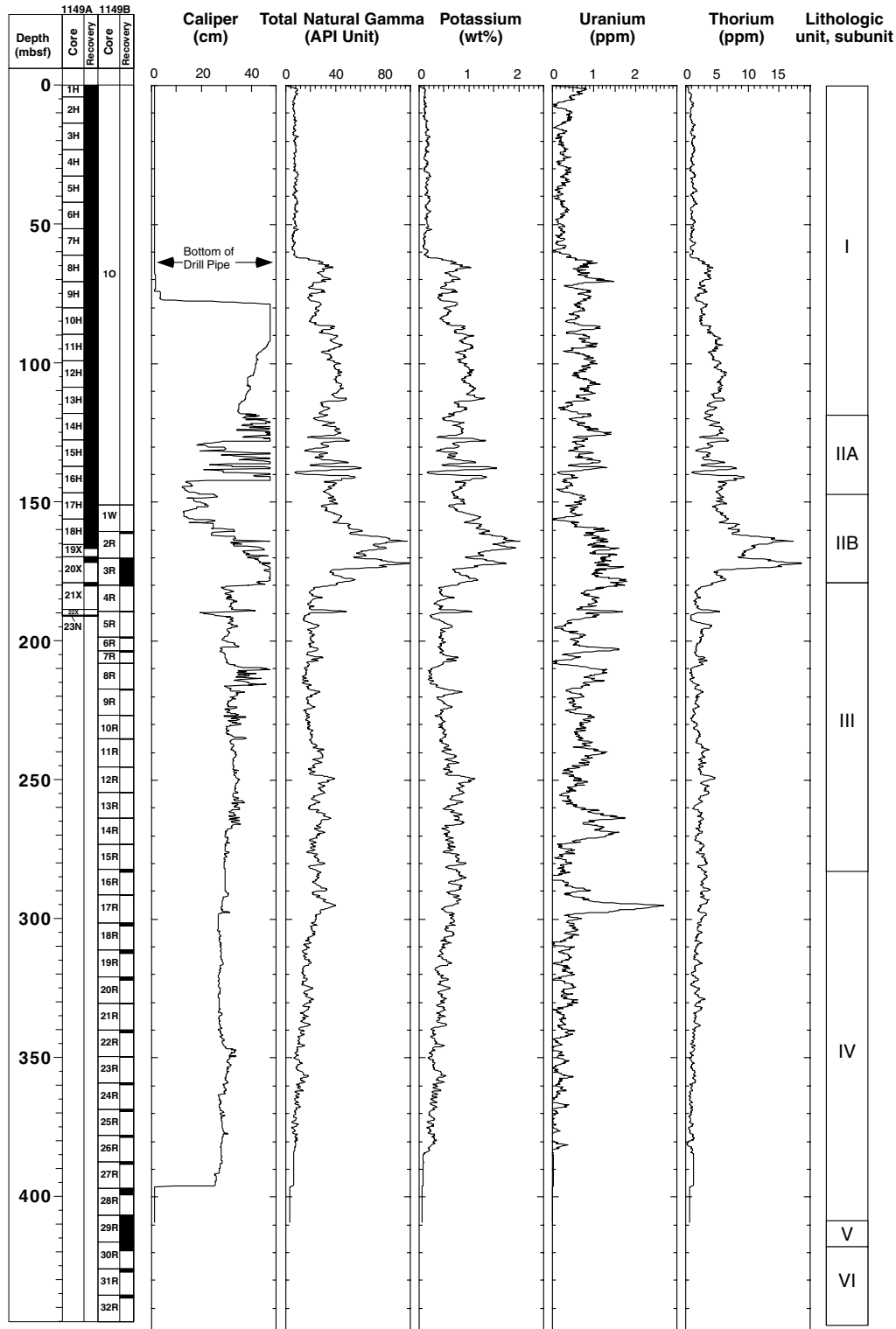


Figure F73. Geophysical logging measurements in Hole 1149B are shown with lithologic units determined from cored intervals from Holes 1149A and 1149B. Resistivity, bulk density, and caliper dimensions each delineate three major intervals within the logged interval that are in general agreement with the lithologic units identified from core samples. *P*-wave velocities also identify three major intervals, but the lowermost increase in velocity is somewhat offset from the identified lithologic boundaries. Note the sudden change in logging parameters at the bottom of the drill pipe.

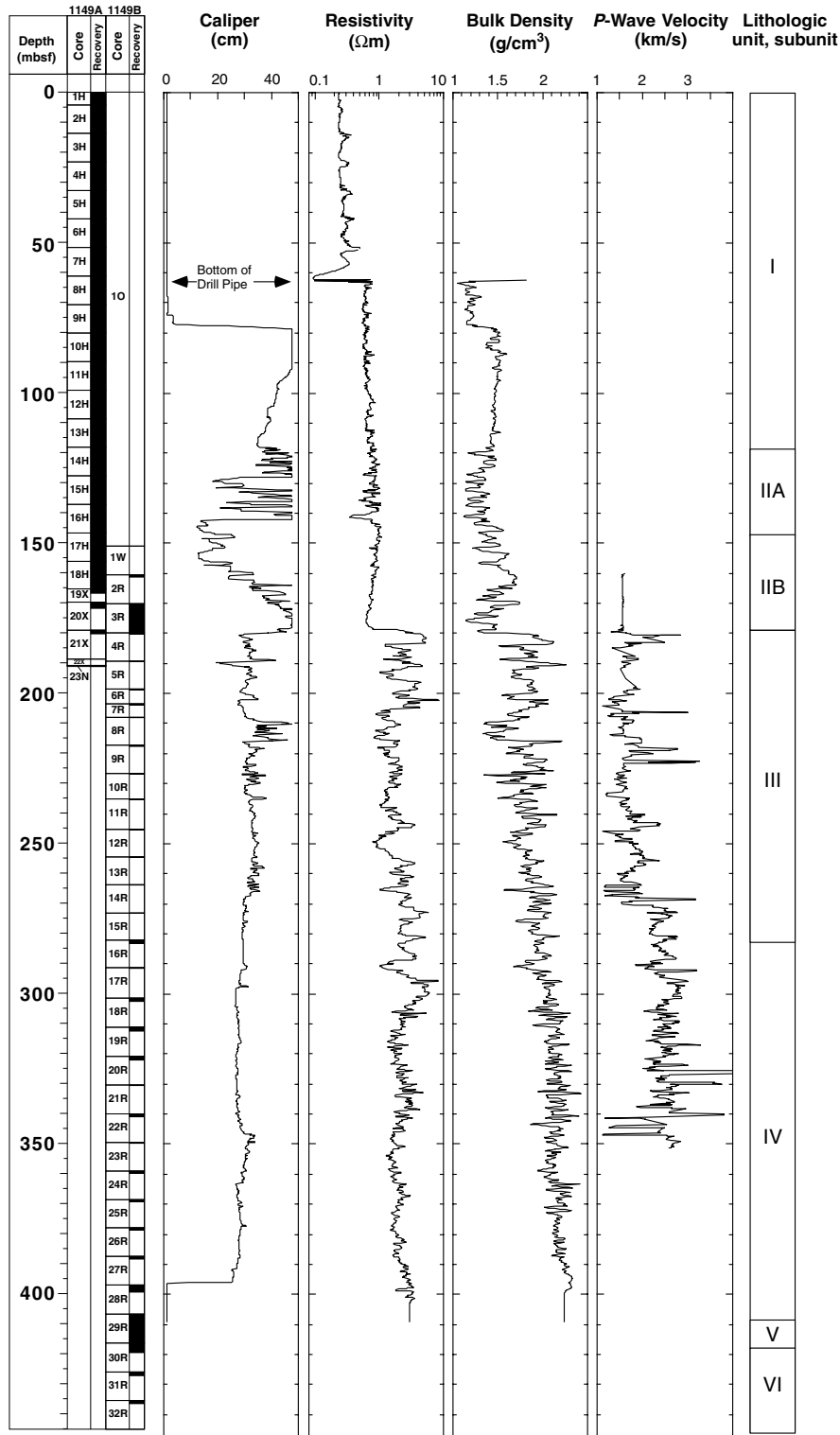


Figure F74. Geochemical logging measurements in Hole 1149B are shown with lithologic units determined from cored intervals from Holes 1149A and 1149B. The relative abundance of each element is shown in units of decimal fraction, which represents the portion of the element relative to all the elements measured. Although logging continued up into the drill pipe on all logging runs, only the data from the section below the drill pipe are shown. The data gap near 150 mbsf is due to a change in the depth to which logging runs were conducted. ([Figure shown on next page.](#))

Figure F74. (Caption on previous page.)

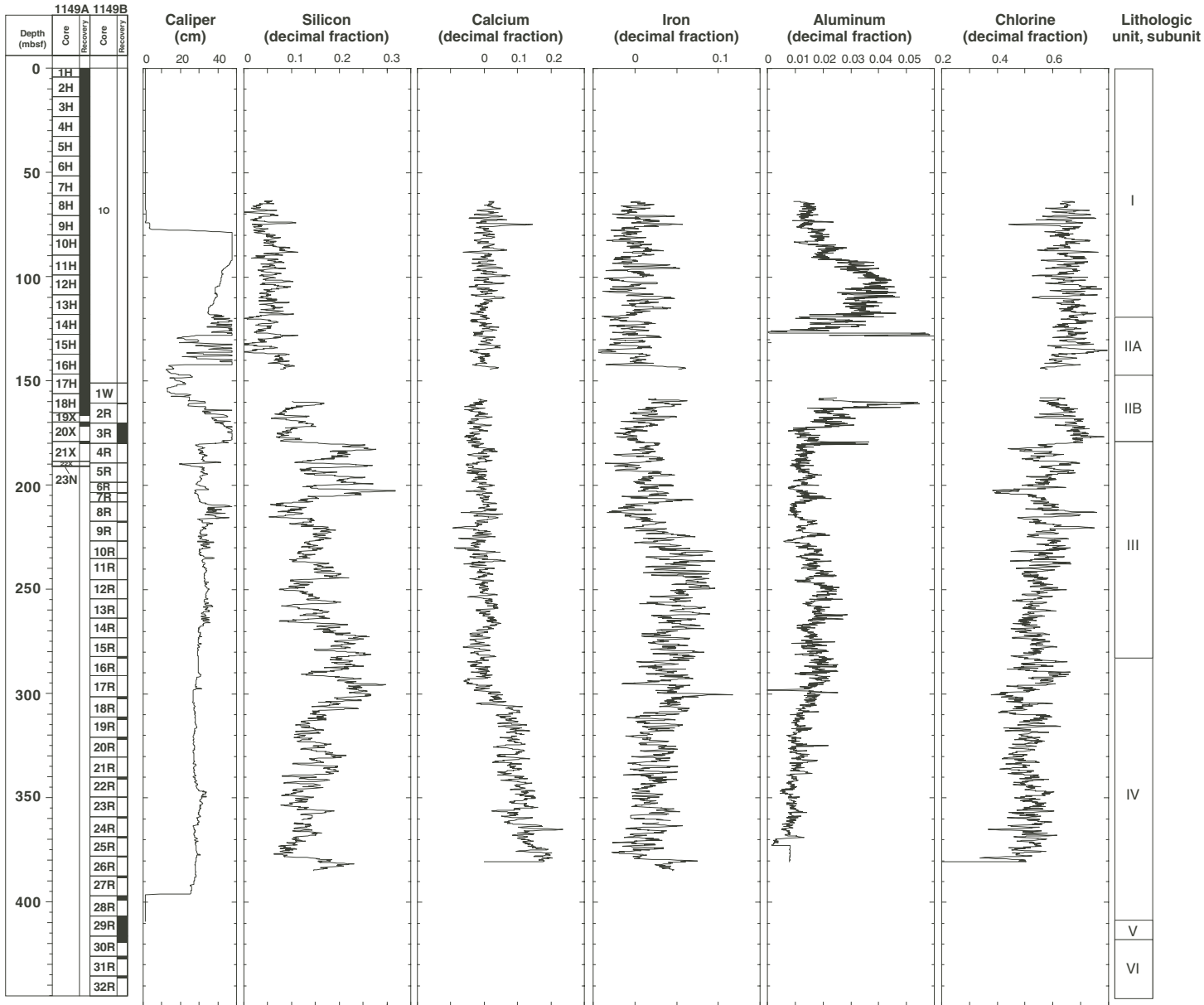


Figure F75. Dipmeter analysis and FMS images recorded between 200 and 380 mbsf in Hole 1149B. The analysis of pass 1 is in black (solid-line tails) and pass 2 in blue (dashed-line tails). The downdip azimuths and the dip values are indicated by the direction of the tadpole's "tails" and by the position in the grid. Hollow tadpoles indicate lower confidence in the quality of the correlation. The "fan plots" give the distribution of the dip azimuth over 20-m intervals.

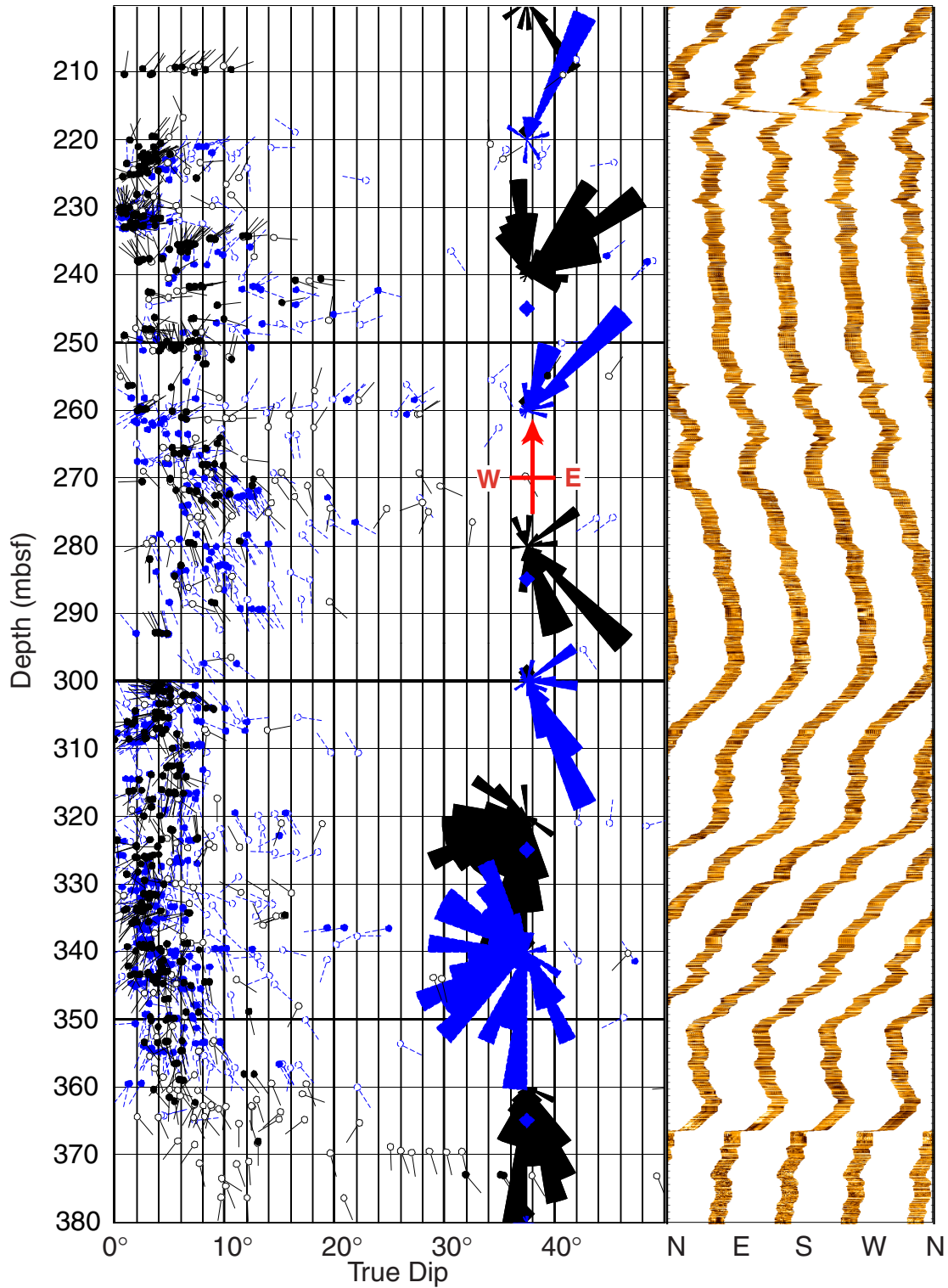


Figure F76. Detail of the FMS images and dip analysis in four intervals, showing the change occurring in the sediment structure at the bottom of Unit III. A, B. Above the transition. The sinusoids show the correlation paths between the different FMS pads that identify individual dipping features. (Continued on next page.)

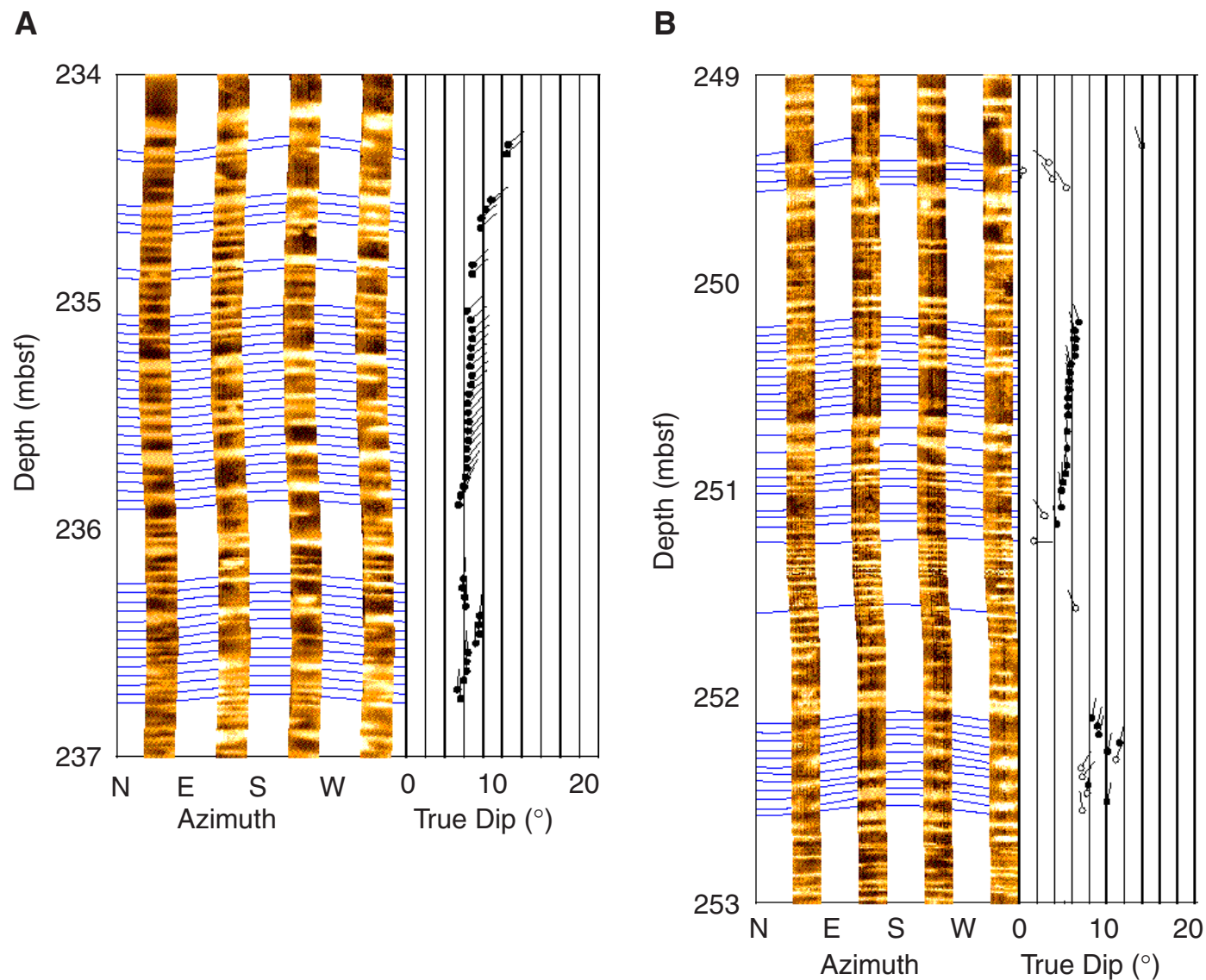


Figure F76 (continued). C, D. Below the transition.

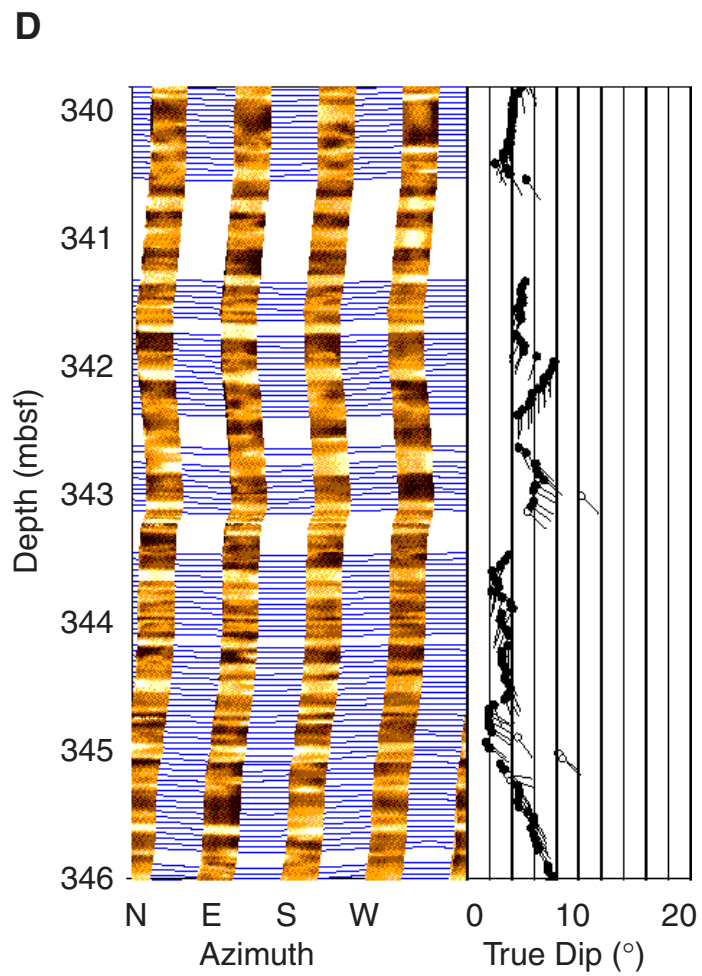
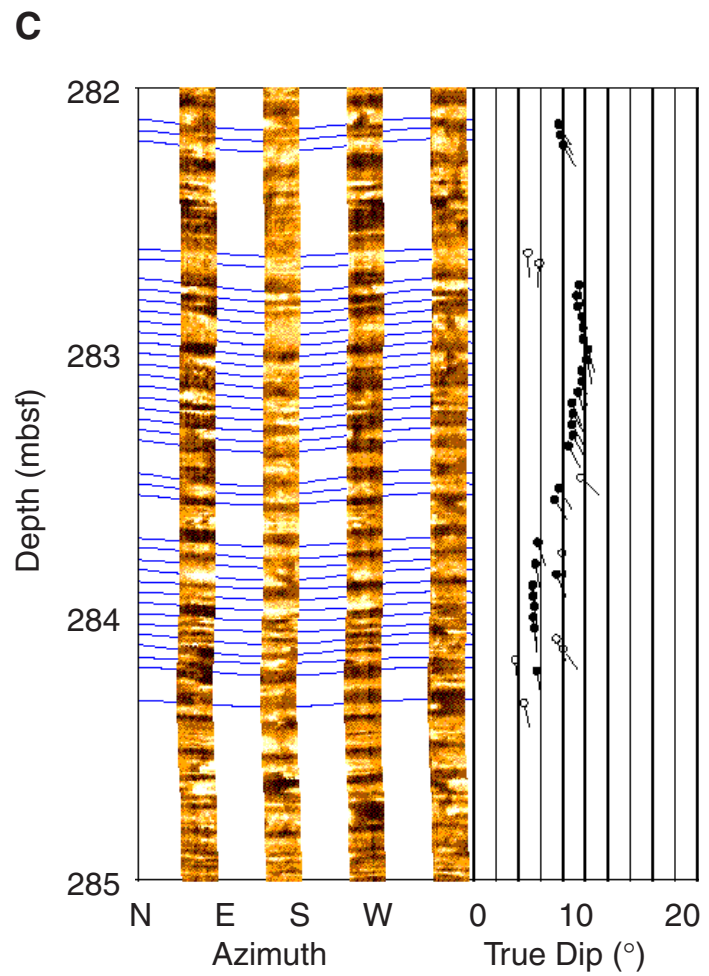


Figure F77. Concentration of perfluorocarbon tracer (PFT) in Site 1149 sediments (core interiors only) (Smith et al., in press). For data see Table T22, p. 189.

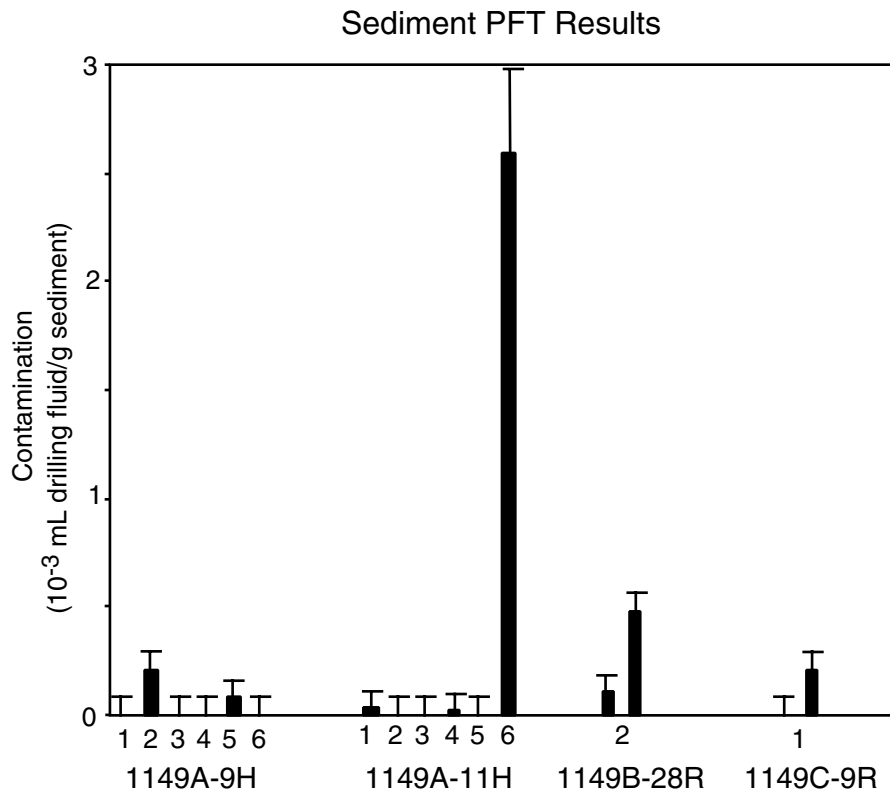


Table T1. Coring summary, Site 1149. (See table notes. Continued on next page.)

Core	Date (1999)	Ship local time	Depth (mbsf)		Length (m)		Recovery (%)	Comments
			Top	Bottom	Cored	Recovered		
185-1149A-								
1H	24 May	0245	0.0	4.2	4.2	4.23	100.7	
2H	24 May	0430	4.2	13.7	9.5	9.95	104.7	Drill string acceleration
3H	24 May	0550	13.7	23.2	9.5	9.81	103.3	Bead test for microbiological contamination study
4H*	24 May	0740	23.2	32.7	9.5	9.91	104.3	Temperature recording
5H	24 May	0855	32.7	42.2	9.5	9.55	100.5	
6H	24 May	1035	42.2	51.7	9.5	9.87	103.9	Temperature recording; Bead test and PFT test for microbiological contamination study
7H	24 May	1150	51.7	61.2	9.5	9.58	100.8	
8H	24 May	1320	61.2	70.7	9.5	9.94	104.6	Temperature recording
9H	24 May	1530	70.7	80.2	9.5	9.38	98.7	Bead test and PFT test for microbiological contamination study
10H	24 May	1800	80.2	89.7	9.5	9.82	103.4	Drill string acceleration
11H	24 May	1950	89.7	99.2	9.5	9.63	101.4	PFT test for microbiological contamination study
12H	24 May	2110	99.2	108.7	9.5	9.93	104.5	Bead test for microbiological contamination study
13H	24 May	2230	108.7	118.2	9.5	9.46	99.6	
14H	24 May	2340	118.2	127.7	9.5	10.05	105.8	
15H	25 May	0055	127.7	137.2	9.5	9.85	103.7	
16H	25 May	0210	137.2	146.7	9.5	9.89	104.1	
17H	25 May	0325	146.7	156.2	9.5	9.89	104.1	
18H	25 May	0440	156.2	164.4	8.2	8.34	101.7	
19X	25 May	0650	164.4	169.8	5.4	1.79	33.2	
20X	25 May	0820	169.8	179.1	9.3	2.06	22.2	
21X	25 May	1010	179.1	188.7	9.6	1.21	12.6	
22X	25 May	1305	188.7	190.9	2.2	0.00	0.0	
23N	25 May	1625	190.9	191.2	0.3	0.30	100.0	Motor driven core barrel
Coring totals:					191.2	174.44	91.2	
185-1149B-								
	26 May	2300	***Drilled from 0.0 to 151.1 mbsf***					
1W	27 May	0040	151.1	160.6	9.5	3.79	39.9	
2R	27 May	0315	160.6	170.3	9.7	0.76	7.8	
3R	27 May	0510	170.3	180.0	9.7	9.73	100.3	
4R	27 May	0735	180.0	189.4	9.4	0.33	3.5	
5R	27 May	0950	189.4	198.7	9.3	0.12	1.3	
6R	27 May	1145	198.7	203.7	5.0	0.32	6.4	
7R	27 May	1335	203.7	208.1	4.4	0.43	9.8	
8R	27 May	1615	208.1	217.4	9.3	0.09	1.0	
9R	27 May	1825	217.4	226.8	9.4	0.40	4.3	
10R	27 May	2035	226.8	236.3	9.5	0.21	2.2	
11R	27 May	2305	236.3	245.4	9.1	0.22	2.4	
12R	28 May	0110	245.4	254.6	9.2	0.14	1.5	
13R	28 May	0325	254.6	263.9	9.3	0.12	1.3	
14R	28 May	0600	263.9	273.3	9.4	0.07	0.7	
15R	28 May	0915	273.3	282.3	9.0	0.03	0.3	
16R	28 May	1625	282.3	292.0	9.7	1.11	11.4	
17R	28 May	2000	292.0	301.6	9.6	0.22	2.3	
18R	28 May	2250	301.6	311.3	9.7	1.10	11.3	
19R	29 May	0125	311.3	320.9	9.6	1.27	13.2	
20R	29 May	0405	320.9	330.5	9.6	1.22	12.7	
21R	29 May	0655	330.5	340.1	9.6	0.17	1.8	
22R	29 May	0910	340.1	349.7	9.6	0.98	10.2	
23R	29 May	1135	349.7	359.2	9.5	0.27	2.8	
24R	29 May	1410	359.2	368.7	9.5	0.66	6.9	
25R	29 May	1650	368.7	378.1	9.4	0.25	2.7	
26R	29 May	1905	378.1	387.6	9.5	0.73	7.7	
27R	29 May	2200	387.6	397.1	9.5	0.89	9.4	
28R	30 May	0345	397.1	406.8	9.7	2.37	24.4	
29R	30 May	1050	406.8	416.4	9.6	3.16	32.9	
30R	30 May	1630	416.4	426.0	9.6	3.19	33.2	
31R	30 May	2215	426.0	435.6	9.6	1.25	13.0	
32R	31 May	0420	435.6	445.2	9.6	1.12	11.7	
Coring totals:					294.1	36.72	12.5	
Drilled:					151.1			
Total:					445.2			
185-1149C-								
1W	3 June	1610	0.0	237.0	237.0	1.63	0.7	
2W	3 June	2200	237.0	283.6	46.6	0.22	0.5	
3R	4 June	0320	283.6	293.2	9.6	0.46	4.8	

Table T1 (continued).

Core	Date (1999)	Ship local time	Depth (mbsf)		Length (m)		Recovery (%)	Comments
			Top	Bottom	Cored	Recovered		
4R	4 June	0840	293.2	302.8	9.6	0.25	2.6	
5R	4 June	1715	302.8	312.4	9.6	0.30	3.1	
6R	4 June	1930	312.4	322.0	9.6	0.48	5.0	
7W	5 June	0200	322.0	388.2	66.2	0.46	0.7	
8R	5 June	1010	388.2	397.9	9.7	0.96	9.9	
9R	5 June	2205	397.9	407.5	9.6	1.00	10.4	
10R	6 June	0330	407.5	417.1	9.6	1.60	16.7	
11R	6 June	1235	417.1	426.7	9.6	1.34	14.0	
Coring totals:					426.7	8.70	2.0	
185-1149D-								
1W	8 June	0610	***Drilled from 0.0 to 272.2 mbsf***					
2R	8 June	0830	272.2	281.6	9.4	0.29	3.1	
3R	8 June	1040	281.6	290.9	9.3	0.31	3.3	
4R	8 June	1330	290.9	300.3	9.4	0.63	6.7	
5R	8 June	1945	300.3	310.0	9.7	0.30	3.1	
6R	9 June	0255	310.0	319.7	9.7	2.07	21.3	
7R	9 June	0745	319.7	329.3	9.6	2.84	29.6	
8R	9 June	1755	329.3	338.8	9.5	3.03	31.9	
9R	10 June	0045	338.8	348.4	9.6	2.75	28.7	
10R	10 June	0645	348.4	357.9	9.5	2.01	21.2	Bead test for microbiological contamination study
11R	10 June	1225	357.9	367.4	9.5	4.60	48.4	Bead test for microbiological contamination study
12R	10 June	1655	367.4	377.0	9.6	0.60	6.3	Bead test for microbiological contamination study
13R	10 June	2215	377.0	386.6	9.6	1.27	13.2	Bead test for microbiological contamination study
14R	11 June	1030	386.6	396.3	9.7	0.36	3.7	Bead test for microbiological contamination study
15R	11 June	1645	396.3	405.9	9.6	0.80	8.3	Bead test for microbiological contamination study
16R	11 June	2225	405.9	415.5	9.6	2.69	28.0	Bead test for microbiological contamination study
17R	12 June	0515	415.5	425.1	9.6	1.61	16.8	
18R	12 June	1125	425.1	434.7	9.6	1.59	16.6	
19R	12 June	1610	434.7	440.4	5.7	1.00	17.5	
Coring totals:					168.2	29.94	17.8	
Drilled:					272.2			
Total:					440.4			

Notes: * = APC cores were oriented in azimuth beginning with Core 4H. PFT = perfluorocarbon tracer. This table is also available in [ASCII format](#).

Table T2. Expanded coring summary, Site 1149. (See table note. Continued on next nine pages.)

Hole 1149A

Latitude: 31.3419991°N (31°20.51994'N)
Longitude: 143.3513031°E (143°21.07819'E)
Depth (mbrf): 5829.30

Core	Date (May 1999)	Ship local time	Depth (mbsf)		Length (m)		Recovery (%)	Section	Length (m)		Section (mbsf)		Catwalk samples	Comments
			Top	Bottom	Cored	Recovered			Liner	Curated	Top	Bottom		
185-1149A- 1H	24	0245	0.0	4.2	4.2	4.23	100.7							
								1	1.5	1.5	0.0	1.5		
								2	1.5	1.5	1.5	3.0		
								3	1.1	1.1	3.0	4.1		
								CC(w/3)	0.13	0.13	4.1	4.23		
								Totals:	4.23	4.23				
2H	24	0430	4.2	13.7	9.5	9.95	104.7							
								1	1.5	1.5	4.2	5.7		
								2	1.5	1.5	5.7	7.2		
								3	1.5	1.5	7.2	8.7		
								4	1.5	1.5	8.7	10.2		
								5	1.5	1.5	10.2	11.7		
								6	1.5	1.5	11.7	13.2		
								7	0.72	0.72	13.2	13.92		
								CC(w/7)	0.23	0.23	13.92	14.15		
								Totals:	9.95	9.95				
3H	24	0550	13.7	23.2	9.5	9.81	103.3							
								1	1.5	1.5	13.7	15.2		
								2	1.5	1.5	15.2	16.7		Liner patch applied on working half
								3	1.5	1.5	16.7	18.2		
								4	1.5	1.5	18.2	19.7		
								5	1.5	1.5	19.7	21.2		
								6	1.5	1.5	21.2	22.7		
								7	0.58	0.58	22.7	23.28		
								CC(w/7)	0.23	0.23	23.28	23.51		
								Totals:	9.81	9.81				
4H	24	0740	23.2	32.7	9.5	9.91	104.3							
								1	1.5	1.5	23.2	24.7		
								2	1.5	1.5	24.7	26.2		
								3	1.5	1.5	26.2	27.7		
								4	1.5	1.5	27.7	29.2		
								5	1.5	1.5	29.2	30.7		
								6	1.5	1.5	30.7	32.2		
								7	0.65	0.65	32.2	32.85		
								CC(w/7)	0.26	0.26	32.85	33.11		
								Totals:	9.91	9.91				
5H	24	0855	32.7	42.2	9.5	9.55	100.5							
								1	1.5	1.5	32.7	34.2		
								2	1.5	1.5	34.2	35.7		
								3	1.5	1.5	35.7	37.2		
								4	1.5	1.5	37.2	38.7		
								5	1.5	1.5	38.7	40.2		
								6	1.5	1.5	40.2	41.7		

Table T2 (continued).

Core	Date (May 1999)	Ship local time	Depth (mbsf)		Length (m)		Recovery (%)	Section	Length (m)		Section (mbsf)		Catwalk samples	Comments
			Top	Bottom	Cored	Recovered			Liner	Curated	Top	Bottom		
6H	24	1035	42.2	51.7	9.5	9.87	103.9	7	0.5	0.5	41.7	42.2		
								CC(w/N)	0.05	0.05	42.2	42.25		
								Totals:	9.55	9.55				
								1	1.5	1.5	42.2	43.7		
								2	1.5	1.5	43.7	45.2		
								3	1.5	1.5	45.2	46.7		
								4	1.5	1.5	46.7	48.2		
								5	1.5	1.5	48.2	49.7		
								6	1.5	1.5	49.7	51.2		
								7	0.61	0.61	51.2	51.81		
7H	24	1150	51.7	61.2	9.5	9.58	100.8	CC(w/7)	0.26	0.26	51.81	52.07		
								Totals:	9.87	9.87				
								1	1.5	1.5	51.7	53.2		
								2	1.5	1.5	53.2	54.7		
								3	1.5	1.5	54.7	56.2		
								4	1.5	1.5	56.2	57.7		
								5	1.5	1.5	57.7	59.2		
								6	1.4	1.4	59.2	60.6		
								7	0.6	0.6	60.6	61.2		
								CC(w/N)	0.08	0.08	61.2	61.28		
8H	24	1320	61.2	70.7	9.5	9.94	104.6	Totals:	9.58	9.58				
								1	1.5	1.5	61.2	62.7		
								2	1.5	1.5	62.7	64.2		
								3	1.5	1.5	64.2	65.7		
								4	1.5	1.5	65.7	67.2		
								5	1.5	1.5	67.2	68.7		
								6	1.5	1.5	68.7	70.2		
								7	0.56	0.56	70.2	70.76		
								CC(w/7)	0.38	0.38	70.76	71.14		
								Totals:	9.94	9.94				
9H	24	1530	70.7	80.2	9.5	9.38	98.7	1	1.5	1.5	70.7	72.2		
								2	1.5	1.5	72.2	73.7		
								3	1.5	1.5	73.7	75.2		
								4	1.5	1.5	75.2	76.7		
								5	1.5	1.5	76.7	78.2		
								6	1.5	1.5	78.2	79.7		
								7	0.28	0.28	79.7	79.98		
								CC(w/N)	0.1	0.1	79.98	80.08		
								Totals:	9.38	9.38				
								10H	24	1800	80.2	89.7		
2	1.5	1.5	81.7	83.2										
3	1.5	1.5	83.2	84.7										
4	1.5	1.5	84.7	86.2										

Table T2 (continued).

Core	Date (May 1999)	Ship local time	Depth (mbsf)		Length (m)		Recovery (%)	Section	Length (m)		Section (mbsf)		Catwalk samples	Comments
			Top	Bottom	Cored	Recovered			Liner	Curated	Top	Bottom		
11H	24	1950	89.7	99.2	9.5	9.63	101.4	5	1.5	1.5	86.2	87.7		
								6	1.5	1.5	87.7	89.2		
								7	0.64	0.64	89.2	89.84		
								CC(w/7)	0.18	0.18	89.84	90.02		
								Totals:	9.82	9.82				
								1	1.5	1.5	89.7	91.2		
								2	1.5	1.5	91.2	92.7		
								3	1.5	1.5	92.7	94.2		
								4	1.5	1.5	94.2	95.7		
								5	1.5	1.5	95.7	97.2		
12H	24	2110	99.2	108.7	9.5	9.93	104.5	6	1.5	1.5	97.2	98.7		
								7	0.53	0.53	98.7	99.23		
								CC(w/N)	0.1	0.1	99.23	99.33		
								Totals:	9.63	9.63				
								1	1.5	1.5	99.2	100.7		
								2	1.5	1.5	100.7	102.2		
								3	1.55	1.55	102.2	103.75		
								4	1.5	1.5	103.75	105.25		
								5	1.5	1.5	105.25	106.75		
								6	1.5	1.5	106.75	108.25		
13H	24	2230	108.7	118.2	9.5	9.46	99.6	7	0.66	0.66	108.25	108.91		
								CC(w/7)	0.22	0.22	108.91	109.13		
								Totals:	9.93	9.93				
								1	1.5	1.5	108.7	110.2		
								2	1.5	1.5	110.2	111.7		
								3	1.5	1.5	111.7	113.2		
								4	1.5	1.5	113.2	114.7		
								5	1.3	1.3	114.7	116		
								6	0.48	0.48	116	116.48		
								7	1.5	1.5	116.48	117.98		
14H	24	2340	118.2	127.7	9.5	10.05	105.8	CC	0.18	0.18	117.98	118.16		Split liner, disturbed, not oriented
								Totals:	9.46	9.46				
								1	1.5	1.5	118.2	119.7		
								2	1.5	1.5	119.7	121.2		
								3	1.5	1.5	121.2	122.7		
								4	1.5	1.5	122.7	124.2		
								5	1.5	1.5	124.2	125.7		
								6	1.5	1.5	125.7	127.2		
								7	0.62	0.62	127.2	127.82		
								CC(w/7)	0.43	0.43	127.82	128.25		
15H	25	0055	127.7	137.2	9.5	9.85	103.7	Totals:	10.05	10.05				
								1	1.5	1.5	127.7	129.2		
								2	1.5	1.5	129.2	130.7		
								3	1.5	1.5	130.7	132.2		

Table T2 (continued).

Core	Date (May 1999)	Ship local time	Depth (mbsf)		Length (m)		Recovery (%)	Section	Length (m)		Section (mbsf)		Catwalk samples	Comments
			Top	Bottom	Cored	Recovered			Liner	Curated	Top	Bottom		
16H	25	0210	137.2	146.7	9.5	9.89	104.1	4	1.5	1.5	132.2	133.7		
								5	1.5	1.5	133.7	135.2		
								6	1.5	1.5	135.2	136.7		
								7	0.6	0.6	136.7	137.3		
								CC(w/7)	0.25	0.25	137.3	137.55		
								Totals:	9.85	9.85				
17H	25	0325	146.7	156.2	9.5	9.89	104.1	1	1.5	1.5	137.2	138.7		
								2	1.5	1.5	138.7	140.2		
								3	1.5	1.5	140.2	141.7		
								4	1.5	1.5	141.7	143.2		
								5	1.5	1.5	143.2	144.7		
								6	1.5	1.5	144.7	146.2		
								7	0.59	0.59	146.2	146.79		
CC(w/7)	0.3	0.3	146.79	147.09										
Totals:	9.89	9.89												
18H	25	0440	156.2	164.4	8.2	8.34	101.7	1	1.5	1.5	146.7	148.2		
								2	1.5	1.5	148.2	149.7		
								3	1.3	1.3	149.7	151		
								4	1.5	1.5	151	152.5		
								5	0.75	0.75	152.5	153.25		
								6	1.5	1.5	153.25	154.75		
								7	1.5	1.5	154.75	156.25		
CC	0.34	0.34	156.25	156.59										
Totals:	9.89	9.89												
19X	25	0650	164.4	169.8	5.4	1.79	33.1	1	1.5	1.5	156.2	157.7		
								2	1.5	1.5	157.7	159.2		
								3	1.5	1.5	159.2	160.7		
								4	1.5	1.5	160.7	162.2		
								5	1.5	1.5	162.2	163.7		
								6	0.66	0.66	163.7	164.36		
								CC(w/6)	0.18	0.18	164.36	164.54		
Totals:	8.34	8.34												
20X	25	0820	169.8	179.1	9.3	2.06	22.2	1	0.84	0.84	164.4	165.24		
								CC	0.95	0.95	165.24	166.19		
								Totals:	1.79	1.79				
21X	25	1010	179.1	188.7	9.6	1.21	12.6	1	1.5	1.5	169.8	171.3		
								CC	0.56	0.56	171.3	171.86		
								Totals:	2.06	2.06				
22X	25	1305	188.7	190.9	2.2	0.0	0.0	1	1.07	1.07	179.1	180.17		
								CC(w/1)	0.14	0.14	180.17	180.31		
								Totals:	1.21	1.21				

Liner damaged, replaced (not oriented, disturbed)

Table T2 (continued).

Core	Date (May 1999)	Ship local time	Depth (mbsf)		Length (m)		Recovery (%)	Section	Length (m)		Section (mbsf)		Catwalk samples	Comments
			Top	Bottom	Cored	Recovered			Liner	Curated	Top	Bottom		
23N	25	1625	190.9	191.2	0.3	0.3	100.0							
								1	0.24	0.24	190.9	191.14		
								CC(w/N)	0.06	0.06	191.14	191.2		
								Totals:	0.3	0.3				
Coring totals:					191.2	174.44	91.2							

Hole 1149B

Latitude: 31.34220°N (31°20.532'N)
Longitude: 143.35100°E (143°21.060'E)
Water depth (mbrf) (offset): 5829.30

Core	Date (May 1999)	Ship local time	Depth (mbsf)		Length (m)		Recovery (%)	Section	Length (m)		Section (mbsf)		Catwalk samples	Comments
			Top	Bottom	Cored	Recovered			Liner	Curated	Top	Bottom		
185-1149B-														
1W	26 27	2300 40	151.1	160.6	9.5	3.79	39.9							
			Drilled from 0.0 to 151.1 mbsf											
								1	1.5	1.5	151.1	152.6		
								2	1.5	1.5	152.6	154.1		
								3	0.56	0.56	154.1	154.66		
								CC(w/3)	0.23	0.23	154.66	154.89	PAL	
								Totals:	3.79	3.79				
2R	27	315	160.6	170.3	9.7	0.76	7.8							
								1	0.59	0.59	160.6	161.19	HS	
								CC(w/1)	0.17	0.17	161.19	161.36	PAL	
								Totals:	0.76	0.76				
3R	27	510	170.3	180	9.7	9.73	100.3							
								1	1.5	1.5	170.3	171.8	HIRONO	
								2	1.5	1.5	171.8	173.3		
								3	1.5	1.5	173.3	174.8		
								4	1.5	1.5	174.8	176.3	IW, SMITH	
								5	1.5	1.5	176.3	177.8	HS	
								6	1.5	1.5	177.8	179.3		
								7	0.63	0.63	179.3	179.93		
								CC(NS)	0.1	0.1	179.93	180.03	PAL	All to PAL
								Totals:	9.73	9.73				
4R	27	735	180.0	189.4	9.4	0.33	3.5							
								1	0.33	0.37	180.0	180.37	PAL, PAL, HIRONO	
								Totals:	0.33	0.37				
5R	27	950	189.4	198.7	9.3	0.12	1.3							
								1	0.12	0.16	189.4	189.56		
								Totals:	0.12	0.16				
6R	27	1145	198.7	203.7	5.0	0.32	6.4							
								1	0.32	0.44	198.7	199.14	PAL, PAL	
								Totals:	0.32	0.44				
7R	27	1335	203.7	208.1	4.4	0.43	9.8							
								1	0.43	0.43	203.7	204.13	PAL, SMITH, PAL	
								Totals:	0.43	0.43				

Table T2 (continued).

Core	Date (May 1999)	Ship local time	Depth (mbsf)		Length (m)		Recovery (%)	Section	Length (m)		Section (mbsf)		Catwalk samples	Comments
			Top	Bottom	Cored	Recovered			Liner	Curated	Top	Bottom		
8R	27	1615	208.1	217.4	9.3	0.09	1.0	1	0.09	0.14	208.1	208.24		
								Totals:	0.09	0.14				
9R	27	1825	217.4	226.8	9.4	0.40	4.3	1	0.4	0.56	217.4	217.96	PAL, HIRONO	
								Totals:	0.4	0.56				
10R	27	2035	226.8	236.3	9.5	0.21	2.2	1	0.21	0.31	226.8	227.11	PAL	
								Totals:	0.21	0.31				
11R	27	2305	236.3	245.4	9.1	0.22	2.4	1	0.22	0.3	236.3	236.6	PAL, PAL	
								Totals:	0.22	0.3				
12R	28	110	245.4	254.6	9.2	0.14	1.5	CC(w/CC)	0.14	0.14	245.4	245.54	PAL, HS	
								Totals:	0.14	0.14				
13R	28	325	254.6	263.9	9.3	0.12	1.3	1	0.12	0.15	254.6	254.75	PAL, PAL	
								Totals:	0.12	0.15				
14R	28	600	263.9	273.3	9.4	0.07	0.7	CC(w/CC)	0.07	0.1	263.9	264	PAL, HS, PAL	
								Totals:	0.07	0.1				
15R	28	915	273.3	282.3	9.0	0.03	0.3	1	0.03	0.03	273.3	273.33	PAL	
								Totals:	0.03	0.03				
16R	28	1625	282.3	292	9.7	1.11	11.4	1	1.06	1.18	282.3	283.48	PAL, SMITH, IW, PA	
								CC(NS)	0.05	0.05	283.48	283.53	PAL	
								Totals:	1.11	1.23				
17R	28	2000	292.0	301.6	9.6	0.22	2.3	1	0.22	0.26	292.0	292.26	PAL, PAL	
								Totals:	0.22	0.26				
18R	28	2250	301.6	311.3	9.7	1.10	11.3	1	1.1	1.3	301.6	302.9	PAL, PAL, HIRONO	
								Totals:	1.1	1.3				
19R	29	125	311.3	320.9	9.6	1.27	13.2	1	1.27	1.44	311.3	312.74	PAL, PAL, PAL, PAL	
								Totals:	1.27	1.44				
20R	29	405	320.9	330.5	9.6	1.22	12.7	1	1.22	1.42	320.9	322.32	IW, PAL, PAL	
								Totals:	1.22	1.42				
21R	29	655	330.5	340.1	9.6	0.17	1.8	CC(w/CC)	0.17	0.17	330.5	330.67	PAL	
								Totals:	0.17	0.17				
22R	29	910	340.1	349.7	9.6	0.98	10.2	1	0.98	1.18	340.1	341.28	IW, PAL, SMITH, PAL	
								Totals:	0.98	1.18				
23R	29	1135	349.7	359.2	9.5	0.27	2.8	CC(w/CC)	0.27	0.36	349.7	350.06	PAL	
								Totals:	0.27	0.36				

Table T2 (continued).

Core	Date (May 1999)	Ship local time	Depth (mbsf)		Length (m)		Recovery (%)	Section	Length (m)		Section (mbsf)		Catwalk samples	Comments
			Top	Bottom	Cored	Recovered			Liner	Curated	Top	Bottom		
24R	29	1410	359.2	368.7	9.5	0.66	6.9							
								1	0.66	0.86	359.2	360.06	PAL, PAL, PAL, PAL	
								Totals:	0.66	0.86				
25R	29	1650	368.7	378.1	9.4	0.25	2.7							
								1	0.25	0.28	368.7	368.98	PAL	
								Totals:	0.25	0.28				
26R	29	1905	378.1	387.6	9.5	0.73	7.7							
								1	0.73	0.87	378.1	378.97	PAL, PAL, PAL, SMI	
								Totals:	0.73	0.87				
27R	29	2200	387.6	397.1	9.5	0.89	9.4							
								1	0.89	0.95	387.6	388.55	PAL, SMITH, IW, PA	
								Totals:	0.89	0.95				
28R	30	345	397.1	406.8	9.7	2.37	24.4							
								1	1.5	1.32	397.1	398.42	PAL, PAL, PAL	
								2	0.87	1.39	398.42	399.81	PAL, SMITH, PFCTS	
								Totals:	2.37	2.71				
29R	30	1050	406.8	416.4	9.6	3.16	32.9							
								1	1.28	1.5	406.8	408.3	PAL, PRESS2, IW, P	
								2	1.5	1.41	408.3	409.71	PAL	
								3	0.38	0.94	409.71	410.65		
								Totals:	3.16	3.85				
30R	30	1630	416.4	426	9.6	3.19	33.2							
								1	1.5	1.5	416.4	417.9		
								2	1.5	1.35	417.9	419.25		
								3	0.19	0.69	419.25	419.94		
								Totals:	3.19	3.54				
31R	30	2215	426.0	435.6	9.6	1.25	13.0							
								1	1.25	1.5	426.0	427.5		
								2	0.0	0.1	427.5	427.6		
								Totals:	1.25	1.6				
32R	31	420	435.6	445.2	9.6	1.12	11.7							
								1	1.12	1.43	435.6	437.03		
								Totals:	1.12	1.43				
Coring totals:						294.1	36.72	12.5						

Hole 1149C

Latitude: 31.34251°N (31°20.550'N)
Longitude: 143.35100°E (143°24.024'E)
Depth (mbrf) (offset): 5829.3

Core	Date (June 1999)	Ship local time	Depth (mbsf)		Length (m)		Recovery (%)	Section	Length (m)		Section (mbsf)		Catwalk samples	Comments
			Top	Bottom	Cored	Recovered			Liner	Curated	Top	Bottom		
185-1149C- 1W	3	1610	0.0	237.0	237.0	1.63	0.7							
								1	1.23	1.23	0.0	1.23		
								2	0.40	0.60	1.2	1.83		
								Totals:	1.63	1.83				

Table T2 (continued).

Core	Date (June 1999)	Ship local time	Depth (mbsf)		Length (m)		Recovery (%)	Section	Length (m)		Section (mbsf)		Catwalk samples	Comments
			Top	Bottom	Cored	Recovered			Liner	Curated	Top	Bottom		
2W	3	2200	237.0	283.6	46.6	0.22	0.5							
								1	0.22	0.35	237.0	237.35		
								Totals:	0.22	0.35				
3R	4	0320	283.6	293.2	9.6	0.46	4.8							
								1	0.46	0.61	283.6	284.21		
								Totals:	0.46	0.61				
4R	4	0840	293.2	302.8	9.6	0.25	2.6							
								1	0.25	0.39	293.2	293.59		
								Totals:	0.25	0.39				
5R	4	1715	302.8	312.4	9.6	0.3	3.1							
								1	0.30	0.36	302.8	303.16	PAL	
								Totals:	0.30	0.36				
6R	4	1930	312.4	322.0	9.6	0.48	5.0							
								1	0.48	0.63	312.4	313.03	PAL	
								Totals:	0.48	0.63				
7W	5	0200	322.0	388.2	66.2	0.46	0.7							
								1	0.46	0.55	322.0	322.55	PAL	
								Totals:	0.46	0.55				
8R	5	1010	388.2	397.9	9.7	0.96	9.9							
								1	0.96	0.96	388.2	389.16	PAL, PFCTST, SMIT	
								Totals:	0.96	0.96				
9R	5	2205	397.9	407.5	9.6	1.00	10.4							
								1	1.00	1.10	397.9	399.00	PFCTST, PAL, PFCT	
								Totals:	1.00	1.10				
10R	6	0330	407.5	417.1	9.6	1.60	16.7							
								1	1.36	1.50	407.5	409.00		
								2	0.24	0.52	409.0	409.52	PRESS2	
								Totals:	1.60	2.02				
11R	6	1235	417.1	426.7	9.6	1.34	14.0							
								1	1.34	1.38	417.1	418.48		
								Totals:	1.34	1.38				
Coring totals:					426.7	8.70	2.0							

Hole 1149D

Latitude: 31.31320°N (31°18.79200'N)
Longitude: 143.4004059°E (143°4.02435'E)
Depth (mbrf) (offset): 5879.00

Core	Date (June 1999)	Ship local time	Depth (mbsf)		Length (m)		Recovery (m)	Section	Length (m)		Section (mbsf)		Catwalk samples	Comments
			Top	Bottom	Cored	Recovered			Liner	Curated	Top	Bottom		
185-1149D-1W	8	0610	0.0	272.2										
								1	1.19	1.48	0	1.48		
								2	0.00	0.12	1.48	1.60		
								Totals:	1.19	1.60				

Table T2 (continued).

Core	Date (June 1999)	Ship local time	Depth (mbsf)		Length (m)		Recovery (m)	Section	Length (m)		Section (mbsf)		Catwalk samples	Comments
			Top	Bottom	Cored	Recovered			Liner	Curated	Top	Bottom		
2R	8	0830	272.2	281.6	9.4	0.29	3.1							
								1	0.29	0.38	272.20	272.58		
								Totals:	0.29	0.38				
3R	8	1040	281.6	290.9	9.3	0.31	3.3							
								1	0.31	0.36	281.60	281.96		
								Totals:	0.31	0.36				
4R	8	1330	290.9	300.3	9.4	0.63	6.7							
								1	0.63	0.78	290.90	291.68		
								Totals:	0.63	0.78				
5R	8	1945	300.3	310.0	9.7	0.3	3.1							
								1	0.30	0.41	300.30	300.71		
								Totals:	0.30	0.41				
6R	9	0255	310.0	319.7	9.7	2.07	21.3							
								1	0.75	1.35	310.00	311.35		
								2	1.32	1.06	311.35	312.41		
								Totals:	2.07	2.41				
7R	9	0745	319.7	329.3	9.6	2.84	29.6							
								1	1.05	1.50	319.70	321.20		
								2	1.45	1.45	321.20	322.65		
								3	0.34	0.29	322.65	322.94		
								Totals:	2.84	3.24				
8R	9	1755	329.3	338.8	9.5	3.03	31.9							
								1	1.50	1.50	329.30	330.80		
								2	1.53	1.50	330.80	332.30		
								Totals:	3.03	3.00				
9R	10	0045	338.8	348.4	9.6	2.75	28.6							
								1	0.90	1.18	338.80	339.98		
								2	1.44	1.50	339.98	341.48		
								3	0.41	0.65	341.48	342.13		
								Totals:	2.75	3.33				
10R	10	0645	348.4	357.9	9.5	2.01	21.2							
								1	0.53	1.50	348.40	349.90		
								2	1.48	0.58	349.90	350.48		
								Totals:	2.01	2.08				
11R	10	1225	357.9	367.4	9.5	4.6	48.4							
								1	1.50	1.34	357.90	359.24		
								2	1.50	1.43	359.24	360.67		
								3	1.50	1.47	360.67	362.14		
								4	0.10	0.55	362.14	362.69		
								Totals:	4.60	4.79				
12R	10	1655	367.4	377.0	9.6	0.6	6.3							
								1	0.60	0.67	367.40	368.07		
								Totals:	0.60	0.67				
13R	10	2215	377.0	386.6	9.6	1.27	13.2							
								1	1.27	1.50	377.00	378.50		
								Totals:	1.27	1.50				
14R	11	1030	386.6	396.3	9.7	0.36	3.7							
								1	0.36	0.45	386.60	387.05		
								Totals:	0.36	0.45				

Table T2 (continued).

Core	Date (June 1999)	Ship local time	Depth (mbsf)		Length (m)		Recovery (m)	Section	Length (m)		Section (mbsf)		Catwalk samples	Comments
			Top	Bottom	Cored	Recovered			Liner	Curated	Top	Bottom		
15R	11	1645	396.3	405.9	9.6	0.8	8.3							
								1	0.80	0.96	396.30	397.26		
								Totals:	0.80	0.96				
16R	11	2225	405.9	415.5	9.6	2.69	28							
								1	0.90	1.48	405.90	407.38		
								2	1.50	1.50	407.38	408.88		
								3	0.29	0.36	408.88	409.24		
								Totals:	2.69	3.34				
17R	12	0515	415.5	425.1	9.6	1.61	16.8							
								1	1.29	1.50	415.50	417.00		
								2	0.32	0.84	417.00	417.84		
								Totals:	1.61	2.34				
18R	12	1125	425.1	434.7	9.6	1.59	16.6							
								1	1.59	1.40	425.10	426.50		
								Totals:	1.59	1.40				
19R	12	1610	434.7	440.4	5.7	1.00	17.5							
								1	1.00	1.15	434.70	435.85		
								Totals:	1.00	1.15				
Coring totals:					168.2	29.94	17.8							

Note: This table is also available in [ASCII format](#).

Table T3. Lithologic units, Site 1149.

Unit/ Subunit	Cored intervals	Depth intervals (mbsf)	Thickness (m)	Lithology	Age
I	1149A-1H, 0 cm, to 13H-CC, 19 cm	0.0-118.2	118.2	Ash- and biogenic silica-bearing clay	late Pleistocene to late Miocene
IIA	1149A-14H-1, 0 cm, to 17H-2, 132 cm	118.2-149.5	31.3	Dark brown pelagic clay with ash layers	Unknown
IIB	1149A-17H-2, 132 cm, to 20X-CC, 55 cm	149.5-179.1	30.5	Dark brown pelagic clay	Unknown
	1149B-2R-1, 0 cm, to 3R-CC, 10 cm	160.6-180.0	30.5		
III	1149A-21X-1, 0 cm, to 23X-CC, 6 cm	179.1-191.5	103.8	Interbedded chert, porcelanite, and siliceous clay	Unknown
	1149B-4R-1, 0 cm, to 16R-1, 63 cm	180.6-282.9	103.8		
IV	1149B-16R-1, 63 cm, to 29R-1, 93 cm	282.9-407.8	125.5	Interbedded radiolarian chert and radiolarian nannofossil marl	late Hauterivian to late Valanginian
	1149C-3R-1, 0 cm, to 15R-1, 3 cm	283.6-400.7	125.5		
	1149D-2R-1, 0 cm, to 5R-1, 16 cm	272.2-300.5			
V	1149B-29R-1, 93 cm, to 29R-2, 139 cm	407.7-408.2	2.0	Fracture filling (meta)sediment in basalt	late Valanginian

Table T4. Carbonate content of sediments, Hole 1149B.

Core, section, interval (cm)	Depth (mbsf)	CaCO ₃ (wt%)
185-1149B-		
16R-1, 18-21	282.48	0.18
16R-1, 63-64	282.93	0.39
16R-1, 83-86	283.13	28.10
16R-1, 101-103	283.31	10.69
17R-1, 9-12	292.09	4.77
18R-1, 9-11	301.69	4.75
18R-1, 105-108	302.65	1.55
19R-1, 16-17	311.46	47.92
19R-1, 20-21	311.50	35.99
19R-1, 129-131	312.59	78.76
20R-1, 13-14	321.03	17.71
22R-1, 42-49	340.52	69.28
27R-1, 48-49	388.08	86.79
28R-1, 40-41	397.50	88.92
28R-1, 98-100	398.08	91.08
28R-1, 116-118	398.26	87.35
28R-2, 10-11	398.52	89.74
28R-2, 116-118	399.58	88.83
29R-1, 3-4	406.83	88.60
29R-1, 18-19	406.98	83.72
29R-1,80-82	407.60	66.94
29R-1, 134-135	408.14	66.64

Note: This table is also available in [ASCII format](#).

Table T5. Igneous core description logs, Holes 1149B, 1149C, and 1149D. (See table notes. Continued on next six pages.)

Core, section numbers	Piece numbers	Analysis	Depth (mbsf)		Interval (cm)	Length (cm)			Subunit number	Lithology	Texture	Structure	Color	Comments	Chilled margin present	
			Top	Bottom		Interval	Unit	Subunit							Top	Base
185-1149B-																
29R-1		PP	406.80	407.77	0-97	97	—	—	—	Sediment	—	Sediment	Pink	Carbonate-rich sediment	—	N
29R-1		—	407.77	408.28	97-148	51	942	78	1-1	Aphyric basalt breccia with sediment cement	Microcrystalline		Dark bluish gray and reddish gray	Contact with overlying sediment not observed, altered basalts with halos around veins	N	N
29R-2	1	TSB(2), PP	408.28	408.55	0-27	27	942	78	1-1	Pink carbonate cement	Microcrystalline	Basalt breccia sediment cement	Dark bluish gray and reddish gray with dark reddish gray veins	Basalt breccia has clasts up to 20 cm and fine-grained pink sedimentary carbonate cement	N	N
29R-2	2-10	—	408.55	409.23	27-95	68	942	68	1-2	Aphyric basalt	Microcrystalline	Pillow/flow	Dark bluish gray and reddish gray	Basalt pieces with halos, rubbly interval	N	N
29R-2	11-14	TSB	409.23	409.68	95-140	45	942	45	1-3	Aphyric basalt	Hypocrystalline to microcrystalline	Pillow	Dark bluish gray and reddish gray	Dark bluish gray halos around dusky red veins and reddish gray altered basalt, chill at base	N	Y
29R-3	1-3	—	409.68	410.11	0-43	43	942	43	1-4	Aphyric basalt	Fine grained to microcrystalline	Pillow	Dark bluish gray and reddish gray	Dark dusky red veins, dark bluish gray halos, reddish gray altered basalt, chill at base	N	Y
29R-3	4-8	XRF	410.11	410.62	43-94	51	942	51	1-5	Aphyric basalt	Microcrystalline	Pillow	Dark bluish gray and reddish gray	Dark dusky red veins, dark bluish gray halos, reddish gray altered basalt, rubbly	N	N
30R-1	1-9	—	416.40	416.95	0-55	55	942	55	1-6	Aphyric basalt	Microcrystalline	Pillow	Dark bluish gray and reddish gray	Fe oxyhydroxides between reddish gray altered basalt and dark bluish gray halos	N	N
30R-1	10A-12	—	416.95	417.44	55-104	49	942	49	1-7	Aphyric basalt	Microcrystalline basalt	Pillow breccia	Dark greenish grey and gray, dusky red	Carbonate cement with <1-cm dusky red and dark green fragments, chilled piece at base	N	Y
30R-1	13-19	—	417.44	417.90	104-150	46	942	46	1-8	Aphyric basalt	Fine grained to microcrystalline	Pillow	Dark bluish gray and reddish gray	Dark greenish gray veins, halos present; altered basalt is dark dusky red in some pieces	N	N
30R-2	1-4	XRF	417.90	419.02	0-112	112	942	112	1-9	Aphyric basalt	Fine grained to microcrystalline	Pillow/flow	Dark bluish gray and reddish gray	Lower rim of pillow is subvertical and highly irregular	N	Y
30R-2	4-7	—	419.02	419.25	112-135	23	942	40	1-10	Aphyric basalt pillows, interpillow breccia	Microcrystalline basalt		Dark reddish gray and dark greenish gray, altered pillow rims white carbonate	Carbonate infilling irregular chilled pillow margin	N	N
30R-3	1	—	419.25	419.42	0-17	17	942	40	1-10	Carbonate-bearing cement	Coarse carbonate			Various chills and pillow rims, brecciated glassy contact between two pillows at base of subunit	N	N
30R-3	2-9	—	419.42	419.94	17-69	52	942	52	1-11	Aphyric basalt	Microcrystalline	Pillow	Dark reddish gray	Top of Subunit 1-11 is rubbly, chill at top	Y	N

Table T5 (continued).

Core, section	Piece numbers	Analysis	Depth (mbsf)		Interval (cm)	Length (cm)			Subunit number	Lithology	Texture	Structure	Color	Comments	Chilled margin present	
			Top	Bottom		Interval	Unit	Subunit							Top	Base
31R-1	1-22	—	426.00	427.20	0-120	120	942	120	1-12	Breccia	Microcrystalline to hypocrystalline	Pillow breccia	Dark greenish gray and gray, dusky red	Green concentric alteration in rounded basalt fragments, red matrix, various glassy chills, rubbly	N	N
31R-1	23-26	—	427.20	427.50	120-150	30	942	40	1-13	Aphyric basalt	Microcrystalline		Gray to light brownish gray	Dusky red veins and carbonate veins, dark bluish gray halos, reddish gray altered basalt, rubbly	N	N
31R-2	1	—	427.50	427.60	0-10	10	942	40	1-13	Aphyric basalt	Microcrystalline	Pillow	Gray to light brownish gray	Fractured carbonate veins, dark bluish gray halos, reddish gray altered basalt	N	N
32R-1	1-4	—	435.60	436.19	0-59	59	942	59	1-14	Aphyric basalt	Microcrystalline	Pillow	Reddish gray to greenish gray	Dusky red veins, carbonate veins, dark bluish gray halos, reddish gray altered basalt, rubbly	N	Y?
32R-1	5-17	—	436.19	437.03	59-143	84	942	84	1-15	Aphyric basalt	Microcrystalline to fine grained at base	Pillow/flow	Reddish gray to greenish gray	Dusky red veins, carbonate veins, dark bluish gray halos, reddish gray altered basalt, rubbly	Y?	N
185-1149C-9R-1	—	—	397.90	398.41	0-51	51	—	—	—	Sediment	-	Sediment	Beige brown	Cherty sediment	N	N
9R-1	1-8	—	398.41	399.00	51-110	59	399	59	1-1	Aphyric basalt	Microcrystalline	Pillow	Dark bluish gray, reddish gray	Contact with overlying cherty sediment not observed, altered basalts with halos around veins, rubbly	N	N
10R-1	1-10	—	407.50	408.22	0-72	72	—	72	1-2	Aphyric basalt	Microcrystalline	Pillow/flow	Dark bluish gray, reddish gray	Chilled pillow rim at top, some carbonate veins, dark bluish gray halos, reddish gray altered basalt	Y	Y
10R-1	11-16	—	408.22	408.55	72-105	33	—	33	1-3	Aphyric basalt	Microcrystalline	Pillow	Dark bluish gray, reddish gray	Chilled pillow rim at top, basalt pieces with halos, contact with carbonate breccia cement at base not chilled	Y	N
10R-1	16-22	—	408.55	409.00	105-150	45	—	87	1-4	Breccia	Microcrystalline basalt fragments	Breccia	Dark bluish gray, reddish gray	Carbonate breccia matrix with 2.5 to 20 cm subangular to angular microcrystalline basalt fragments	N	N
10R-2	1-9	—	409.00	409.42	0-42	42	—	87	1-4	Breccia	Microcrystalline basalt fragments	Breccia	Dark bluish gray, reddish gray	Carbonate breccia matrix with 2.5 to 20 cm subangular to angular microcrystalline basalt fragments	N	N
10R-2	9-10	—	409.42	409.52	42-52	10	—	54	1-5	Aphyric basalt	Fine grained to microcrystalline	Pillow	Dark bluish gray, reddish gray	Dark dusky red veins, dark bluish gray halos, reddish gray altered basalt, rubbly	Y	N
11R-1	1A-3	—	417.10	417.54	0-44	44	—	54	1-5	Aphyric basalt	Fine grained to microcrystalline	Pillow	Dark bluish gray, reddish gray	Dark bluish gray halos around dusky red veins, reddish gray altered basalt, chill at base	N	Y

Table T5 (continued).

Core, section	Piece numbers	Analysis	Depth (mbsf)		Interval (cm)	Length (cm)			Subunit number	Lithology	Texture	Structure	Color	Comments	Chilled margin present	
			Top	Bottom		Interval	Unit	Subunit							Top	Base
11R-1	3-13	—	417.54	418.48	44-138	94	—	94	1-6	Aphyric basalt	Fine grained to microcrystalline	Pillow/flow	Dark bluish gray, reddish gray	Altered hyaloclastite at top, dark dusky red veins, dark bluish gray halos, reddish gray altered basalt	Y	N
185-1149D-5R-1	—	—	300.30	300.46	0-16	16	—	—	—	Sediment	Fine-grained chert	Sediment	Red brown	Cherty sediment, contact with basement not recovered	N	N
5R-1	1	—	300.46	300.52	16-22	6	6	—	1	Aphyric basalt	Microcrystalline	Pillow	Dark bluish gray, reddish gray	More olivine phenocrysts, different alteration style	N	N
5R-2	2-5	—	300.52	300.71	22-41	19	747	288	2-1	Aphyric basalt	Microcrystalline	Flow	Dark bluish gray, reddish gray	Small pieces with pronounced halos, speckled appearance	N	N
6R-1	1-21	—	310.00	311.34	0-134	134	—	—	—	Aphyric basalt	Microcrystalline	Flow	Reddish gray, bluish gray	Red veins, halos, speckled appearance, no chills	N	N
6R-2	1-11	—	311.34	312.40	0-106	106	—	—	—	Aphyric basalt	Microcrystalline	Flow	Reddish gray, bluish gray	Very pronounced halos, carbonate veins, no chills	N	N
7R-1	1-4	—	319.70	319.99	0-29	29	—	—	—	Aphyric basalt	Microcrystalline	Flow	Reddish gray, bluish gray	Fractured pieces with dark red veins and carbonate veins	N	N
7R-1	5	—	319.99	320.12	29-42	13	—	13	2-2	Hyaloclastite	Hypocrystalline	Breccia	Dark green	Elongate green clasts with red rims, clasts up to 3-4 cm long in a green matrix, cement supported	N	N
7R-1	6-7	—	320.12	320.26	42-56	14	—	14	2-3	Aphyric basalt	Microcrystalline	Pillow	Reddish gray, bluish gray	Two pieces, not oriented; there may be material missing	N	Y
7R-1	8-9	—	320.26	320.40	56-70	14	—	14	2-4	Aphyric basalt	Microcrystalline	Pillow	Reddish gray, bluish gray	Two pieces, not oriented; there may be material missing	Y	N
7R-1	10	—	320.40	320.45	70-75	5	—	5	2-5	Hyaloclastite	Hypocrystalline	Breccia	Dark green and white	Dark green altered glassy clasts; cement is carbonate with some pale greenish clays	N	N
7R-1	11-20	—	320.45	321.20	75-150	75	—	75	2-6	Aphyric basalt	Microcrystalline	Pillow/flow	Reddish gray, bluish gray	Pronounced halos, dark red veins, carbonate veins	N	N
7R-2	1-6	—	321.20	321.75	0-55	55	—	55	2-7	Aphyric basalt	Microcrystalline	Pillow/flow	Reddish gray, bluish gray	Small pieces at top and one fractured piece, pronounced halos, dark red veins, carbonate veins	N	Y
7R-2	7-16	—	321.75	322.40	55-120	65	—	65	2-8	Aphyric basalt	Microcrystalline	Pillow/flow	Reddish gray, bluish gray	2-cm interpillow material and glass at top, halos, carbonate veins, red veins throughout	Y	Y
7R-2	16-20	—	322.40	322.64	120-144	24	—	53	2-9	Aphyric basalt	Microcrystalline	Pillow/flow	Reddish gray, bluish gray	Rubbly and fractured basalt pieces, chill with small amounts of glass in the top piece	Y	N

Table T5 (continued).

Core, section	Piece numbers	Analysis	Depth (mbsf)		Interval (cm)	Length (cm)			Subunit number	Lithology	Texture	Structure	Color	Comments	Chilled margin present	
			Top	Bottom		Interval	Unit	Subunit							Top	Base
7R-3	1-3	—	322.64	322.93	0-29	29	—			Aphyric basalt	Microcrystalline	Pillow/flow	Reddish gray, bluish gray	1-cm-wide vein with carbonate or recrystallized interpillow material and a very small amount of breccia	N	N
8R-1	1-15	—	329.30	330.80	0-150	150	—	165	2-10	Aphyric basalt	Microcrystalline	Flow	Reddish gray, bluish gray	Pronounced halos, dark red veins, carbonate veins	N	N
8R-2	1	—	330.80	330.95	0-15	15	—			Aphyric basalt	Microcrystalline	Flow	Reddish gray, bluish gray	One fractured piece with pronounced halos, dark red veins, carbonate veins	N	N
8R-2	2	—	330.95	331.35	15-55	40	713	40	3-1	Aphyric basalt	Microcrystalline	Pillow	Reddish gray, bluish gray	4 cm of interpillow material at top with wavy contact; basalt has a slightly speckled appearance	Y	Y
8R-2	3	—	331.35	331.40	55-60	5	—	5	3-2	Hyaloclastite	Microcrystalline basalt	Breccia	Dark green and white	Glass and altered glass clasts in a carbonate matrix	Y	Y
8R-2	4-8	—	331.40	331.81	60-101	41	—	41	3-3	Aphyric basalt	Microcrystalline	Pillow	Reddish gray, bluish gray	Thin dark red veins, carbonate veins, halos present	Y	N
8R-2	9-13	—	331.81	332.22	101-142	41	—	41	3-4	Aphyric basalt	Microcrystalline, hypocrySTALLINE at base	Pillow	Reddish gray, bluish gray	Thin dark red veins, carbonate veins, halos present	Y	N
9R-1	1-2	—	338.80	338.90	0-10	10	—	10	3-5	Aphyric basalt	Microcrystalline	Pillow	Reddish gray, bluish gray	Subvertical glassy chill on Piece 2, dark red veins, carbonate veins, halos present	N	Y
9R-1	3-6	—	338.90	339.15	10-35	25	—	25	3-6	Aphyric basalt	Microcrystalline	Pillow	Reddish gray, bluish gray	Small pieces with chills near vertical pillow contact or pile of pillows with material not recovered	Y	Y
9R-1	7-10	—	339.15	339.46	35-66	31	—	31	3-7	Aphyric basalt	Microcrystalline	Pillow	Reddish gray, orange, bluish gray	Dark bluish gray halos with orange-brown Fe oxyhydroxide zone adjacent to reddish gray basalt	Y	Y
9R-1	11-18	—	339.46	339.98	66-118	52	—	52	3-8	Aphyric basalt	Microcrystalline	Pillow/flow	Reddish gray, orange, greenish gray	Abundant carbonate veins, horizontal glassy chill at the base	Y	Y
9R-2	1-4	—	339.98	340.69	0-71	71	—	71	3-9	Aphyric basalt	Microcrystalline with fine-grained center	Pillow/flow	Reddish gray, bluish gray	Pronounced halos, abundant dark red veins and carbonate veins, horizontal chill at the base	N	Y
9R-2	5-16	—	340.69	341.48	71-150	79	—	79	3-10	Aphyric basalt	Microcrystalline with fine-grained center	Pillow/flow	Reddish gray, bluish gray	Glassy chill on pieces at top and base, thin dark red veins, carbonate veins, halos present	Y	Y
9R-3	1-10	—	341.48	342.13	0-65	65	—	92	3-11	Aphyric basalt	Microcrystalline	Pillow/flow	Reddish gray, bluish gray, gray	Dark bluish gray halos with orange-brown Fe oxyhydroxide zone adjacent to reddish gray basalt, carbonate, red veins	N	N

Table T5 (continued).

Core, section	Piece numbers	Analysis	Depth (mbsf)		Interval (cm)	Length (cm)			Subunit number	Lithology	Texture	Structure	Color	Comments	Chilled margin present	
			Top	Bottom		Interval	Unit	Subunit							Top	Base
10R-1	1-4	—	348.40	348.67	0-27	27	—			Aphyric basalt	Microcrystalline	Pillow/flow	Reddish gray, bluish gray, gray	Dark bluish gray halos with orange brown Fe oxyhydroxide zone adjacent to reddish gray basalt, carbonate, red veins	N	N
10R-1	5	—	348.67	348.73	27-33	6	—	6	3-12	Hyaloclastite	Hypocrystalline altered basalt clasts	Breccia	Dark greenish gray, white	Breccia with carbonate matrix and light greenish gray clays, clasts up to 5 cm	N	N
10R-1	6A-6C	—	348.73	349.47	33-107	74	—	74	3-13	Aphyric basalt	Microcrystalline with fine-grained center	Pillow/flow	Greenish gray	One coherent piece, halos present but more diffuse	N	N
10R-1	7-8	—	349.47	349.70	107-130	23	—	23	3-14	Aphyric basalt	Microcrystalline	Pillow	Dark greenish gray white, gray	Contains some brecciated pieces with carbonate cement, mix of large fractured clasts and small ones	N	N
10R-1	9-10	—	349.70	349.90	130-150	20	—	35	3-15	Aphyric basalt	Microcrystalline	Pillow	Greenish gray to gray	Pronounced halos, dark red veins, carbonate veins	N	N
10R-2	1	—	349.90	350.05	0-15	15	—			Aphyric basalt	Microcrystalline	Pillow	Greenish gray to gray	Pronounced halos, dark red veins, carbonate veins	N	N
10R-2	2-7	—	350.05	350.49	15-59	44	—	56	3-16	Aphyric basalt	Microcrystalline	Pillow	Greenish gray to gray	Rubbly pieces, some brecciated pieces with carbonate cement	N	N
11R-1	1-2	—	357.90	358.02	0-12	12	—			Aphyric basalt	Microcrystalline	Pillow	Greenish gray to gray	Rubbly pieces, some brecciated pieces with carbonate cement	N	N
11R-1	3-6	—	358.02	358.34	12-44	32	—	32	3-17	Hyaloclastite	Microcrystalline to hypocrystalline clasts, fine clay cement	Breccia	Dark green with weak red alteration	Variable clast size 1 mm up to 5 cm, dark grayish green altered glass clasts with light greenish gray matrix	N	N
11R-1	7-14	—	358.34	359.24	44-134	90	652	233	4-1	Aphyric basalt	Microcrystalline to hypocrystalline	Flow	Variable gray to very dark gray	?Flow top, highly altered with irregular carbonate-filled void spaces, rusty brown to dark brown veins	N	N
11R-2	1-10	—	359.24	360.67	0-143	143	—			Aphyric basalt	Microcrystalline to hypocrystalline	Flow	Variable gray to very dark gray	Four thin <5-cm intervals of fine breccia with carbonate cement, highly altered with irregular carbonate-filled voids	N	N
11R-3	1-6	—	360.67	362.14	0-147	147	—	147	4-2	Breccia	Microcrystalline to hypocrystalline clasts, coarse cement	Breccia	Gray to very dark gray, white	One piece (#4) is similar to hyaloclastite in Subunit 3-17; breccia has subangular frayed clasts of variable size	N	N
11R-4	1-6	—	362.14	362.69	0-55	55	—	91	4-3	Aphyric basalt	Microcrystalline	Flow	Variable gray to very dark gray	Pronounced halos present in some pieces, dark red veins, carbonate veins	N	N
12R-1	1-9	—	367.40	367.76	0-36	36	—			Aphyric basalt	Microcrystalline	Flow	Reddish gray, bluish gray, gray	Rubbly subunit with some brecciated pieces, several carbonate-filled voids	N	N

Table T5 (continued).

Core, section	Piece numbers	Analysis	Depth (mbsf)		Interval (cm)	Length (cm)			Subunit number	Lithology	Texture	Structure	Color	Comments	Chilled margin present	
			Top	Bottom		Interval	Unit	Subunit							Top	Base
12R-1	9-13	—	367.76	368.07	36-67	31	—	31	4-4	Aphyric basalt	Microcrystalline	Pillow	Reddish gray, bluish gray, gray	Rubby subunit with some brecciated pieces, several carbonate-filled voids	Y	N
13R-1	1-2	—	377.00	377.26	0-26	26	—	26	4-5	Hyaloclastite	Microcrystalline to hypocrySTALLINE clasts, fine clay cement	Breccia	Dark green with weak red alteration	Dark greenish gray matrix, variable clast size 1 mm to 5 cm; clasts are subrounded altered glass	N	N
13R-1	3-12	—	377.26	377.83	26-83	57	—	57	4-6	Aphyric basalt	Microcrystalline	Pillow	Variable gray to very dark gray	Fractured rubby pieces; some are brecciated; carbonate veins present; basalt has a mottled appearance	N	N
13R-1	13-16	—	377.83	378.08	83-108	25	—	25	4-7	Hyaloclastite	Microcrystalline to hypocrySTALLINE clasts, fine clay matrix	Breccia	Dark green and very dark gray	Clast-supported hyaloclastite with small green altered glass clasts and very dark gray basalt clasts up to 5 cm	N	N
13R-1	17-22	—	378.08	378.50	108-150	42	—	42	4-8	Aphyric basalt	Microcrystalline	Pillow	Variable gray to very dark gray	Fractured rubby pieces, highly altered with mottled appearance, irregular carbonate-filled vesicles up to 1 cm long	N	N
14R-1	1-2	—	386.60	386.72	0-12	12	649	12	5-1	Aphyric basalt	Microcrystalline	Pillow	Gray to bluish gray	Rubby pieces, halos present in some pieces, thin dark red veins, carbonate veins	N	N
14R-1	3-4	—	386.72	386.84	12-24	12	—	12	5-2	Breccia	Microcrystalline to hypocrySTALLINE	Breccia	Dark greenish gray and white	Hyaloclastite with small green altered glass clasts and very dark gray basalt clasts up to 5 cm, carbonate and clay matrix	N	N
14R-1	5-8	—	386.84	387.05	24-45	21	—	21	5-3	Aphyric basalt	Microcrystalline	Pillow	Gray to bluish gray	Rubby pieces, halos present in some pieces, thin dark red veins, carbonate veins	N	N
15R-1	1-3	—	396.30	396.47	0-17	17	—	17	5-4	Breccia	Microcrystalline	Breccia	Greenish gray to bluish gray	Small rubby hyaloclastite pieces with green altered glass clasts and very dark gray basalt clasts, green clay cement	N	N
15R-1	4-15	—	396.47	397.26	17-96	79	—	79	5-5	Aphyric basalt	Microcrystalline	Pillow	Gray to bluish gray	Rubby pieces, pronounced halos present in some pieces, thin dark red veins, carbonate veins	N	N
16R-1	1-21	—	405.90	407.40	0-150	150	—	273	5-6	Breccia	Microcrystalline to hypocrySTALLINE	Breccia	Dark greenish, very dark gray	Clast-supported breccia/hyaloclastite with small green altered glass clasts and very dark gray basalt clasts, variable size	N	N
16R-2	1-9	—	407.40	408.63	0-123	123	—			Breccia	Microcrystalline to hypocrySTALLINE	Breccia	Variable very dark gray, white	Clast-supported breccia with very dark gray basalt clasts, variable size, sub-mm to 10 cm, clay and carbonate cement	N	N

Table T5 (continued).

Core, section	Piece numbers	Analysis	Depth (mbsf)		Interval (cm)	Length (cm)			Subunit number	Lithology	Texture	Structure	Color	Comments	Chilled margin present	
			Top	Bottom		Interval	Unit	Subunit							Top	Base
16R-2	10-13	—	408.63	408.88	123-148	25	—	61	5-7	Aphyric basalt	Microcrystalline	Pillow/flow	Gray to bluish gray	Halos present in some pieces, thin carbonate veins, vesicles up to 2 mm in diameter filled with smectite and carbonate	N	N
16R-3	1-6	—	408.88	409.24	0-36	36	—			Aphyric basalt	Microcrystalline	Pillow/flow	Gray to bluish gray	Rubby, halos present in some pieces, thin carbonate veins	N	N
17R-1	1-20	—	415.50	417.00	0-150	150	—	174	5-8	Breccia	Microcrystalline to hypocrySTALLINE	Breccia	Dark greenish gray, white	Basalt clasts range in size up to 10 cm; halos are present in some of the basalt clasts	N	N
17R-2	1-4	—	417.00	417.24	0-24	24	—			Breccia	Microcrystalline to hypocrySTALLINE	Breccia	Dark greenish gray, white	Breccia with carbonate and dark grayish green clay matrix; some parts clast supported, other parts matrix supported	N	N
17R-2	5-14	—	417.24	417.84	24-84	60	315	60	6-1	Aphyric basalt	Microcrystalline	Pillow/flow	Dark gray	Rubby pieces, pronounced halos present in some pieces, thin dark red veins, carbonate veins, last piece finer grained	N	N
18R-1	1-4	—	425.10	425.52	0-42	42	—	42	6-2	Aphyric basalt	Microcrystalline	Pillow	Dark gray	Pronounced halos present in some pieces, carbonate veins	N	Y
18R-1	5-16	—	425.52	426.49	42-139	97	—	97	6-3	Aphyric basalt	Microcrystalline with fine-grained center	Pillow/flow	Dark gray	Chills at top and base of subunit and subvertical glassy chill on Piece 7, carbonate veins and halos present	Y	Y
19R-1	1-5	—	434.70	434.94	0-24	24	—	24	6-4	Breccia	Microcrystalline clasts	Breccia	Gray to dark gray	Angular basalt clasts up to 5 cm; some contain halos in carbonate cement	N	N
19R-1	6-15	—	434.94	435.47	24-77	53	—	53	6-5	Aphyric basalt	Fine grained to microcrystalline	Pillow/flow	Dark gray	Halos present in some pieces, thin dark red veins, carbonate veins	N	Y
19R-1	16-22	—	435.47	435.86	77-116	39	—	39	6-6	Aphyric basalt	Fine grained to microcrystalline	Pillow	Dark gray	Rubby small pieces, pronounced halos present in some pieces, thin dark red veins, carbonate veins	N	N

Notes: Lithology is shown diagrammatically in Figure F32C, p. 94. PP = physical properties, — = no analysis, TSB(2) = second thin section billet, TSB = thin section billet, XRF = X-ray fluorescence, Y = yes, N = no. This table is also available in [ASCII format](#).

Table T6. Location of volcanic glass, Site 1149.

Core, section, interval (cm)	Piece number	Comments
185-1149B-		
31R-1, 104-108	20	Thin glass margin
31R-1, 109-113	21	Thin glass margin
185-1149C-		
10R-2, 12-15	3	Margin
185-1149D-		
7R-2, 120-125	16	Thin margin on one of three subpieces
8R-2, 55-58	3	Glass piece in breccia
9R-1, 6-8	2	Pieces 1 and 3 also have glass
9R-1, 32-34	6	Glass margin
9R-1, 64-66	10	Glass margin
9R-2, 68-71	4	Margin
9R-2, 71-76	5	Margin
9R-3, 51-54	9	Margin

Note: This table is also available in [ASCII format](#).

Table T7. Primary mineralogy of thin sections, Site 1149.

Thin section number	Core, section, interval (cm), piece	Depth (mbsf)	Unit	Phenocrysts						Groundmass										
				Plagioclase		Pyroxene		Olivine		Plagioclase		Pyroxene		Olivine		Oxides		Glass	Vesicles	
				(vol%)	Size (mm)	(vol%)	Size (mm)	(vol%)	Size (mm)	(vol%)	Size (mm)	(vol%)	Size (mm)	(vol%)	Size (mm)	(vol%)	Size (mm)	(vol%)	(vol%)	Size (mm)
185-1149B-																				
91	29R-1, 133-136, 3	408.13	1						52	0.1	21	0.06	2	0.1	5	<0.05	20	1	0.2	
92	29R-2, 27-32, 2	408.57	1	<<1	0.4			<<1	0.2	45	0.1	26	0.02	1	0.1	4	<0.01	24	1	0.1
185-1149C-																				
94	11R-1, 43-45, 3	417.53	1		2	0.1			1	0.1					3	<0.01	94	1	0.1	
95	11R-1, 116-118, 11	418.26	1		<1	0.2			35	0.2	23	<0.05	1	0.1	4	<0.01	37	1	0.1	

Note: This table is also available in [ASCII format](#).

Table T8. Shipboard X-ray fluorescence (XRF) analyses and ICP-AES and -MS analyses,* Holes 1149B, 1149C, and 1149D.

Hole:	Shipboard XRF		ICP-AES and ICP-MS																	
	1149B	1149B	1149B	1149B	1149B	1149B	1149B	1149B	1149B	1149C	1149C	1149C	1149C	1149D	1149D	1149D	1149D	1149D	1149D	1149D
Core, section:	29R-3	30R-2	29R-2	29R-3	30R-2	30R-3	30R-1	32R-1		9R-1	10R-1	10R-2	11R-1	6R-2	9R-2	15R-1	16R-3	16R-3	17R-1	17R-2
Interval (cm):	45-50	91-94	105-110	45-50	91-94	46-52	148-150	136-142		91-94	14-16	41-44	71-74	82-85	13-17	29-32	0-2	27-30	80-83	79-84
Piece number:	4	4	12	4	4	6	19	17		6	3	9	4	10	1	7	1	5	9	14
Unit:	1	1	1	1	1	1	1	1		1	1	1	1	2	3	5	5	5	5	5
Depth (mbsf):	410.16	418.81	409.35	410.16	418.81	419.71	417.88	436.96		398.81	407.64	409.41	417.81	312.17	340.11	396.59	408.88	409.15	416.30	417.79
SiO ₂	50.97	52.40	50.29	50.45	51.71	50.31	49.75	49.98		50.90	49.55	48.94	50.12	50.77	51.00	51.04	49.43	50.16	49.29	50.05
TiO ₂	1.87	1.77	1.79	1.80	1.69	1.64	1.67	1.88		1.82	1.76	1.59	1.67	1.77	1.79	1.94	1.75	1.83	1.94	1.81
Al ₂ O ₃	15.17	15.62	15.51	15.63	16.01	15.50	15.66	16.98		15.66	15.18	14.81	15.69	15.46	15.63	16.83	16.01	16.61	16.41	16.46
Fe ₂ O ₃	9.14	7.02	10.34	9.51	7.19	11.36	11.00	10.79		8.61	12.70	11.12	10.12	9.91	9.22	8.21	9.95	8.62	11.64	9.75
MnO	0.20	0.16	0.16	0.17	0.13	0.15	0.16	0.12		0.14	0.19	0.19	0.15	0.14	0.13	0.15	0.24	0.18	0.19	0.15
MgO	7.87	8.53	7.41	7.78	8.28	7.38	7.39	7.23		7.89	6.72	7.11	7.53	7.23	6.98	8.01	6.44	7.34	6.57	6.35
CaO	11.21	11.69	10.96	11.19	11.59	10.53	10.42	8.84		11.53	10.55	12.87	11.23	10.90	11.67	9.74	12.46	11.45	9.16	11.58
Na ₂ O	2.83	2.77	2.75	2.73	2.69	2.73	2.75	2.98		2.79	2.79	2.61	2.73	2.90	2.86	3.22	2.74	2.97	2.98	2.94
K ₂ O	0.36	0.41	0.40	0.35	0.37	0.58	0.67	0.60		0.29	0.49	0.36	0.33	0.53	0.32	0.42	0.60	0.42	1.35	0.49
P ₂ O ₅	0.14	0.12	0.20	0.22	0.16	0.21	0.27	0.21		0.20	0.18	0.17	0.21	0.19	0.22	0.22	0.23	0.22	0.24	0.24
Total	99.76	100.47	99.87	99.88	99.90	100.50	99.87	99.87		99.88	100.18	99.88	99.87	99.86	99.87	99.89	99.91	99.89	99.89	99.89
LOI	1.41	1.27	2.33	2.26	2.66	3.24	3.62	5.08		2.26	2.35	3.34	3.22	2.00	2.15	3.25	2.52	3.22	3.63	2.69
Nb	5	3	3	4	3	2	2	3		4	2	2	3	3	3	4	7	7	7	7
Zr	—	—	111	120	106	91	92	103		112	104	91	89	107	112	124	127	129	138	127
Y	39	42	36	37	40	32	35	43		39	39	33	35	35	43	40	33	32	31	33
Sr	133	124	131	131	120	118	116	123		137	114	113	119	125	127	139	182	179	175	183
Rb	7	6	8	5	3	14	13	11		4	12	8	6	10	4	3	9	3	17	9
Zn	127	156	105	126	149	96	97	118		118	115	101	99	94	87	143	102	114	117	106
Cu	—	—	50	68	98	56	53	59		109	105	83	64	39	44	93	93	57	77	85
Ni	—	—	67	73	87	61	61	79		83	53	69	81	59	62	69	126	100	67	119
Cr	—	—	225	217	231	238	232	208		201	156	191	233	164	155	170	298	292	310	290
V	—	—	347	353	341	343	337	341		377	390	333	325	329	300	347	319	323	329	322
Ce	20	18	12	13	11	10	11	12		13	12	11	12	12	15	14	17	18	19	17
Ba	20	119	15	19	95	13	18	21		15	9	10	15	16	10	16	34	39	41	28

Notes: *ICP data were acquired in a shore-based laboratory at the Centre de Recherches Pétrographiques et Géo-chimiques-Centre National de la Recherche Scientifique (CRPG-CNRS), Nancy, France (major elements by ICP-AES, trace elements by ICP-MS; errors are <4% on all elements). — = undetermined. ICP-AES = inductively coupled plasma-atomic emission spectroscopy; MS = mass spectrometry. LOI = loss on ignition. This table is also available in [ASCII format](#).

Table T9. Summary of vein types, Holes 1149B and 1149C.

Vein type	Number	Average width (mm)	Width (mm)		Dark + brown halo		Dark halo	
			Minimum	Maximum	(%)	Half width (mm)	(%)	Half width (mm)
Carbonate (>90%)	123	1.6	0.1	18	51	6.3	23	6.1
Saponite (>90%)	185	0.4	0.1	3	46	4.6	16	3.7
Fe oxyhydroxide (10%-20%)	148	0.4	0.1	3	62	4.6	21	5.2
Mixed (carbonate/saponite/Fe oxyhydroxides)	33	1.7	0.1	12	40	6.8	32	5.8
Total:	489	0.9	0.1	18	48	5.4	30	5.4

Note: This table is also available in [ASCII format](#).

Table T10. Summary of vein types, Hole 1149D.

Vein type	Number	Average width (mm)	Width (mm)		Dark + brown halo		Dark halo	
			Minimum	Maximum	(%)	Half width (mm)	(%)	Half width (mm)
Carbonate (>90%)	127	1.3	0.1	12	36	6	35	5.6
Saponite (>90%)	222	0.2	0.1	2	36	4.5	31	4.3
Fe oxyhydroxide (10%-20%)	320	0.4	0.1	2	35	6.7	59	5.2
Mixed veins (carbonate/saponite/Fe oxyhydroxides)	48	1.6	0.1	12	67	6	17	5.3
Total:	717	0.6	0.1	18	38	5.8	44	5

Note: This table is also available in [ASCII format](#).

Table T11. Interstitial water data, Site 1149. (See table notes. Continued on next page.)

Core, section, interval (cm)	Depth (mbsf)	pH	Alkalinity (mM)	Salinity	SO ₄ (mM)	NH ₄ (μM)	H ₄ SiO ₄ (μM)	PO ₄ (μM)	Ca (mM)	Mg (mM)	Na (mM CB)	Na (mM.IC)	K (mM)	Li (μM)	Sr (μM)	Fe (μM)	Mn (μM)	Cl (mM Titr)	Cl (mM IC)
185-1149A-																			
1H-1, 140-150	1.40	7.50	2.635	34.5	29.87	18	559	19	10.62	52.32	478	479	12.16	37	87	0	187	554	552
1H-2, 140-150	2.90	7.53	3.355	34.5	28.15	37	499	33	10.80	52.84	473	480	11.79	32	90	0		553	554
2H-1, 140-150	5.60	7.77	2.723	34.5	27.95	77	608	28	11.29	51.77	476	483	13.08	27	91	0		557	555
2H-2, 140-150	7.10	7.53	2.640	34.5	27.99	105	571	34	11.22	51.45	479	480	12.07	26	91			558	556
2H-3, 140-150	8.60	7.47	2.600	34.5	27.85	94	698	34	11.41	51.58	477	480	11.93	25	92			557	556
2H-4, 140-150	10.10	7.67	2.763	34.5	28.00	110	659	29	11.01	50.64	481	482	12.60	25	92			558	559
2H-5, 140-150	11.60	7.52	2.644	34.5	27.95	112	651	29	11.21	50.68	481	481	12.29	25	91			559	560
2H-6, 140-150	13.10	7.79	2.827	34.5	27.89	120	630	27	10.92	50.23	484	483	12.63	25	91			561	560
3H-1, 140-150	15.10	7.68	2.688	34.5	27.97	140	611	24	11.60	50.73	484	483	12.21	25	93	0	182	563	562
3H-2, 140-150	16.60	7.62	2.638	34.5	27.80	148	636	28	11.45	50.15	486	484	12.10	25	91			563	559
3H-3, 140-150	18.10	7.79	2.601	35.0	27.76	162	634	21	11.85	50.26	484	486	13.15	26	93			564	562
3H-4, 140-150	19.60	7.70	2.597	35.0	27.71	158	621	16	11.78	50.41	483	487	12.25	25	92			562	564
3H-5, 140-150	21.10	8.15	3.010	35.0	28.39	164	608	16	12.27	51.40	483	488	11.92	25	96			563	565
3H-6, 140-150	22.60	7.95	2.593	35.0	29.17	177	546	5	11.81	49.44	488	493	13.23	25	93			563	565
4H-1, 140-150	24.60	7.89	2.547	35.0	28.06	162	531	5	11.97	49.86	486	490	13.26	27	95			565	565
4H-2, 140-150	26.10	8.06	2.533	35.0	27.94	180	607	5	11.74	48.26	491	489	13.37	26	93		95	566	567
4H-3, 140-150	27.60	7.56	2.381	35.0	28.00	194	625	9	12.10	49.61	485	486	12.16	26	93			563	566
4H-4, 140-150	29.10	8.15	2.562	35.0	27.81	196	487	7	11.68	48.10	485	490	14.31	26	92			561	564
4H-5, 140-150	30.60	7.52	1.964	35.0	27.92	172	676	10	12.18	49.66	485	489	12.37	26	93			564	564
4H-6, 140-150	32.10	7.72	2.332	35.0	27.83	189	658	8	12.10	49.35	488	489	12.47	27	94			566	566
5H-1, 140-150	34.10	7.58	2.183	35.0	27.59	178	605	12	12.05	48.73	486	483	11.63	27	94	0		562	556
5H-2, 140-150	35.60	7.59	2.131	35.0	27.82	172	709	13	12.25	48.98	487	491	11.96	28	93		204	564	564
5H-3, 140-150	37.10	7.47	2.638	35.0	27.81	185	713	12	12.58	49.42	487	487	11.84	29	94			565	565
5H-4, 140-150	38.60	7.49	1.894	35.0	27.90	162	695	12	12.42	48.66	487	490	11.67	29	93			563	560
5H-5, 140-150	40.10	7.63	2.003	35.0	28.22	167	698	10	12.71	49.11	487	488	11.75	30	95			564	565
5H-6, 140-150	41.60	7.53	1.865	35.0	27.33	151	654	10	12.80	49.24	484	486	12.00	29	93			564	563
6H-1, 140-150	43.60	7.57	1.889	35.0	27.38	167	713	10	12.55	48.63	485	491	11.40	31	93	0		562	565
6H-2, 140-150	45.10	7.40	1.756	35.0	27.54	180	753	11	12.45	48.40	487	488	11.45	31	95		282	564	563
6H-3, 140-150	46.60	7.36	1.577	35.0	27.64	167	671	8	12.72	48.68	487	489	10.95	31	93			564	562
6H-4, 140-150	48.10	7.47	1.760	35.0	27.22	156	685	7	12.74	48.43	488	485	10.95	31	94			565	561
6H-5, 140-150	49.60	7.43	1.753	35.0	27.52	180	688	7	12.93	48.82	486	490	11.80	31	93			565	564
6H-6, 140-150	51.10	7.35	1.505	35.0	27.16	172	727	8	12.90	48.31	488	482	11.03	33	95			566	558
7H-1, 140-150	53.10	7.31	3.251	35.0	28.04	161	662	7	13.03	48.83	489	489	10.95	32	96	0	284	565	566
7H-2, 140-150	54.60	7.39	1.610	35.0	27.10	174	664	8	12.91	48.49	489	487	10.91	33	95			567	559
7H-3, 140-150	56.10	7.33	1.652	35.0	27.63	183	735	8	13.09	48.03	489	491	11.32	33	94			566	563
7H-4, 140-150	57.60	7.48	1.561	35.0	27.71	186	667	7	13.41	48.98	488	489	10.74	31	97			567	565
7H-5, 140-150	59.10	7.43	1.516	35.0	26.78	180	685	8	13.12	48.04	488	481	10.68	31	97			566	554
7H-6, 130-140	60.50	7.53	1.516	35.0	26.84	172	664	7	13.21	48.03	487	486	11.51	32	96			566	558
8H-3, 140-150	65.60	7.36	1.543	35.0	26.62	167	744	5	13.08	47.21	488	481	11.17	34	94	0		565	552
9H-3, 140-150	75.10	7.23	1.524	35.0	26.51	148	761	4	13.16	46.48	490	484	10.98	37	95		293	566	555
10H-3, 140-150	84.60	7.33	1.433	35.0	26.63	143	783	3	12.29	46.64	489	483	11.02	40	95	0		564	557
11H-3, 140-150	94.10	7.33	1.434	35.0	27.38	128	803	3	14.20	46.07	486	488	10.70	42	95		302	561	563
12H-3, 140-150	103.60	7.30	1.491	35.0	26.34	121	790	3	14.84	46.02	483	484	10.41	41	97			561	561
14H-2, 140-150	121.10	7.35	2.220	34.0	25.40	89	494	11	15.63	47.41	472	474	9.33	41	97	0	191	555	555
16H-3, 140-150	141.60	7.54	2.067	34.0	25.28	83	231		15.73	48.67	467	465	9.38	51	94			553	547
18H-3, 140-150	160.60	7.35	2.621	34.0	25.09	59	231	1	15.84	47.61	473	475	9.40	53	84		6	557	555
20X-1, 140-150	171.20	7.39	2.169	34.0	24.52	47	418	1	16.03	47.27	472	479	10.24	52	83	0	3	558	564

Table T11 (continued).

Core, section, interval (cm)	Depth (mbsf)	pH	Alkalinity (mM)	Salinity	SO ₄ (mM)	NH ₄ (μM)	H ₄ SiO ₄ (μM)	PO ₄ (μM)	Ca (mM)	Mg (mM)	Na (mM CB)	Na (mM.IC)	K (mM)	Li (μM)	Sr (μM)	Fe (μM)	Mn (μM)	Cl (mM Titr)	Cl (mM IC)
185-1149B-																			
3R-4, 140-150	176.20	7.17	2.141	34.0	25.16	29	609		16.63	49.71	466	475	10.51	54	93		2	557	
16R-1, 93-98	283.23	7.27	1.154	35.5	24.96	47	625		31.83	41.05	468	472	8.41	50	373	0	11	572	
20R-1, 25-35	321.15	7.83	0.958	35.5	21.25	39	242		42.27	37.18	449	458	6.76	53	202			572	
22R-1, 20-25	340.30	7.52	0.587	35.5	21.45	60	255		51.57	33.56	452	438	5.47	90	250		11	585	
27R-1, 49-55	388.09			40.0	19.03	55	119		97.92	23.69	428	436	4.59	77	378	0	5	638	
29R-1, 28-35	407.08	6.90	0.341	40.0	19.45	62	232		135.32	14.56	348	355	2.82	45	250			612	

Notes: CB = calculated by charge balance, IC = measured by ion chromatography, Titr = measured by titration. Missing values = not analyzed, 0 = below detection limit. This table is also available in [ASCII format](#).

Table T12. Concentrations of CH₄ in the headspace gases, Site 1149.

Core, section, interval (cm)	Depth (mbsf)	CH ₄ (ppmv)
185-1149A-		
1H-2, 0-5	1.50	2
2H-5, 0-5	10.20	3
3H-5, 0-5	19.70	3
4H-5, 0-5	29.20	5
5H-5, 0-5	38.70	5
7H-5, 0-5	57.70	4
8H-4, 0-5	65.70	4
9H-4, 0-5	75.20	3
10H-4, 0-5	84.70	4
11H-4, 0-5	94.20	3
12H-4, 0-5	103.75	3
13H-4, 0-5	113.20	3
14H-3, 0-5	121.20	4
15H-5, 0-5	133.70	3
16H-4, 0-5	141.70	2
17H-2, 0-5	148.20	2
18H-4, 0-5	160.70	2
20X-CC, 0-5	171.30	2
21X-1, 0-5	179.10	2
185-1149B-		
2R-1, 0-5	160.60	2
3R-5, 0-5	176.30	2
12R-CC, 0-5	245.40	2
14R-CC, 0-5	263.90	2

Note: This table is also available in [ASCII format](#).

Table T13. Lithologic description of sediment samples taken for X-ray fluorescence analysis, Site 1149.

Core, section, interval (cm)	Depth (mbsf)	Brief description
185-1149A-		
1H-2, 68-70	2.18	Ash and silica-bearing clay
3H-5, 112-116	20.82	Clay, moderately mottled, dominant lithology
5H-4, 69-73	37.89	Clay, dominant lithology
7H-2, 77-82	53.97	Clay
9H-4, 39-43	75.59	Clay and ash-bearing siliceous ooze
11H-4, 84-87	95.04	Diatomaceous clay
12H-1, 54-57	99.74	Ash-rich clay, <10% biogenic silica
13H-4, 57-61	113.77	Clay
15H-4, 104-109	133.24	Clay, intensely mottled
17H-7, 62-66	155.37	Clay, no structural features
19X-CC, 86-90	166.10	Silt-bearing clay
21X-1, 61-63	179.71	Zeolitic clay, with or without ash
185-1149B-		
3R-7, 56-59	179.86	Clay
16R-1, 18-21	282.48	Porcelanite
18R-1, 9-11	301.69	Pink radiolarian limestone or marlstone
20R-1, 13-15	321.03	Radiolarian marlstone, calcareous radiolarian marlstone, or radiolarian limestone
22R-1, 46-49	340.52	Soft, calcareous nannofossil chalk with discontinuous chert laminations
26R-1, 34-36	378.44	Clayey nannofossil ooze, irregularly laminated, with oblique and randomly oriented dissolution seams
28R-1, 87-89	397.97	Radiolarian-bearing nannofossil marl with calcite-filled bedding-parallel veins

Note: This table is also available in [ASCII format](#).

Table T14. Geochemical data for carbonate-poor sediments, Site 1149.

Core, section, interval (cm)	Depth (mbsf)	Major elements (wt%)												Trace elements (ppm)						
		SiO ₂	TiO ₂	Al ₂ O ₃	Fe ₂ O ₃	MnO	MgO	CaO	Na ₂ O	K ₂ O	P ₂ O ₅	Total	LOI	Nb	Y	Sr	Rb	Zn	Ce	Ba
185-1149A-																				
1H-2, 68-70	2.18	61.830	0.795	16.665	7.610	0.180	3.075	2.575	3.945	2.765	0.140	99.580	8.696	9	24	160	94	117	61	680
3H-5, 112-116	20.82	64.515	0.765	16.835	5.770	0.290	2.880	1.740	4.185	3.365	0.110	100.455	8.656	10	24	152	107	118	61	630
5H-4, 69-73	37.89	63.205	0.785	16.785	7.080	0.125	2.875	2.255	4.325	2.835	0.145	100.415	8.783	9	28	156	95	120	61	663
7H-2, 77-82	53.97	62.920	0.740	16.210	6.820	0.315	2.620	2.750	4.440	2.665	0.320	99.800	8.443	8	31	169	86	109	64	610
9H-4, 39-43	75.59	61.075	0.815	16.585	8.505	0.280	2.950	3.410	4.215	2.350	0.120	100.305	8.191	7	27	151	74	121	51	509
11H-4, 84-87	95.04	61.925	0.820	17.240	7.715	0.360	2.800	2.635	4.210	2.665	0.150	100.520	8.641	9	33	160	90	122	63	444
12H-1, 54-57	99.74	61.500	0.818	16.913	8.110	0.320	2.875	3.023	4.213	2.508	0.135	100.413	8.337	10	33	133	99	120	65	455
13H-4, 57-61	113.77	59.695	0.845	17.950	8.665	0.305	3.590	2.100	4.370	2.805	0.130	100.455	9.147	10	34	132	96	129	71	471
15H-4, 104-109	133.24	58.985	0.840	19.870	8.110	1.325	3.790	0.680	3.160	3.250	0.170	100.180	9.528	11	38	126	119	142	107	473
17H-7, 62-66	155.37	54.195	0.920	18.120	9.010	3.660	3.485	1.970	2.675	3.790	1.095	98.920	9.356	19	204	286	98	210	238	479
19X-CC, 86-90	166.10	57.665	0.775	20.580	8.355	1.545	3.420	0.840	2.130	4.390	0.440	100.140	8.242	13	78	154	150	173	150	355
21X-1, 61-63	179.71	70.180	0.425	9.255	4.640	0.880	2.210	4.315	2.770	2.780	2.915	100.370	8.115	6	346	197	64	135	65	257
185-1149B-																				
3R-7, 56-59	179.86	57.955	0.765	15.795	8.240	2.115	4.075	2.365	2.460	4.415	1.435	99.620	12.154	17	225	223	109	227	163	485
16R-1, 18-21	282.48	83.970	0.440	4.980	4.405	0.725	2.015	0.510	1.050	1.705	0.180	99.980	4.668	19	31	111	44	99	75	2513
18R-1, 9-11	301.69	92.610	0.175	1.615	1.870	0.030	0.825	2.785	0.235	0.705	0.120	100.970	4.831	2	14	41	22	35	26	551

Notes: wt% = weight percent; ppm = parts per million; and LOI = loss on ignition. Major element concentrations are measured after ignition, and the data thus sum to ~100% with respect to the dry sample weight. Trace-element data for all samples are measured on unignited powder; therefore, the concentration data reported include the volatiles (see Fig. F57, p. 120). This table is also available in [ASCII format](#).

Table T15. Geochemical data for carbonate-rich sediments, Site 1149.

Core, section, interval (cm)	Depth (mbsf)	Major element ratio											Trace elements (ppm)						
		Fe/Al	MnO/ Al ₂ O ₃	P ₂ O ₅ / Al ₂ O ₃	SiO ₂ / Al ₂ O ₃	Ba/Al	Sr/Al	K ₂ O/ Al ₂ O ₃	Na ₂ O/ Al ₂ O ₃	MgO/ Al ₂ O ₃	Al/T	Nb/Al	Nb	Y	Sr	Rb	Zn	Ce	Ba
185-1149B-																			
20R-1, 13-15	321.03	1.12	0.097	0.050	26.7	0.105	0.010	0.344	0.235	0.220	12.3	0.000203	3	21	150	30	48	37	1549
22R-1, 46-49	340.52	1.41	0.117	0.034	11.8	0.299	0.036	0.041	BD	0.439	19.1	0.000092	1	22	396	17	19	36	3264
26R-1, 34-36	378.44	2.64	0.117	0.085	22.7	0.144	0.054	0.246	0.028	BD	16.5	0.000134	1	20	405	19	32	21	1070
28R-1, 87-89	397.97	4.81	0.956	0.286	13.9	0.559	0.112	0.198	BD	BD	20.1	BD	BD	17	270	9	BD	17	1347

Notes: BD = below detection limit. This table is also available in [ASCII format](#).

Table T16. Summary of physical properties of discrete samples from Holes 1149A, 1149B, 1149C, and 1149D with lithology and lithologic units as defined in "Lithostratigraphy," p. 11, and "Lithologic Units," p. 22. (See table note. Continued on next two pages.)

Core, section, interval (cm)	Depth (mbsf)	Wet bulk density (g/cm ³)		Grain density (g/cm ³)	Porosity (%)	Void ratio	Water content (bulk) (%)	Lithologic unit	Igneous structure
		Gravimetric	GRAPE						
185-1149A-									
1H-1, 61-63	0.61	1.36	1.34	2.68	79.8	3.96	60.1	Unit I	
1H-2, 69-71	2.19	1.45	1.44	2.76	75.5	3.08	53.3	Unit I	
1H-3, 40-42	3.40	1.46	1.46	2.67	73.9	2.83	52.0	Unit I	
2H-1, 45-47	4.65	1.40	1.40	2.63	76.7	3.29	56.1	Unit I	
2H-2, 31-33	6.01	1.49	1.46	2.84	74.4	2.91	51.2	Unit I	
2H-3, 122-124	8.42	1.28	1.28	2.65	84.0	5.25	67.0	Unit I	
2H-4, 43-45	9.13	1.35	1.35	2.63	79.9	3.97	60.7	Unit I	
2H-5, 47-49	10.67	1.39	1.40	2.62	77.4	3.42	57.2	Unit I	
2H-6, 62-64	12.32	1.39	1.39	2.70	78.3	3.60	57.7	Unit I	
2H-7, 40-42	13.60	1.39	1.41	2.65	77.5	3.44	57.1	Unit I	
3H-1, 83-85	14.53	1.39	1.39	2.66	77.7	3.49	57.3	Unit I	
3H-2, 110-112	16.30	1.39	1.42	2.63	77.0	3.35	56.6	Unit I	
3H-3, 98-100	17.68	1.44	1.44	2.59	73.6	2.78	52.4	Unit I	
3H-4, 76-78	18.96	1.46	1.47	2.62	72.9	2.69	51.2	Unit I	
3H-5, 31-33	20.01	1.42	1.45	2.66	75.5	3.09	54.3	Unit I	
3H-6, 113-115	22.33	1.37	1.40	2.66	78.5	3.66	58.5	Unit I	
3H-7, 33-35	23.03	1.39	1.40	2.60	76.5	3.26	56.2	Unit I	
4H-1, 111-113	24.31	1.44	1.45	2.67	74.7	2.95	53.1	Unit I	
4H-2, 112-114	25.82	1.45	1.41	2.72	75.1	3.02	53.2	Unit I	
4H-3, 114-116	27.34	1.44	1.43	2.66	74.6	2.94	53.2	Unit I	
4H-4, 92-94	28.62	1.40	1.40	2.61	76.2	3.21	55.7	Unit I	
4H-5, 117-119	30.37	1.43	1.42	2.68	75.8	3.13	54.4	Unit I	
4H-6, 123-125	31.93	1.40	1.38	2.59	76.1	3.18	55.7	Unit I	
4H-7, 52-54	32.72	1.44	1.35	2.65	74.3	2.90	52.8	Unit I	
5H-1, 111-113	33.81	1.44	1.46	2.59	73.2	2.73	51.9	Unit I	
5H-2, 119-121	35.39	1.46	1.45	2.57	71.6	2.52	50.1	Unit I	
5H-3, 22-24	35.92	1.49	1.48	2.55	69.5	2.28	47.7	Unit I	
5H-4, 96-98	38.16	1.45	1.44	2.69	74.2	2.88	52.3	Unit I	
5H-5, 33-35	39.03	1.41	1.41	2.58	75.5	3.08	55.0	Unit I	
5H-6, 97-99	41.17	1.42	1.42	2.62	75.5	3.08	54.6	Unit I	
5H-7, 36-38	42.06	1.42	1.44	2.66	75.9	3.15	54.8	Unit I	
6H-1, 112-114	43.32	1.41	1.42	2.57	74.8	2.98	54.3	Unit I	
6H-2, 78-80	44.48	1.42	1.40	2.56	74.3	2.89	53.6	Unit I	
6H-3, 87-89	46.07	1.45	1.39	2.83	76.3	3.21	53.8	Unit I	
6H-4, 111-113	47.81	1.43	1.43	2.58	74.2	2.88	53.4	Unit I	
6H-5, 84-86	49.04	1.45	1.48	2.58	72.4	2.63	51.0	Unit I	
6H-6, 100-102	50.70	1.42	1.43	2.61	74.8	2.96	53.8	Unit I	
6H-7, 22-24	51.42	1.42	1.45	2.57	74.6	2.93	53.9	Unit I	
7H-1, 71-73	52.41	1.47	1.45	2.57	71.2	2.47	49.6	Unit I	
7H-2, 71-73	53.91	1.43	1.41	2.46	71.7	2.54	51.4	Unit I	
7H-3, 106-108	55.76	1.43	1.41	2.69	75.3	3.06	53.8	Unit I	
7H-4, 99-101	57.19	1.47	1.47	2.61	71.8	2.55	49.9	Unit I	
7H-5, 75-77	58.45	1.42	1.40	2.58	74.4	2.91	53.6	Unit I	
7H-6, 89-91	60.09	1.41	1.42	2.56	74.8	2.96	54.2	Unit I	
7H-7, 37-39	60.97	1.43	1.42	2.58	74.2	2.88	53.3	Unit I	
8H-1, 117-119	62.37	1.41	1.42	2.61	75.6	3.10	54.9	Unit I	
8H-2, 111-113	63.81	1.48	1.48	2.51	69.4	2.27	48.1	Unit I	
8H-3, 54-56	64.74	1.58	1.55	2.65	66.2	1.96	43.0	Unit I	
8H-4, 72-74	66.42	1.43	1.42	2.64	74.8	2.97	53.5	Unit I	
8H-5, 49-51	67.69	1.41	1.41	2.57	74.8	2.98	54.2	Unit I	
8H-6, 48-50	69.18	1.43	1.43	2.65	74.8	2.97	53.5	Unit I	
8H-7, 39-41	70.59	1.44	1.46	2.59	73.6	2.79	52.5	Unit I	
9H-1, 54-56	71.24	1.42	1.41	2.58	74.6	2.93	53.8	Unit I	
9H-2, 59-61	72.79	1.44	1.44	2.63	74.2	2.88	52.8	Unit I	
9H-3, 55-57	74.25	1.37	1.40	2.60	78.3	3.61	58.7	Unit I	
9H-4, 72-74	75.92	1.43	1.41	2.63	74.8	2.97	53.6	Unit I	
9H-5, 80-82	77.50	1.44	1.46	2.60	74.0	2.85	52.8	Unit I	
9H-6, 62-64	78.82	1.43	1.44	2.68	75.5	3.08	54.0	Unit I	
10H-1, 61-63	80.81	1.40	1.40	2.57	75.4	3.07	55.0	Unit I	
10H-2, 52-54	82.22	1.43	1.48	2.64	74.8	2.97	53.5	Unit I	
10H-3, 57-59	83.77	1.42	1.44	2.56	74.4	2.91	53.7	Unit I	
10H-4, 91-93	85.61	1.39	1.38	2.61	76.7	3.29	56.4	Unit I	
10H-5, 111-113	87.31	1.40	1.40	2.64	77.0	3.35	56.5	Unit I	
10H-6, 68-70	88.38	1.41	1.42	2.60	75.4	3.07	54.8	Unit I	
11H-1, 61-63	90.31	1.43	1.46	2.61	74.4	2.90	53.2	Unit I	

Table T16 (continued).

Core, section, interval (cm)	Depth (mbsf)	Wet bulk density (g/cm ³)		Grain density (g/cm ³)	Porosity (%)	Void ratio	Water content (bulk) (%)	Lithologic unit	Igneous structure
		Gravimetric	GRAPE						
11H-2, 59-61	91.79	1.46	1.46	2.61	72.4	2.63	50.8	Unit I	
11H-3, 54-56	93.24	1.44	1.43	2.60	73.8	2.81	52.6	Unit I	
11H-4, 63-65	94.83	1.41	1.41	2.63	75.7	3.12	54.9	Unit I	
11H-5, 53-55	96.23	1.41	1.42	2.61	75.4	3.07	54.6	Unit I	
11H-6, 60-62	97.80	1.43	1.44	2.55	73.6	2.78	52.8	Unit I	
12H-1, 57-59	99.77	1.38	1.39	2.58	77.0	3.35	57.1	Unit I	
12H-2, 70-72	101.40	1.38	1.38	2.65	78.1	3.58	58.0	Unit I	
12H-3, 72-74	102.92	1.42	1.39	2.73	76.6	3.27	55.1	Unit I	
12H-4, 72-74	104.47	1.39	1.42	2.66	77.4	3.42	56.9	Unit I	
12H-5, 70-72	105.95	1.36	1.37	2.65	79.2	3.81	59.5	Unit I	
12H-6, 91-93	107.66	1.38	1.41	2.70	79.0	3.75	58.7	Unit I	
12H-7, 33-35	108.58	1.38	1.40	2.54	76.4	3.23	56.5	Unit I	
13H-1, 67-69	109.37	1.40	1.40	2.63	76.5	3.25	55.9	Unit I	
13H-2, 70-72	110.90	1.34	1.33	2.56	79.6	3.91	61.0	Unit I	
13H-3, 70-72	112.40	1.35	1.38	2.68	80.5	4.13	61.2	Unit I	
13H-4, 70-72	113.90	1.33	1.36	2.61	80.9	4.24	62.5	Unit I	
13H-5, 78-80	115.48	1.33	1.34	2.61	80.5	4.13	61.8	Unit I	
13H-7, 63-65	117.11	1.30	1.29	2.55	81.7	4.45	64.2	Unit I	
14H-1, 90-92	119.10	1.33	1.42	1.99	68.6	2.19	52.9	Unit IIA	
14H-2, 100-102	120.70	1.39	1.47	2.22	69.7	2.30	51.5	Unit IIA	
14H-3, 103-105	122.23	1.38	1.50	1.96	61.6	1.60	45.6	Unit IIA	
14H-4, 136-138	124.06	1.39	1.53	1.91	59.1	1.45	43.7	Unit IIA	
14H-5, 114-116	125.34	1.37	1.46	2.11	68.0	2.13	50.9	Unit IIA	
14H-6, 130-132	127.00	1.37	1.49	2.01	64.8	1.84	48.4	Unit IIA	
14H-7, 43-45	127.63	1.39	1.46	2.06	64.4	1.81	47.4	Unit IIA	
15H-1, 125-127	128.95	1.34	1.40	2.14	71.6	2.53	54.7	Unit IIA	
15H-2, 131-133	130.51	1.43	1.46	2.55	73.4	2.76	52.6	Unit IIA	
15H-3, 113-115	131.83	1.34	1.41	2.16	72.3	2.61	55.3	Unit IIA	
15H-4, 110-112	133.30	1.42	1.52	2.12	63.9	1.77	46.1	Unit IIA	
15H-5, 115-117	134.85	1.37	1.42	2.18	69.7	2.30	52.0	Unit IIA	
15H-6, 100-102	136.20	1.38	1.45	2.10	66.7	2.01	49.4	Unit IIA	
15H-7, 32-34	137.02	1.38	1.45	2.10	66.9	2.02	49.6	Unit IIA	
16H-1, 97-99	138.17	1.37	1.47	2.03	66.0	1.94	49.5	Unit IIA	
16H-2, 50-52	139.20	1.40	1.49	2.11	65.2	1.87	47.6	Unit IIA	
16H-3, 84-86	141.04	1.35	1.39	2.29	74.0	2.84	55.9	Unit IIA	
16H-4, 98-100	142.68	1.38	1.44	2.19	69.6	2.29	51.6	Unit IIA	
16H-5, 104-106	144.24	1.44	1.57	2.05	59.7	1.48	42.5	Unit IIA	
16H-6, 104-106	145.74	1.41	1.47	2.15	65.4	1.89	47.4	Unit IIB	
16H-7, 38-40	146.58	1.35	1.41	2.16	71.1	2.46	53.9	Unit IIB	
17H-1, 89-91	147.59	1.36	1.42	2.15	70.1	2.35	52.7	Unit IIB	
17H-2, 95-97	149.15	1.36	1.52	1.88	60.8	1.55	45.7	Unit IIB	
17H-3, 73-75	150.43		1.56				42.4	Unit IIB	
17H-4, 104-106	152.04		1.60				41.9	Unit IIB	
17H-5, 21-23	152.71		1.66				39.8	Unit IIB	
17H-6, 99-101	154.24		1.57				45.5	Unit IIB	
17H-7, 70-72	155.45		1.59				44.1	Unit IIB	
18H-1, 69-71	156.89		1.54				46.1	Unit IIB	
18H-2, 70-72	158.40		1.56				44.6	Unit IIB	
18H-3, 70-72	159.90		1.59				41.3	Unit IIB	
18H-4, 70-72	161.40		1.70				34.9	Unit IIB	
18H-5, 70-72	162.90		1.70				36.2	Unit IIB	
18H-6, 38-40	164.08		1.70				35.5	Unit IIB	
19X-1, 33-35	164.73		1.51				39.8	Unit IIB	
20X-1, 82-84	170.62		1.59				40.6	Unit IIB	
21X-1, 45-47	179.55		1.42				45.7	Unit IIB	
23N-1, 1-3	190.91	2.03		2.25	18.0	0.22	9.1	Unit III (porcelanite)	
185-1149B-									
2R-1, 28-30	160.88	1.50	1.51	2.64	70.8	2.43	48.5	Unit IIB	
4R-1, 22-24	180.22	1.92	1.28	2.15	20.7	0.26	11.1	Unit III (porcelanite)	
5R-1, 4-6	189.44	2.56	2.30	2.58	1.8	0.02	0.7	Unit III (chert)	
6R-1, 30-32	199.00	1.98	1.17	2.17	16.2	0.19	8.4	Unit III (porcelanite)	
7R-1, 3-5	203.73	1.98	1.54	2.23	20.9	0.26	10.8	Unit III (porcelanite)	
7R-1, 15-17	203.85	1.89	0.85	2.37	35.3	0.55	19.1	Unit III (porcelanite)	
8R-1, 10-12	208.20	2.52	0.82	2.55	1.9	0.02	0.8	Unit III (chert)	
9R-1, 30-32	217.70	2.50	1.79	2.54	2.8	0.03	1.2	Unit III (chert)	
10R-1, 12-14	226.92	2.52	1.65	2.59	4.1	0.04	1.7	Unit III (chert)	
11R-1, 23-25	236.53	2.05	1.38	2.38	25.0	0.33	12.5	Unit III (porcelanite)	
13R-1, 6-8	254.66	2.10		2.31	17.0	0.21	8.3	Unit III (porcelanite)	

Table T16 (continued).

Core, section, interval (cm)	Depth (mbsf)	Wet bulk density (g/cm ³)		Grain density (g/cm ³)	Porosity (%)	Void ratio	Water content (bulk) (%)	Lithologic unit	Igneous structure
		Gravimetric	GRAPE						
14R-CC, 0-2	263.90	1.99		2.43	31.5	0.46	16.2	Unit IV (chalk)	
16R-1, 55-57	282.85	1.94	1.43	2.65	43.9	0.78	23.2	Unit IV (chalk)	
16R-1, 79-81	283.09	1.92	1.05	2.46	37.9	0.61	20.3	Unit IV (chalk)	
17R-1, 5-7	292.05	2.13	1.12	2.50	25.7	0.35	12.4	Unit IV (marl)	
18R-1, 15-17	301.75	2.04	1.57	2.59	35.1	0.54	17.6	Unit IV (marl)	
18R-1, 59-61	302.19	1.24	2.06	2.62	86.2	6.24	71.0	Unit IV (chalk)	
19R-1, 127-129	312.57	2.26	1.37	2.77	29.4	0.42	13.3	Unit IV (marl)	
21R-CC, 13-15	330.63	2.62		2.65	2.3	0.02	0.9	Unit IV (chert)	
22R-1, 42-44	340.52	2.21	1.15	2.79	32.9	0.49	15.2	Unit IV (chalk)	
22R-1, 71-73	340.81	1.51	1.98	2.66	70.4	2.38	47.8	Unit IV (chalk)	
23R-CC, 3-7	349.73	2.45	0.75	2.49	2.5	0.03	1.0	Unit IV (chert)	
24R-1, 31-33	359.51	2.51	1.88	2.57	3.7	0.04	1.5	Unit IV (chert)	
24R-1, 51-54	359.71	2.53	0.43	2.56	1.9	0.02	0.8	Unit IV (chert)	
25R-1, 24-28	368.94	2.55	1.10	2.57	1.8	0.02	0.7	Unit IV (chert)	
26R-1, 50-52	378.60	2.82	1.47	2.90	4.1	0.04	1.5	Unit IV (marl)	
27R-1, 14-16	387.74	2.15	1.72	2.74	34.7	0.53	16.6	Unit IV (marl)	
27R-1, 59-63	388.19	2.44	1.69	2.48	2.7	0.03	1.1	Unit IV (marl)	
28R-1, 116-118	398.26	2.55	1.70	2.72	10.1	0.11	4.1	Unit IV (marl)	
28R-2, 36-38	398.78	2.19	1.60	2.75	32.2	0.48	15.1	Unit IV (marl)	
28R-2, 57-58	398.99	2.73	1.31	2.80	3.9	0.04	1.5	Unit IV (marl)	
29R-1, 60-62	407.40	2.39		2.81	23.7	0.31	10.2	Unit IV (marl)	
29R-1, 67-68	407.47	2.26	0.63	2.71	26.6	0.36	12.1	Unit IV (marl)	
29R-1, 131-132	408.11	2.38	1.97	2.69	18.7	0.23	8.0	Unit 1-1 (basalt breccia)	Basalt breccia
29R-2, 49-55	408.79	2.47	1.81	2.74	15.9	0.19	6.6	Unit 1-2 (aphyric basalt)	Pillow/flow
29R-2, 89-95	409.17	2.64	2.16	2.76	7.0	0.08	2.7	Unit 1-2 (aphyric basalt)	Pillow/flow
29R-3, 70-72	410.41	2.69	1.14	2.81	6.4	0.07	2.5	Unit 1-5 (aphyric basalt)	Pillow
30R-1, 42-46	416.82	2.80	1.86	2.91	5.5	0.06	2.0	Unit 1-6 (aphyric basalt)	Pillow
31R-1, 26-28	426.26	2.62	2.07	2.77	8.7	0.10	3.4	Unit 1-12 (aphyric basalt)	Pillow breccia
31R-2, 2-4	427.52	2.71	2.17	2.89	9.7	0.11	3.7	Unit 1-13 (aphyric basalt)	Pillow
185-1149C-									
3R-1, 55-57	284.15	1.79		2.40	44.1	0.79	25.2	Unit IV (marl)	
4R-1, 18-20	293.38	2.64		2.67	1.7	0.02	0.7	Unit IV (chert)	
5R-1, 14-16	302.94	2.57	1.43	2.60	2.4	0.02	0.9	Unit IV (chert)	
6R-1, 38-40	312.78	2.42	1.76	2.51	6.3	0.07	2.7	Unit IV (chert)	
8R-1, 67-69	388.87	2.37		2.81	24.7	0.33	10.7	Unit IV (marl)	
185-1149D-									
2R-1, 27-29	272.47	2.42		2.49	5.1	0.05	2.2	Unit IV (chert)	
4R-1, 40-42	291.30	2.53	1.06	2.56	2.2	0.02	0.9	Unit IV (chert)	
5R-1, 30-35	300.60	2.66	2.24	2.81	8.0	0.09	3.1	Unit 2-1 (aphyric basalt)	Flow
6R-1, 72-74	310.72	2.69	2.15	2.81	6.6	0.07	2.5	Unit 2-1 (aphyric basalt)	Flow
6R-2, 15-18	311.50	2.80	2.15	2.89	4.9	0.05	1.8	Unit 2-1 (aphyric basalt)	Flow
7R-1, 21-24	319.91	2.69	2.29	2.79	6.0	0.06	2.3	Unit 2-1 (aphyric basalt)	Flow
7R-2, 16-18	321.36	2.65	1.92	2.78	7.3	0.08	2.8	Unit 2-7 (aphyric basalt)	Pillow/flow
7R-2, 106-110	322.26	2.70	2.09	2.79	5.4	0.06	2.1	Unit 2-8 (aphyric basalt)	Pillow/flow
8R-1, 62-64	329.92	2.73	2.20	2.87	7.2	0.08	2.7	Unit 2-10 (aphyric basalt)	Flow
8R-1, 88-90	330.18	2.77	1.64	2.88	5.9	0.06	2.2	Unit 2-10 (aphyric basalt)	Flow
8R-2, 130-132	332.10	2.70	1.74	2.87	9.3	0.10	3.5	Unit 3-4 (aphyric basalt)	Pillow
9R-1, 88-90	339.68	2.73	2.13	2.85	6.6	0.07	2.5	Unit 3-8 (aphyric basalt)	Pillow/flow
9R-2, 92-94	340.90	2.76	2.26	2.89	6.7	0.07	2.5	Unit 3-10 (aphyric basalt)	Pillow/flow
9R-3, 27-29	341.75	2.71	1.72	2.82	6.0	0.06	2.3	Unit 3-11 (aphyric basalt)	Pillow/flow
10R-1, 6-8	348.46	2.77	2.32	2.90	6.9	0.07	2.5	Unit 3-11 (aphyric basalt)	Pillow/flow
10R-2, 27-29	350.17	2.55	0.79	2.74	11.4	0.13	4.6	Unit 3-16 (aphyric basalt)	Pillow
11R-1, 103-105	358.93	2.72	2.16	2.92	10.3	0.12	3.9	Unit 4-1 (aphyric basalt)	Flow
11R-2, 7-9	359.31	2.54	1.94	2.75	11.8	0.13	4.7	Unit 4-1 (aphyric basalt)	Flow
11R-3, 1-3	360.68	2.60	2.14	2.78	10.4	0.12	4.1	Unit 4-2 (basalt breccia)	Breccia
11R-4, 16-18	362.30	2.65	1.32	2.80	8.5	0.09	3.3	Unit 4-3 (aphyric basalt)	Flow
12R-1, 50-52	367.90	2.54	0.88	2.87	18.0	0.22	7.3	Unit 4-4 (aphyric basalt)	Pillow

Note: This table is also available in [ASCII format](#).

Table T17. Average wet bulk density, porosity, and velocity of each lithologic unit and each lithology, calculated from discrete sample measurements.

	Lithology	Wet bulk density (g/cm ³)	Grain density (g/cm ³)	Porosity (%)	Water content (%)	P-wave velocity (x direction) (m/s)
185-1149A, 1149B, 1149C, 1149D:						
Unit I	Clay	1.42	2.62	75.5	54.8	1528
Unit IIA	Clay	1.38	2.12	67.1	49.9	1520
Unit IIB	Clay	1.40	2.20	67.6	43.5	1514
Unit III	Chert	2.52	2.57	2.7	1.1	5167
	Porcelanite	2.06	2.30	19.5	10.0	3429
Unit IV	Chert	2.52	2.57	3.0	1.2	4958
	Chalk	1.80	2.60	50.5	32.3	2280
	Marl	2.32	2.69	22.8	10.9	2676
Basement	Basalt	2.66	2.82	8.8	3.5	4821

Note: This table is also available in [ASCII format](#).

Table T18. Compressional wave velocity measured on split cores and discrete samples. (See table note. Continued on next three pages.)

Core, section, interval (cm)	Depth (mbsf)	P-wave velocity (m/s)			Lithologic unit
		x direction	y direction	z direction	
185-1149A-					
1H-1, 63	0.62	1517	1500	1500	Unit I
1H-2, 70	2.20	1530	1503	1509	Unit I
1H-3, 41	3.41	1522	1509	1512	Unit I
2H-1, 45	4.65			1494	Unit I
2H-1, 69	4.86	1521	1503		Unit I
2H-2, 49	6.19	1519	1515		Unit I
2H-3, 64	7.84	1528	1522	1517	Unit I
2H-4, 45	9.15	1521	1514	1508	Unit I
2H-5, 49	10.69	1521	1504	1504	Unit I
2H-6, 62	12.33	1514	1508	1512	Unit I
2H-7, 41	13.62	1533	1504	1511	Unit I
3H-1, 84	14.53	1528	1506	1504	Unit I
3H-2, 114	16.34		1503	1527	Unit I
3H-3, 98	17.68	1534	1516	1515	Unit I
3H-4, 79	18.98	1532	1525	1517	Unit I
3H-5, 32	20.01	1534	1525	1516	Unit I
3H-6, 113	22.31	1517	1503		Unit I
3H-7, 36	23.04	1510	1480	1497	Unit I
4H-1, 114	24.33	1526		1508	Unit I
4H-2, 114	25.81	1529	1506		Unit I
4H-3, 117	27.35	1520	1503	1507	Unit I
4H-4, 95	28.63	1538	1504	1511	Unit I
4H-5, 116	30.38	1513	1498	1504	Unit I
4H-6, 124	31.94	1535			Unit I
4H-7, 53	32.73		1509	1503	Unit I
4H-7, 61	32.81	1533			Unit I
5H-1, 113	33.83	1572			Unit I
5H-2, 120	35.40	1527	1506	1509	Unit I
5H-3, 21	35.91	1549	1530	1531	Unit I
5H-4, 96	38.16	1531	1502	1511	Unit I
5H-5, 33	39.03	1529	1504	1506	Unit I
5H-6, 97	41.17	1526		1512	Unit I
5H-7, 45	42.15	1537		1526	Unit I
6H-1, 111	43.31	1529	1505	1505	Unit I
6H-2, 79	44.49	1515			Unit I
6H-3, 88	46.08	1520			Unit I
6H-4, 110	47.80	1533	1501	1507	Unit I
6H-5, 85	49.05	1530			Unit I
6H-6, 101	50.71	1536			Unit I
6H-7, 29	51.49	1527	1506	1501	Unit I
7H-1, 78	52.48	1543	1589	1514	Unit I
7H-2, 81	54.01	1522		1506	Unit I
7H-3, 100	55.70	1524	1501	1506	Unit I
7H-4, 100	57.20	1523	1504	1505	Unit I
7H-5, 76	58.46	1528			Unit I
7H-6, 90	60.10	1530			Unit I
7H-7, 38	60.97	1544			Unit I
8H-1, 118	62.38	1539			Unit I
8H-2, 113	63.83	1562			Unit I
8H-3, 55	64.75	1554			Unit I
8H-4, 73	66.43	1524		1532	Unit I
8H-5, 79	67.99	1535	1501	1515	Unit I
8H-6, 47	69.17	1532	1506	1505	Unit I
8H-7, 39	70.59	1543			Unit I
9H-1, 54	71.24	1538	1505	1516	Unit I
9H-2, 59	72.79	1512	1520	1506	Unit I
9H-3, 55	74.25	1514	1521	1512	Unit I
9H-4, 79	75.99	1521			Unit I
9H-5, 81	77.51	1515	1517	1513	Unit I
9H-6, 62	78.82	1521	1506		Unit I
10H-1, 64	80.84	1513			Unit I
10H-2, 53	82.23	1527	1506	1514	Unit I
10H-3, 57	83.77	1518		1522	Unit I
10H-4, 90	85.60	1515	1519	1515	Unit I
10H-5, 112	87.32	1512			Unit I

Table T18 (continued).

Core, section, interval (cm)	Depth (mbsf)	P-wave velocity (m/s)			Lithologic unit
		x direction	y direction	z direction	
10H-6, 69	88.39	1508	1512	1508	Unit I
10H-7, 6	89.26	1514			Unit I
11H-1, 62	90.32	1520	1527		Unit I
11H-2, 59	91.79	1521	1510	1517	Unit I
11H-3, 54	93.24	1506	1514	1506	Unit I
11H-4, 64	94.84	1510		1514	Unit I
11H-5, 53	96.23	1523	1521	1525	Unit I
11H-6, 60	97.80	1529	1525	1521	Unit I
11H-7, 21	98.91	1521			Unit I
12H-1, 58	99.78	1518	1526	1527	Unit I
12H-2, 70	101.40	1551	1545		Unit I
12H-3, 67	102.87	1550	1564		Unit I
12H-4, 70	104.45	1526	1547	1525	Unit I
12H-5, 70	105.95	1507	1515		Unit I
12H-6, 91	107.66	1500	1547		Unit I
12H-7, 33	108.57	1519	1517		Unit I
13H-1, 70	109.40	1505	1520		Unit I
13H-2, 70	110.90	1559			Unit I
13H-3, 70	112.40	1536			Unit I
13H-4, 47	113.67	1554			Unit I
13H-5, 79	115.49	1533			Unit I
13H-7, 63	117.11	1571			Unit I
14H-1, 90	119.10	1522			Unit IIA
14H-2, 101	120.71	1512			Unit IIA
14H-3, 104	122.24	1525			Unit IIA
14H-4, 137	124.07	1518			Unit IIA
14H-5, 122	125.42	1512			Unit IIA
14H-6, 132	127.01	1511			Unit IIA
14H-7, 44	127.64	1502			Unit IIA
15H-1, 119	128.89	1516			Unit IIA
15H-2, 135	130.55	1515			Unit IIA
15H-3, 114	131.84	1530			Unit IIA
15H-4, 119	133.39	1516			Unit IIA
15H-5, 121	134.91	1524			Unit IIA
15H-6, 101	136.21	1514			Unit IIA
15H-7, 33	137.03	1544			Unit IIA
16H-1, 97	138.17	1519			Unit IIA
16H-2, 52	139.22	1523			Unit IIA
16H-3, 85	141.05	1533			Unit IIA
16H-4, 99	142.69	1519			Unit IIA
16H-5, 105	144.25	1533			Unit IIA
16H-6, 104	145.74	1522			Unit IIB
17H-1, 89	147.59	1512			Unit IIB
17H-2, 95	149.15	1523			Unit IIB
17H-3, 73	150.43	1518			Unit IIB
17H-4, 104	152.04	1514			Unit IIB
17H-5, 21	152.71	1520			Unit IIB
17H-6, 100	154.25	1517			Unit IIB
17H-7, 70	155.45	1503			Unit IIB
18H-1, 70	156.90	1501			Unit IIB
18H-2, 70	158.40	1492			Unit IIB
18H-3, 70	159.90	1497			Unit IIB
18H-4, 70	161.40	1534			Unit IIB
18H-5, 70	162.90	1526			Unit IIB
18H-6, 38	164.08	1527			Unit IIB
19X-1, 34	164.74	1507			Unit IIB
20X-1, 83	170.62	1503			Unit IIB
21X-1, 45	179.55	1539			Unit IIB
185-1149B-					
2R-1, 29	160.88	1478			Unit IIB
3R-1, 70	171.00	1508			Unit IIB (pelagic clay)
3R-2, 70	172.50	1512			Unit IIB (pelagic clay)
3R-3, 70	174.00	1511			Unit IIB (pelagic clay)
3R-4, 70	175.50	1522			Unit IIB (pelagic clay)
3R-5, 70	177.00	1514			Unit IIB (pelagic clay)
3R-6, 70	178.50	1520			Unit IIB (pelagic clay)
3R-7, 25	179.55	1505			Unit IIB (pelagic clay)
4R-1, 10	180.10	3413	3427	2540	Unit III (porcelanite)

Table T18 (continued).

Core, section, interval (cm)	Depth (mbsf)	P-wave velocity (m/s)			Lithologic unit
		x direction	y direction	z direction	
4R-1, 33	180.33	4958			Unit III (chert)
5R-1, 12	189.52	5146			Unit III (chert)
6R-1, 6	198.76	5138			Unit III (chert)
6R-1, 40	199.10	3851	4067	3560	Unit III (porcelanite)
7R-1, 4	203.73	3307	3278	3391	Unit III (porcelanite)
7R-1, 6	203.76	2914			Unit III (porcelanite)
8R-1, 8	208.18	5014			Unit III (chert)
9R-1, 31	217.70	6382	5067		Unit III (chert)
9R-1, 43	217.83	5048			Unit III (chert)
10R-1, 21	227.01	5110			Unit III (chert)
11R-1, 14	236.44	5022			Unit III (chert)
13R-1, 3	254.63	3870			Unit III (porcelanite)
13R-1, 7	254.66	4966	3709		Unit III (chert)
15R-1, 2	273.32	3219			Unit III (porcelanite)
16R-1, 43	282.73	2069			Unit IV (chalk)
16R-1, 80	283.09	2165	2425	2409	Unit IV (chalk)
16R-1, 106	283.36	2110			Unit IV (chalk)
17R-1, 23	292.23	3315			Unit IV (chalk)
18R-1, 12	301.72	2380			Unit IV (chalk)
18R-1, 70	302.30	2320			Unit IV (chalk)
18R-1, 123	302.83	4946			Unit IV (chert)
19R-1, 45	311.75	2095			Unit IV (chalk)
19R-1, 90	312.20	2695			Unit IV (chalk)
19R-1, 128	312.58	3185	3194	2883	Unit IV (marl)
20R-1, 10	321.00	2174			Unit IV (chalk)
20R-1, 58	321.48	2349			Unit IV (chalk)
20R-1, 97	321.87	4828			Unit IV (chert)
20R-1, 117	322.07	3036			Unit IV (marl)
22R-1, 29	340.39	3062			Unit IV (marl)
22R-1, 60	340.70	2413			Unit IV (chalk)
22R-1, 98	341.08	4990			Unit IV (chert)
24R-1, 32	359.52	4886	4808	4886	Unit IV (chert)
24R-1, 38	359.58	4991			Unit IV (chert)
26R-1, 4	378.14	1953			Unit IV (chalk)
26R-1, 31	378.41	2021			Unit IV (chalk)
26R-1, 81	378.91	4861			Unit IV (chert)
27R-1, 44	388.04	2172			Unit IV (chalk)
28R-1, 54	397.64	2369			Unit IV (chalk)
28R-2, 25	398.67	1935			Unit IV (chalk)
28R-2, 78	399.20	4903			Unit IV (chert)
29R-1, 38	407.18	2035			Unit IV (marl)
29R-1, 82	407.62	2381			Unit IV (marl)
29R-1, 99	407.79	3825			Unit 1-1 (aphyric basalt)
29R-1, 132	408.12	4051			Unit 1-1 (aphyric basalt)
29R-2, 52	408.82	4260			Unit 1-2 (aphyric basalt)
29R-3, 90	410.61	4606			Unit 1-4 (aphyric basalt)
30R-1, 43	416.83	5210			Unit 1-6 (aphyric basalt)
30R-1, 67	417.07	4922			Unit 1-7 (basalt with vein)
30R-2, 45	418.35	4840			Unit 1-9 (aphyric basalt)
30R-2, 84	418.74	5051			Unit 1-9 (aphyric basalt)
31R-1, 26	426.26	4519			Unit 1-12 (basalt breccia)
31R-1, 87	426.87	4349			Unit 1-12 (basalt breccia)
31R-2, 3	427.53	5017			Unit 1-13 (basalt with vein)
32R-1, 34	435.94	5647			Unit 1-14 (aphyric basalt)
32R-1, 98	436.58	4904			Unit 1-15 (aphyric basalt)
185-1149C-					
8R-1, 15	388.35	2356			Unit IV (marl)
9R-1, 20	398.10	2223			Unit IV (chalk)
9R-1, 76	398.66	4173			Unit 1-1 (aphyric basalt)
10R-1, 28	407.78	4836			Unit 1-2 (aphyric basalt)
10R-1, 96	408.46	4984			Unit 1-3 (aphyric basalt)
10R-1, 139	408.89	4823			Unit 1-4 (basalt breccia)
10R-2, 44	409.44	5427			Unit 1-5 (aphyric basalt)
11R-1, 6	417.16	5203			Unit 1-5 (aphyric basalt)
11R-1, 31	417.41	5167			Unit 1-5 (aphyric basalt)
185-1149D-					
2R-1, 17	272.37	4525			Unit IV (chert)
2R-1, 33	272.53	5493			Unit IV (chert)

Table T18 (continued).

Core, section, interval (cm)	Depth (mbsf)	P-wave velocity (m/s)			Lithologic unit
		x direction	y direction	z direction	
3R-1, 3	281.63	5226			Unit IV (chert)
3R-1, 28	281.88	5328			Unit IV (chert)
4R-1, 35	291.25	4439			Unit IV (chert)
5R-1, 9	300.39	5186			Unit IV (chert)
5R-1, 29	300.59	4569			Unit 2-1 (aphyric basalt)
6R-1, 64	310.64	4636			Unit 2-1 (aphyric basalt)
6R-2, 12	311.47	4825			Unit 2-1 (aphyric basalt)
6R-2, 58	311.93	5264			Unit 2-1 (aphyric basalt)
7R-2, 103	322.23	4947			Unit 2-8 (aphyric basalt)
7R-3, 19	322.84	5167			Unit 2-9 (aphyric basalt)
8R-1, 58	329.88	4804			Unit 2-10 (aphyric basalt)
8R-1, 86	330.16	4997			Unit 2-10 (aphyric basalt)
8R-1, 136	330.66	5094			Unit 2-10 (aphyric basalt)
8R-2, 134	332.14	4876			Unit 3-4 (aphyric basalt)
9R-1, 94	339.74	5147			Unit 3-8 (aphyric basalt)
9R-2, 18	340.16	5159			Unit 3-9 (aphyric basalt)
9R-2, 100	340.98	4786			Unit 3-10 (basalt with vein)
9R-3, 30	341.78	5198			Unit 3-10 (aphyric basalt)
10R-1, 19	348.59	5063			Unit 3-11 (aphyric basalt)
10R-1, 47	348.87	4787			Unit 3-13 (aphyric basalt)
10R-2, 8	349.98	4795			Unit 3-15 (aphyric basalt)
11R-1, 64	358.54	5141			Unit 4-1 (basalt with vein)
11R-1, 124	359.14	4439			Unit 4-1 (basalt with vein)
11R-2, 73	359.97	4827			Unit 4-1 (basalt with vein)
11R-2, 111	360.35	4780			Unit 4-1 (basalt with vein)
11R-3, 28	360.95	4677			Unit 4-2 (basalt breccia)
11R-3, 72	361.39	4704			Unit 4-2 (basalt breccia)
12R-1, 65	368.05	4884			Unit 4-4 (basalt breccia)
13R-1, 93	377.93	3408			Unit 4-7 (hyaloclastite)
13R-1, 123	378.23	4667			Unit 4-8 (aphyric basalt)
15R-1, 40	396.70	4508			Unit 5-5 (aphyric basalt)
16R-1, 40	406.30	4897			Unit 5-6 (breccia)
16R-1, 120	407.10	4121			Unit 5-6 (breccia)
16R-2, 124	408.62	5090			Unit 5-7 (aphyric basalt)
16R-3, 29	409.17	5020			Unit 5-7 (aphyric basalt)
17R-1, 40	415.90	5039			Unit 5-8 (breccia)
17R-2, 81	417.81	4965			Unit 6-1 (aphyric basalt)
18R-1, 75	425.85	5282			Unit 6-3 (aphyric basalt)
19R-1, 75	435.45	4862			Unit 6-5 (aphyric basalt)

Note: This table is also available in [ASCII format](#).

Table T19. Thermal conductivity (TC) values, Holes 1149A, 1149B, 1149C, and 1149D.

Core, section, interval (cm)	Depth (mbsf)	TC (W/[m·K])
185-1149A-		
1H-2, 70	2.20	0.85
2H-4, 70	9.40	0.80
3H-4, 70	18.90	0.85
4H-4, 70	28.40	0.83
5H-4, 75	37.95	0.79
6H-2, 70	44.40	0.81
6H-4, 75	47.45	0.88
6H-6, 75	50.45	0.86
7H-4, 75	56.95	0.85
8H-2, 75	63.45	0.85
8H-4, 75	66.45	0.85
8H-6, 75	69.45	0.80
9H-4, 75	75.95	0.81
10H-4, 75	85.45	0.80
11H-4, 75	94.95	0.85
12H-4, 73	104.48	0.85
13H-4, 75	113.95	0.82
14H-4, 75	123.45	0.92
15H-4, 75	132.95	0.89
16H-4, 75	142.45	0.90
17H-2, 75	148.95	0.87
18H-4, 75	161.45	0.96
19X-1, 45	164.85	0.82
20X-1, 75	170.55	0.90
21X-1, 50	179.60	0.78
185-1149B-		
29R-3, 9	409.80	1.62
30R-1, 43	416.83	1.64
31R-1, 30	426.30	1.45
32R-1, 33	435.93	1.57
185-1149C-		
9R-1, 74-83	398.69	1.69
10R-1, 26-34	407.80	1.61
11R-1, 1-12	417.17	1.68
185-1149D-		
6R-2, 10-15	311.48	1.63
7R-1, 50-55	320.23	1.58
8R-1, 132-139	330.66	1.59
9R-2, 9-15	340.10	1.60
10R-1, 1-12	348.47	1.50
11R-2, 60-68	359.88	1.59
17R-1, 34-43	415.89	1.36
18R-1, 70-87	425.89	1.66

Note: This table is also available in [ASCII format](#).

Table T20. Shear strength, Hole 1149A.

Core, section, interval (cm)	Depth (mbsf)	Shear strength (kPa)
185-1149A-		
2H-1, 66.4	4.86	20.4
2H-2, 55.3	6.25	29.0
2H-4, 51.7	9.22	30.1
2H-6, 69.3	12.39	133.0
3H-1, 72.6	14.43	49.8
3H-3, 103.5	17.74	47.5
3H-5, 39.9	20.10	98.6
3H-7, 48.3	23.18	66.5
4H-2, 120.4	25.90	68.9
4H-4, 107.8	28.78	115.7
4H-6, 133.4	32.03	122.2
5H-2, 126.9	35.47	49.2
5H-4, 84.1	38.04	58.3
5H-6, 104.8	41.25	99.6
6H-2, 66.2	44.36	73.3
6H-4, 117	47.87	50.8
6H-6, 109.2	50.79	49.5
7H-2, 86.4	54.06	50.6
7H-4, 107.9	57.28	63.0
7H-6, 96.9	60.17	94.3
8H-2, 117.1	63.87	56.8
8H-4, 88.5	66.58	66.8
9H-2, 64.6	72.85	50.6
9H-4, 78	75.98	72.1
10H-2, 60	82.30	59.7
10H-4, 95.6	85.66	55.8
10H-6, 74.9	88.45	63.8
11H-2, 65	91.85	136.9
11H-4, 69.2	94.89	73.8
11H-6, 66.1	97.86	53.5
12H-2, 75.1	101.45	80.2
12H-4, 75.2	104.50	106.3
12H-6, 97.6	107.73	98.8
13H-2, 74.8	110.95	46.7
13H-4, 61.8	113.82	73.7
13H-7, 67.6	117.16	136.4
14H-2, 94	120.64	117.9
14H-4, 126.8	123.97	104.3
14H-6, 122.7	126.93	99.9
15H-2, 136.5	130.57	108.2
15H-4, 112.9	133.33	125.1
15H-6, 94.4	136.14	105.5
16H-2, 55.2	139.25	122.3
16H-4, 92.4	142.62	130.3
16H-6, 97.7	145.68	126.3
17H-2, 87.9	149.08	147.2
17H-4, 96.5	151.96	123.7
17H-6, 94.9	154.20	106.8
18H-2, 72.9	158.43	153.0
18H-4, 67	161.37	127.1
18H-6, 60	164.30	113.4
19X-1, 63.2	165.03	79.6
20X-1, 77.7	170.58	59.3
21X-1, 63.6	179.74	18.8

Note: This table is also available in [ASCII format](#).

Table T21. List of samples taken for microbiological analysis, Site 1149.

Core, section	Biomass	Cultivation					Preservation		Tracers	
	ATP	SM	SF	M	Pressure	Frozen	AODC	DNA	Spheres	PFT
185-1149A-										
1H-1	X	X	X				X	X		
1H-2	X						X	X		
2H-1	X						X	X		
2H-2	X	X	X				X	X		
2H-3	X						X	X		
2H-4	X						X	X		
2H-5	X						X	X		
2H-6	X	X	X				X	X		
3H-1	X						X	X	X	
3H-2	X	X	X	X			X	X	X	
3H-3	X						X	X	X	
3H-4	X						X	X	X	
3H-5	X						X	X	X	
3H-6	X	X	X				X	X	X	
4H-1	X						X	X		
4H-2	X	X	X		X	X	X	X		
4H-3	X						X	X		
4H-4	X	X	X				X	X		
4H-5	X						X	X		
4H-6	X						X	X		
5H-1	X						X	X		
5H-2	X	X	X				X	X		
5H-3	X						X	X		
5H-4	X						X	X		
5H-5	X	X	X	X			X	X		
5H-6	X						X	X		
6H-1	X	X	X		X	X	X	X	X	X
6H-2	X						X	X	X	X
6H-3	X						X	X	X	X
6H-4	X						X	X	X	X
6H-5	X						X	X	X	X
6H-6	X	X	X	X			X	X	X	X
7H-6	X	X	X	X			X	X		
8H-3	X						X	X		
9H-3	X	X	X	X	X	X	X	X	X	X
10H-3	X						X	X		
11H-3	X	X	X	X	X	X	X	X		X
12H-3	X						X	X	X	
14H-3	X						X	X		
16H-3	X						X	X		
18H-3	X						X	X		
20X-1	X	X	X	X	X	X	X	X		
185-1149B-										
3R-4	X	X	X	X			X	X		
7R-CC							X	X		
16R-1					X		X	X		
22R-1		X	X	X	X		X	X		
26R-1							X	X		
27R-1							X	X		
28R-2							X	X		X
185-1149C-										
8R-1		X	X	X			X	X		
9R-1										X

Notes: ATP = adenosine triphosphate; SM = sulfate medium; SF = sulfate-free medium; M = methanogen medium; AODC = acridine orange direct count; and PFT = perfluorocarbon tracer. This table is also available in [ASCII format](#).

Table T22. Results of perfluorocarbon tracer tests, Site 1149.

Core, section	Lithology	Position	Weight (g)	PFT (g)	Drilling fluid (mL)	Drilling fluid/rock (mL/g)
Sediment:						
185-1149A-						
9H-1	Unconsolidated	Interior	5.69	0.0E+00	0.0E+00	0.0E+00
		Exterior	6.50	3.9E-09	3.9E-03	6.1E-04
9H-2	Unconsolidated	Interior	5.67	1.2E-09	1.2E-03	2.1E-04
		Exterior	5.57	2.2E-08	2.2E-02	4.0E-03
9H-3	Unconsolidated	Interior	5.56	0.0E+00	0.0E+00	0.0E+00
		Exterior	6.01	1.6E-08	1.6E-02	2.6E-03
9H-4	Unconsolidated	Interior	6.28	0.0E+00	0.0E+00	0.0E+00
		Exterior	5.80	3.5E-10	3.5E-04	6.1E-05
9H-5	Unconsolidated	Interior	5.60	4.6E-10	4.6E-04	8.2E-05
		Exterior	6.46	2.5E-08	2.5E-02	3.8E-03
9H-6	Unconsolidated	Interior	5.98	0.0E+00	0.0E+00	0.0E+00
		Exterior	6.22	0.0E+00	0.0E+00	0.0E+00
11H-1	Unconsolidated	Interior	6.95	2.2E-10	2.2E-04	3.1E-05
		Exterior	7.14	5.4E-10	5.4E-04	7.6E-05
11H-2	Unconsolidated	Interior	7.16	4.0E-11	4.0E-05	5.6E-06
		Exterior	7.33	8.0E-10	8.0E-04	1.1E-04
11H-3	Unconsolidated	Interior	6.66	2.0E-11	2.0E-05	3.0E-06
		Exterior	5.74	0.0E+00	0.0E+00	0.0E+00
11H-4	Unconsolidated	Interior	6.65	1.4E-10	1.4E-04	2.2E-05
		Exterior	7.78	8.5E-11	8.5E-05	1.1E-05
11H-5	Unconsolidated	Interior	7.66	0.0E+00	0.0E+00	0.0E+00
		Exterior	7.62	1.5E-09	1.5E-03	2.0E-04
11H-6	Unconsolidated	Interior	4.39	1.2E-08	1.2E-02	2.6E-03
		Exterior	4.64	5.6E-10	5.6E-04	1.2E-04
185-1149B-						
28R-2	Marl	Interior	9.37	9.9E-10	9.9E-04	1.1E-04
		Interior	12.43	6.0E-09	6.0E-03	4.8E-04
		Exterior	2.85	4.1E-09	4.1E-03	1.4E-03
	Chert	Exterior	4.38	1.0E-08	1.0E-02	2.3E-03
		Exterior	7.03	1.7E-08	1.7E-02	2.5E-03
		Exterior	4.74	1.1E-08	1.1E-02	2.3E-03
185-1149C-						
9R-1	Chalk	Interior	7.16	8.2E-12	8.2E-06	1.1E-06
		Interior	3.13	6.5E-10	6.5E-04	2.1E-04
		Exterior	1.61	1.9E-07	1.9E-01	1.2E-01
		Exterior	1.62	1.8E-08	1.8E-02	1.1E-02
		Exterior	3.4	6.6E-09	6.6E-03	1.9E-03

Notes: PFT = Perfluorocarbon tracer. Table modified from Smith et al. (in press).
This table is also available in [ASCII format](#).

Table T23. Results of fluorescent microsphere tests on sediment samples, Site 1149.

Core, section	Outer edge*	Intermediate*	Center*
185-1149A-			
3H-1			0
3H-2			0
3H-3			0
3H-4			0
3H-5			0
3H-6			0
6H-1			0
6H-2			0
6H-3			0
6H-4			0
6H-5			0
6H-6			0
9H-1	2.98E+05	1.13E+05	0
9H-2	4.70E+06	0	0
9H-3	3.50E+06	0	0
9H-4	1.09E+06	2.00E+05	0
9H-5	8.10E+05	0	0
9H-6	0	0	0
12H-1	1.30E+04	0	0
12H-2	4.40E+04	0	0
12H-3	1.00E+03	0	0
12H-4	3.00E+03	0	0
12H-5	0	0	0
12H-6	0	0	0

Notes: * = number of microspheres per milliliter of sediment suspension. Blank spaces = no data. Table modified from Smith et al. (in press). This table is also available in [ASCII format](#).